The Characterisation of Microemulsions Using NMR Measurements of Diffusion

By

Susan J. Law

A thesis submitted to
The University of Birmingham
For the degree of
DOCTOR OF PHILOSOPHY

School of Chemistry
College of Engineering and Physical Sciences

UNIVERSITY OF BIRMINGHAM

November 2014

Abstract

This thesis investigates how nuclear magnetic resonance (NMR) measurements of diffusion are used to characterise reverse micelles (RMs) in water-in-oil (w/o) microemulsions. The average droplet sizes were determined at varying water to surfactant ratios (ω) and droplet volume fractions (ϕ_d), by converting the diffusion coefficients from the surfactant molecules into hydrodynamic radii using the Stokes-Einstein equation. The size distributions of AOT/*n*-octane/water RMs were obtained by the application of a constrained form of the inverse Laplace transform. The AOT/iso-octane/water/pentanol and CTAB/hexanol/water systems were also studied, where the alcohols act as co-surfactants. Molecular exchange processes were observed between the RMs and the continuous phase, at varying NMR experimental parameters at different ω and ϕ_d. There was a decrease in droplet sizes with the addition of pentanol to the AOT/iso-octane/water system, which was observed with consideration to the changes in the viscosity of the continuous phase due to the partitioning and exchange of co-surfactant molecules.

Molecular simulations of solvated RMs were set up at the same values of ω as the NMR experiments. The simulations, which were constructed with all-atom forcefields, displayed the interactions between the molecules in the continuous and dispersed phases and showed the RM shape fluctuations and development. The AOT/iso-octane/water/pentanol droplets formed split RMs and were smaller than RMs in the AOT/iso-octane/water system at values of $\omega < 20$. These observations were reflected in the experimental results. The CTAB/hexanol/water droplets formed oblate RMs initially, which continued to fragment into smaller droplets, due to hexanol molecules penetrating the micelle interface.

Dedicated to the memory of my parents,

Francis David Law and Doris Law

and my beautiful brother

Andrew Michael Law.....

Acknowledgements

I would like to say a huge thank you to my supervisor, Melanie Britton for her encouragement and continuous support throughout the PhD. She has not only been a fantastic teacher and learning facilitator, but has always been understanding and supportive with issues inside and outside the academic sphere. Without this understanding from my supervisor, I would not have been able to cross the marathon finishing line. It has been a privilege to be part of the research team, where the members are so supportive of each other. I would like to thank Heather and Jan for all their help at the start of my PhD, Christian for sharing time in the DLS lab and to Matt and Catherine for all their help and advice. A special thank you must go to Amanda for making sure I didn't pull all my hair out when setting up and analysing molecular simulations and for all the NMR and microemulsion discussions. I would like to thank dearest Antoine for all his patience and words of wisdom. I would also like to say a big thank you to Dr. John Wilkie for all his time and help in teaching me and supporting me in my molecular simulations work and I must also thank Mark Oakley for all his invaluable help and advice.

It would not have been possible to complete my PhD without the countless number of people, who freely gave up their time to look after my children. The list is endless, but I need to thank in particular my mother and father-in-law, Teresa and Peter, my sisters and brothers and in particular my nephew Lee and brother Andy. Also Janet Isitt, a dear lady and dearest friends Wendy Spooner, Lisa Taylor and Emma Malpass. I would also like to thank my husband, Nigel, without whom, this adventure would not have been possible and to my beautiful children Elisabeth and William, thank you for being so lovely.

I hereby declare that the work presented in this thesis is entirely the original work of the author, except when other people's research is discussed and referred to, where it is acknowledged and referenced appropriately.

Table of Contents

List of Figures

List of Tables

List of Abbreviations

AOT – sodium bis(2-ethylhexyl) sulfosuccinate

BPPSTE – bipolar pulse pair stimulated echo

CTAB - cetyltrimethylammonium bromide

DEXSY– diffusion exchange spectroscopy

DLS – dynamic light scattering

FCS – fluorescence correlation spectroscopy

ILT – inverse Laplace transform

NMR – nuclear magnetic resonance

PGSTE – pulsed gradient stimulated echo

PGSE – pulsed field gradient spin echo

REXSY– relaxation exchange spectroscopy

RMs – reverse micelles

SAXS – small angle x-ray scattering

SANS – small angle neutron scattering

ST – Stejskal-Tanner

1. Introduction

1.1. Microemulsions and Reverse Micelles

1.1.1. Phase Behaviour of Reverse Micelles and Micelles

Reverse micelles (RMs) are self-assembled, nano-sized water droplets, which are surrounded and stabilised by a surfactant layer, in an organic solvent. They are formed at specific ratios of water, surfactant and organic solvent in microemulsions. As the concentration ratios vary between oil, water and surfactant, there are transitions between varying nano-structures. The concentrations at which these transitions occur are mapped in phase diagrams.[1,2] Phase diagrams give information about the critical micelle formation (CMC) and the limiting concentrations of when water-in-oil (w/o), (Figure 1.1(a)) or oil-in-water (o/w) (Figure 1.1(c)) RMs form. Water-in-oil RMs are formed when the surfactant hydrophobic tail is directed towards the continuous organic phase and the hydrophilic headgroup is embedded in the water droplet. Micelles and o/w RMs, however, form oil droplets with the surfactant tails embedded in the oil droplet and the headgroups directed towards the aqueous continuous phase.[3]

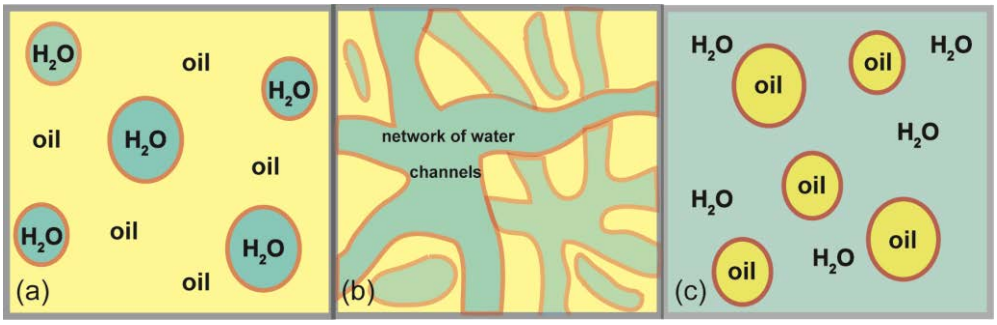

Figure 1.1: *A schematic representation of the transition from w/o RMs (a), to bicontinuous structures (b) and o/w RMs (c).*

At the transition point between w/o and o/w RMs, bicontinuous structures are formed (Figure 1.1 (b)),[3] where water channels, rather than discrete droplets are present.

In this thesis, the formation, sizes and dynamics of water-in-oil (w/o) RMs, which are thermodynamically stable[4] ranging in droplet size from 1 – 20 nm, are investigated. The formation of RMs is driven by the hydrophobic effect, where the amphiphilic nature of the surfactant creates a more energetically favourable system between the oil and water molecules. In a solution of oil and water, the interfacial tension[5] is of the order 50 mN m^{-1}. If surfactant molecules are added, the interfacial tension decreases to 10^{-2} mN m^{-1}, as the surfactant molecules are adsorbed between the water-oil interface.[4,5] Microemulsions are formed if the surfactant is capable of lowering the free surface energy, *G*, of the system to a minimum, such that it is counterbalanced by the entropy of dispersion of the droplets.[4,5] The low interfacial tension required to form a microemulsion is governed by the volume and surface area of the RMs. The surface area and subsequent volume of the RMs is related to the optimum packing conditions of the surfactant molecules needed to minimise the unfavourable water-hydrocarbon interactions. The packing parameter, S_p, is given by eq 1.1, where υ is the volume of the hydrocarbon tail, a_0 is the surfactant headgroup surface area and l is the length of a fully extended surfactant tail.[3,5,6]

$$S_p = \frac{\upsilon}{a_0 l} \qquad \text{eq 1.1}$$

Micelles are formed when $S_p < 0.33$, which induces, what is conventionally referred to as a positive curvature at the water/oil interface, whereas RMs are formed when $S_p > 1$, inducing a negative curvature.[3,5,6] Emulsions form opaque solutions, whereas microemulsions have the distinguishing feature of forming transparent solutions and this is due to the small size of the RMs,[7] up to 20 nm, being less than the wavelength of visible light (400 – 700 nm). The light is therefore not scattered by the droplets.[8]

There are a variety of surfactants, including AOT (sodium bis(2-ethylhexyl)sulfosuccinate) and CTAB (cetyltrimethylammonium bromide) (Figure 1.2).

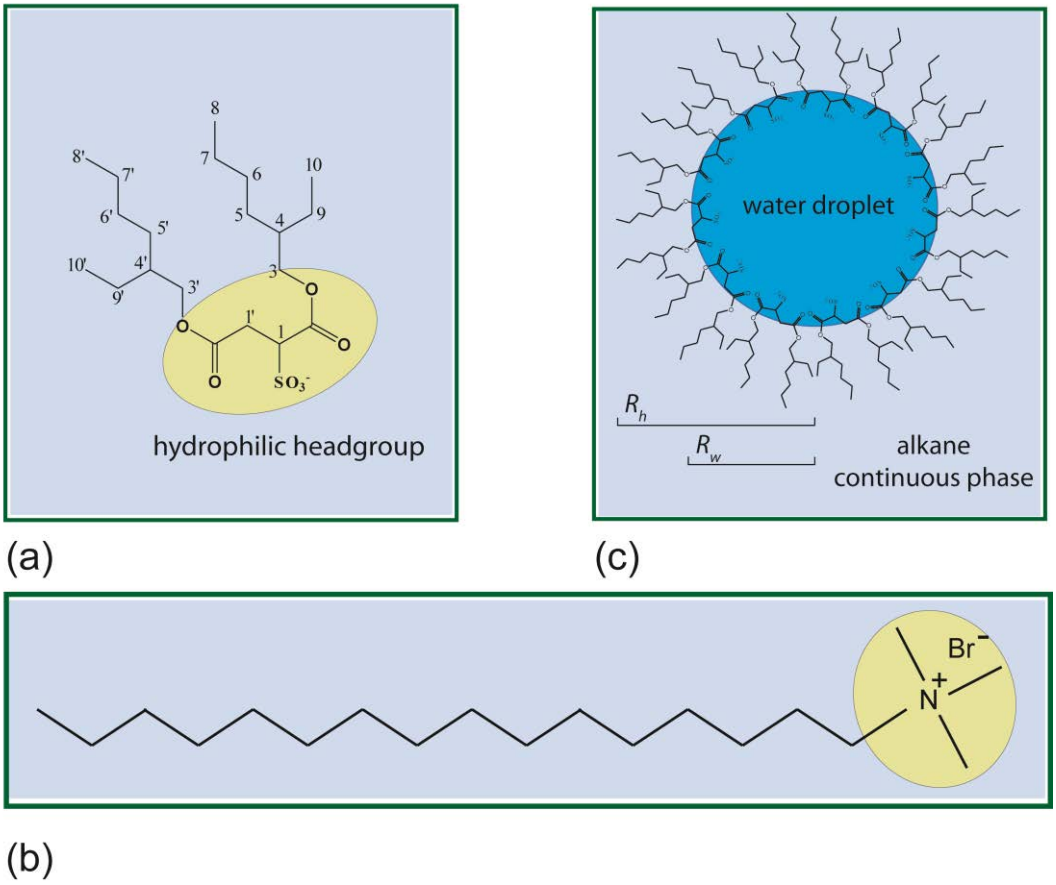

Figure 1.2: *The chemical structure of anionic sodium bis(2-ethylhexyl)sulfosuccinate AOT (a) and cationic cetyltrimethylammonium bromide (CTAB) (b) highlighting the polar, hydrophilic headgroup and a representation of an AOT/water/n-alkane RM (c).*

The surfactant mainly used in this study is anionic AOT. It has been previously characterised and well-reported,[1,9-12] due to its relative stability in solubilising water to form ternary microemulsions, without the necessity of a co-surfactant.[13] The cationic surfactant, CTAB, does require a co-surfactant to form microemulsions. The co-surfactant is required to lower the interfacial tension to further minimise the unfavourable water-hydrocarbon interactions. The addition of a co-surfactant also affects the packing parameters and changes the shape and

flexibility of the RM interface, which is dependent on the length and headgroup size of the co-surfactant molecules.[5] Common co-surfactants are medium-chain alcohols,[14] where the hydroxyl moiety resides favourably in the RM interface. However, short-chained alcohols, methanol and ethanol have been shown to reside within the RM water droplet.[15] The surfactant CTAB more commonly forms quarternary systems,[16,17] unless the co-surfactant can act as a dual-purpose co-surfactant and continuous phase, such as in the CTAB/water/hexanol system.[18] In this microemulsion, the hexanol forms both the co-surfactant and continuous phase.[19]

The common attributes that surfactants possess are hydrophilic headgroups and hydrophobic tails (Figure 1.2). The anionic surfactant AOT[1] (Figure 1.2 (a)) has a double hydrocarbon chain and is soluble in alkanes, with a molecular length[1] of approximately 1.1 nm. The cationic CTAB (Figure 1.2 (b)) however, has a single tail and an extended length of 2.8 nm.[20] As Figure 1.2 (c) illustrates, R_w denotes the radius of the water droplet, from the centre of the droplet to the interface where the water molecules meet the surfactant head. The R_h is the hydrodynamic radius, which spans from the centre of the droplet to the interface between the surfactant tails and the continuous phase. The thickness of 0.9 nm has been reported for the AOT/water RM interface,[21] which was indicative of minimal oil penetration in the interface. The term interphase[5,16,22] is used to describe the composition and dimensions between the oil and water interface and is used when describing the aggregation numbers of RMs, including the surfactant molecules with the associated solvated oil molecules.[5]

The AOT/water/alkane RM is depicted in Figure 1.2 (c) as a spherical structure, but in reality RMs evolve into many different shapes, depending on their composition and size. Many variables in the microemulsions can be changed, which affect the stability of the micellar

solutions, including chain length of the organic species in the continuous phase,[23] counter-ions from the surfactant,[24] the chain length, the structure and polarity of the surfactant.[25] Many studies have shown how tuning these variables can alter the dynamics of the microemulsion, which may ultimately affect reaction rates and outcomes.[24,26]

1.1.2. Applications of Reverse Micelles and Microemulsions

There is a lot of interest in reverse micelles (RMs) and microemulsions, as they are used in a range of applications, which include oil recovery,[27] drug delivery[8,28] and enzymology.[29,30] There have been extensive investigations, particularly in drug delivery, to find suitable non-toxic combinations of surfactants and co-surfactants to transport poorly soluble drugs through a variety of topical routes.[28] There has also been interest in the increased activity of enzymes in RMs with varying microemulsion compositions.[29,30]

Other applications include nanoparticle synthesis[31-33] and biological modelling.[34] All these applications are able to have a degree of control to modify the reaction rate and potentially change the reaction outcomes, by adjusting the microemulsion parameters. It is important and relevant, therefore, to determine the sizes and probe the dynamics of RMs and to understand the location and effects of additives on the RM environment, in order to rationalise reaction outcomes. In nanoparticle synthesis and biological modelling, the reactants are initially partitioned between separate microemulsions and may be compartmentalised between different phases of the microemulsion, either in the dispersed aqueous or continuous oil phases or in the micellar interface.[35,36] As the RMs collide, they fuse to form dimers and reform into droplets.[26] During this process, the RMs become microreactors, exchanging the contents between droplets.[31]

When the autocatalytic Belousov-Zhabotinsky (BZ) reaction[37] takes place in a microemulsion, specifically in AOT/*n*-octane/water microemulsion, there is the potential to form stationary or *Turing* patterns, which are used in biological modelling.[34] However these patterns are only observed at specific combinations of microemulsion parameters and reactant concentrations. Vanag and Epstein have extensively explored the range of chemical patterns which can be produced.[34,38] The patterns in Figure 1.3 were obtained at the same reactant concentrations but at differing microemulsion dilutions, with droplet fractions of 0.6 and 0.4 producing respectively the dash waves in Figure 1.3 (a) and the segmented spirals in Figure 1.3(b).[38]

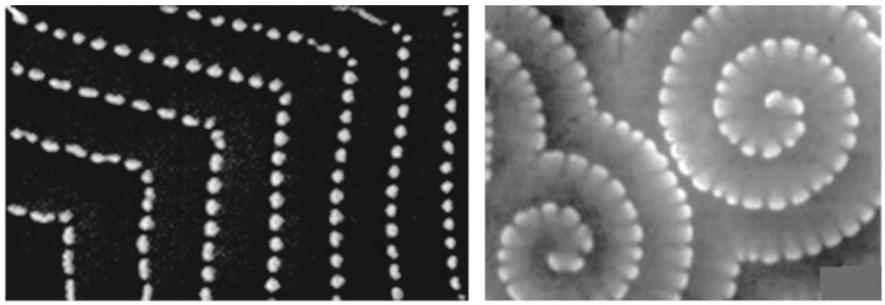

Figure 1.3: *Dash waves (a) and segmented spiral patterns (b) that are produced from the BZ–AOT autocatalytic reaction.[38](Reprinted with permission)*

The reactants are partitioned into two separate microemulsions, where they reside in the aqueous dispersed phase within the RMs. The rate at which the RMs diffuse and collide in the BZ-AOT system affects how quickly the autocatalytic reaction proceeds. As the mixing between RMs partitions the reactants with different diffusivities, tailoring the size and dilution of the RMs affects the reaction-diffusion process and the reaction outcomes.

Microemulsions are used as a medium to synthesise nanoparticles. The reactants, a metal salt and a reducing agent, are partitioned between two microemulsions. The nanoparticles are formed in the inorganic phase and the rate of nucleation can be altered, depending on the

polarity and structure of the surfactant and the dilution of the microemulsion.[31,33] The size of the nanoparticles can be controlled by the amount of water present in the droplet,[32] which determines the curvature and rigidity of the interface of the templating RMs. The solvent used as the continuous phase can also affect the rate of aggregation of the nanoparticles due to the steric stabilisation.[33] A microemulsion has the capability of producing the sought-after, stable and uniform nanoparticles, with a narrow size distribution.[31] The surfactant CTAB (cetyltrimethylammonium bromide) has been of particular interest because of the capability of being an effective template for forming mono-disperse and stable nanoparticles.[31]

1.1.3. Dimensions, Composition and Parameters of Reverse Micelles

The sizes and concentration of RMs are dependent on two main parameters. The ratio of the water to surfactant, ω, governs the size of the droplets (eq 1.2)

$$\omega = \frac{[water]}{[surfactant]} \qquad \text{eq 1.2}$$

It is well documented[1,11,39] that as ω increases, the hydrodynamic radii (R_h) of the water droplets increase linearly[13] up to $\omega \approx 40$. The other main parameter is the droplet volume fraction,[1] ϕ_d, where V_{aq} is the volume of water, V_{surf} is the volume of surfactant and V_{oil} is the volume of the organic continuous phase (eq 1.3).

$$\phi_d = \frac{V_{aq} + V_{surf}}{V_{aq} + V_{surf} + V_{oil}} \qquad \text{eq 1.3}$$

The droplet volume fraction of water is given by eq 1.4

$$\phi_w = \frac{V_{aq}}{V_{aq} + V_{surf} + V_{oil}} \qquad \text{eq 1.4}$$

For the surfactant AOT, by combining equations 1.3 and 1.4 and assuming the volume of an AOT molecule is 640 Å^3 and a water molecule as 30 Å^3, then the droplet volume fraction[40] can be related to the ω by eq 1.5.

$$\phi_d = \phi_w\left(1 + \frac{21.6}{\omega}\right) \qquad \text{eq 1.5}$$

Where there is an alcohol present in the microemulsion acting as a co-surfactant, then χ is used to describe the ratio between the surfactant and the alcohol (eq 1.6).

$$\chi = \frac{[\text{surfactant}]}{[\text{alcohol}]} \qquad \text{eq 1.6}$$

An alternative expression is used to describe the ratio of co-surfactant and surfactant in microemulsions (eq 1.7), an example being the CTAB/pentanol/hexane/water system, where pentanol acts as a co-surfactant.[17]

$$P_0 = \frac{[\text{alcohol}]}{[\text{surfactant}]} \qquad \text{eq 1.7}$$

The term reverse (inverse or inverted) micelle is typically used for microemulsions, which are at lower water concentrations. As the water within the droplet is in confinement, it is restricted and behaves differently to bulk water.[13,41-43] Differential scanning calorimetry

measurements[13] showed that at $\omega < 10$, due to the strong binding of the water molecules to the surfactant, the droplet water does not freeze and it is only as ω increases, the micellar water is observed freezing at temperatures from –30 °C.[13] Electron spin resonance (ESR)[13] and nuclear magnetic resonance (NMR) techniques[44] found that 3 types of water exist within the RM, described as bound, trapped and free. ESR techniques determined that thirteen water molecules are affected by one AOT molecule, with 2 strongly bound to each AOT Na^+ ion and the remaining 11 weakly associated.[13] However, Maitra[44] calculated that 6 water molecules would be bound to one AOT molecule for $\omega > 10$ and also stated that for $\omega < 10$, due to a decrease in the interfacial area of AOT, not all the surfactant molecules would be directly in the interface. There would also be a decrease in the number of bound water molecules due to packing restrictions.[44] As the RMs increase in size, the packing restraints decrease and the surfactant molecules are all able to reside directly in the interface.[44] Maitra determined the aggregation numbers for the AOT/water/iso-octane RMs at varying $\omega = 4 – 50$, with the number of AOT molecules ranging from 35 – 1380, respectively.[44]

The term, reverse micelle, is often used to exclusively describe droplets in microemulsions at $\omega < 10$. There is a transition[13,42,43] between ω values of 10 – 15, where true RM structures, which are described as rigid macromolecules, cease to exist and the solutions are more frequently described as water-in-oil microemulsions. These conventions are not consistently used and the transition point varies for different systems. There are different views on the various forms of water and its position in the microemulsion. It has also been discussed that water may be non-negligible in the continuous phase.[14,45] For systems of AOT/iso-octane/water at $\omega > 10$, the RM[39] greatly increase in size up to $\omega = 60 – 70$. As ϕ_d increases, the droplets become more concentrated up to a critical ϕ_d value, which is unique to different systems, known as the *percolation* point, which is where the RMs lose the stability to form

discrete droplets and develop into bicontinuous structures.[46] Conductivity studies are used to monitor the percolation point as the ion transport increases due to the formation of water channels. The conductivity of the system therefore increases at the percolation point.[35,47,48] Without the addition of water,[39,49] the R_h of the AOT/ iso-octane RMs is 15.0 ± 0.3 Å and this is independent of the concentration[39] and stable in the temperature range of 253 to 368 K. However, neutron scattering studies have suggested that RMs are never fully dehydrated.[49] Levinger *et al*.[35] also found when increasing the molarity of AOT above 0.2 M for stock solutions of AOT in iso-octane, aggregates of AOT/octane can form,[35] which may affect the final aggregation number of the resulting RMs. It is therefore important to consider that different methods of making microemulsions may affect the characteristics and sizes of the resulting RMs.[50]

1.2. Characterisation of Reverse Micelles

The RMs in AOT/*n*-octane/water microemulsions are some of the most studied in the literature.[51] There are techniques, which are used to measure various characteristics; conductivity measurements are used to measure the percolation point,[52] reaction kinetics have been studied through stopped flow experiments,[40] and collision frequency through measuring reaction rates.[21] It is difficult, however, to establish how probe molecules or reactants actually affect the microemulsion and hence the characteristic one is trying to measure. There are a number of papers reporting the R_h of RMs in the AOT/alkane/water systems using dynamic light scattering (DLS),[2,35,39,48,53] fluorescence correlation spectroscopy (FCS),[54] small angle x-ray scattering (SAXS),[41,55,56] and small angle neutron scattering (SANS),[49] as a function of ω and ϕ_d. A brief description of these techniques is given to illustrate their advantages and limitations when characterising microemulsions.

1.2.1. Dynamic Light Scattering (DLS)

Dynamic Light Scattering (DLS), also known as Photon Correlation Spectroscopy (PCS), measures the mutual (collective) diffusion coefficient, D_m of particles. It is widely used to measure the sizes, and size distributions, of RMs.[2,39,57] The technique relies on the continuous motion of particles in solutions and their diffusive behaviour, according to the size of the particles and the viscosity of the solvent. There is a decrease in the rate of diffusion, as the particles increase in size. The rate of diffusion is also dependent on the viscosity and temperature of the solution. A monochromatic laser light source at a wavelength (λ) of approximately 600 nm is fired at the sample and in doing so, the particles scatter the light in random directions.[58,59] The scattered light is measured on a detector (Figure 1.4). The light intensities, which are measured, vary due to destructive and constructive interferences and the light intensity fluctuations are obtained from the resultant interferences over a period of time.

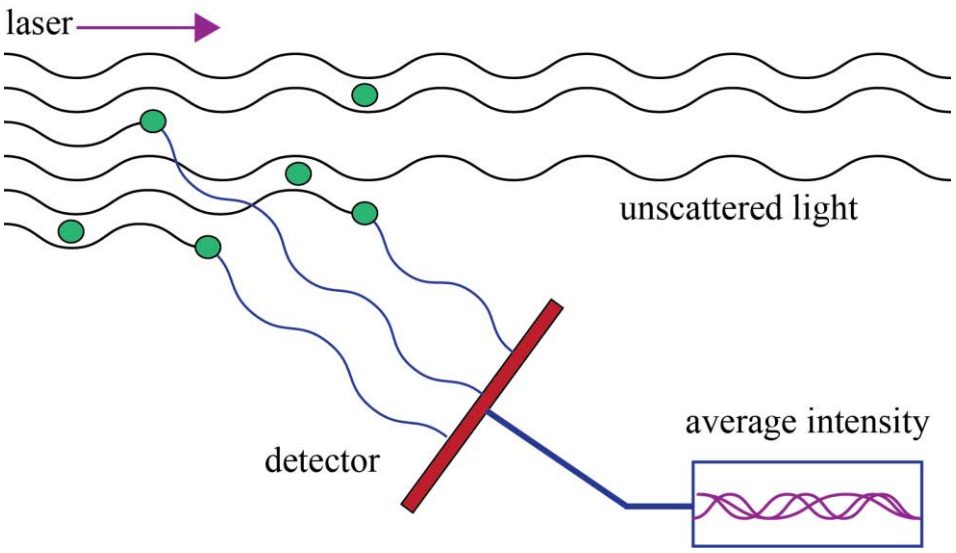

Figure 1.4: *A schematic representation of dynamic light scattering.*

The signal intensity fluctuations are evaluated using a normalised autocorrelation function, $g^2(\tau)$ of intensities between times t and (t + τ) (eq 1.8).[58]

$$g^2(\tau) = \frac{\langle I(t).I(t+\tau)\rangle}{\langle I(t)\rangle^2} \qquad \text{eq 1.8}$$

If the signal intensity at time t is compared to itself, then $g^2(\tau) = 1$ and there is a perfect correlation.[59] As τ increases, the correlation between the signal intensities at time t and (t + τ) reduces and $g^2(\tau)$ tends towards zero. When there is no correlation between the compared signal intensities then $g^2(\tau) = 0$. The time it takes for the auto-correlation function to decay to zero depends on the size distribution of the particles. The normalised autocorrelation function, $g^2(\tau)$, is converted to the autocorrelation function of the electric field of the scattered light, $g^{(1)}(\tau)$, using the Siegert relationship (eq 1.9).

$$g^{(2)}(\tau) = \left|g^{(1)}(\tau)\right|^2 + 1 \qquad \text{eq 1.9}$$

From the autocorrelation function,(eq 1.10), the decay rate, Γ, is obtained, where *B* is an instrumental constant[58] and when the particles are mono-disperse, there will be a single exponential decay curve.

$$g^{(1)}(\tau) = B \cdot \exp(-\Gamma\tau) \qquad \text{eq 1.10}$$

For smaller particles, which are moving quickly, a steeper and rapidly decaying exponential curve is obtained, with a large decay constant, as the fluctuations in light intensity change more rapidly.[58] For larger particles, a slower exponential decay is obtained, with a smaller decay constant. The conversion to a distribution of decay rates is achieved, as the decay rate is inversely proportional to the particle diameter and in the case of non-interacting, spherical

particles,[60] eq 1.10 can be written as a sum of exponentials (eq 1.11), where c_i represents the normalised intensity weight of the particles with the decay rate Γ_i .[60]

$$g^{(1)}(\tau) = \sum_{i=1}^{n} c_i \exp(-\Gamma_i \tau) \qquad \text{eq 1.11}$$

By applying the inverse Laplace transform to eq 1.11, it is possible to obtain the distribution of decay rates,[60] that can then be converted to a distribution of diffusion coefficients,[58] using eq 1.12.

$$\Gamma = Dq^2 \qquad \text{eq 1.12}$$

where q is the scattering vector given by eq 1.13, where θ is the scattering angle; λ is the wavelength of incident light and n is the refractive index of the solvent.

$$q = \left(\frac{4\pi n \sin\frac{\theta}{2}}{\lambda} \right) \qquad \text{eq 1.13}$$

Finally, the Stokes-Einstein relation (eq 1.14) affords the transformation of the diffusion distribution into a distribution of R_h, where η is the viscosity of the continuous phase, in which the RMs are diffusing, T is the temperature of the microemulsion and k_B is the Boltzmann constant.

$$R_h = \frac{k_B T}{6\pi\eta D} \qquad \text{eq 1.14}$$

These distributions are often transformed into number distributions in order to facilitate particle size analysis.[58,59] Volume and number distributions can be generated from the transformation of the intensity size distributions using Mie Theory,[61-63] which provides methods of calculating how light is scattered from homogeneous spheres.[64]

DLS measurements present both analytical and experimental limitations that have to be considered for each studied system. First, the inversion of data, through applying the inverse Laplace transform to eq 1.11 to obtain the distribution of decay rates is limited.[60] This is due to the fact that the Laplace transform is mathematically ill-conditioned, due to the existence of an infinite number of solutions. The inverse Laplace transform is also extremely sensitive to experimental errors, therefore any noise present can also be inverted, giving misleading results. Accurate data collection is therefore required, which is not contaminated by noise and controls are needed on the number of solutions generated. To minimise these issues, a constrained form of the inverse Laplace transform is commonly used in DLS. This is implemented in a program called CONTIN, which was developed and written by Provencher.[65] Several experimental limitations to DLS are found in microemulsion measurements. One issue arises when the microemulsion is too dilute, the signal-to-noise is poor but on increasing the concentration, multiple scattering may occur.[61] DLS is sensitive to the presence of dust particles and there have been extensive studies on the effects of dust, as they produce bursts of high intensity scattered light.[66,67] Other problems can arise when the dielectric constant of the droplets matches the continuous organic phase, causing the droplets to become *invisible* in light scattering experiments.[54] This condition is known as optical matching and if measurements are taken near this point, it can lead to an underestimation of the R_h of RMs.[54] There is also a variation in the refractive index[68] of microemulsions as a function of ω and ϕ_d, which can cause errors in calculating the resulting data.[54] The refractive

indices were measured for AOT/water/heptane microemulsions with values of $\omega = 0 – 40$ and $\phi_d = 0 – 0.7$. The refractive index increased as ϕ_d increased and the increase was more rapid as ω decreased. The variation in the refractive index is also an issue for analysing poly-disperse systems.[68]

Finally, there are limitations in DLS when performing the size analysis, to produce volume and number distributions, where Mie Theory is used in the conversions.[64] Therefore this technique is difficult to use, to determine the correct particle size distributions in systems which have poly-dispersed particles or droplets. This is due to the contribution of light scattered from the smaller particles being dominated by the light scattered from the larger particles, which makes the population of larger particles or droplets appear greater than it actually is. Therefore small errors in the data collection can lead to large errors when generating the number distributions[60,63] and hence the conversion to number distributions is discouraged.[61]

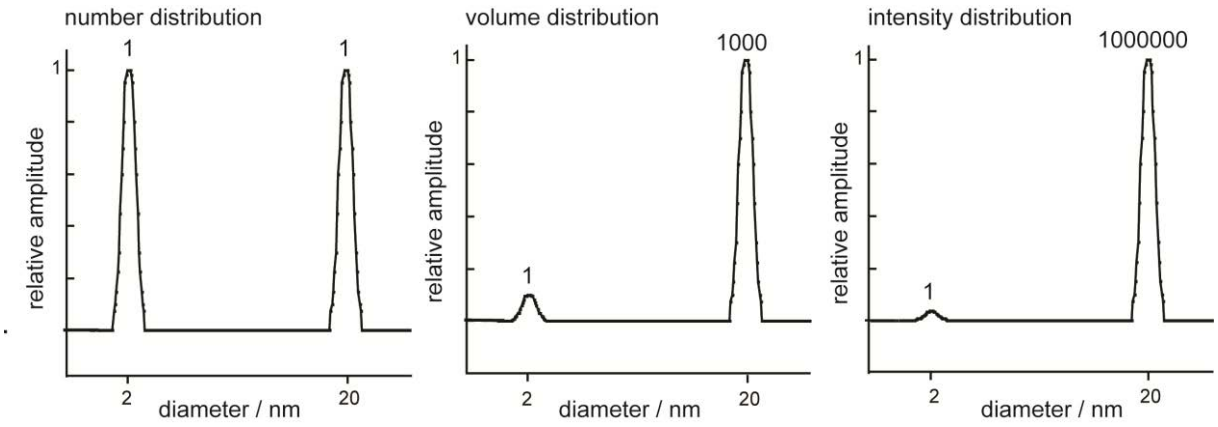

Figure 1.5: *Charts showing the number, volume and intensity distributions for a mixture containing an equal number of particles with diameters of 2 and 20 nm.*

In order to understand the nature of number, volume and intensity distributions, the case of a mixture containing equal numbers of 2 nm and 20 nm particles is considered (Figure 1.5). Obviously a number distribution will produce 2 peaks of the same intensity, whereas a volume distribution will produce a distribution with an integral 1000 times greater for the larger particle as the volume of the 20 nm particle is 1000 times greater than the volume of the 2 nm particle. The integral for the intensity distribution for the 20 nm particle, however, is 10^6 times greater than that of the 2 nm particle. The intensity of the scattered light is proportional to the sixth power of the particle diameter, therefore larger particles scatter more light than smaller particles.[59] This illustrates the potential of obtaining erroneous values, especially in calculating number distributions, as any error in the intensity distribution will be magnified through the conversion.

There have been numerous studies concerning sizing RMs in AOT microemulsions using DLS, with the most extensive by Zulauf and Eicke,[39] where they observed how droplet sizes increased with increasing ω and temperature. Another study illustrated how the changes in shapes of the RMs in an AOT/iso-octane/water microemulsions[53] can be related to the variation in the shapes of the size distributions obtained from DLS measurements. These observations have been related to deviations from spherical to oblate RMs[53] as ω decreases. DLS has been used to study the changes in the distributions of droplet radii with the addition of BZ reactants over varying periods of time[34,38] and dilution.[69] The transition between bimodal droplet distributions to monomodal distributions was observed during 24 hrs, with another study reporting a transition from a monomodal to a bimodal distribution of droplet radii, at $\phi_d = 0.5$, which was near to the percolation point.[69]

1.2.2. Fluorescence Correlation Spectroscopy (FCS)

Fluorescence correlation spectroscopy (FCS) is a light scattering technique. In FCS, the molecules within a system are labelled with fluorescent probes[10] and it is the fluctuations of the diffusing fluorescent particles, that are measured using an autocorrelation function. The diffusion coefficient is determined from eq 1.15, where ω_0 is the width of the laser beam and τ_d is the average time for a particle to move through the optical probing region.[54]

$$\tau_d = \frac{\omega_0^2}{4D} \qquad \text{eq 1.15}$$

This technique has advantages compared to the other sizing techniques, as measurements can be made at high dilutions. FCS does not suffer from difficulties associated with optical matching points and there is the ability to compensate for errors evolving from changes in the refractive index,[54] which can be an issue in DLS. FCS has also been used to observe the dynamics in the AOT/iso-octane/water microemulsion by labelling the RMs with the fluorescent molecule (Cy3), which resides within the water droplet and is insoluble in iso-octane.[70] The formation of a Cy3-H dimer was found in the smallest RMs. However the formation of the Cy3 dimer was observed alongside the formation of transient coalescing RM dimers. From the diffusion coefficient of the RM dimer and assuming a prolate ellipsoid shape of the transient structures, the size of the coalescing RM was found to be twice the size of a single RM.[70]

1.2.3. Small Angle Neutron Scattering (SANS)

Small Angle Neutron Scattering (SANS) technique does not follow the motion of particles and therefore differs from DLS and FCS techniques. In SANS, a beam of neutrons is fired at

the sample[23,49,71] with an intensity I_0 and scattered with intensity I_S across an area defined by r^2 dΩ, where r is the distance from the sample and dΩ is the angle of the area detected (Figure 1.6).[49]

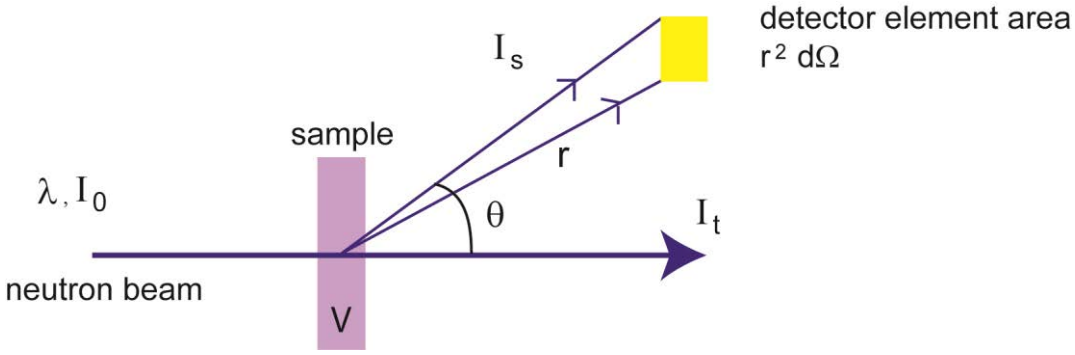

Figure 1.6: *A schematic representation of small angle neutron scattering (SANS).*

Different atomic species scatter the neutrons either coherently or incoherently. The neutrons are scattered by the atomic nuclei or the associated magnetic moments from unpaired electron spins.[49,71] Hydrogen atoms scatter neutrons coherently at 180° out of phase with other atomic species, which is described by a negative scattering length of -3.74 fm.[23,49] Deuterium, however, scatters neutrons at a length of 6.67 fm, therefore deuterated species are used in SANS to obtain contrasting scattering length densities between different molecules.[49,71] In microemulsion systems where the surfactant, alkane solvent and water are composed mainly of hydrogen atoms, one of the molecules is typically deuterated to provide adequate contrast between the molecules in the system. Typically, D_2O is used to form the water droplet within the RM,[23,72] hence the water radius, R_w, is obtained from SANS measurements, rather than the hydrodynamic radius, R_h. The ratio of the scattered neutrons to the incident neutrons is defined as the *differential cross section* (DCS) of the sample (eq 1.16), where the scattered neutron intensity is measured for an area r^2 dΩ where r is the distance and dΩ is the angle from the sample.

$$d\sigma(Q) = \frac{I_s r^2 d\Omega}{I_0} \qquad \text{eq 1.16}$$

The scattering cross section per unit volume is given by eq 1.17.

$$\frac{d\Sigma}{d\Omega}(Q) \equiv \frac{1}{V}\frac{d\sigma}{d\Omega}(Q) \qquad \text{eq 1.17}$$

The scattered intensities are measured in reciprocal space, which is also known as Fourier space.[71] The data is fitted to model solutions whilst in reciprocal space. The intensity of the neutrons (DCS) is proportional to the density of the particles in the sample, which is given by the product of two structure factors, S(Q) and P(Q), which are the inter-particle and particle structure (or form factors), respectively (eq 1.18).[49]

$$\frac{d\Sigma}{d\Omega}(Q) = n_p P(Q) S(Q) \qquad \text{eq 1.18}$$

The aim of a SANS experiment is to determine the structure factors. The particle structure factor represents the scattering from a single particle or RM. The inter-particle structure factor is a correlation function between the interaction potentials between the centres of the particles,[71] or RMs and therefore is related to the droplet volume fraction. The experimental timescale of SANS is not effected the motion and diffusion of particles and does not measure a time correlation function, as in some of the other techniques. It does, however, have issues with calculating the structure factors, particularly, S(Q), where the interactions between the particles, or the RMs have to be determined. This is where the assumption that at high dilution, S(Q) tends towards unity, is frequently used for microemulsions.[23,49,72] Both structure factors are calculated from repeating measurements with varying contrasts. Therefore different deuterated schemes are used with the sample of interest to obtain the variation in contrast. Models are then made in order to fit the data.[71] Usually when making

the models, too many unknowns are presented. This is due to the phase information being lost, when measuring the scattered intensities in reciprocal space.[73] Therefore at least one approximation or known, such as the shape of the particles is required, to determine another structural characteristic, such as the size of the particle. In the case of measuring the R_w of RMs, the hard sphere potential is used.[71] SANS has been used to observe changes in R_w at critical temperatures in the AOT/iso-octane/water RMs[74] at ω = 40 at varying droplet fractions. It was found that the droplet model broke down at $\phi_d > 0.2$. As SANS profiling is sensitive to the effects of poly-dispersity, the technique has also been used to detect deviations from mono-disperse systems. The poly-dispersity was found to increase as the organic solvent was changed from heptane to dodecane.[43] SANS has therefore been used to deduce that the RM structure is dependent on the increase in attractive interactions due to the increase in hydrocarbon chain length of the organic solvent.[23,74] The technique has shown that attractive interactions increase with droplet size.[75] Eastoe *et al.*[76] reported a variation in the form factor at low droplet fractions, when the counter-ions $M^{n+}(AOT)_n$ were varied, with rod-like and spherical RMs being formed, with transition and alkali metals, respectively.

1.2.4. Small Angle X-ray Scattering (SAXS)

Small angle x-ray scattering can measure particles from 1 to 100 nm. In this technique, a beam of x-rays is fired through the sample and the variation of electron density scatters the x-rays at different intensities. The scattered intensity of radiation, like SANS, is detected in reciprocal space.[77] Therefore, similarly to the SANS technique, when the scattering intensities are collected, phase information is lost, hence the original structure is not completely recovered.[77] The Fourier transform of this data is an average of the scattered x-rays. Three structural aspects are usually desired from SAXS, including the shape, the packing of the

particles and the poly-dispersity.[73,77] Typically two of the structural aspects are known in order to obtain information about the other morphological feature of the system.[77] The issue for poly-disperse systems is that it is difficult to resolve the separate sizes, due to the averaging of the intensity data.[73,77] After the scattering data is collected, data corrections are performed, to recover the highest quality scattering patterns.[77] This process separates the scattering signals of interest from instrumental and sampling distortions. The data is then fitted to models to obtain the desired physical parameters.[77]

SAXS has been used to analyse AOT/alkane/water microemulsions and has also shown, similar to SANS,[23] that RMs deviate from the spherical model as the solvent chain length increases.[78] For the AOT/*n*-octane/water system at $\omega = 20$, the presence of elongated particles has been observed using the SAXS technique.[41] SAXS information has been coupled with data obtained from conductivity experiments and DLS, to understand the percolation mechanism and the effect of alcohols on the structures in AOT/IPM/water microemulsions.[79] From understanding how the scattering intensity curves related to the enlargement of the RMs as a function of ω, a decrease in RM size was observed with increasing concentration of the alcohol. The variation in the shapes of the scattering curves also indicated the presence of dimers and oligomers at different ranges of ω with various alcohols.[79]

1.2.5. Nuclear Magnetic Resonance (NMR)

Nuclear magnetic resonance (NMR) techniques have been used to characterise and study the behaviour of RMs and microemulsions and an overview of them is given here. A more in-depth description of NMR techniques and methodology is provided in chapter 2.

Typically, the variation in mobility and motion of the water molecules in RMs has been measured through NMR relaxation and diffusion experiments.[12] The decreasing number of water molecules, with decreasing ω disrupts the formation of hydrogen bonding and the characteristics of this water confinement are paralleled with how water may behave in biological systems,[35,80-82] such as mitochondria. NMR techniques have shown how the water peak in the ^{1}H NMR spectrum is observed shifting downfield, as ω increases, As more water is added to the system and the droplet size increases, the chemical shift moves towards that of ordinary water.[82] The observed chemical shift of the water peak is a weighted average of the bound and free water, which are in fast exchange with each other, which also produces an average diffusion coefficient.[35,80-82] Wong reported using spectroscopic studies and measuring rotational times,[82] that at $\omega > 6$, the water molecules started to behave as bulk water. At low ω values, the water was less mobile due to the ion-dipole interactions with the counter-ions,[82] and it was the decreasing number of water molecules which disrupted the hydrogen bonding. The spin-lattice and spin-spin relaxation rates, which are related to the motion of the molecules ($1/T_1$) and ($1/T_2$), which are discussed in detail in chapter 2, were found to decrease with increasing volume of water. When discussing the diffusion of the water molecules, the Lindman equation,[83] eq 1.19, illustrates how the observed diffusion coefficient, D_{obs}, is the weighted average of the bound (D_{mic}) and free water molecules and P is the proportion of bound water molecules.

$$D_{obs} = PD_{mic} + (1-P)D_{free} \qquad \text{eq 1.19}$$

NMR techniques measure the self-diffusion coefficients (D_s) of different molecules in a system and have the advantages of being able to probe optically opaque, turbid solutions. These methods provide accurate measurements of diffusion coefficients and offer several

advantages over the light scattering technique, including being unaffected by the presence of dust particles. NMR techniques do not require any optical parameters, such as the refractive indices of the molecules, to obtain the diffusion coefficient of the RMs. Therefore experimental errors do not occur from optical matching or the mismatch of the refractive indices. The sizes of RMs in an AOT/water/octane microemulsion have been previously measured using diffusion measurements and converting to R_h , using the Stokes-Einstein equation[45] (1.2.1 eq 1.14) and has been investigated at varying ϕ_d. An increase in the diffusion coefficient, (D) and a decrease in R_h was observed as a function of ϕ_d.[45] Other studies have measured the micellar water and oil diffusion coefficients[47,84] and one reported that for a system with the AOT/water/iso-octane microemulsion, D values measured with NMR were always greater than those obtained from DLS.[47] The different diffusion coefficients of RMs with and without co-surfactants have been investigated through NMR diffusion methods.[14] It has been observed that D for the molecules in the AOT microemulsions were generally slower than those systems requiring co-surfactants.[14] In a recent study,[16] the Lindman equation (eq 1.19) was used to determine the proportions of co-surfactant that was present in the continuous phase and interphase of the CTAB/water/hexane/pentanol microemulsion. The proportion of co-surfactant in the continuous phase was important to obtain, as changes in the viscosity of the system and hence the sizes of the RMs were more accurately determined, when using the Stokes-Einstein equation.[16] Where the average sizes of RMs have been obtained from NMR measurements of diffusion, the size distributions of RMs are not reported. However, size distributions and the poly-dispersity for polymers,[85] colloidal systems,[86,87] and porous media[88] have been determined, using a log-normal distribution fitting procedures.

1.3. Microemulsion Dynamics and the Challenges of Characterisation

1.3.1. The Diffusion and Exchange Processes in Microemulsions

The structure and dynamics of the AOT/water/octane systems have been investigated primarily with scattering methods[2,39,57,89] and NMR techniques.[10,12] When comparing the different techniques, the experimental observation times must be considered and what can be measured within the timescales available, particularly when investigating the diffusion of dynamic systems. The droplet collision rate is an experimental factor, which affects the diffusion of the RMs. DLS and NMR experimental timescales differ[47] with DLS recording experimental auto-correlation times up to 1 – 2 ms, whereas NMR achieves observation times from 10 ms. SANS and SAXS techniques, however, do not measure the motion of the RMs and are not affected by the RM collision rate.

The rate of coalescence is determined from the rates of diffusion of the RMs. The rate of diffusion is exploited in many particle sizing techniques, as the diffusion of the molecules is related to the droplet size and the viscosity of the continuous phase.[2,49,54,57] The diffusion coefficients (*D)* can therefore be converted to R_h, by applying the Stokes-Einstein equation (1.2.3 eq 1.14). However, these techniques measure different diffusion coefficients (*D*). DLS and FCS measure a collective or mutual diffusion coefficient (D_m),[90] where a single value for *D* is obtained from the motion of the collection of particles within a system in a flux of concentration gradients,[91] where *n* is the number of particles. (eq 1.20)

$$\frac{\partial n}{\partial t} = D_m \nabla^2 n \qquad \text{eq 1.20}$$

The self-diffusion coefficient is measured in NMR diffusion techniques. The self-diffusion coefficient (D_s) is a measure of the diffusion of separate molecules within a mixture.[49,90,92,93] The self-diffusion of a molecule travelling during time t in one dimension is given by eq 1.21, where z_{rms} is the root mean square distance.[94]

$$z_{rms} = \sqrt{2Dt} \qquad \text{eq 1.21}$$

Both D_m and D_s have been measured and compared in several studies which characterise and size RM at varying ϕ_d [48,81] and temperature.[39,48] However D of probe molecules has been determined using scattering methods, to explore the D_s of RMs.[90,95] Measurements of D are sensitive to inter-droplet interactions or collisions, which cause the obstruction effect.[12,45,81,96] The values of D_m and D_s in a system,[93,97,98] based on the assumption that the particles or in this case, the RMs are spheres, only become comparable as ϕ_d approaches the dilute limit or where attractive or repulsive droplet interactions can be neglected.[49] As the inter-droplet dynamics vary with ϕ_d, ω and temperature, the D_s for RMs, should be determined at infinite dilution in order to evaluate self-diffusion without interactions.[93,97,98] Depending on the ionic nature of the surfactant, whether there are attractive or repulsive potential interactions between the particles, or RMs,[90,93,98] the relationship between the diffusion coefficient and ϕ_d varies between the scattering and NMR methods.

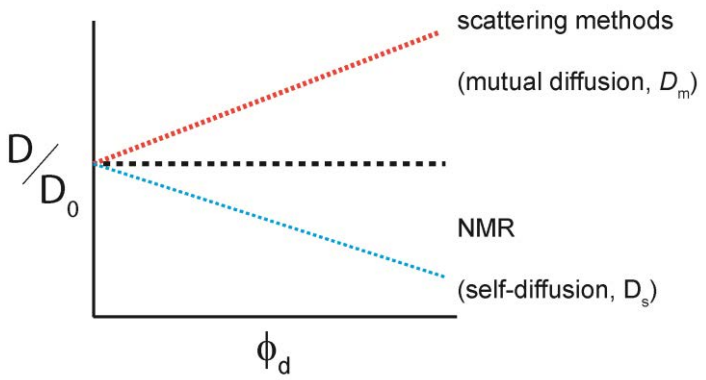

Figure 1.7: *A schematic showing the variation of D_s and D_m as a function of ϕ_d for repulsive interactions.*

Figure 1.7 illustrates how D_s and D_m for particles with a *repulsive* potential interaction vary as a function of ϕ_d.[90] It has been found [2,57,90] that for particles with attractive interactions, as for RMs formed from the anionic AOT surfactant, D_s decreases, as does D_m, but they have different quantitative values.[93] When using the D_m to evaluate RM size, there have been studies which implement the infinite dilution law and convert D to D_0 using the expression, (eq 1.22) [48,81,89,96] where D is the observed diffusion coefficient, D_0 is the diffusion coefficient at infinite dilution, ϕ_d is the droplet fraction and α is the *virial* coefficient.

$$D = D_0(1+\alpha\phi_d) \qquad \text{eq 1.22}$$

The virial coefficient is determined from the hydrodynamic interactions and repulsive or long-range attractive potentials involved in microemulsion systems. Anionic AOT droplets have an attractive potential interaction, which has a model $\alpha = -2$ when measuring D_s.[93,98] There are two virial coefficients for a hard sphere particle (solute) model,[99,100] which evolve from the interaction potentials U_r .[99] The virial coefficient (α) is related to (B) the osmotic pressure,[99]

and β, which represents the contribution from the frictional coefficient and is dependent on the droplet volume fraction of the system. (eq 1.23)

$$\alpha = B - \beta \qquad \text{eq 1.23}$$

There are different derivations and values of β which are outlined by Felderhof.[100] The virial coefficient varies in different systems,[99] as the osmotic pressure term varies with different microemulsion parameters, including the chain length of the alcohol co-surfactant. When extrapolating to D_0, changes have been observed in the virial coefficient (α) as a function of ω and oil chain length, with α becoming increasingly negative (–1.1, –3.6, –5.1) as a function of increasing ω (20, 40 and 60, respectively).[57] This was explained by the increasing attractive interactions from the increasing size of the RMs.[57] Nicholson and Clarke[2] observed variation in the poly-dispersity of an AOT/heptane/water microemulsions as a function of ω. At $\phi_d = 0.24$, the poly-dispersity increased as a function of ω whereas at $\phi_d = 0.06$, a decrease was observed.

Microemulsions are dynamic systems with the RMs continually colliding, fusing and reforming,[38] exchanging the molecular species, which reside in the water cores. Molecular exchange takes place in microemulsions between molecules in the interphase and the continuous phase and this exchange is reported to take place on a fast timescale in the order of microseconds,[21,96] however it has recently been observed on a millisecond timescale in a CTAB/water/pentanol/hexane microemulsion.[16] Molecular exchange rates have been found to depend on the droplet size, temperature and solvent chain length in the system.[21] Proton exchange between the molecular species[18] in microemulsions between alcohol co-surfactants

and micellar water at varying pH has also been investigated and the results are discussed further in 1.3.3.

One schematic representation (Figure 1.8) can be used to explain inter-droplet exchange, which is also referred to as solubilisate exchange.

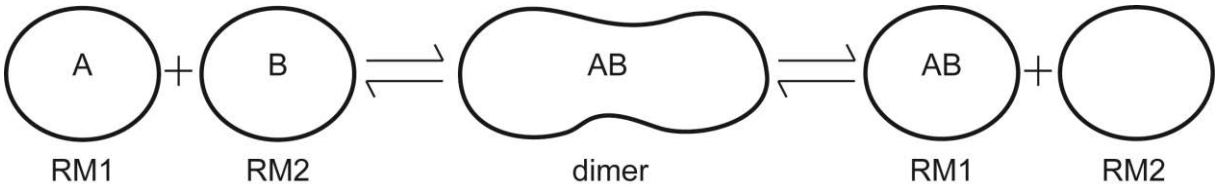

Figure 1.8: *A schematic representation of the coalescence of droplets and the exchange of reactants A and B.*

As the droplets collide, they fuse to form an intermediate dimer, where exchange of the contents within the water droplets takes place.[101] The dimer then splits to reform individual droplets. The solubilisate[21] exchange rate takes place on a millisecond to microsecond time scale, depending on the microemulsion parameters.[21] The surfactant AOT is able to form stable RMs without a co-surfactant and has been the focus of many studies of exchange rates to deduce the rate of droplet coalescence.[21,40,96] The inter-droplet exchange rates between RMs have been measured by monitoring the rate of fast chemical reactions taking place in the microemulsion,[21] as the exchange of material between RMs occurs through droplet collisions. The number of micellar encounters taking place is controlled by the diffusion and is typically determined from equation 1.24. Smoluchowski[21,84] derived this relationship to determine the rate of coagulation of sols where R is the gas constant, T is the absolute temperature and η is the solvent viscosity. (eq 1.24)

$$k_{DC} / dm^3 mol^{-1} s^{-1} = 8N(2r)10^3 D \qquad \text{eq 1.24}$$

$$= 8000RT / 3\eta$$

The Smoluchowski equation accounts for the *transient state* of encounters,[102] from time dependent diffusion processes, whereas Debye[103] extended the equation to express the collision frequency based purely on the electrostatic interactions and charge effects between ions. Umberger[102] explored combining both the charge and transient processes to obtain an alternative expression for the encounter frequency of two particles in a liquid, (eq 1.25)

$$\frac{4\pi DRn_a^0 n_b^0}{f} = \text{encounter frequency} \qquad \text{eq 1.25}$$

where $R = r_A + r_B$, which is the distance between the two droplets when an encounter occurs (Figure 1.9)[102] with n_A and n_B being the number of particles of A and B and f a factor to account for the effect of inter-ionic forces on the rate of diffusion (D).

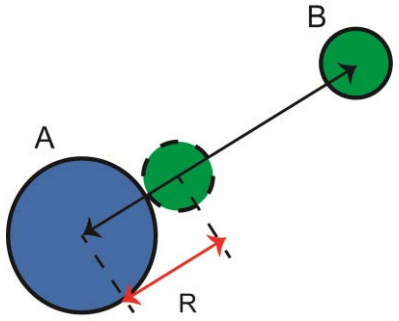

Figure 1.9: *Diagram of a droplet encounter.*

1.3.2. ***Intermolecular Forces***

The forces which exist between droplets and the interfacial flexibility of the RMs affect the collision and exchange rates of RMs and hence the diffusion of the molecules.[79] In AOT

systems, the RMs have attractive interactions. This is due to the interpenetration of the surfactant tails from neighbouring RMs.[75] These interactions are termed as a *stickiness* parameter and increases as a function of ω and therefore the droplet size.[75] The attractive interactions increase as the droplet size increases, due to an enhancement of the attraction for larger droplets at short distances in a continuous phase of comparatively small solvent molecules.[104] This increased contact between larger droplets, which leaves cavities containing smaller solvent molecules is called the depletion effect.[104] The stickiness parameter has been reported to decrease as a function of ϕ_d for RMs where $\omega = 40$, which was due to depletion forces and was found to be dependent on the solvent packing fraction.[104] The stickiness parameter was also found to increase, as the length of the solvent chain length increased.[104]

1.3.3. The Effects of Additives in Microemulsions

There are numerous studies on the effects of additives on the RM environment.[46,52,105] Conductivity measurements are used to determine whether additives assist, retard or have no effect on the percolation point, illustrating whether the additives cause the micellar interface to become more or less stable.[46,52,105] The effects of additives with varying physical attributes have been observed[52] and explained with respect to the effects on packing parameters of RMs and the intermolecular forces. For example, crown ethers, capture the Na^+ counterion of the AOT surfactant, which screens the headgroup charges, inducing a decrease in the headgroup volume and an increase in the percolation point.[52] Binks[36] used NMR relaxation measurements and molecular simulations of AOT/water RMs, to show that as the droplet size increased to $\omega > 20$, the $Ru(bpy)^{2+}$ cation moved into the RM interface, rather than being present in the micellar water (Figure 1.10). The exchange processes were therefore

increasingly restricted between the cation and water ions, as the droplet size increased, which was also evident from a decrease in the T_1 relaxation times.[36]

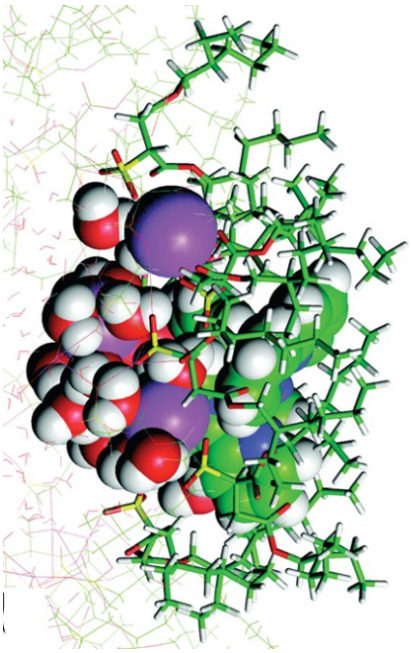

Figure 1.10: *A molecular simulation showing a part of the interface of an AOT/water RM. The* $[Ru(bpy)_3]^{2+}$ *complexes, water molecules, and sodium ions are shown in spacefilling mode with AOT molecules surrounding. The colours of the atoms are: oxygen, red; nitrogen, blue; sulfur, yellow; carbon, green; hydrogen, white; and both sodium and ruthenium ions, purple. (Reprinted with permission)*[36]

DLS has been used to study the changes in the distributions of droplet radii with the addition of BZ reactants over varying periods of time.[34,38] When measuring fresh microemulsions at ω = 15 and ϕ_d = 0.55, near to the percolation point, with acidic additives, a bimodal droplet distribution was observed, with droplet sizes of 20 and 2 nm. However, a transition to a monomodal distribution was observed a day later with R_h = 3.6 nm. In another study of microemulsions loaded with H_2SO_4, malonic acid and $NaBrO_3$, a transition was observed

from a monomodal to a bimodal distribution of droplet radii, as ϕ_d increased near to the percolation point.[69]

The effect of alcohols on RMs is of interest, as they are often used as co-surfactants in microemulsions. Short-chained alcohols, reside in the micellar water pool, with longer chained alcohols being located in the RM interface in AOT/water/*n*-decane systems.[15] In an AOT/IPM/water system, the alcohols induced an increase in the interfacial flexibility, when the alcohol chain-length was decreased and as the alcohol concentration increased.[79] Increasing droplet attractive interactions were considered to take place with the reduction of the alcohol chain length.[79] The adsorption of short-chained alcohols in RMs has been reported to make the interface more flexible and labile, as the alcohols penetrate between the surfactant tails.[84,106] The rigidity of the interface increases as the alcohol chain length is increased,[79] therefore the percolation point may be assisted or retarded depending on the size, shape and concentration of the alcohol. In an AOT/decane/water microemulsion, toluene retarded the percolation point, whereas benzoyl alcohol assisted percolation. Toluene interacted with the hydrophobic tails of AOT, creating an inhibiting effect,[107] whereas the interfacial adsorption of the benzoyl alcohol caused an effective increase of the surfactant headgroup and the decrease of the percolation point. This highlights how the interplay between the structure and polarity of the surfactant, the RM size and the physical characteristics of the additives affects the stability of RMs.

1.3.4. The Determination of pH in Microemulsions

The determination of the pH within RMs has been of interest, particularly in enzymology, as RMs are used to model enzymatic reactions in cellular structures, which occur with changes

in pH.[108] Variations in the pH within RMs, when exploring enzymatic reactions, however, can lead to the misinterpretation of results, leading to what has been described as pH artifacts.[109] Therefore, there is a need to understand more about how changes in pH affect RMs. However, measuring the pH within the RMs is difficult, as the standard pH meters cannot be used to measure nano-scale water droplets.[110] The normal conventions of describing pH in RMs do not apply, as there are less than 10^7 water molecules present,[110] thus making the interpretation of measuring the pH difficult, as the IUPAC conventions are not applicable.[18,80,110] Probe molecules have been used to monitor the effect of changing the pH on the RM environment. The vanadium complex, $[VO_2dipic]^-$ and the free $dipic^{2-}$, have been used as probes in AOT microemulsions, as changes in the ^1H NMR chemical shifts for the free $dipic^{2-}$ occur as a function of pH.[35] It was found, however, that the vanadium complex was residing in the hydrophobic interface, away from the water pool and this unexpected observation raised questions about the effects of the location of the probe.[35] Studies probing the variation in pH of the micellar environment can prove difficult,[111] as the probes themselves may induce changes to the behaviour of the RMs. Fluorescence pH-sensitive probes obtained measurements that suggested RMs act as buffers, as the measured intensity remained constant over a wide pH range (1-12). Alternative methods have been employed to monitor the changes in pH without a probe molecule.[18] In the CTAB/hexanol/water microemulsion, the exchange processes between hexanol, which is the co-surfactant and the continuous phase, and the water pool have been exploited. As the pH decreased the water and alcohol peaks coalesced to form a single peak.[18] This was due to the exchange between the water and the hydroxyl hexanol group protons being catalysed by the acid.[18] The exchange rate was also reflected in changes in the T_2 relaxation times of the water within the droplet.

1.4. Molecular Simulations

Molecular simulations are used to model how molecules in a system interact with each other with consideration to the intermolecular forces and potential energies, including van der Waals forces and hydrogen bonding.[112] As the droplet size or the composition of the RM interface is varied with changes in ω, there may be shape fluctuations in the RMs.[113] Furthermore with the addition of a co-surfactant, the flexibility of the interface may change, resulting in further changes to the droplet shape and deviations from spherical RMs. Molecular simulations are able to show the overall fluctuations in the structures of RMs as the molecules move over the simulation time into the most favourable orientations.[114] The capability of monitoring the group or individual molecular movements, also gives the potential of probing molecular diffusion and exchange processes.[115]

There are several different forcefields, which have been used to set up the molecular simulations for AOT/water/iso-octane RMs. The forcefields define the parameters for each of the atoms or groups of atoms in the simulation, including bond lengths, partial charges, dihedral angles and van der Waals radii. The most common forcefields used to generate RMs have been AMBER (Assisted Model Building and Energy Refinement),[112] in studies with AOT[36,116] and CTAB[16] and CHARMM (Chemistry at Harvard Molecular Mechanics)[117,118] with studies of AOT.[114,119] There are variations in how the simulation models are constructed, in order to reduce the simulation time and the computer power required. The *all-atom* simulation model utilises all the parameters for all the atoms in the RM,[114] whereas *coarse-grained* model groups clusters of atoms together, such as the tails of the surfactant.[120] The *united atom* model groups smaller numbers of atoms, such as the H, C, methyl and methylene as one and has been used to construct the solvent molecules in a AOT/water/iso-octane system,[114] in order to cut down on the required computer resources and increase simulation

times. Martinez *et al.*[51] reviewed the developments in molecular simulations for systems involving AOT RMs. The investigations showed that the shapes of the RMs in unrestrained systems deviated from spherical models, but there was a dependency on the types of forcefield used in the initial configurations. This highlights the challenges of applying forcefields to micellar systems, as there are so many combinations between the molecular species involved, and also a dependency on the density of the systems.[51]

One limitation of molecular simulations with RMs, which involve so many molecules, is that they need considerable computer time and resources to generate. Hence many of the simulations are run for much shorter periods of time and from preassembled structures.[114] However, with longer simulation times, there is increasing confidence that the RM has reached equilibrium, especially with structures that are generated from preassembled reverse micelles.[114] The minimum simulation time of 2 ns is recommended for pre-assembled reverse micelles. AOT/water/iso-octane systems have previously been simulated up to 425 ns.[114] These simulations were started from a random configuration of the molecules.

There are differences in methods of solvating droplets in molecular simulations, as RMs are solvated with a wide variety of organic solvents. Although methods have been developed to make organic solvent boxes,[121] they can considerably increase the computer time and resources to run the simulations. A recent study has used a hexane organic solvent box, to model a RM in a CTAB/water/pentanol/hexane system. As the solvent box was constructed using an all-atom forcefield, there was the capability to observe the dynamics of the alcohol co-surfactant and analyse the exchange between the interface of the RM and the hexane continuous phase.[16] An all-atom iso-octane solvent box has previously been used to solvate AOT/water RMs[119] at $\omega < 7$. Other molecular simulations of RMs have used solvent

molecules constructed with a united-atom forcefield[114] or have been constructed without the solvent molecules.[36] However, as the latter simulations did not have periodic boundaries, the molecular dynamic runs had to be terminated when water molecules escaped from the RM.[36]

Molecular simulations are able to show the potential changes in shapes of RMs and deviations from spherical models. Vasquez *et al*. observed at $\omega < 10$ the AOT/water/iso-octane RMs equilibrated to form cylindrically shaped structures, but the shapes fluctuated greatly and were difficult to characterise geometrically.[114] At $\omega \geq 10$, the RM shape fluctuations decreased and the RMs became increasingly spherical with increasing water content. The motion of the molecules within RMs can also be analysed. The rotational and translational diffusion data of the water molecules within AOT/water/iso-octane RMs has been obtained from coarse grained models, supporting the theories that the translational diffusion of water molecules in RMs only tend towards the value of bulk water in the centre of the water core as the droplet size increases.[120] Molecular simulations are used to illustrate the different locations, proportions and effects of different molecular species in RMs and frequently support experimental findings. One study showed that varying the metal counter-ions associated with the surfactant from Na^+ to Li^+, K^+, and Cs^+ affected the formation of the RM. As the dimensions of the ion decreased, the aggregation energy increased.[116] A molecular simulation has shown how the $Ru(bpy)^{2+}$ cation resides within the AOT/water RM interface.[36]

Although there are a considerable number of molecular simulations for the AOT/alkane/water RMs, there are less simulations that show the behaviour of CTAB in reverse micelles. One study has shown the behaviour and dynamics in the quarternary CTAB/water/pentanol /hexane system.[16] This may be due to the fact in ternary CTAB systems, the co-surfactant required to form the RM may also act as the continuous phase, therefore solvating the RM is

essential in order to construct and run a molecular simulation for a sufficient time to keep the RM intact. The development and use of the organic solvent boxes[16] has therefore enabled RMs which require a co-surfactant to reach equilibrium.

Molecular simulations are an effective way of visualising the shapes of RMs, which can provide support and understanding of experimental data. As the Stokes-Einstein equation is commonly used to size RMs and assumes that the RMs are spherical, any deviations from this shape are of interest. Molecular simulations provide a method of evaluating the extent of the asphericity[114] of the RMs as a function of time. The semi-axes of elliptical RMs (Figure 1.11) can be determined from equation 1.26, where I_1, I_2 and I_3 are the principal moments of inertia ($I_1 > I_2 > I_3$) and M is the mass of the RM.[120]

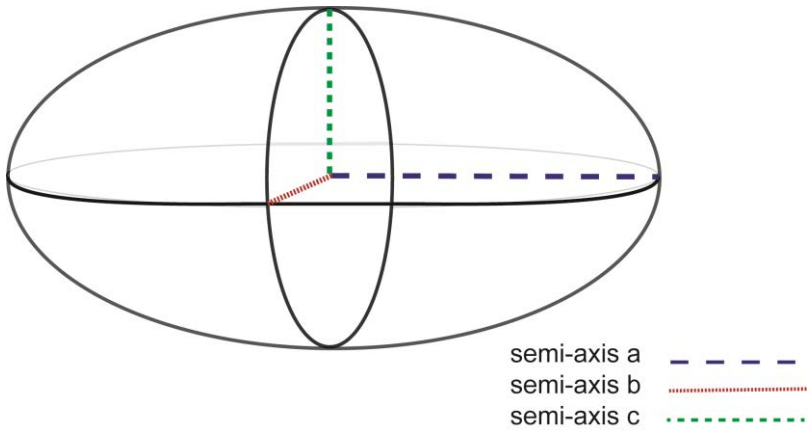

Figure 1.11: *A diagram showing the semi-axes of an ellipse.*

The values of the moments of inertia can be readily obtained from molecular simulations.

$$I_1 = \frac{1}{5}M\left(a^2 + b^2\right)$$

$$I_2 = \frac{1}{5}M\left(a^2 + c^2\right) \qquad \text{eq 1.26}$$

$$I_3 = \frac{1}{5}M\left(b^2 + c^2\right)$$

The eccentricity (*e*) is used as a measure of the asphericity of the RM[120] and is obtained from the ratio between the semi-axes *a* and *c* (eq 1.27). If the RM is perfectly spherical, then the eccentricity is zero. As the RM increasingly deviates from a spherical shape, either becoming a prolate ellipsoidal, oblate ellipsoidal or cylindrical shape, the eccentricity tends towards 1.

$$e = \sqrt{1 - \frac{c^2}{a^2}} \qquad \text{eq 1.27}$$

Molecular simulations give the opportunity to probe the shapes and dynamics of RMs, supporting and questioning the results obtained from other characterisation techniques as discussed in (1.2).

1.5. Thesis Outline

The work carried out and presented in this thesis draws upon previous research about the chemistry and characterisation of microemulsions. The techniques used to probe these chemical systems are reviewed, including the use of molecular simulations to model the behaviour of the systems. These topics are reviewed in chapter 1. The main objective of the research was to understand how NMR techniques could be used to characterise RMs in

microemulsions. Therefore, chapter 2 reviews and covers the principles of NMR, particularly methods of measuring molecular diffusion which can be used to probe the behaviour and characterise microemulsions. The sizes of RMs have been determined through the conversion of diffusion data to hydrodynamic radii, using the Stokes-Einstein equation. In chapter 3, however, the size distributions of RMs at varying omega values and including additives were determined, using NMR measurements of diffusion with the application of the inverse Laplace transform. The results obtained from NMR experiments were compared with other techniques, particularly DLS. Following this, the AOT/*n*-octane/water microemulsions were investigated at lower droplet volume fractions to evaluate droplet sizes at infinite dilution. The NMR experimental parameters were also varied, using shorter observational times, to explore the dynamics and exchange occurring in microemulsions. These findings are discussed in chapter 4. In chapter 5, the sizes of the RMs in the AOT/iso-octane/water /pentanol microemulsion were measured, by determining the proportions and position of the pentanol molecules in the microemulsion. Also in chapter 5, there was an investigation into the capability of co-surfactant pentanol molecules to monitor variations in pH in RMs. Molecular simulations were carried out to support the findings from the NMR experiments with RMs formed with AOT/iso-octane/water at varying ω values. AOT/iso-octane /water/pentanol droplets were set up to further understand where the pentanol co-surfactant molecules reside in the microemulsion and what effects there were on RM shapes and sizes. A CTAB/hexanol/water RM was also simulated to investigate the proportion of hexanol in the interface and to observe the shape fluctuations of the RM. The molecular simulation research is covered in chapter 6.

1.6. References

(1) De, T. K.; Maitra, A. *Adv. Colloid Interface Sci.* **1995**, *59*, 95.

(2) Nicholson, J. D. Clarke. J. H. R. In *Surfactants in Solutions,* Edited by Mittal and Lindman; Plenum: 1984; Vol. 3, p 1663.

(3) Degennes, P. G.; Taupin, C. *J. Phys. Chem.* **1982**, *86*, 2294.

(4) Ruckenstein, E.; Chi, J. C. *J. Chem. Soc., Faraday Trans. 2* **1975**, *71*, 1690.

(5) Oldfield, C. In *Biotechnology and Genetic Engineering Review*,1994, p 255.

(6) Mitchell, D. J.; Ninham, B. W. *J. Chem. Soc. Faraday Trans. 2* **1981**, *77*, 601.

(7) Hoar, T. P.; Schulman, J. H. *Nature* **1943**, *152*, 102.

(8) Bagwe, R. P.; Kanicky, J. R.; Palla, B. J.; Patanjali, P. K.; Shah, D. O. *Crit. Rev. Ther. Drug* **2001**, *18*, 77.

(9) Correa, N. M.; Silber, J. J.; Riter, R. E.; Levinger, N. E. *Chem. Rev.* **2012**, *112*, 4569.

(10) Gradzielski, M. *Curr. Opin. Colloid Interface Sci.* **2008**, *13*, 263.

(11) Langevin, D. *Annu. Rev. Phys. Chem.* **1992**, *43*, 341.

(12) Soderman, O. Olsson, U. *Encyclopedia Magn. Reson.* **2007**.

(13) Hauser, H.; Haering, G.; Pande, A.; Luisi, P. L. *J. Phys. Chem.* **1989**, *93*, 7869.

(14) Lindman, B.; Stilbs, P.; Moseley, M. E. *J. Colloid Interface Sci.* **1981**, *83*, 569.

(15) PerezCasas, S.; Castillo, R.; Costas, M. *J. Phys. Chem. B* **1997**, *101*, 7043.

(16) Mills, A. J.; Wilkie, J.; Britton, M.M. *J. Phys. Chem. B* **2014**, *118*, 10767.

(17) Palazzo, G.; Carbone, L.; Colafemmina, G.; Angelico, R.; Ceglie, A.; Giustini, M. *Phys. Chem. Chem. Phys.* **2004**, *6*, 1423.

(18) Halliday, N. A.; Peet, A. C.; Britton, M. M. *J. Phys. Chem. B* **2010**, *114*, 13745.

(19) Ekwall, P.; Mandell, L.; Solyom, P. *J. Colloid Interface Sci.* **1971**, *35*, 266.

(20) Anachkov, S. E.; Danov, K. D.; Basheva, E. S.; Kralchevsky, P. A.; Ananthapadmanabhan, K. P. *Adv. Colloid Interface Sci.* **2012**, *183*, 55.

(21) Fletcher, P. D. I.; Howe, A. M.; Robinson, B. H. *J. Chem. Soc. Faraday Trans. 1* **1987**, *83*, 985.

(22) Bisal, S.; Bhattacharya, P. K.; Moulik, S. P. *J. Phys. Chem.* **1990**, *94*, 350.

(23) Robinson, B. H.; Toprakcioglu, C.; Dore, J. C.; Chieux, P. *J. Chem. Soc., Faraday Trans.* **1984**, *80*, 13.

(24) Stahla, M. L.; Baruah, B.; James, D. M.; Johnson, M. D.; Levinger, N. E.; Crans, D. C. *Langmuir* **2008**, *24*, 6027.

(25) Sedgwick, M.; Cole, R. L.; Rithner, C. D.; Crans, D. C.; Levinger, N. E. *J. Am. Chem. Soc.* **2012**, *134*, 11904.

(26) Jada, A.; Lang, J.; Candau, S. J.; Zana, R. *Colloid Surface* **1989**, *38*, 251.

(27) Bera, A.; Kumar, T.; Ojha, K.; Mandal, A. *Fuel* **2014**, *121*, 198.

(28) Gupta, S. *Curr. Sci. India* **2011**, *101*, 174.

(29) Fanun, M. *Microemulsions : properties and applications*; CRC Press: Boca Raton, 2009.

(30) Fletcher, P. D. I.; Freedman, R. B.; Mead, J.; Oldfield, C.; Robinson, B. H. *Colloid Surface* **1984**, *10*, 193.

(31) Capek, I. *Adv. Colloid Interface Sci.* **2004**, *110*, 49.

(32) Chen, M. J.; Yang, W. T.; Yin, M. Z. *Small* **2013**, *9*, 2715.

(33) Eastoe, J.; Hollamby, M. J.; Hudson, L. *Adv. Colloid Interface Sci.* **2006**, *128*, 5.

(34) Vanag, V. K.; Epstein, I. R. *Phys. Rev. Lett.* **2003**, *90*.

(35) Baruah, B.; Roden, J. M.; Sedgwick, M.; Correa, N. M.; Crans, D. C.; Levinger, N. E. *J. Am. Chem. Soc.* **2006**, *128*, 12758.

(36) Binks, D. A.; Spencer, N.; Wilkie, J.; Britton, M. M. *J. Phys. Chem. B* **2010**, *114*, 12558.

(37) Winfree, A. T. *J. Chem. Educ.* **1984**, *61*, 661.

(38) Vanag, V. K. *Phys-Usp.* **2004**, *47*, 923.

(39) Zulauf, M.; Eicke, H. F. *J Phys Chem-Us* **1979**, *83*, 480.

(40) Jain, T. K.; Cassin, G.; Badiali, J. P.; Pileni, M. P. *Langmuir* **1996**, *12*, 2408.

(41) Balakrishnan, S.; Javid, N.; Weingartner, H.; Winter, R. *Chem. Phys. Chem.* **2008**, *9*, 2794.

(42) Charlton, I. D.; Doherty, A. P. *J. Phys. Chem. B* **2000**, *104*, 8061.

(43) Fletcher, P. D. I.; Galal, M. F.; Robinson, B. H. *J. Chem. Soc., Faraday Trans.* **1984**, *80*, 3307.

(44) Maitra, A. *J. Phys. Chem.* **1984**, *88*, 5122.

(45) Fedotov, V. D.; Zuev, Y. F.; Archipov, V. P.; Idiyatullin, Z. S.; Garti, N. *Colloids and Surf.,A* **1997**, *128*, 39.

(46) Moulik, S. P.; Paul, B. K. *Adv. Colloid Interface Sci.* **1998**, *78*, 99.

(47) Caboi, F.; Capuzzi, G.; Baglioni, P.; Monduzzi, M. *J. Phys. Chem. B* **1997**, *101*, 10205.

(48) Nazario, L. M. M.; Hatton, T. A.; Crespo, J. P. S. G. *Langmuir* **1996**, *12*, 6326.

(49) Chen, S. H. *Annu. Rev. Phys. Chem.* **1986**, *37*, 351.

(50) Goddeeris, C.; Cuppo, F.; Reynaers, H.; Bouwman, W. G.; Van den Mooter, G. *Int. J. Pharm.* **2006**, *312*, 187.

(51) Martinez, A. V.; Dominguez, L.; Malolepsza, E.; Moser, A.; Ziegler, Z.; Straub, J. E. *J. Phys. Chem. B* **2013**, *117*, 7345.

(52) Paul, B. K.; Mitra, R. K. *J. Colloid Interface Sci.* **2006**, *295*, 230.

(53) Vasquez, V. R.; Williams, B. C.; Graeve, O. A. *J Phys Chem B* **2011**, *115*, 2979.

(54) Pal, N.; Verma, S. D.; Singh, M. K.; Sen, S. *Anal. Chem.* **2011**, *83*, 7736.

(55) Hirai, M.; Hirai, R. K.; Iwase, H.; Arai, S.; Mitsuya, S.; Takeda, T.; Seto, H.; Nagao, M. *J. Phys. Chem. Solids* **1999**, *60*, 1359.

(56) Liu, J. C.; Li, G. Z.; Han, B. X. *Chin.Chem.Lett* **2001**, *12*, 1023.

(57) Hou, M. J.; Shah, D. O. *Langmuir* **1987**, *3*, 1086.

(58) Coulter, B. In *Delsa Nano Submicron Particle Size and Zeta Potential Manual* 2008.

(59) Malvern instruments; *Zetasizer Nano Series User Manual,* **2004**.

(60) Finsy, R. *Adv. Colloid Interface Sci.* **1994**, *52*, 79.

(61) ASTM In *Standard E2490*; ASTM International: West Conshohocken, PA, 2009.

(62) DeVos, C.; Deriemaeker, L.; Finsy, R. *Langmuir* **1996**, *12*, 2630.

(63) *Particle size distribution: assessment and characterization*; Provder, T., Ed.; American Chemical Society: Washington, D.C., 1987.

(64) Hergert, W.; Wriedt, T. In *Springer series in optical sciences 169*; Springer,: Berlin ; London, 2012, p 1 online resource.

(65) Provencher, S. W. *Comput. Phys. Commun.* **1982**, *27*, 229.

(66) Ruf, H. *Langmuir* **2002**, *18*, 3804.

(67) Ruf, H.; Gould, B. J.; Haase, W. *Langmuir* **2000**, *16*, 471.

(68) Goffredi, M.; Liveri, V. T.; Vassallo, G. *J. Solution Chem.* **1993**, *22*, 941.

(69) Alvarez, E. V.; Carballido-Landeira, J.; Guiu-Souto, J.; Taboada, P.; Munuzuri, A. P. *J. Chem. Phys.* **2011**, *134*, 094512.

(70) McPhee, J. T.; Scott, E.; Levinger, N. E.; Van Orden, A. *J. Phys. Chem. B* **2011**, *115*, 9585.

(71) Hammouda, B. Probing Nanoscale Structures-The SANS Toolbox. *National Institute of Standards and Technology Center for Neutron Research* [Online Early Access].

(72) Toprakcioglu, C.; Dore, J. C.; Robinson, B. H.; Howe, A.; Chieux, P. *J. Chem. Soc., Faraday Trans.* **1984**, *80*, 413.

(73) Pauw, B. R. In *Looking At Nothing*; Weblog, Ed. 2013.

(74) Kotlarchyk, M.; Chen, S. H.; Huang, J. S.; Kim, M. W. *Phys. Rev. A* **1984**, *29*, 2054.

(75) Huang, J. S.; Safran, S. A.; Kim, M. W.; Grest, G. S.; Kotlarchyk, M.; Quirke, N. *Phys. Rev. Lett.* **1984**, *53*, 592.

(76) Eastoe, J.; Fragneto, G.; Steytler, D. C.; Robinson, B. H.; Heenan, R. K. *Physica B* **1992**, *180*, 555.

(77) Pauw, B. R. *J. Phys.: Condens. Matter* **2013**, *25*, 383201.

(78) Hirai, M.; Kawai-Hirai, R.; Sanada, M.; Iwase, H.; Mitsuya, S. *J. Phys. Chem. B* **1999**, *103*, 9658.

(79) Zhang, X. G.; Chen, Y. J.; Liu, J. X.; Zhao, C. Z.; Zhang, H. J. *J. Phys. Chem. B* **2012**, *116*, 3723.

(80) Levinger, N. E. *Science* **2002**, *298*, 1722.

(81) Monduzzi, M.; Caboi, F.; Moriconi, C. *Colloids and Surf.,A* **1997**, *130*, 327.

(82) Wong, M.; Thomas, J. K.; Nowak, T. *J. Am. Chem. Soc.* **1977**, *99*, 4730.

(83) Nilsson, P. G.; Lindman, B. *J. Phys. Chem.* **1983**, *87*, 4756.

(84) Clarkson, M. T.; Beaglehole, D.; Callaghan, P. T. *Phys. Rev. Lett.* **1985**, *54*, 1722.

(85) Chen, A.; Wu, D. H.; Johnson, C. S. *J. Am. Chem. Soc.* **1995**, *117*, 7965.

(86) Griffiths, P. C.; Cheung, A. Y. F.; Davies, J. A.; Paul, A.; Tipples, C. N.; Winnington, A. L. *Magn. Reson. Chem.* **2002**, *40*, S40.

(87) Valentini, M.; Vaccaro, A.; Rehor, A.; Napoli, A.; Hubbell, J. A.; Tirelli, N. *J. Am. Chem. Soc.* **2004**, *126*, 2142.

(88) Song, Y. Q. *Concepts Magn. Reson. A* **2003**, *18A*.

(89) Bohidar, H. B.; Behboudnia, M. *Colloids and Surf.,A* **2001**, *178*, 313.

(90) Finsy, R. *Part. Part. Syst. Char.* **1990**, *7*, 74.

(91) Callaghan, P. T. *Translational dynamics and magnetic resonance : principles of pulsed gradient spin echo NMR*; Oxford University Press: Oxford ; New York, 2011.

(92) Dahirel, V.; Ancian, B.; Jardat, M.; Meriguet, G.; Turq, P.; Lequin, O. *Soft Matter* **2010**, *6*, 517.

(93) Ohtsuki, T.; Okano, K. *J. Chem. Phys.* **1982**, *77*, 1443.

(94) Claridge, T. D. W. *High-resolution NMR techniques in organic chemistry*; 1st ed.; Pergamon: Amsterdam ; New York, 1999.

(95) Phillies, G. D. J. *J. Colloid Interface Sci.* **1982**, *86*, 226.

(96) Fletcher, P. D. I., Howe, A.M. Perrin N.M. Robinson B.H. Toprakcioglu C. Dore J.C, In *Surfactants in Solution,* Edited by Mittal and Lindman; Plenum Press: 1984; Vol. 3.

(97) Lekkerkerker, H. N. W.; Coulon, P.; Vanderhaegen, R.; Deblieck, R. *J. Chem. Phys.* **1984**, *80*, 3427.

(98) Monduzzi, M.; Olsson, U.; Soderman, O. *Langmuir* **1993**, *9*, 2914.

(99) Brunetti, S.; Roux, D.; Bellocq, A. M.; Fourche, G.; Bothorel, P. *J. Phys. Chem.* **1983**, *87*, 1028.

(100) Felderhof, B. U. *J. Phys. A: Math. Gen.* **1978**, *11*, 929.

(101) Jada, A.; Lang, J.; Zana, R. *J. Phys. Chem.* **1989**, *93*, 10.

(102) Umberger, J. Q.; Lamer, V. K. *J. Am. Chem. Soc.* **1945**, *67*, 1099.

(103) Debye, P. *Trans. Electrochem.Soc.* **1942**, *82*, 282.

(104) Cassin, G.; Badiali, J. P.; Pileni, M. P. *J. Phys. Chem.* **1995**, *99*, 12941.

(105) Bhattacharyya, K. *Acc. Chem. Res.* **2003**, *36*, 95.

(106) Lindman, B.; Stilbs, P. In *Surfactants in Solution,* Edited by Mittal and Lindman; Plenum Press New York and London: 1982; Vol. 3, p 1651.

(107) Dutkiewicz, E.; Robinson, B. H. *J. Electroanal. Chem.* **1988**, *251*, 11.

(108) Pileni, M. P. *J. Phys. Chem.* **1993**, *97*, 6961.

(109) Walde, P.; Mao, Q. C.; Bru, R.; Luisi, P. L.; Kuboi, R. *Pure Appl.Chem.* **1992**, *64*, 1771.

(110) Crans, D. C.; Levinger, N. E. *Acc. Chem. Res.* **2012**, *45*, 1637.

(111) Hasegawa, M. *Langmuir* **2001**, *17*, 1426.

(112) D.A. Case, T. A. D., T.E. Cheatham, III, C.L. Simmerling, J. Wang, R.E. Duke, R.Luo, R.C. Walker, W. Zhang, K.M. Merz, B. Roberts, S. Hayik, A. Roitberg, G. Seabra,J. Swails, A.W. Götz, I. Kolossváry, K.F.Wong, F. Paesani, J. Vanicek, R.M.Wolf, J. Liu,X. Wu, S.R. Brozell, T. Steinbrecher, H. Gohlke, Q. Cai, X. Ye, J. Wang, M.-J. Hsieh, G.Cui, D.R. Roe, D.H. Mathews, M.G. Seetin, R. Salomon-Ferrer, C. Sagui, V. Babin, T.Luchko, S. Gusarov, A. Kovalenko, and P.A. Kollman 2012.

(113) Safran, S. A. *J. Chem. Phys.* **1983**, *78*, 2073.

(114) Gardner, A.; Vasquez, V. R.; Clifton, A.; Graeve, O. A. *Fluid Phase Equilib.* **2007**, *262*, 264.

(115) Mudzhikova, G. V.; Brodskaya, E. N. *Colloid J.* **2006**, *68*, 738.

(116) Longhi, G.; Fornili, S. L.; Liveri, V. T.; Abbate, S.; Rebeccani, D.; Ceraulo, L.; Gangemi, F. *Phys. Chem. Chem. Phys.* **2010**, *12*, 4694.

(117) Chanda, J.; Chakraborty, S.; Bandyopadhyay, S. *J. Phys. Chem. B* **2005**, *109*, 471.

(118) Schlenkrich, M. B., J.; MacKerell, A. D.; Karplux, M. *In Biological Membranes: A Molecular Perspective from Computation and Experiment;*; Birkhauser: Boston, 1996.

(119) Abel, S.; Sterpone, F.; Bandyopadhyay, S.; Marchi, M. *J. Phys. Chem. B* **2004**, *108*, 19458.

(120) Mudzhikova, G. V.; Brodskaya, E. N. *Colloid J.* **2006**, *68*, 729.

(121) Fox, T.; Kollman, P. A. *J. Phys. Chem. B* **1998**, *102*, 8070.

2. Nuclear Magnetic Resonance (NMR)

2.1. Principles of NMR

2.1.1. Nuclear Spin

A nucleus is NMR active if it has nuclear spin (angular momentum). Nuclear spin only arises when nuclei have unpaired nucleons, giving a spin quantum number, I which is non-zero.[1,2] ^{1}H is the nuclide most commonly used in magnetic resonance $I = ½$ which has an abundance [2] of almost 100%, but there are other NMR active nuclei, which are commonly used such as ^{13}C, with $I = ½$ and ^{2}H, with $I = 1$.[2-4] Angular momentum is a vector quantity, having both size and direction and a nucleus with angular momentum has an associated magnetic moment ($\boldsymbol{\mu}$) (eq 2.1), where γ is a constant, which is known as the magnetogyric ratio.[2,4] It is a measure of the magnetic strength of the nucleus.

$$\mu = \gamma I \qquad \text{eq 2.1}$$

When a nucleus is put into an external magnetic field, $\boldsymbol{B}_0$, the nuclear spins align with the field. The external magnetic field also removes the degeneracy of the spins, inducing the spins to move to different discrete energy levels.[2,4,5] The number of energy levels is determined by the spin quantum number.

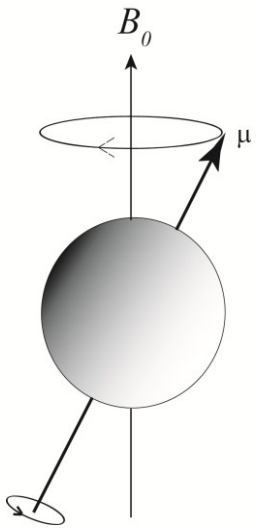

Figure 2.1: *A diagram showing a spinning nucleus precessing in the presence of an applied magnetic field (B_0).*

The application of the static magnetic field, $\boldsymbol{B}_0$, causes the spinning nucleus to *precess* at a specific frequency, known as the Larmor frequency (Figure 2.1). This is related to the magnetogyric ratio,[2,3,6] γ and directly proportional to the strength of $\boldsymbol{B}_0$. The Larmor frequency is stated in radians per second (eq 2.2) or Hz (eq 2.3)

$$\omega = -\gamma B_0 \qquad \text{eq 2.2}$$

$$\nu = \frac{-\gamma B_0}{2\pi} \qquad \text{eq 2.3}$$

In the case of I = ½, there is a distribution of spins between two different energy levels. The two spin states are spin up at the lower energy, denoted as α spins, (m = + ½) and spin down, at a higher energy level, denoted as β spins (m = -½). A transition from one energy level to another is only possible if the energy is exactly equal to the difference between the energy levels. This is due the quantised spin states,[2] with the allowed transitions given by the

selection rule $\Delta m_I = \pm 1$. The energy required to move between the levels is related to γ and $\boldsymbol{B}_0$ (eq 2.4)

$$\Delta E = \frac{h\gamma B_0}{2\pi} \qquad \text{eq 2.4}$$

The population of nuclei at the lower energy level is slightly greater than that at the higher energy level (Figure 2.2).[4,5]

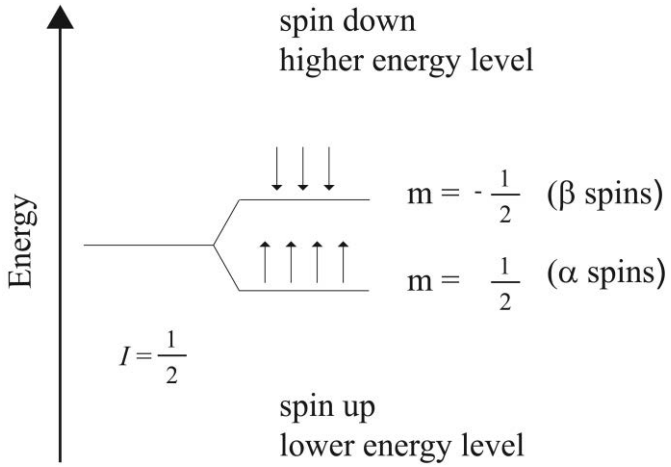

Figure 2.2: *A schematic representation showing the energy levels and populations of spin up and spin down nuclei, when I = ½.*

The spin populations on the different energy levels can be calculated from eq 2.5

$$\frac{N_{1/2}}{N_{-1/2}} = e^{\Delta E/kT} \qquad \text{eq 2.5}$$

There is a specific difference in the spin populations at differing energy levels. If the magnetic moments from the individual spins are added together, there will be a resultant vector quantity of magnetization, (Figure 2.3) with specific size and direction.[4] This is conventionally known as the macroscopic vector of magnetization $\boldsymbol{M}_0$. Manipulating and monitoring the size of this

resultant vector of magnetization (the nuclear spins) is a key concept in nuclear magnetic resonance.[2] Vector diagrams can be used to describe the position and relative size of the magnetization and is one means to explain and describe NMR experiments but it does have limitations.

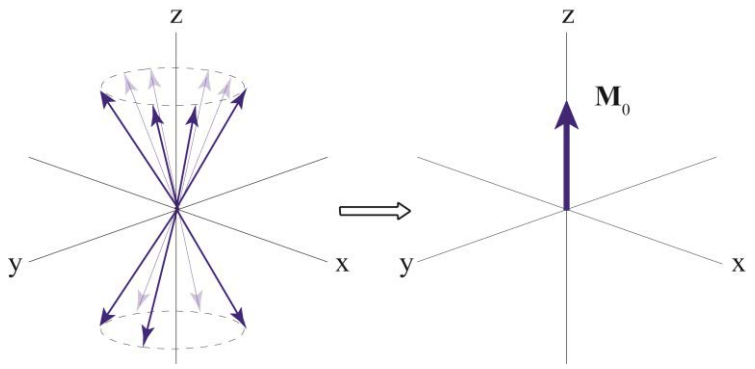

Figure 2.3: *A schematic diagram showing the summation of the individual magnetic vectors to produce the macroscopic vector of magnetization (**M**$_0$).*

The nuclear spins and resultant $\boldsymbol{M}_0$ can be manipulated by the application of a radiofrequency pulse (rf).[5] When a radiofrequency (rf) pulse is applied, the direction and angle of the resultant magnetization is affected. Conventionally,[4] the *z* axis is in the direction of the external magnetic field ($\boldsymbol{B}_0$). A 90° rf pulse takes the resultant $\boldsymbol{M}_0$ from the *z* axis down to the *xy* plane, which is also known as the *transverse* plane. At this angle the spins are *in phase* and are precessing at the same frequency. The pulse angle is related to the strength and duration of the radiofrequency pulse.[4] (eq 2.6)

$$\theta = \frac{360\gamma}{2\pi} B_1 t \qquad \text{eq 2.6}$$

The transition of $\boldsymbol{M}_0$ to the transverse plane, is where an NMR signal is at its maximum intensity. The NMR signal is produced as the rotating vector of magnetization induces an

oscillating current in the rf coil, which was originally used to apply rf pulses to the system. This oscillating current is weak but is adequate to produce the NMR signal.[2] After an rf pulse is applied, the spins will, after a time, go back to the original Boltzmann distribution to the different energy levels with the resultant $\boldsymbol{M}_0$ once more in line with $\boldsymbol{B}_0$. The time it takes for the spins to regain the Boltzmann distribution is dependent on relaxation processes which are specific to different chemical environments.[3-6] As the spins return to thermal equilibrium, the Free Induction Decay (FID) signal is produced.[3-6]

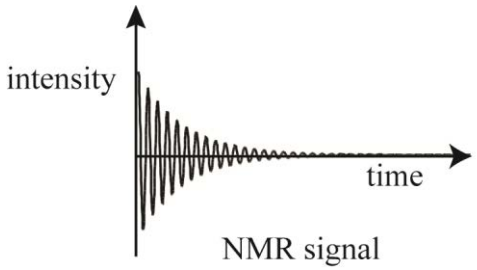

Figure 2.4: *A diagram of free induction decay.*

The FID or NMR signal is collected as a function of time (Figure 2.4).[5] The time signal has to be converted to a frequency spectrum, as this is where the potential to distinguish the various molecules within a sample is realised, because the different chemical species will precess at different frequencies, as they experience different chemical environments. There is an inverse relationship between time and frequency[5] (eq 2.7).

$$\frac{1}{t} = \nu \qquad \text{eq 2.7}$$

In order to convert time data into frequency data to produce a *spectrum*, a Fourier transform is applied.[3] The Fourier transform produces two signals in the frequency domain resulting in two spectra, which originate from sine and cosine functions (eq 2.8)

$$f(\omega) = \int_{-\infty}^{+\infty} f(t)[\cos(\omega t) - i\sin(\omega t)]dt \qquad \text{eq 2.8}$$

These signals are known as the real (absorption) and imaginary (dispersion) parts of the spectrum, respectively. The *real* part is what is presented in an NMR spectrum.[3]

2.1.2. Chemical Shift

The NMR frequency of the nucleus, as explained in the previous section, is dependent on γ and $\boldsymbol{B}_0$, however the protons within a molecule will not precess at exactly the same frequencies, as the proton frequency is also dependent on and affected by the local electron density distribution.[4] A static magnetic field $\boldsymbol{B}_0$ induces motion of the electrons in the atoms within a molecule. The motion of the electrons then generates another small magnetic field, which opposes $\boldsymbol{B}_0$. If a proton is in the proximity of an electronegative atom, the electron density around that proton will be reduced and the proton will experience a deshielding effect where the magnetic field generated by the electrons is reduced, which in turn augments the effect of the applied field, $\boldsymbol{B}_0$ causing the proton to precess at a higher frequency. Chemical shifts originate from the deshielding and shielding effects occurring between the nuclei within a molecule.[4] It is why different proton signals can be distinguished within a molecule and chemical mixtures can also be probed.[5] Intramolecular and intermolecular hydrogen bonding causes deshielding which affects the chemical shifts of molecules.[4] Intermolecular hydrogen bonding can cause small but significant shifts and these shifts may vary if the hydrogen bonding is disrupted by changing the temperature or the dilution of the system.[4]

2.1.3. J Coupling

J coupling or spin-spin coupling arises from intra-molecular magnetic interactions between nuclei[4] with the bonding electrons between atoms having an effect on the magnetic fields between nuclear spins. Taking the example of two protons denoted A and X, where A is in the α spin state with a value of m = ½, the magnetic field of X will oppose the external field, causing a reduction in frequency, whereas for m= −½, the field adds to $\boldsymbol{B}_0$ at X and increases the frequency. Therefore for AX protons, there won't be one peak but two peaks from the interaction of proton A with the different spin states[4] of proton X. The spin-spin coupling constant between proton A and proton X is given by eq 2.9

$$E = h J_{AX} m_A m_X \qquad \text{eq 2.9}$$

where m_A and m_X are the magnetic quantum numbers and J_{AX} is the coupling constant between the two protons.[4]

2.1.4. Relaxation processes

On applying a 90° rf pulse at thermal equilibrium, the α and β states become *saturated* and have an equal population of spins. However, after the rf pulse, the nuclear spins return to their original distributions through two different relaxation processes, T_1, spin lattice or longitudinal relaxation and T_2, spin-spin or transverse relaxation.[2,4-6] In order to achieve the resonance condition where the spins are able to make the transition between energy levels, the rf pulse must be equal to the Larmor frequency. The relaxation times of the nuclei are dependent on a number of factors including inter and intra-molecular interactions between species, the tumbling time, τ_c, of the molecules and the presence of paramagnetic molecules.[6]

T_1 is the time for the nuclei to return to the Boltzmann distribution of spin-up (α) and spin-down (β) nuclei.[6] Molecular interactions, through space, by dipolar coupling and fluctuations in the magnetic field at the Larmor frequency induce transitions between the, α and β states. Dipolar coupling occurs as a consequence of the interaction of the magnetic dipoles between neighbouring protons and this is dependent on the orientations and distance of the neighbouring protons.[3,4] The distance dependency is $1/r^3$ and the orientation dependency[4] is $3\cos^2\theta$-1. The distances and orientation between the protons will depend on how quickly the protons move in relation to each other. This is determined by the tumbling of the molecules, which is given by $1/\tau_c$, where τ_c is the rotational correlation time. This is the time taken for a molecule to rotate through one radian.[3] Paramagnetic species have unpaired electrons which create relatively large magnetic moments and therefore cause a decrease in the relaxation time. As discussed previously in section (1.2.5), measurements of relaxation rates $1/T_1$ and $1/T_2$ have been used to monitor the restricted motion in water molecules in RMs at low ω. The relaxation rate of the water molecules increased, as the RMs decreased in size and this was due to the restricted motion due to the ion-dipole interactions with the surfactant counter-ions.[7]

On applying a 90° rf pulse, the nuclear spins have phase coherence. However immediately after the rf pulse, the spins start to lose their phase coherence. Spins experience slightly different magnetic fields and therefore some precess at higher or lower frequencies. The T_2 relaxation value is the time for the spins to completely dephase.[5,6] The transverse relaxation process is a combination of T_2, which is intrinsic to the sample and T_{2B0}, which arises from fluctuations and inhomogeneties in the magnetic field $\boldsymbol{B}_0$. The T_2 time is therefore obtained

from a combination of factors and is known as T_2^* (eq 2.10). Both $T_1$and T_2 relaxation processes occur simultaneously[5] with T_2 being less or equal to T_1.

$$\frac{1}{T_2^*} = \frac{1}{T_2} + \frac{1}{T_{2B_0}} \qquad \text{(eq 2.10)}$$

2.2. Relaxation Experiments

2.2.1. T_1 Relaxation Inversion Recovery

An inversion recovery experiment measures T_1 relaxation time.[3] An initial 180° pulse flips the magnetization vector onto the -*z* axis (Figure 2.5), thus inverting the spin population.

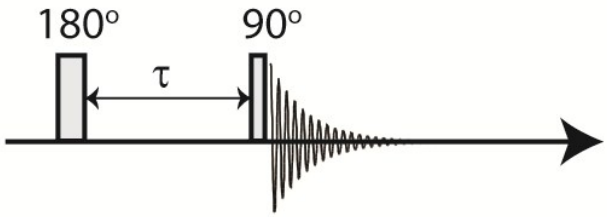

Figure 2.5: *Schematic representation of the pulse sequence of the inversion recovery experiment to measure T_1 relaxation.*

The magnetization vector then proceeds to relax through T_1 processes, along the *z* axis. However the magnetization cannot be observed in this axis so after a delay time, τ , a 90° pulse is applied, which puts the magnetization into the transverse plane (Figure 2.5) when an FID is acquired. The pulse sequence is repeated for multiple values of τ, which is the delay time between the 180° and 90° pulse The resulting signal intensity is therefore dependent on

the delay time for that experiment. It is essential that τ is long enough so that complete relaxation of the protons occurs between the two pulses, so τ is set at $5T_1$ to ensure full relaxation is achieved. The signal intensities taken from specific peak of interest in the NMR spectrum are plotted against time (τ) (Figure 2.6).

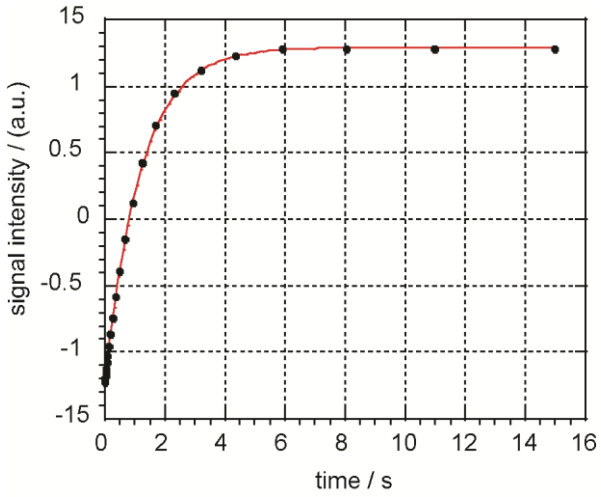

Figure 2.6: *A plot showing the relationship between signal intensity for protons in water as a function of* τ *during an inversion recovery experiment. The red line is the fitting to eq 2.11.*

The T_1 relaxation time is obtained by fitting the data[5] to eq 2.11

$$M_z = M_0\left(1 - 2e^{\left(-t/T_1\right)}\right) \qquad \text{eq 2.11}$$

2.2.2. Hahn Echo Experiment

The T_2 relaxation time can be measured through a spin-echo sequence, which was developed by Hahn[8] in 1950. The pulse sequence is shown schematically in Figure 2.7.

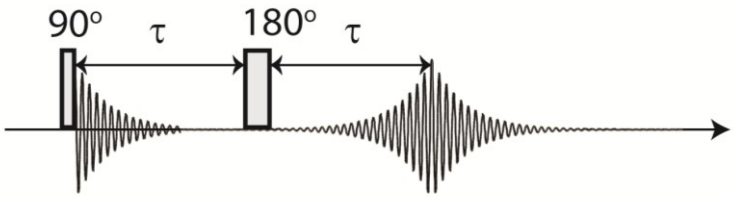

Figure 2.7: *Schematic representation of the pulse sequence of a Hahn spin-echo experiment to measure T_2 relaxation.*

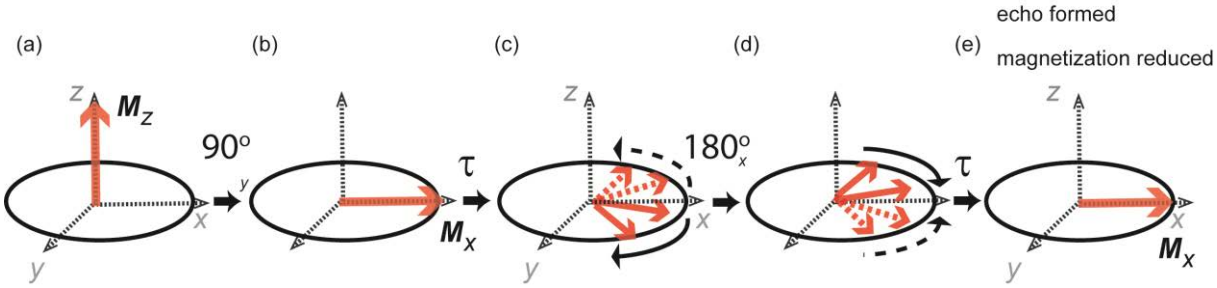

Figure 2.8: *A schematic representation of the spin manipulation during the Hahn spin-echo experiment; $\boldsymbol{M}_z$, the magnetization vector represents the spins aligned with $\boldsymbol{B}_0$ (a); the magnetization vector is put into the transverse plane after a 90°$_y$ pulse (b); the spins start to de-phase (c); a 180°$_x$ pulse flips the spins (d); the spins are refocused with reduced magnetization (e).*

The first 90° r.f. pulse puts the magnetization into the transverse plane (Figure 2.8(b)) where the nuclei initially have phase coherence, precessing at the same frequency. However the spins start to de-phase immediately, due to the inhomogeneities (Figure 2.8(c)), that exist in the static and local magnetic fields, generated from inter and intra-molecular interactions.[3] After time, τ, a 180° pulse is applied (Figure 2.8(d)), which flips the magnetization vector into the -*xy* transverse plane. This has the effect that, after the same time, τ, the magnetization will

be refocused (Figure 2.8(e)) and the spins will be re-phased forming the spin echo.[4,5] On refocusing the spins, there will have been a loss of magnetization due to T_2 relaxation processes, therefore the magnetization will be reduced. The signal acquisition now takes place.[3] The experiment is repeated at varying values of τ.

In a Hahn echo experiment the effects of molecular diffusion can contribute to the de-phasing of the spins. If the spins, during time τ, diffuse to a place where $\boldsymbol{B}_0$ is different, the spins will experience a different magnetic field and may not be fully refocused. The loss of magnetization will not just due to T_2 relaxation, but also the effects of diffusing in an inhomogeneous magnetic field. Therefore T_2^* is measured rather than T_2 and this effect increases as τ increases. In the cases where molecular diffusion affects the spin echo, the T_2 will be inaccurate.

2.2.3. Carr-Purcell-Meiboom-Gill and T_2 Relaxation

The effects of diffusion can be problematic when determining relaxation times as τ increases. The Carr-Purcell-Meiboom-Gill (CPMG) experiments are used to measure T_2 relaxation time by minimising the effects of diffusion by using a short value of τ in a multiple of echoes (n) (Figure 2.9).

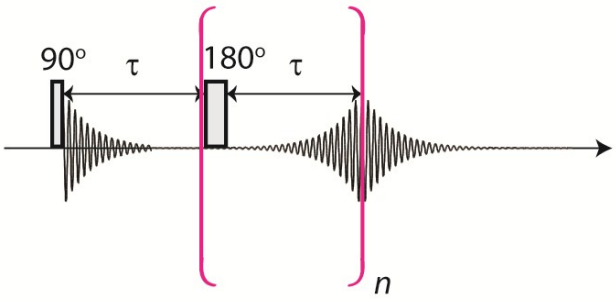

Figure 2.9: *The pulse sequence of the CPMG experiment to measure T_2 relaxation.*

The signal intensity is dependent on number of experiments (n) or echoes. The T_2 relaxation rate can be determined from measuring the amplitude of the echoes against time[3] (Figure 2.10).

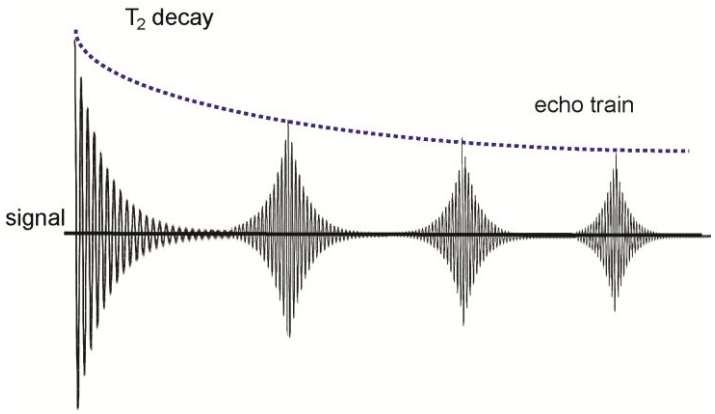

Figure 2.10: *A schematic representation of the decreasing amplitudes of the echoes, during the CPMG sequence. The T_2 relaxation rate is determined from the amplitude of the echoes.*

The T_2 relaxation time is obtained from fitting the data to an exponential function (eq 2.12), using non-linear least squares fitting (Figure 2.11). If molecules of interest in a system have two populations which have two different relaxation times, then the data is fitted to a bi-exponential function. (eq 2.13)

$$M_{x/y} = M_0 e^{-t/T_2} \qquad \text{eq 2.12}$$

$$M_{x/y} = P\left(M_0 e^{-t/T_2}\right) + (1-P)\left(M_0 e^{-t/T_2}\right) \qquad \text{eq 2.13}$$

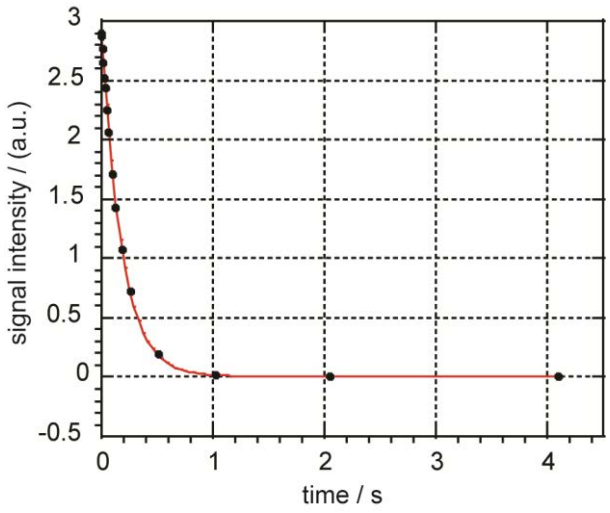

Figure 2.11: *A plot showing the relationship between signal intensity for protons in water as a function of* τ *during a CPMG experiment.*

The duration of τ needs to be short in order to suppress any effects from diffusion.[8] One advantage of the CPMG experiment over the Hahn echo is that the T_2 relaxation time can be measured with the CPMG sequence rather than the T_2^*.

2.2.4. The Nuclear Overhauser Effect (Cross relaxation)

The nuclear Overhauser effect occurs when two inequivalent protons, denoted in Figure 2.12 as I and S, have a dipolar coupling through space. The effect can be used to identify inter-nuclear distances and therefore aids in identifying the positions and stereochemistry of non-

bonded protons within a molecule. There are six possible pathways for the spin-lattice relaxation to occur between four energy levels. It is the movement of spins and the resulting population differences that can give rise to enhanced or inverted proton signals.[4] The W_1 relaxation mechanisms arise from single spin flipping of nucleus I or S between α and β states. The W_0 and W_2 relaxation pathways, however, occur when both spins flip together, in the same direction for W_2 pathway and in the opposite direction for W_0 pathway. This is known as cross relaxation.[4]

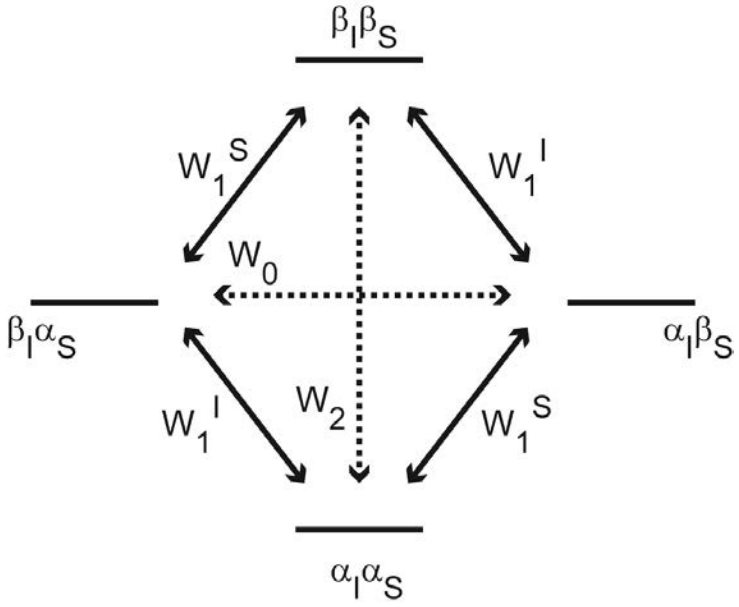

Figure 2.12: *A schematic representation of the relaxation pathways available between the energy levels for the spins α and β between the coupled nuclei I and S.*[4]

2.3. Pulsed Field Gradient Experiments (PFG)

2.3.1. Fundamental Concepts of PFG experiments

The PFG experiments used in this study to size and characterise droplets in microemulsions are described here, as well as the techniques available to analyse the data. There are many reviews of PFG experiments.[3,9-11] They describe the variety of experiments which exist to probe and measure the diffusion of molecular species. They also outline modifications made to the experiments in order to suppress the production of artifacts caused by physical phenomena. There are various PFG experiments available to measure molecular diffusion but care is needed when choosing the experiment and experimental parameters which will give the most accurate and precise data.[9,12] ^{1}H NMR pulsed field gradient experiments are used to measure the self-diffusion coefficients of molecules. Using PGSE experiments to illustrate the fundamental principles, this method[6] applies two magnetic field gradient pulses of strength $\boldsymbol{G}$ and duration, δ, which are separated by an observation time Δ.

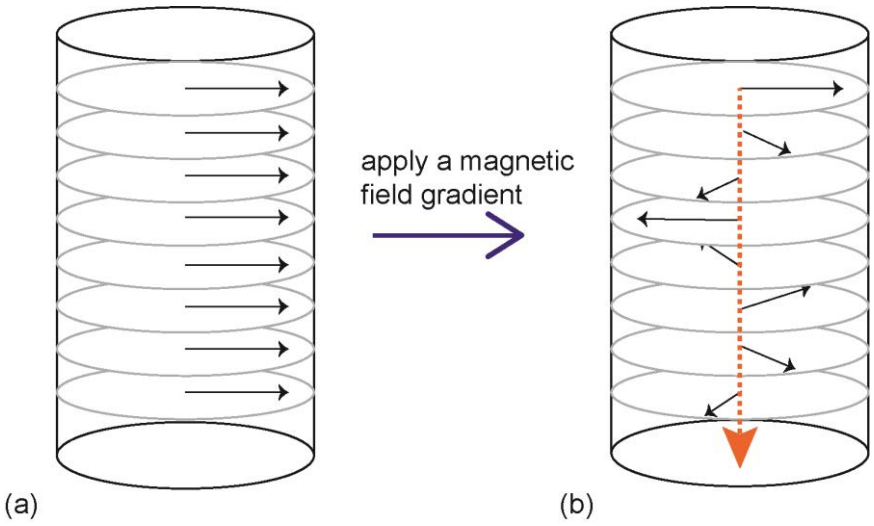

Figure 2.13: *A schematic representation showing the spins at different frequencies when a magnetic field gradient (dotted arrow) is applied.*

After a 90° rf pulse the spins are all in phase (Figure 2.13 (a)). When a magnetic gradient is applied through a specific direction in a sample, the spins will precess at increasing frequencies with increasing magnetic strength[9] (Figure 2.13 (b)). The magnitude of the magnetic field (***B***) at a distance r is given by equation 2.14, where $\boldsymbol{B}_0$ is the external magnetic field strength and ***G*** is the magnetic gradient strength.

$$B(r) = B_0 + G \cdot r \qquad \text{eq 2.14}$$

When the first magnetic gradient is applied, the spins are therefore spatially encoded through a helix of phase (Figure 2.13 (b)). In the case where there is no diffusion, after a period of time Δ, after applying a second gradient, the spins would be refocused, in the absence of any relaxation processes, with the same signal intensity. However, in the case where there is diffusion, where molecular motion is incoherent and random, the molecules are displaced from their original positions during the time period Δ. When the second field gradient is applied to refocus the spins, there is a distribution of phase shifts in the MR signal due to the diffusion of the spins, which results in a reduction of the signal intensity, producing an attenuation of the MR signal.[3,6] PFG experiments have been developed to measure spin diffusion from the Hahn spin echo, through to 1965 when Stejskal and Tanner[13] developed the method of pulsing the magnetic gradient.

2.3.2. Pulsed Field Gradient Spin Echo (PGSE)

The pulsed gradient spin echo applies two rf pulses (Figure 2.14). The initial 90° pulse takes the $\boldsymbol{M}_0$ down into the transverse plane onto the $+x$ axis, after which the first magnetic field gradient pulse is applied (Figure 2.14).

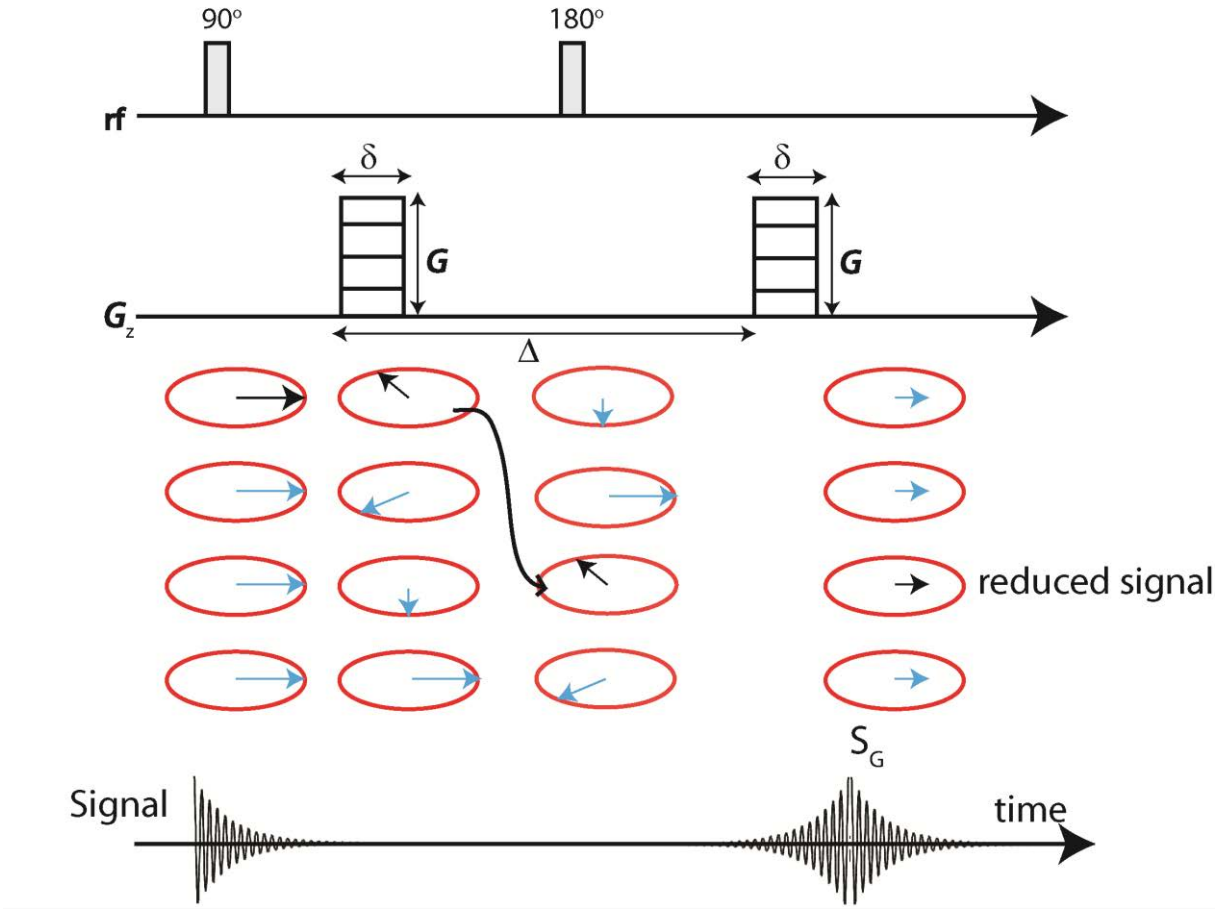

Figure 2.14: *A schematic representation of the pulsed field gradient spin echo pulse sequence, showing the effect of the applied gradients on the spins in the case where there is diffusion.*

The following 180° pulse takes the $\boldsymbol{M}_0$ through to the $-x$ axis, where the echo is formed. After the second magnetic field gradient pulse is applied the signal is acquired. The MR signal is acquired over a range of $\boldsymbol{G}$ values and a diffusion coefficient can be calculated using the Stejskal-Tanner relationship (eq 2.15) where S($\boldsymbol{G}$) is the signal amplitude at gradient amplitude $\boldsymbol{G}$, S(0) is the signal amplitude at zero gradient and γ is the magnetogyric ratio.

$$\frac{S(\boldsymbol{G})}{S(0)} = \exp\left[-\gamma^2\delta^2\boldsymbol{G}^2 D\left(\Delta - \frac{\delta}{3}\right)\right] \qquad \text{eq 2.15}$$

In order to ensure the signal attenuates to ≤ 1% , the values of $\boldsymbol{G}$, δ and Δ are varied.[3] The main disadvantage with the PGSE experiment is that after the first 90° pulse, the magnetization is stored in the transverse plane during the observation time, Δ . Therefore, during this time in the transverse plane, there can be a loss of magnetization through relaxation processes. This means that any resulting attenuation of the signal would not evolve solely from diffusion processes but also from relaxation. Another issue arising due to the magnetization being stored in the transverse plane is *J* coupling evolution.[14] This causes peak phase distortions, resulting in difficulties when analysing spectra. A method of suppressing *J* modulation has been reported for CPMG experiment by incorporating an extra 90° pulse after the initial spin echo to reverse the apparent sense of *J* modulation.[15] Another 180° pulse then refocuses the modulation caused by the first spin echo.[15] This double spin echo sequence produces a "perfect echo" and can be incorporated in both relaxation and diffusion experiments to suppress *J* modulation.[15]

2.3.3. Pulsed Gradient Stimulated Echo (PGSTE)

In PGSTE experiments (Figure 2.15), a stimulated echo is used, which uses three rf pulses. After the first 90° pulse, the magnetization is taken down to the transverse plane, where the first magnetic gradient pulse is applied, after which a second 90° pulse is applied, taking the $\boldsymbol{M}_0$ to the *-z* axis (longitudinal axis). After the observation time, Δ, a 90° pulse is applied, taking the $\boldsymbol{M}_0$ into the *–xy* transverse plane, where the final magnetic gradient pulse is applied, to refocus the spins. The signal is then acquired.

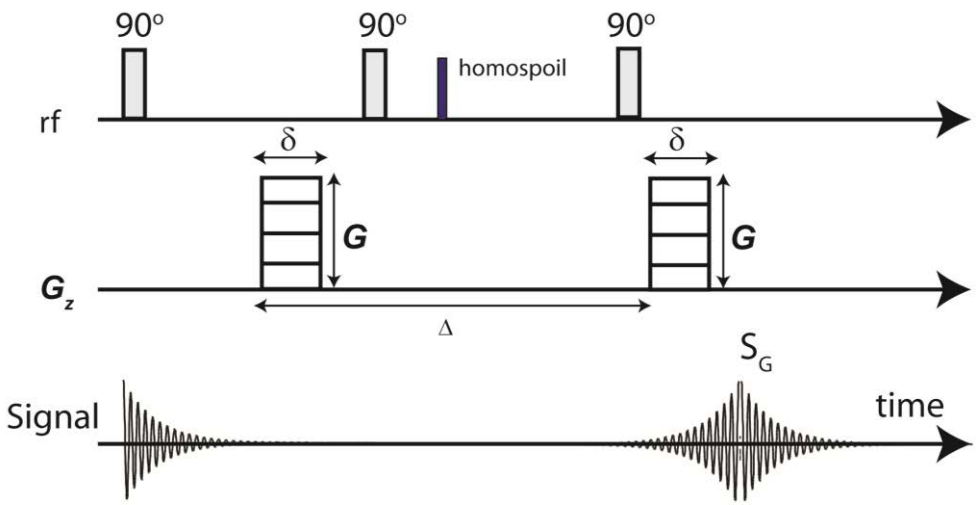

Figure 2.15: *A schematic representation of the pulsed field stimulated spin echo pulse sequence.*

As the magnetization is stored in the longitudinal axis during the relatively long observation time, the spins are less susceptible to T_2 relaxation which can be the case in PGSE experiments. This is beneficial in samples where the T_2 is significantly shorter than T_1, which is frequently the case for protons in surfactant molecules in a reverse micelle.[16] Another advantage of using the stimulated echo experiment compared to the spin echo (PGSE) experiment, is that there are less peak distortions which are caused by *J*-coupling as the magnetization is stored in the longitudinal axis rather than the transverse plane.[14] The disadvantage of the PGSTE experiment is that there is a reduction in the signal intensity by a factor of 2. The magnetization vector is the summation of two orthogonal parts. The loss of signal occurs, as the second 90° pulse transfers only one part of the magnetization vector from the transverse plane to the longitudinal axis, whilst the other is lost through homospoil gradients (Figure 2.15) and phase cycling.[3] Homospoil gradients are required to eliminate residual magnetization, which is not brought down to the transverse plane by the original 90°

pulse. As the PGSTE experiment produces four spin echoes and the stimulated echo, phase cycling is required to eliminate any effects from the echoes.[9] Phase cycling is used to eliminate unwanted signal components[17] at the end of a cycle.

2.3.4. Bipolar Pulse Pair Stimulated Echo (BPSTE)

As PFG experiments apply magnetic field gradients, they can be subjected to unwanted effects, such as eddy currents, which are electrical currents produced from changes in a magnetic field.[9,11,18] Eddy currents become more apparent as the magnitude and the rate at which the field strength increases.[1,3,9] It is then that eddy currents are induced into the metal structures surrounding the magnet and the probe.[10,18] Eddy currents generate their own magnetic fields, known as *eddy gradients* [11] with lifetimes of milliseconds, which distort the gradient pulses resulting in artifacts in the diffusion data. Various solutions to suppress the effects of eddy currents have been explored. Hardware considerations help to negate the production and suppress the effects of eddy currents,[10] including the use of shielded gradient coils or small gradient coils in a wide bore magnet however other strategies are often required. Varying the shape of the gradient pulses has been used to control the rate at which the gradients rise and fall.[9] Alternatively, pulse sequences have been developed, to delay the acquisition until the eddy currents have dispelled.[9] These are known as *longitudinal-eddy-current-delay* (LED) sequences. These are effective if the T_1 relaxation time is longer than the delay time, which occurs after the second magnetic gradient pulse. One of the most effective methods has been to use bipolar pulsed pair (BPP) gradients (Figure 2.16). Instead of a single gradient pulse, there are two gradients at half the pulse duration δ/2.

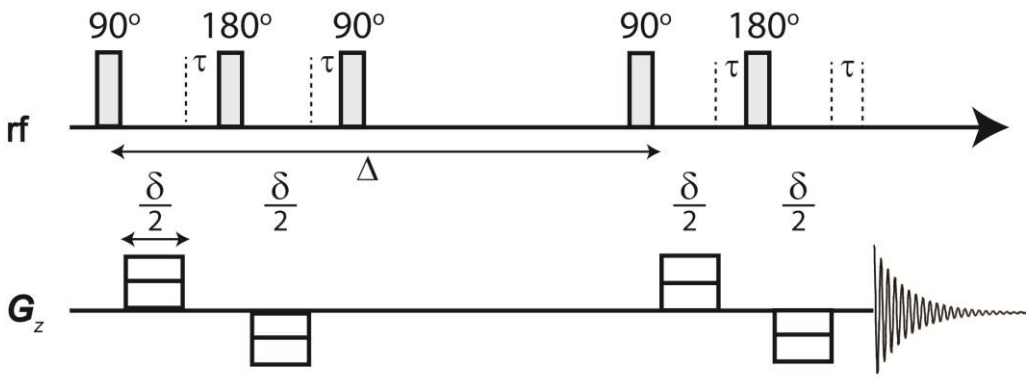

Figure 2.16: *A schematic representation of the bipolar pulsed pair stimulated spin echo pulse sequence (BPPSTE).*

The two gradients are, most importantly of opposite polarities and are separated by a 180° pulse.[3,9,18] The eddy gradients produced from the first half pulse prior to the 180° pulse are cancelled by the eddy gradients produced from the second half pulse with the opposite polarity, thereby suppressing the effect of the eddy currents.[3,9,18] The Stejskal-Tanner equation is modified slightly to account for a gradient pulse recovery delay time (τ), which is required for the bipolar pulse pairs.[3,10] (eq 2.16)

$$\frac{S(\boldsymbol{G})}{S(0)} = \exp\left[-\gamma^2\delta^2\boldsymbol{G}^2 D\left(\Delta - \frac{\delta}{3} - \frac{\tau}{2}\right)\right] \qquad \text{eq 2.16}$$

2.3.5. The Effect of Cross Relaxation on PFG experiments.

PFG experiments with stimulated echoes (STE) have the advantage of being able to store the magnetization on the longitudinal axis to suppress any T_2 relaxation effects during the diffusion time, however STE experiments and bipolar longitudinal eddy current delay (BPLED) sequences have been subject to cross relaxation effects,[9,12,19,20] where, during the diffusion time there can be an exchange of longitudinal spin polarization.[19] This is due to the nuclear Overhauser effect (NOE) and can cause the usual mono-exponential signal decays obtained from unrestricted diffusion to become non-exponential decays. The nuclear Overhauser effect arises from through-space interactions[9] between neighbouring water and surfactant molecules within the micellar interface. This effect has been observed in other macromolecular systems between the water molecules and the matrix forming the macromolecular structure.[12,19] This interaction, which can build up over longer observation times[19] has been found to distort the signal attenuations, in low viscous solutions,[20] especially where $\Delta > 20$ ms producing artifacts in the subsequent decays. The decays are found to become non-exponential with the observation time and this can lead to the incorrect conclusions that there is either restricted diffusion or anomalous diffusion occurring within a system or that a molecular species is moving at two diffusion coefficients.[9] It has been found that cross relaxation effects become more prominent with increasing observation time (Δ). Chen and Shapiro[20] found that for a system with benzoic acid and human serum albumin, the effect of the NOE was not observed at $\Delta = 20$ ms. Cross relaxation has been observed in macromolecular systems between the water protons and the polymer matrix when using PGSTE sequences,[21] whilst this phenomenon has been observed using bipolar pulsed pair (BPP) sequences in molecular capsules.[12] It is also found in low viscous solutions.[20] Therefore

when measuring the diffusion of molecules in a macromolecular system, the effects of cross-relaxation need to be checked for.[21]

2.4. Analysis Techniques for PFG Experiments

When the NMR diffusion data is collected there are different methods and techniques available to analyse the diffusion coefficients. The chemical shifts of the different species within the mixture are resolved through obtaining the NMR spectrum.[11] The diffusion data can be obtained for separate molecular species within a mixture by analysing peaks of interest at the specific chemical shifts, making sure there isn't masking between two molecular species. The diffusion data is obtained by measuring the decreasing peak amplitudes as the gradient pulse strength is increased. Alternatively, the integral of the peak of interest can be measured.

2.4.1. The Stejskal-Tanner Equation

By plotting the signal attenuation, measured from the PFG experiment against the increasing field gradient strength values, a Gaussian decay will be produced. As all the experimental parameters are known for the Stejskal-Tanner equation, (eq 2.12), the decay can be fitted with non-linear least squares,[22] using kaleidagraph software,[23] to obtain the average self-diffusion coefficient (Figure 2.17).

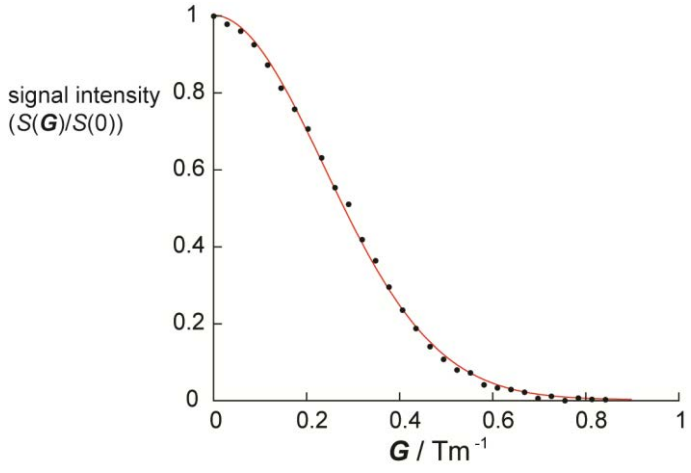

Figure 2.17: *A plot of diffusion data fitted mono-exponentially to the Stejskal-Tanner equation.*

When analysing a mixture of chemicals, as with microemulsions, it is beneficial to choose peaks which do not overlap or mask one another as this will generate diffusion data for two different chemical species and could be mistaken for one chemical species generating two diffusion coefficients. If the molecule of interest is diffusing at two different rates, due to being in different environments within a system then the diffusion decay data will fit a bi-exponential decay curve and it is possible to obtain the two average self-diffusion coefficients and their proportions within a system, which is valuable when detecting different sizes of particles within a system (Figure 2.18).

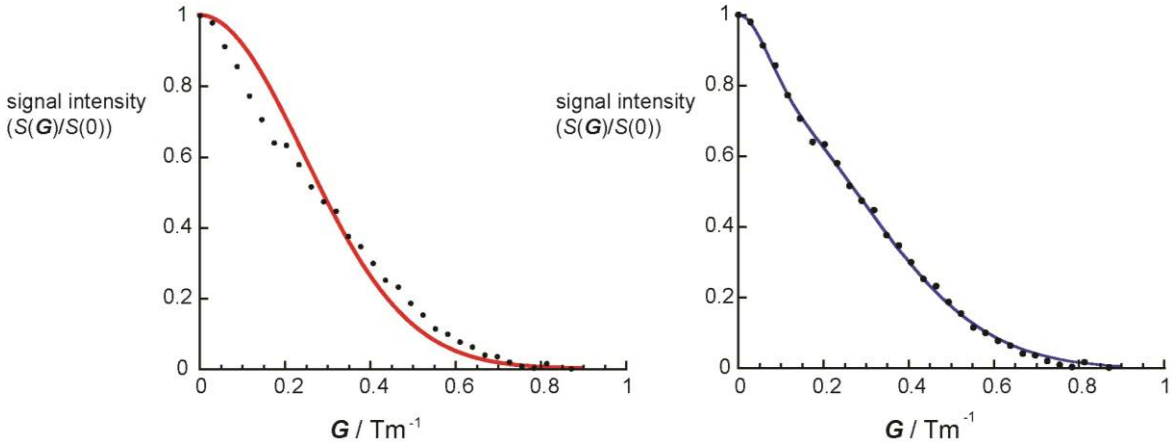

Figure 2.18: *Plots of diffusion data for a system where the molecule of interest is diffusing at 2 different rates, fitted to a mono-exponential (a) and a bi-exponential fit (b).*

The proportions of the two diffusion coefficients are extracted from fitting to the bi-exponential form of Stejskal Tanner equation, (eq 2.17) where P is the proportion of the diffusion coefficient D_1.

$$\frac{S(\boldsymbol{G})}{S(0)} = P\exp\left[-\gamma^2\delta^2\boldsymbol{G}^2 D_1\left(\Delta-\frac{\delta}{3}\right)\right] + (1-P)\exp\left[-\gamma^2\delta^2\boldsymbol{G}^2 D_2\left(\Delta-\frac{\delta}{3}\right)\right] \qquad \text{eq 2.17}$$

An alternative method of recording the diffusion data is by plotting the signal attenuation as a function of q^2, which is given by ($\gamma^2 \boldsymbol{G}^2 \delta^2 (\Delta - \delta/3)$) and fitting to linear least squares (Figure 2.19).

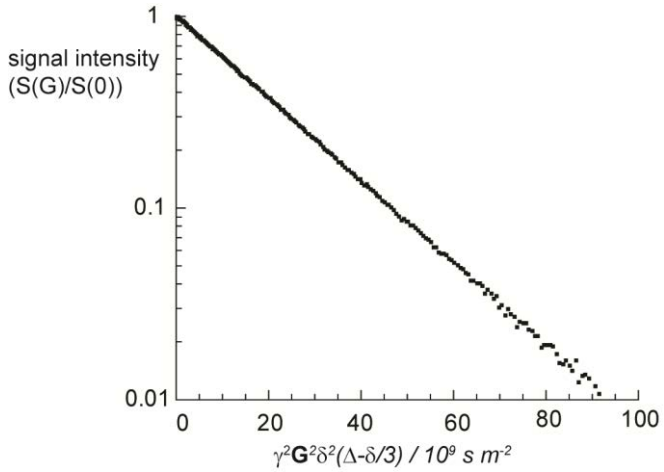

Figure 2.19: *A plot showing the signal intensity for a PGSTE experiment plotted as a function of q^2.*

2.4.2. Inverse Laplace Transform

An alternative method of analysing diffusion data is by applying the inverse Laplace transform (ILT) to obtain a distribution of diffusion coefficients. ILTs have been used to generate distributions from 1D diffusion PFG experiments with emulsions[24] and in porous media.[25] There are different methods used for the numerical inversion of data, which are reviewed by Mitchell *et al*.[26] In the case of 2D diffusion-diffusion exchange experiments (DEXSY), a double inverse Laplace transform can also be applied to data which is acquired in two-dimensions. The resulting data shows cross-diagonal peaks if a molecular species is diffusing at one diffusion coefficient. However, when a molecular species is exchanging between two populations diffusing at two different diffusion coefficients, off-diagonal peaks

are observed,[25,27] hence the dynamics and exchange between molecular species can be probed. In ILT, the exponential forms of the time-related data are transformed into distributions, where *S(t)* is the time-related data and *R(t)* is the probability distribution of the time-related data (Figure 2.20) (eq 2.18).[11]

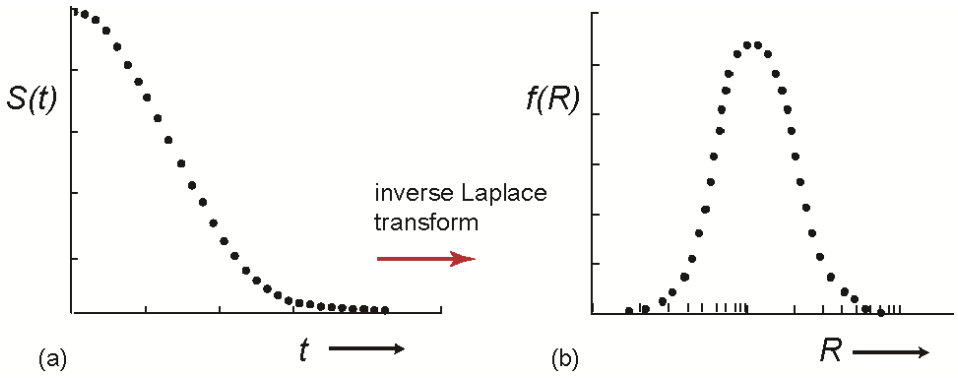

Figure 2.20: *Charts showing the time-related data, S(t), (a) and the probability distribution of the time-related data, R(t), (b).*

$$f(t) = \mathcal{L}^{-1}\{S(t)\} = \frac{1}{2\pi i}\int_{\gamma-i\infty}^{\gamma+i\infty} S(t)exp(Rt)\,dt \qquad \text{eq 2.18}$$

Borgia *et al.*[28] describe how relaxation and diffusion data from NMR experiments are sums of exponentially decaying components. This allowed equation 2.18 to be written specifically for diffusion data as shown in eq 2.19, where $G(D_j)$ is the distribution of diffusion coefficients and ε_i is the noise generated from the experiment.

$$S(t_i) = g_i = \sum G(D_j)\exp\left(-(\gamma\delta G)^2\left(\Delta - \delta/3\right)D_i\right) + \varepsilon_i \qquad \text{eq 2.19}$$

ILT can generate an infinite number of solutions, as the integral limits indicate (eq 2.18) and can produce "mathematically ill-posed problems" by fitting noise. The ill-posed problems arise when noise is included as a measurement, multiplying the function of time by an ever

increasing exponential function.[11] This makes the ILT very sensitive to noise and imposes the use of constraints in order to obtain accurate data. In this study, the application of non-negative least squares with a Tikhonov regularisation, is used.[11,26,29] The equation, 2.19, can be discretized into a matrix form, eq 2.20.[11,29,30]

$$M = KF + E \qquad \text{eq 2.20}$$

Inversion of eq 2.20 is ill-posed as small changes in M can create large changes in F.[29] One method used to fit the data is to minimize the expression, $\|M - KF\|^2 + \alpha\|F\|^2$. The first term in the expression measures the difference between the data and the fit.[29] The second term is a Tikhonov regularisation, which includes the use of the smoothing parameter (α) to calculate the smoothness of the inversion and making it less ill-conditioned.[29] One constraint consists in fitting a smoothing parameter, α, in order to control the increasing product of the function of time and the exponential function (which in this case is the diffusion data).[28,29]

There are also several methods to choose the most appropriate and optimum smoothing parameter. The method used in this study was developed by Fordham *et al.*,[30] which has been previously described as the S-curve method.[29] The smoothing parameter controls a cut-off point to minimise fitting the noise. The optimal value of α is determined by repeating the ILT for different α and measuring χ^2, the error of the fit, as a function of α (Figure 2.21).[11]

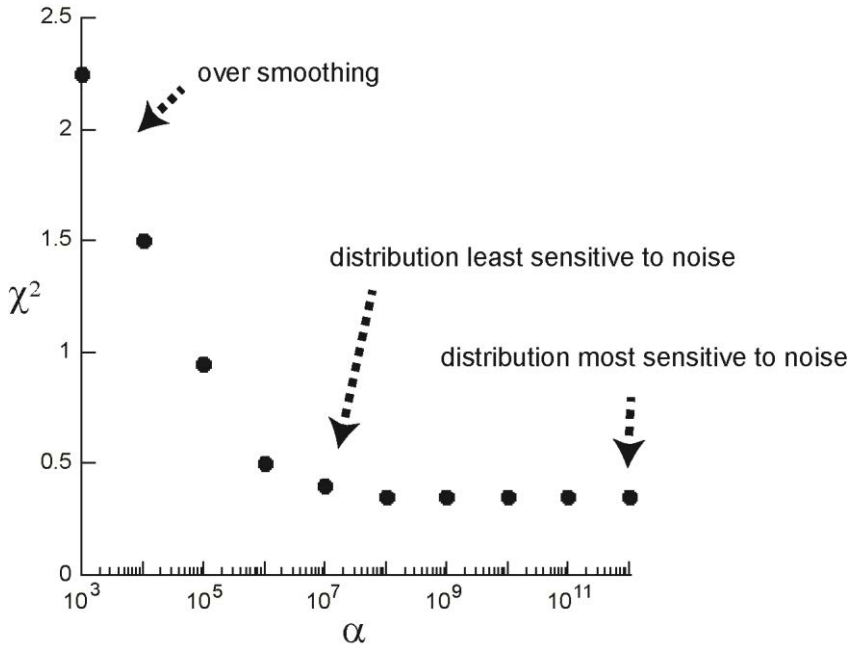

Figure 2.21: *A chart showing how to obtain the smoothing parameter.*

The lowest value of α is chosen before χ^2 rapidly increases. This increase corresponds to the point where the narrowest distribution, G(D) is obtained, without generating spurious peaks fitted by the noise.[28,30] If the chosen α value is too high, it is more prone to noise artifacts, whereas if α is too low then it is subject to over-smoothing, where the precision of the distribution is compromised. In addition to the smoothing constraint, conditions concerning the nature of G(D) and the noise have to be met (or assumed) in order to obtain quantitative diffusion coefficient distributions from the ILT. The G(D) has to be non-negative and smooth and the noise has to be additive, Gaussian and have a zero mean.[10,28,29,31] Typically, ILT analysis produces plots of G(D)D vs log(D), where G(D) is the distribution function with respect to D. A modal average diffusion coefficient can be obtained from the maximum of the distribution. In the case of multi-exponential diffusion, the proportions of the diffusion coefficients in a distribution are obtained by summing the G(D)D for the individual peaks corresponding to each diffusion coefficient.

Note that the inverse Laplace transform was discussed in (1.2.1), in relation to Dynamic Light Scattering. This technique uses the computer program to constrain the ILT (CONTIN, developed by Steven Provencher).[32,33] The developments in the constrained regularization[28-32] provides a method to apply the ILT. Although there are challenges using the ILT, it is frequently used as a tool to analyse data and provide distributions of data in DLS[34-36] and NMR[24,37,38] experiments.

2.5. References

(1) Callaghan, P. T. *Principles of nuclear magnetic resonance microscopy*; Clarendon, 1991.

(2) Levitt, M. H. *Spin dynamics : basics of nuclear magnetic resonance*; John Wiley & Sons: Chichester ; New York, 2001.

(3) Claridge, T. D. W. *High-resolution NMR techniques in organic chemistry*; 1st ed.; Pergamon: Amsterdam ; New York, 1999.

(4) Hore, P. J. *Nuclear magnetic resonance*; Oxford University Press: Oxford, 1995.

(5) Hornak, J. P. In http://www.cis.rit.edu/htbooks/nmr/; Hornak, J. P., Ed. 1997-2014.

(6) Britton, M. M. *Chem. Soc. Rev.* **2010**, *39*, 4036.

(7) Wong, M.; Thomas, J. K.; Nowak, T. *J. Am. Chem. Soc.* **1977**, *99*, 4730.

(8) Hahn, E. L. *Phys. Rev.* **1950**, *80*, 580.

(9) Price, W. S. *NMR studies of translational motion*; Cambridge University Press: Cambridge, 2009.

(10) Johnson, C. S. *Prog. Nucl. Magn. Reson. Spectrosc.* **1999**, *34*, 203.

(11) Callaghan, P. T. *Translational dynamics and magnetic resonance : principles of pulsed gradient spin echo NMR*; Oxford University Press: Oxford ; New York, 2011.

(12) Avram, L.; Cohen, Y. *J. Am. Chem. Soc.* **2005**, *127*, 5714.

(13) Stejskal, E. O.; Tanner, J. E. *J. Chem. Phys.* **1965**, *42*, 288.

(14) Torres, A. M.; Zheng, G.; Price, W. S. *Magn. Reson. Chem.* **2010**, *48*, 129.

(15) Aguilar, J. A.; Nilsson, M.; Bodenhausen, G.; Morris, G. A. *Chem. Commun.* **2012**, *48*, 811.

(16) Law, S. J.; Britton, M. M. *Langmuir* **2012**, *28*, 11699.

(17) Freeman, R. *A handbook of nuclear magnetic resonance*; 2 ed.; Longman Group: London, 1988.

(18) Wu, D. H.; Chen, A. D.; Johnson, C. S. *J. Magn. Reson. Ser. A* **1995**, *115*, 260.

(19) Dvinskikh, S. V.; Furo, I. *J. Magn. Reson.* **2000**, *146*, 283.

(20) Chen, A.; Shapiro, M. *J. Am. Chem. Soc.* **1999**, *121*, 5338.

(21) Peschier, L. J. C.; Bouwstra, J. A.; deBleyser, J.; Junginger, H. E.; Leyte, J. C. *J. Magn. Reson. Ser. B* **1996**, *110*, 150.

(22) Wolfrum; http://mathworld.wolfram.com, Ed. 2014.

(23) Kaleidagraph4.1; Software, S., Ed. Reading, PA, USA, 2011.

(24) Malassagne-Bulgarelli, N.; McGrath, K. M. *Soft Matter* **2013**, *9*, 48.

(25) Callaghan, P. T.; Godefroy, S.; Ryland, B. N. *Magn. Reson. Imaging* **2003**, *21*, 243.

(26) Mitchell, J.; Chandrasekera, T. C.; Gladden, L. F. *Prog. Nucl. Magn. Reson. Spectrosc.* **2012**, *62*, 34.

(27) Galvosas, P.; Qiao, Y.; Schonhoff, M.; Callaghan, P. T. *Magn. Reson. Imaging* **2007**, *25*, 497.

(28) Borgia, G. C.; Brown, R. J. S.; Fantazzini, P. *J. Magn. Reson.* **1998**, *132*, 65.

(29) Song, Y. Q.; Venkataramanan, L.; Hurlimann, M. D.; Flaum, M.; Frulla, P.; Straley, C. *J. Magn. Reson.* **2002**, *154*, 261.

(30) Fordham, E. J.; Sezginer, A.; Hall, L. D. *J. Magn. Reson. Ser. A* **1995**, *113*, 139.

(31) Chen, A.; Wu, D. H.; Johnson, C. S. *J. Am. Chem. Soc.* **1995**, *117*, 7965.

(32) Provencher, S. W. *Comput. Phys. Commun.* **1982**, *27*, 229.

(33) Provencher, S. W. *Comput. Phys. Commun.* **1982**, *27*, 213.

(34) Vasquez, V. R.; Williams, B. C.; Graeve, O. A. *J Phys Chem B* **2011**, *115*, 2979.

(35) Vanag, V. K.; Epstein, I. R. *Phys Rev Lett* **2003**, *90*, 098301.

(36) Alvarez, E. V.; Carballido-Landeira, J.; Guiu-Souto, J.; Taboada, P.; Munuzuri, A. P. *J. Chem. Phys.* **2011**, *134*, 094512.

(37) Valentini, M.; Vaccaro, A.; Rehor, A.; Napoli, A.; Hubbell, J. A.; Tirelli, N. *J. Am. Chem. Soc.* **2004**, *126*, 2142.

(38) Griffiths, P. C.; Cheung, A. Y. F.; Davies, J. A.; Paul, A.; Tipples, C. N.; Winnington, A. L. *Magn. Reson. Chem.* **2002**, *40*, S40.

3. The Sizing of Reverse Micelles in AOT/*n*-octane/water Microemulsion

3.1. Introduction

Reverse micelles (RMs) are used in a number of applications including biological modelling,[1,2] and nanoparticle synthesis.[3,4] In these applications, changes in the microemulsion parameters, such as the size and dilution of the RMs, determines the rates of diffusion, exchange and ultimately the kinetics of the reactions involved in the different phases of the microemulsion. Determining and appreciating the sizes of the RMs can lead to a better understanding of how the microemulsion parameters affect the outcomes of the reactions involved in the applications. In biological modelling, the autocatalytic Belousov-Zhabotinsky, (BZ), reaction forms chemical patterns in an AOT/*n*-octane/water microemulsion, but only shows this potential at specific values of ω, ϕ_d and reactant concentrations. The variation in the concentration of the acidic additive, malonic acid, at specific ϕ_d as Figure 3.1 shows, gives rise to different chemical patterns.

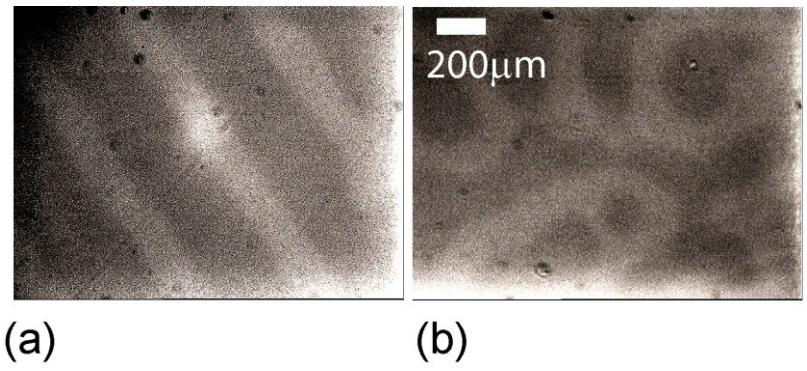

Figure 3.1: *The different patterns which can be formed in the BZ-AOT reaction from 0.08 M (a) and 0.15 M (b) malonic acid, at ϕ_d = 0.4 for (a) and ϕ_d =0.35 (b).*

In nanoparticle synthesis, the variation in the size of the RMs,[3-5] which is governed by the water to surfactant ratio, is one of the factors which determines the size and polydispersity of the nanoparticles. Investigations in adjusting the parameters in CTAB quarternary microemulsions have been of particular interest, as CTAB microemulsions form sought-after mono-disperse and stable nanoparticles.[3]

The determination of the sizes, structure and polydispersity of RMs is therefore widespread and there are many techniques, which are employed to do this. Traditionally dynamic light scattering methods (DLS) have been used to size RMs,[6] but as with all techniques, it has a few limitations and drawbacks.[7-10] In this technique, the diffusion coefficients (D) for the particles in a system are obtained from measuring the temporal fluctuations of scattered light from the diffusing particles in a liquid suspension. Where the particles are spherical, D is converted to the R_h using the Stokes-Einstein relation (eq 3.1), where η is the dynamic viscosity of the continuous phase, T is the temperature of the system and k_B is the Boltzmann constant.

$$R_h = \frac{k_B T}{6\pi\eta D} \qquad \text{eq 3.1}$$

DLS also determines droplet size distributions and the polydispersity of the droplets in the sample by implementing a constrained form of the inverse Laplace transform. Other techniques, which are used to characterise RMs, include fluorescence correlation spectroscopy (FCS),[11] small angle neutron scattering (SANS)[12] and small angle x-ray scattering (SAXS).[13] NMR spectroscopy has been used to obtain the average diffusion coefficients of the molecules in microemulsion systems[14-21] and converted to obtain an average R_h using the Stokes-Einstein relation, but unlike DLS, the inverse Laplace transform

(ILT) has not been reported to determine droplet size distributions of RMs. The ILT has been previously used to analyse PFG diffusion data to measure size distributions in porous media,[22] polymers [23,24] and colloidal systems.[25,26] The ILT is not regarded as a robust analytical tool and has to be used with caution, as it is sensitive to noise and generates many solutions. However, the ILT has been used in this study to size RMs in microemulsions in 1-dimensional diffusion experiments. There is also the potential of probing the exchange phenomena in microemulsions by applying the ILT in 2-dimensional NMR experiments, such as diffusion-diffusion exchange spectroscopy (DEXSY)[27] and relaxation-relaxation exchange spectroscopy (REXSY).[28] The diffusion and relaxation measurements, for the surfactant, cosurfactant or water molecules in 2D experiments could lead to more understanding of the exchange behaviour between the dispersed and continuous phases of the microemulsions.

The changes in droplet sizes as a function of water to surfactant ratio, ω, volume droplet fraction, ϕ_d, composition and solution age were determined for sodium bis(2-ethylhexyl) sulfosuccinate AOT/*n*-octane/water and cetyltrimethylammonium bromide, (CTAB)/hexanol /water microemulsions. This was achieved by analysing the diffusion coefficients for the surfactant protons in the RMs, which were measured by pulsed field gradient stimulated echo (PGSTE) experiments using the Stejskal-Tanner relation (2.3.2 eq 2.15) and by applying the inverse Laplace transform to obtain distributions of diffusion coefficients. AOT microemulsions have been extensively characterised and are used in many applications. CTAB microemulsions have been widely studied in the literature,[29-31] however it has been more challenging to obtain the droplet sizes in these systems, particularly with DLS.[30] One recent study has, however, determined the RM size in the CTAB/water/hexane/pentanol

system and has been able to probe the dynamics in this system, using PFG diffusion experiments.[32]

3.2. Experimental

3.2.1. Preparation of AOT/n-octane/water Microemulsions

A stock solution of 1.5 M AOT (sodium bis(2-ethylhexyl) sulfosuccinate; Fluka ≥ 96 %) in *n*-octane (Acros 97 %) was prepared by dissolving 111.14 g AOT in 70 ml *n*-octane. Microemulsions were prepared at water-to-surfactant ratios of ω = 5.3 – 35, by adding the correct volume of water (Nanopure filtered, 18 MΩ) to the 1.5 M AOT solution to produce the required ω and diluting with *n*-octane to give ϕ_d = 0.15. (See Appendix I for further details)

3.2.2. Preparation of AOT/n-octane/water Microemulsions with Additives

AOT microemulsions were also prepared with additives and studied as a function of time and ϕ_d. The first[1,2] was prepared at ω = 15 and ϕ_d = 0.55, loaded with H_2SO_4 (Fisher > 95%) = 0.4 M and malonic acid (Alfa Aesar 99%) = 0.6 M. Diffusion measurements were taken at t = 2 h and t = 24 h. Another microemulsion[33] was prepared at ω = 12, and ϕ_d = 0.5, 0.4, 0.25 and 0.15 with H_2SO_4 = 0.25 M, malonic acid = 0.25 M and $NaBrO_3$ (Alfa Aesar 99.5%) = 0.16 M. In both preparations, two microemulsions at the required ω were made. Microemulsion 1 (ME1) contained the acidic additives, malonic acid and H_2SO_4. Microemulsion 2 (ME2) contained the $NaBrO_3$ in the case of the study as a function of ϕ_d. Aliquots of the separate microemulsions were then mixed and the required amount of extra *n*-octane was added to give

$\phi_d = 0.45$.[2] In the case of the study as a function of time, ME1 contained the acid additives and ME2 did not contain any additives.

AOT/*n*-octane/water/H^+ microemulsions were prepared to analyse the relaxation times, T_1 and T_2 of water and AOT H_3 headgroup protons, with and without acid additives. These were made using the same methods previously discussed at ω = 6 – 25, ϕ_d = 0.45 with H_2SO_4 (Fisher > 95%) = 0.12 M and malonic acid (Alfa Aesar 99%) = 0.12 M. The microemulsions without acid were prepared in the range of ω = 9.2 – 20 at ϕ_d = 0.45.

3.2.3. Preparation of CTAB/water/hexanol Microemulsions

CTAB/hexanol/water microemulsion was prepared with CTAB (cetyltrimethylammonium bromide; Sigma ≥ 98%), 1-hexanol (Acros 98 %) and water (Nanopure filtered, 18 MΩ) at ω = 7.2, and ϕ_d = 0.4, giving a 3:1 ratio % w of CTAB/water.[30] The CTAB was added to the hexanol, where initially the CTAB remained undissolved. When the required volume of water was added, an endothermic process was observed. The solution then became clear as it formed the microemulsion.

3.2.4. NMR Experiments

All NMR experiments were performed on a Bruker DMX300- spectrometer equipped with a 7.0 T superconducting magnet, operating at a frequency of 300.13 MHz.

3.2.5. NMR Diffusion Measurements

Diffusion measurements were taken 2 hours after the samples were prepared. PGSTE experiments were performed at 289 ± 0.3 K. A 10 mm radiofrequency coil was used and a total of 64 signal averages were collected with a repetition time of 1s. Typical parameters used in these experiments were: δ = 4 ms, Δ= 100 ms, with a maximum gradient, $\boldsymbol{G}_{max}$ = 0.9 T m^{-1} and 32 gradient steps, ensuring the signal attenuated so that $S(\boldsymbol{G})/S(0) \leq 0.01$ at $\boldsymbol{G}_{max}$. The gradient system was calibrated by measuring the diffusion coefficient of *n*-octane. A value of $1.998 \times 10^{-9} \pm 0.002$ m^2s^{-1} was measured at 289 ± 0.3 K, which is the expected value compared to the previously reported temperature dependency of the diffusion coefficient for *n*-octane.[34] For the AOT microemulsions, diffusion data was collected for proton H_3 on the AOT molecule (Figure 3.2) and for the CTAB/hexanol/water microemulsions, the data from the proton H_a of the CTAB molecule was analysed.

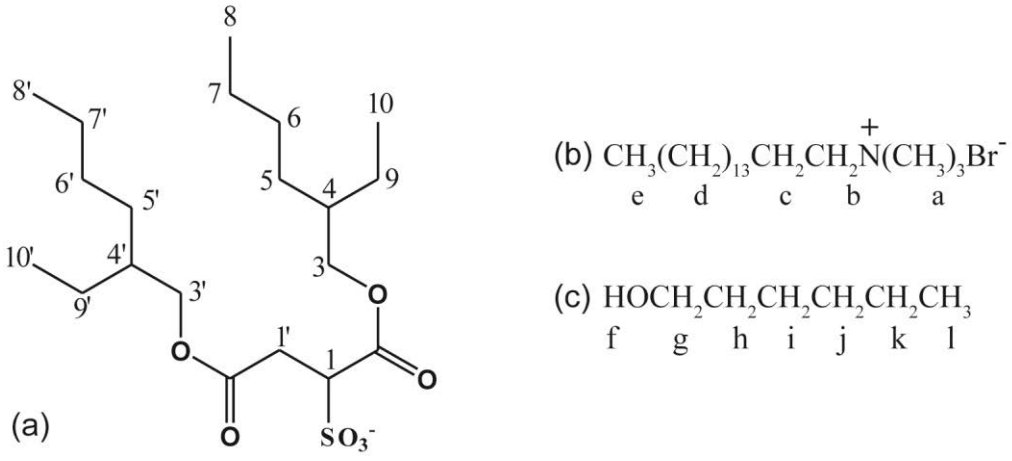

Figure 3.2: *The molecular structure and numbering scheme for protons in the AOT molecule (a) and CTAB (b) and hexanol (c) molecules.*

Typical signal-to-noise ratios, calculated as the maximum signal divided by the standard deviation of the noise, were around 65 for the H_3 peak in the AOT microemulsions. The typical signal to noise ratio for the CTAB H_a signal was 1000. Typical PGSTE diffusion data at 32 and 256 gradient steps, for the H_3 peak in an AOT/octane/water microemulsion, are shown in (Figure 3.3).

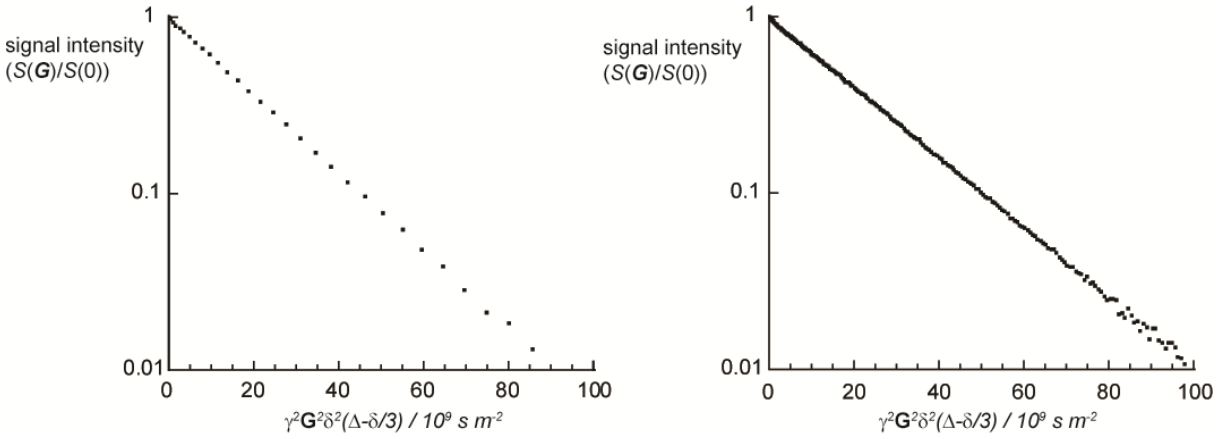

Figure 3.3: *PGSTE diffusion data for the H_3 peak in the AOT/n-octane/water microemulsion at ω = 15 and ϕ_d = 0.15, where Δ= 100 ms, δ = 4 ms and G = 0.9 T m^{-1}. A total of 32 (a) or 256 (b) gradient steps were collected, with 64 signal averages.*

3.2.6. Analysis of the Diffusion Data

The average diffusion coefficients (D) of all the microemulsions were obtained using the Stejskal-Tanner (ST) equation (2.3.2 eq 2.15). Diffusion coefficient distributions were determined using the inverse Laplace transformation (ILT).[35,36] In the ILT analysis, plots of G(D)D *vs* log(D) are produced, where G(D) is the distribution function with respect to D (See 2.4.2). A constrained regularization ILT method[23,35-39] was used, where the smoothing parameter α was determined. The optimal value of α, was obtained by repeating the ILT and measuring χ^2, the error of the fit, as a function of α[38,39] (See section 2.4.2). The lowest value

of α was chosen, before χ^2 rapidly increased, corresponding to the point where the narrowest distribution was possible, without introducing peaks which were generated by fitting the noise (Figure 3.4).[38]

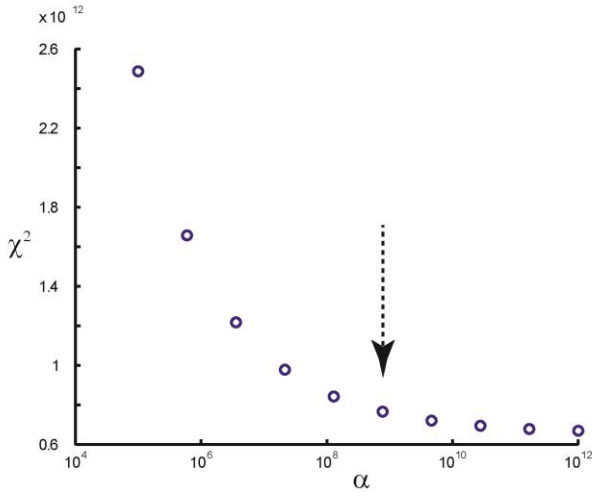

Figure 3.4: *A plot of χ^2 as a function of the smoothing parameter (α) for an AOT/n-octane/water microemulsion at ω= 5.3 and ϕ_d = 0.15, with a total of 256 gradient steps.*

The hydrodynamic radii, R_h, were determined from an average diffusion coefficient or diffusion coefficient distribution, using the Stokes-Einstein relation. The dynamic viscosity values of 0.563 and 5.85 cP were used for *n*-octane and hexanol, respectively, at T = 290 K. Errors were determined from an analysis of the variation between repeated experiments for a given system.

3.2.7. Inversion Recovery T_1 Relaxation Time

Inversion recovery experiments were carried out to measure T_1 relaxation times of the water and AOT H_3 protons in the AOT/*n*-octane/water/H^+ system at varying ω and ϕ_d = 0.45. T_1

measurements were also taken for the microemulsion without acid additives. A 10 mm radiofrequency coil was used and measurements were performed at 289 ± 0.3 K. Sixteen scans were accumulated for 33 experiments. The repetition time between each scan was 12 s. There were 4 signal averages. The 90° r. f. pulse was 12 μs and the 180° pulse was 24 μs. The spectral width was 20 kHz. The signal intensities for specific peaks in the AOT/octane/H_2O/H^+ were plotted against τ and the T_1 relaxation time was found by fitting the data to the equation found in section (2.2.1 eq 2.11), using non-linear least squares. The data was processed using Prospa[40] and Kaleidagraph[41] software.

3.2.8. Carr Purcell Meiboom Gill (CPMG) T_2 Relaxation

CPMG experiments were performed to measure T_2 relaxation time of the systems as described in section (2.2.3). A 10 mm radiofrequency coil was used. The spectral width was 20 kHz and sixteen scans were accumulated for 16 experiments. τ was set at 1 ms. The repetition time between each scan was 12 s. The measurements were performed at 289 ± 0.3 K. The amplitude of the echo was plotted against time for specific peaks in the AOT/*n*-octane/water/H^+ system and the T_2 relaxation time was found from fitting the data to the equations found in section (2.2.2), (eq 2.12), for mono-exponential and (eq 2.13) for bi-exponential decays.

3.2.9. Dynamic Light Scattering measurements of AOT/n-octane/water Microemulsion at varying ω

DLS measurements were performed on a Delsa-Nano Submicron (Class 1 Laser) Particle Size Analyser. All solutions were filtered prior to measuring with a 0.2 μm PTFE (Acrosdisc CR

13, PALL) filter membranes. The microemulsions were allowed to equilibrate for 300 s at 290 K and data was accumulated for 100 s with 5 repetitions. The time domain correlation method was used with CONTIN analysis,[35] which applies a constrained form of the inverse Laplace transform to generate the resulting R_h distributions. A refractive index of 1.3975 was used for *n*-octane with a viscosity of 0.563 cP at 290 K. DLS measurements were made for the AOT/*n*-octane/H_2O samples at $\omega = 5.3 - 35$ with a droplet fraction of $\phi_d = 0.15$.

3.3. Results and Discussion

3.3.1. ^1H NMR Spectra

The ^{1}H NMR spectra for the AOT/*n*-octane/water and CTAB/hexanol/water microemulsions are shown (Figure 3.5).

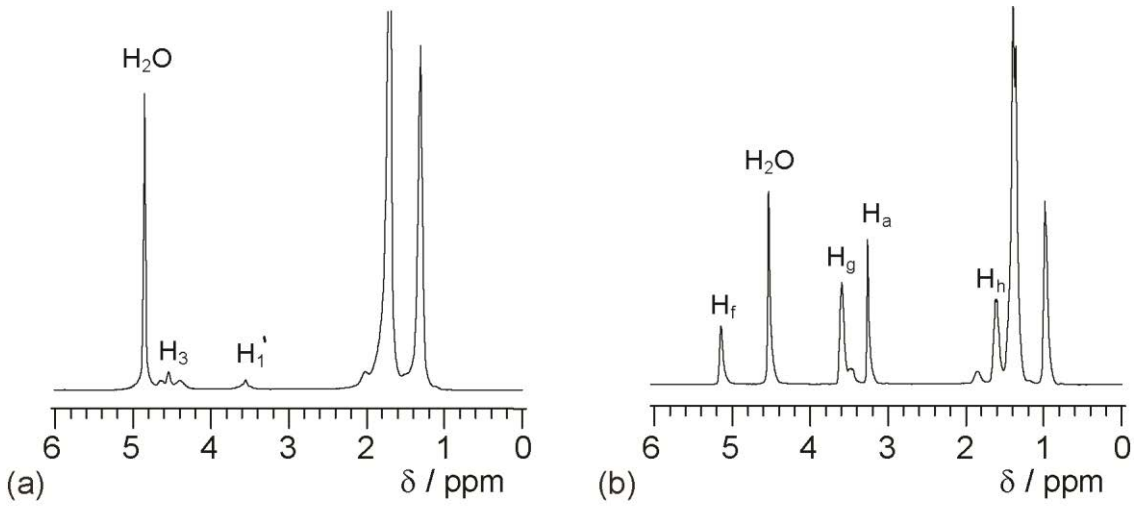

Figure 3.5: *^1H NMR spectra of AOT/n-octane/water (a) and CTAB/hexanol/water (b) microemulsions.*

The AOT/*n*-octane/water[42] and CTAB/hexanol/water[30] microemulsions have been characterised in the literature using the peak assignments obtained from NMR spectroscopy. The corresponding peak assignments are shown in (Table 3.1(a)) for the AOT/*n*-octane/water and (Table 3.1(b)) for the CTAB/hexanol/water microemulsions. The peaks of interest are the AOT H_3 proton (δ = 4.52 ppm) and water (δ = 4.84 ppm) in the AOT/*n*-octane/water microemulsion.

peak assignments	δ / ppm
H_8, H_8', H_{10}, H_{10}', $H_{(octane)}$	1.29
H_5, H_5', H_6, H_6', H_7, H_7', H_9, H_9', $H_{(octane)}$	1.70
H_1	4.61
H_1'	3.54
H_3	4.52
H_3'	4.38
H_4, H_4'	1.99
H_2O	4.84

(a)

peak assignments	δ / ppm
H_f	5.09
H_2O	4.48
H_g	3.54
H_b	3.42
H_a	3.22
H_c	1.79
H_h	1.56
H_d, H_i, H_j, H_k,	1.34
H_e, H_l	0.94

(b)

Table 3.1: *^{1}H NMR peak assignments for AOT/n-octane/water (a) and CTAB/hexanol/water (b) microemulsions.*

The water peak at δ = 4.84 ppm shifts as a function of ω. As ω increases, the water peak shifts downfield, also revealing an AOT H_1 proton, which is masked by the water peak at ω =

5.3. This is due to the water peak being an average of the rapidly exchanging bound and free water and as the RM size increases, the micellar water behaves more like bulk water, resulting in a chemical shift downfield, tending towards the chemical shift of ordinary water.[43] The two peaks with higher signal intensity at δ = 1.29 ppm and δ = 1.70 ppm are from *n*-octane. The octane peaks mask the proton signals from the AOT surfactant tails. This made it difficult to measure the diffusion coefficient of the *n*-octane in the continuous phase. The peaks of interest in the CTAB/hexanol/water microemulsion were the CTAB surfactant headgroup H_a proton (δ = 4.52 ppm), as this proton would reside in the micelle interface and the water peak at (δ = 4.48 ppm). The hexanol proton, H_g (δ = 3.54 ppm) was also analysed. This peak was unaffected by masking of other protons in the system.

3.3.2. DLS Measurements of Droplet Sizes in the AOT/n-octane/water Microemulsions at varying ω

The analysis of the Dynamic Light Scattering (DLS) data for the samples in AOT/*n*-octane/water microemulsions gave average droplet sizes shown in Table 3.2.

ω	Number distribution R_h / nm	Volume distribution R_h / nm	Intensity distribution R_h / nm
5.3	1.20	1.75	9.6
15	1.65	2.40	13
25	3.15	4.60	33
35	3.90	5.60	16

Table 3.2: *The mean average R_h values from the number, volume and intensity distributions of AOT/n-octane/water microemulsions at varying ω and ϕ_d = 0.15 obtained from DLS measurements.*

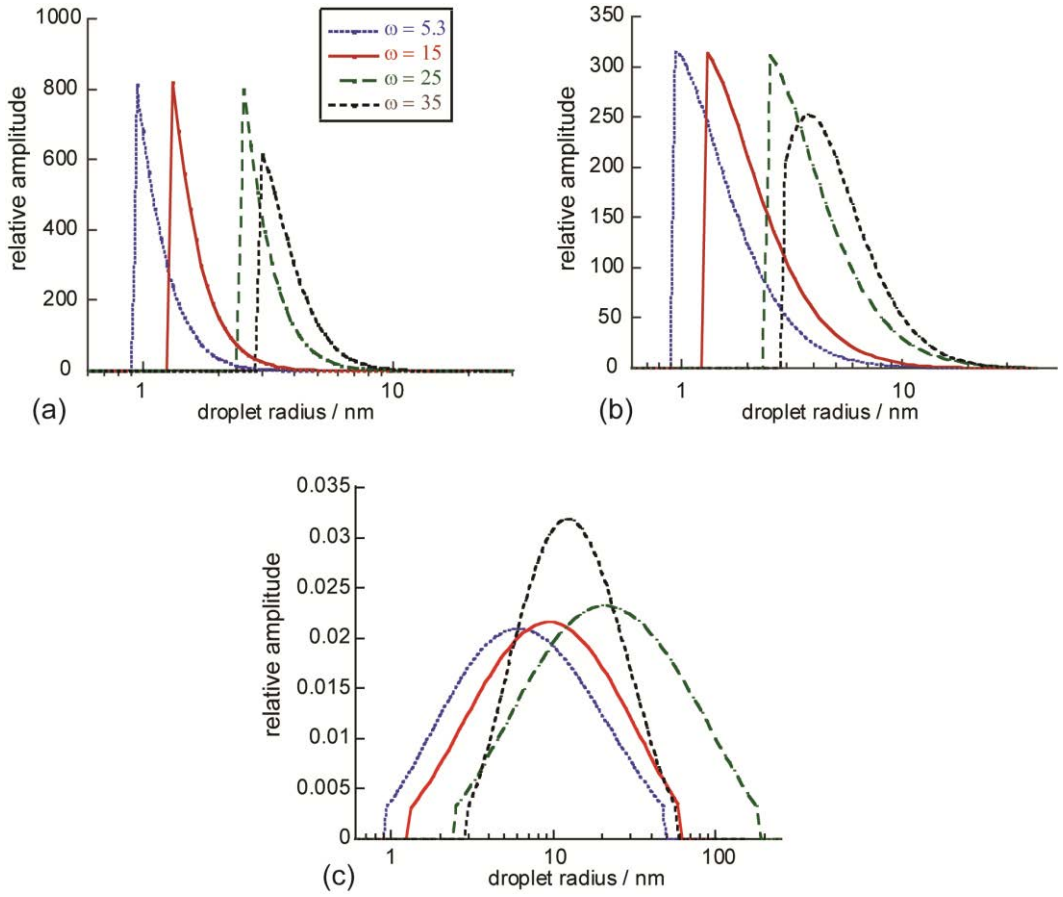

Figure 3.6: *The number distributions (a) volume distributions (b) and the intensity distributions (c) of AOT/n-octane/water microemulsions at varying ω and ϕ_d = 0.15 obtained from Dynamic Light Scattering (DLS) measurements.*

The number distributions for the AOT/*n*-octane/water microemulsions obtained from DLS measurements are shown (Figure 3.6). The conversion from the intensity distributions to number distributions involves dividing by d^6, where d is the diameter, resulting in number distributions, which are not smooth and Gaussian, but are transformed to a weighted distribution, with a rapid increase in the relative amplitudes at lower values of R_h giving a sharp rise to a peak maximum. Therefore the conversion from intensity to number distributions, particularly when using a logarithmic scale, results in a change from Gaussian

shaped intensity distribution to non-Gaussian shaped number distributions. The values obtained from the number distributions from the DLS measurements are significantly lower than those obtained from the PGSTE experiments. This may be due to errors being generated when transforming from the intensity to number distributions (Table 3.2). The American Society for Testing and Materials (ASTM)[44] recommend not converting from intensity to number distributions, as any noise from the original data produces uncertainties. Measurements at low concentrations also produce more signal-to-noise. The original intensity of light is obtained from an expression involving the scattering form factor P which varies between 4 orders of magnitude.[8] In order to convert into the volume distributions, the intensity is divided by d^3P, where d is the diameter, and then divide again by d^3 in order to obtain the number distribution. Any noise from the original data is magnified to give erroneous results[8] which may have occurred in these experiments. The data can also be skewed, when a small number of large particles are present.[7] This may have been the cause of the higher value for the intensity distribution at $\omega = 25$.

3.3.3. The Diffusion Data and Droplet Sizes of AOT/n-octane/water RMs at varying ω

The average diffusion coefficients were obtained for RMs in the AOT/*n*-octane/water microemulsion for $\omega = 5.3 - 35$ at $\phi_d = 0.15$, by fitting the diffusion data from the surfactant headgroup proton H_3 to the Stejskal-Tanner equation. As the H_3 surfactant proton resides in the interface of the RM, this provides a measure of the diffusion coefficient (D) of the RM. The R_h of the RMs were obtained by using the Stokes-Einstein relation. The values for the diffusion coefficient and R_h are shown in Table 3.3

ω	D / 10^{-11} m^2s^{-1}	R_h / nm
5.3	5.88 ± 0.49	6.6 ± 0.56
15	4.86 ± 0.4	7.8 ± 0.60
25	4.07 ± 0.3	9.3 ± 0.63
35	3.49 ± 0.2	10.9 ± 0.65

Table 3.3: *The average diffusion coefficient and corresponding R_h for AOT/n-octane/water microemulsions at varying ω, ϕ_d =0.15. The diffusion coefficients were obtained from fitting the diffusion data to the Stejskal-Tanner (ST) equation.*

The diffusion coefficient increases as the ω decreases and therefore due to the inverse relationship between the diffusion coefficient and R_h, the R_h decreases as ω decreases (Figure 3.7). The errors were calculated from an average deviation from 3 separate experiments.

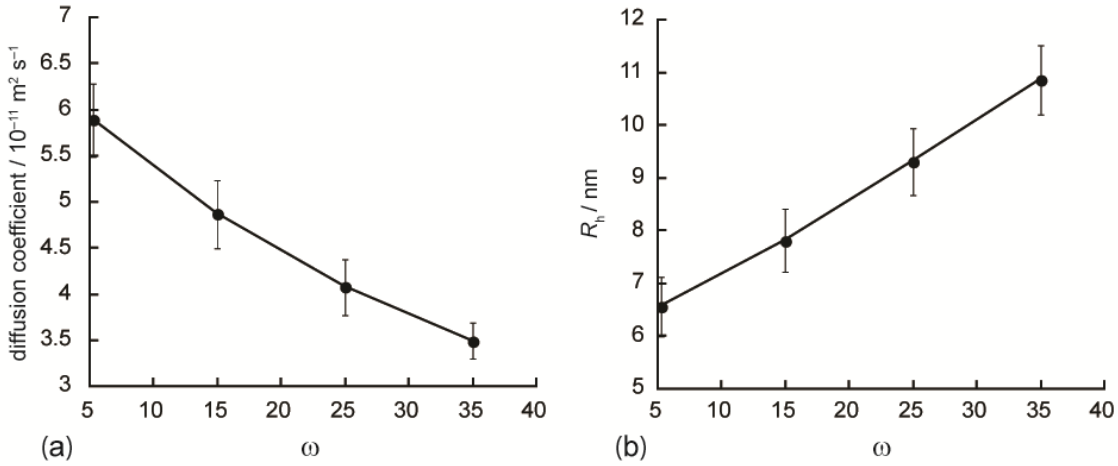

Figure 3.7: *Plots of the average diffusion coefficients (a) and R_h (b) for H_3 in the RM of AOT/n-octane/water microemulsions, at varying ω at ϕ_d = 0.15. The diffusion coefficients were determined using the 32 gradient step PGSTE data and fitted to the ST equation. The lines are drawn for guidance only.*

The inverse Laplace transform (ILT) produced a distribution of diffusion coefficients which were then converted to a distribution of RM sizes using the Stokes-Einstein equation.

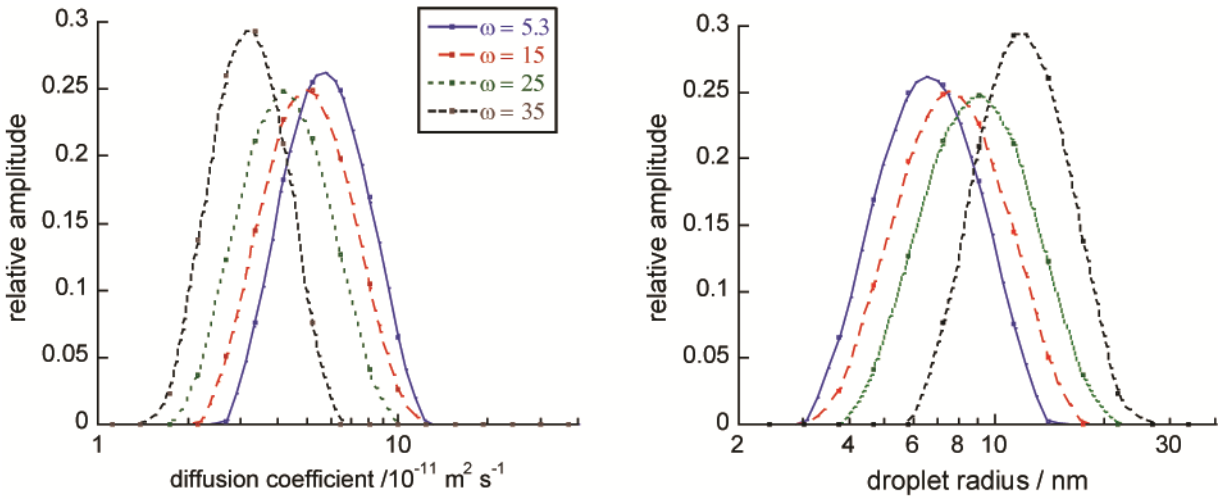

Figure 3.8: *Plots of the diffusion coefficient distributions (a) and droplet size distributions using 32 gradient steps for H_3 in the RM for AOT/n-octane/water microemulsions, at varying ω and $\phi_d = 0.15$, using the ILT.*

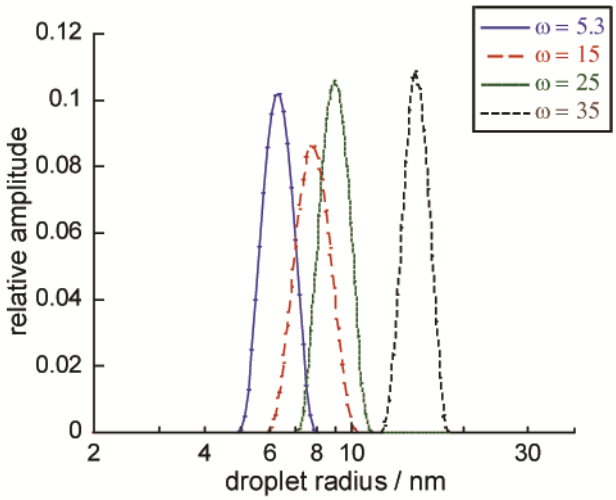

Figure 3.9: *Plots of the droplet size distributions using 256 gradient steps.*

The size distributions were obtained for both experiments with 32 (Figure 3.8) and 256 gradient steps (Figure 3.9). The comparison of the RM size distributions using 32 or 256 gradient steps, showed good agreement between the R_h values produced. Analysis of the distribution maxima (mode average) for the PGSTE experiments analysed using the ILT, with 32 and 256 gradient steps, is shown in Table 3.4. The experiments with 256 gradient steps were carried out to generate more data points giving an increase in the accuracy of the resulting distributions when applying the ILT. The DLS technique obtains many data points to generate the R_h distributions. It was therefore important to increase the number of gradient steps in the PGSTE experiments.

ω	$D/10^{-11}$ m^{2}s^{-1} (32 steps)	R_h/ nm	$D/10^{-11}$ m^{2}s^{-1} (256 steps)	R_h/ nm
5.3	5.71	6.5 ± 0.5	5.91	6.3 ± 0.5
15	4.99	7.5 ± 0.7	4.80	7.8 ± 0.7
25	4.15	9.1 ± 0.8	4.20	8.9 ± 0.8
35	3.18	11.8 ± 2	2.55	14.7 ± 2

Table 3.4: *The mode average diffusion coefficients and corresponding R_h obtained from the distribution maxima for AOT/n-octane/water microemulsions at varying ω and ϕ_d = 0.15.*

It is clear that the width of the distributions is dependent on the number of gradient steps, (Figure 3.8 and Figure 3.9) as well as the parameters used in the ILT analysis, such that the (α) value used with 256 steps produced narrower distributions. Therefore, data for the polydispersity of the microemulsion cannot be obtained from the distributions, as the distribution widths are determined from experimental and analysis parameters. The experiments with 256 gradient steps enabled an increase in the smoothing parameter, α. This resulted in a narrower distribution being produced, without fitting to noise. Although the distribution widths change from the experiments at 32 and 256 gradient steps, the average R_h,

taken from the peak maxima of the distributions (Table 3.4) were found not to change significantly.

The results from the PFG diffusion measurements were compared with other methods reported in the literature, mainly from light scattering techniques (Figure 3.10). There are a number of papers reporting the R_h of RMs in this system using dynamic light scattering (DLS),[43,45-48] fluorescence correlation spectroscopy (FCS),[11] small angle x-ray scattering (SAXS),[13,49,50] and small angle neutron scattering (SANS),[12] as a function of ω and ϕ_d. Using these methods, the sizes that are typically reported are in the range of R_h = (2.5 – 9.5 nm) for ω = (5.3 – 35). It is clear that the R_h determined from the PGSTE data are larger.

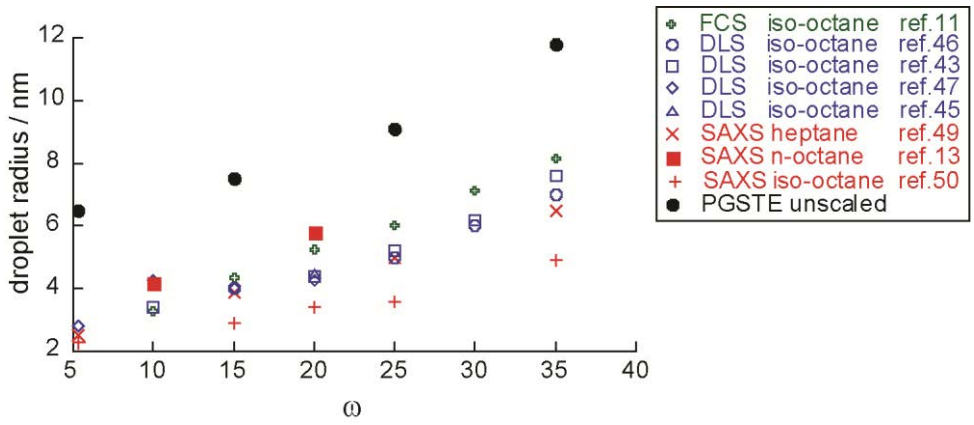

Figure 3.10: *Plot of droplet size dependence on ω for values reported in the literature using DLS,[43,45-47] FCS,[11] and SAXS[13,49,50] methods. (*The values given for R_h were determined using the r_w value reported in ref.13 with 2× 1.5 nm added to account for the width of the surfactant layer around the water core).*

The origins of these differences arise from the droplet volume fraction of the microemulsions in the PFG experiments being higher than the DLS experiments. As the droplet fraction

increases the diffusing RMs will collide and interact more frequently. This creates an obstruction effect, which will cause the diffusion coefficient to decrease, which results in an over-estimation of the R_h.[14] The interaction between the RMs is observed in the variation of D which is described by two mechanisms.[51] The first mechanism arises from the RM excluding a fraction of the total volume for the diffusing molecule, leading to a lengthening of the diffusion paths, which is called the "obstruction path". The second mechanism concerns the direct interaction between the RMs and molecules in the microemulsion, which leads to a further decrease in D. In the case of AOT, there is an attractive interaction between the RMs, which leads to a further decrease in D with increasing concentration. The shapes of the RMs can also affect the obstruction effect, with oblate structures having different diffusive and obstructive properties from spherical and prolate structures, which have similar properties.[51] An assumption was made that a droplet volume fraction of 0.15 was low enough to minimise RM interactions.[52] However, Caboi *et al*.[14] reported that the RM interactions are minimised at $\phi_d < 0.1$. The SAXS technique does not measure the motion of particles and is therefore not affected by RM obstruction effects, which is an explanation why the values from SAXS are lower than the PFG experiments. DLS and FCS techniques, however, do measure the motion of the RMs and are therefore affected by RM collisions and obstruction. The droplet volume fraction of 0.15 was used in the DLS experiments (Section 3.3.2) as this was the minimum dilution that could be used to obtain an auto-correlation function with a viable decay (See 1.2.1). Further dilution resulted in inadequate or no decay resulting in invalid data. Further discrepancies may lie in errors from the PGSTE associated with the exchange of surfactant molecules during the observation time (Δ) between droplets of different sizes. There may also be errors in the DLS data, which arise from the conversion from intensity to number distributions.[8] The use of number distributions is discouraged as errors generated from the

intensity distributions can be magnified by a factor of 10^6 by the time the number distribution is calculated.[8]

3.3.4. The Diffusion Data and Droplet Sizes of CTAB/hexanol/water RMs

The diffusion coefficient and droplet size distribution for the CTAB/hexanol/water microemulsion at $\omega = 7.2$, $\phi_d = 0.4$ were determined using PGSTE experiments (Figure 3.11). A diffusion coefficient of 3.87×10^{-11} m^2s^{-1} was obtained, resulting in $R_h = 0.93$ nm from fitting to the Stejskal-Tanner (ST) equation and $D = 4.05 \times 10^{-11}$ m^2s^{-1} obtained from the ILT analysis, resulting in $R_h = 0.9$ nm. The droplet size was obtained from the peak maximum of the droplet size distribution (Figure 3.11). A bi-exponential decay was obtained by fitting the diffusion data for the hexanol H_g proton to the Stejskal-Tanner relation, resulting in 32% of the hexanol diffusing at 8.69×10^{-11} m^2s^{-1} and 68% diffusing at 1.59×10^{-10} m^2s^{-1}. The hexanol molecules act as both the co-surfactant[53] and the solvent, which is partitioned between the RM and the continuous phase in a dynamic equilibrium. This is due to the surfactant CTAB not forming a microemulsion without a co-surfactant. This is why the two diffusion coefficients are observed for the hexanol molecule. As found in these experiments, the smaller proportion of hexanol, at 32% resides in the interface.[53] It would be expected that the diffusion coefficient of the hexanol in the micelle interface would be comparable with the CTAB headgroup diffusion coefficient, however the hexanol was observed diffusing at a faster rate. The slower hexanol diffusion coefficient is therefore a weighted average of the molecules exchanging between the continuous phase and the interphase.[32] When using the Lindman equation (1.2.5 eq 1.19) an estimate of 20% of the hexanol molecules reside in the

interface. This was calculated by using the D_{mic} from the CTAB diffusion coefficient and D_{free} from the faster hexanol diffusion coefficient.

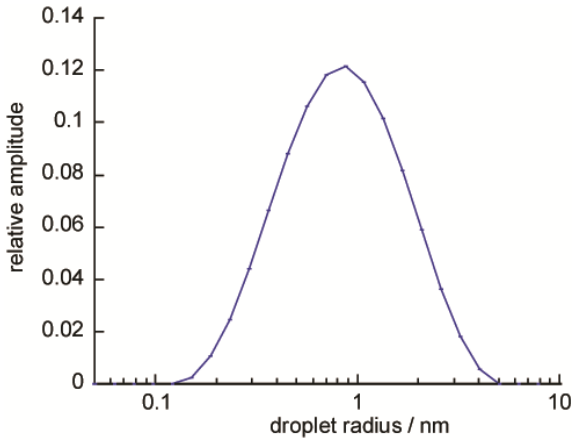

Figure 3.11: *Droplet size distribution for RMs in the CTAB/hexanol/water microemulsion at* ω *=7.2 and* ϕ_d *= 0.4. Size distributions were produced by applying the Stokes-Einstein relation to diffusion coefficient distributions produced by inverse Laplace transformation of the PGSTE data for CTAB* H_a *proton.*

Previous droplet sizes of 1.1 nm were obtained for a CTAB/hexanol/water microemulsion (2.6:1 ratio % w of CTAB: water), using the technique of fluorescence quenching.[54] However, there is no DLS data available in the literature as one study illustrates, it has proved difficult to obtain reliable data.[55] There were further investigations into the shape and size of the CTAB/hexanol/water RMs, using molecular simulations. When applying the Stokes-Einstein equation, a spherical shape is assumed, therefore any variation from this needed to be ascertained. Molecular simulations were set up for ω = 7.2, to provide further insight into the molecular interactions and shape fluctuations of the CTAB/hexanol/water RMs. The results of the molecular simulations are discussed in Chapter 6.

3.3.5. *Variation of the R_h of AOT /n-octane/water Microemulsions with Additives*

The effect of additives on the size and stability of the RMs was investigated for two AOT/*n*-octane/water microemulsions. The AOT/*n*-octane/water microemulsions at ω = 15 and ϕ_d = 0.55 and loaded with H_2SO_4 (0.4 M) and malonic acid (0.6 M) were observed as a function of time, with *D* being measured at 2 and 24 hours after initial preparation (Figure 3.12).

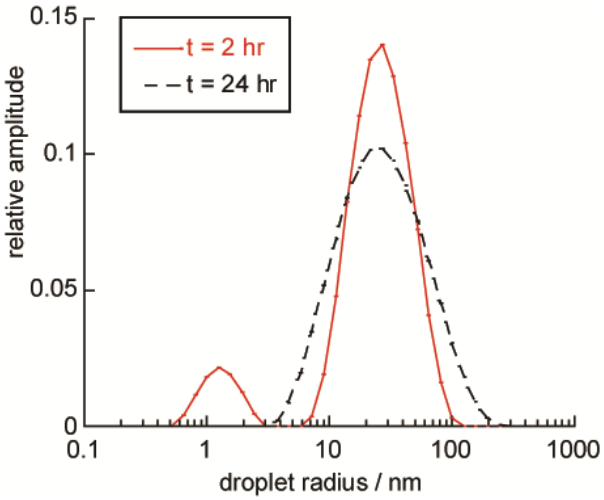

Figure 3.12*: Droplet size distributions for RMs in the AOT/n-octane/water microemulsion loaded with [H_2SO_4] = 0.4 M and [malonic acid] = 0.6 M at ω =15, ϕ_d = 0.55.*

Whilst the droplet sizes for the AOT/*n*-octane/water microemulsion were larger than the literature values found from scattering methods, the values for the microemulsions with additives compared well with the values observed previously, investigated by Vanag *et al*. determined with DLS.[1,2]

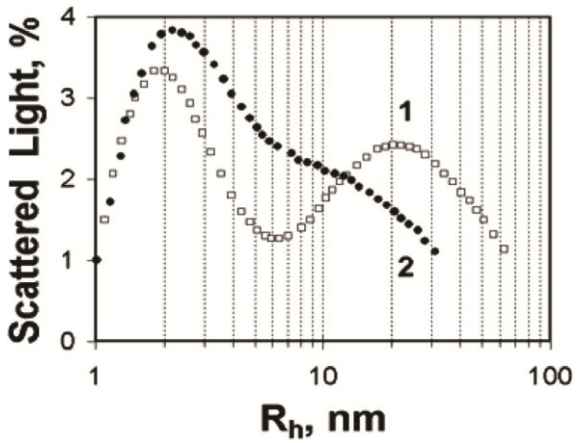

Figure 3.13: *Distribution of R_h of water nanodroplets. Curves 1and 2 were obtained in light-scattering experiments for fresh and one day old microemulsions (ω =15, ϕ_d = 0.5) respectively, loaded with H_2SO_4 (0.4 M) and MA (0.6 M). Copyright (2003) by The American Physical Society.*[1,2]

This system had been known to produce a bimodal droplet size distribution which became monomodal over a period of time ($t \geq 24$ h). Likewise in the PGSTE experiments, a bimodal distribution was observed at $t = 2$ h, which became monomodal after 24 h. In the fresh sample which was measured after 2 hours, two peaks were observed at 1.3 and 25.8 nm, which compares closely to the values observed by Vanag *et al*. with peaks at 2 and 20 nm (Figure 3.13).[1,2] At 24 h, after mixing, the sample became unimodal with a single peak observed at 25.1 nm. This value, is significantly higher than that observed in the DLS measurements[1,2] where a unimodal distribution was observed, with a peak maximum at 2.6 nm (Figure 3.13). The size distributions for RMs previously obtained in a system by Alvarez *et al*.[33] are shown in Figure 3.14. This microemulsion was loaded with H_2SO_4 = 0.25 M, malonic acid = 0.25 M and $NaBrO_3$ = 0.16 M and similar to the observations of Alvarez *et al*.[33] as there was a transition from bimodal to unimodal size distributions as a function of volume fraction, rather than time. Bimodal behaviour was observed at of 0.5 with R_h of 2.4 and 42.1 nm for the two

peaks, whereas Alvarez *et al*.[33] observed two distributions with peak maxima centred at 2 – 3 nm and 20 – 30 nm.[33]

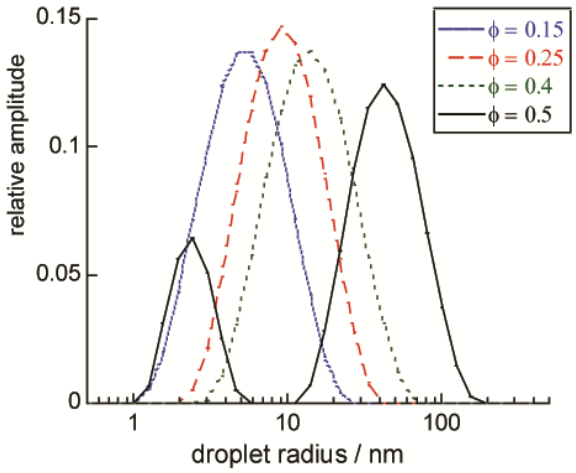

Figure 3.14*: Droplet size distributions for RMs in the AOT/n-octane/water microemulsion loaded with [H_2SO_4] = 0.25 M and [malonic acid] = 0.25 M and [$NaBrO_3$] = 0.16 M at* ω *=12 and* ϕ_d *= 0.15 – 0.5.*

As ϕ_d was reduced, the system became unimodal and droplet sizes of 13.8 nm (ϕ_d = 0.40), 9.1 nm (ϕ_d = 0.25) and 5.2 nm (ϕ_d = 0.15) were observed. Uni-modal distributions have also been observed by DLS; however the peak for the distribution presented by Alvarez *et al*.[33] was lower at 2 – 3 nm. It was also not reported if the DLS data was the number, volume or intensity distributions. Whilst the values for the R_h show an agreement with previous DLS measurements, the actual distributions of droplets differ. This may be due to how the diffusion coefficients of the RMs are determined and what the PGSTE experiments actually measure. More investigations are required on the effects of acidic additives on the formation of RMs.

3.3.6. Scaling of the R_h of AOT/n-octane/water Microemulsions

The differences between the number distributions of R_h values in the bimodal systems obtained from the DLS and the NMR techniques may be due to what the techniques actually measure. In the DLS technique, the intensity distributions are converted to number distributions using the Mie Theory.[56] PGSTE data, therefore, should also be scaled to produce a droplet size number distribution. As the PGSTE signal is integrated over all the surfactant molecules, the surfactant molecules in the larger droplets will contribute more to the distribution of D than the smaller droplets. The scaling procedure should be applied particularly in bimodal systems where the size ranges correspond to droplets with different numbers of surfactant molecules. Therefore in bimodal systems, for larger droplets, which contain more surfactant molecules, it is necessary to take this into account by scaling to produce a number distribution. The droplet sizes are determined from the diffusion coefficients of the surfactant molecules, which are all located in the RMs. As the AOT surfactant molecules surround the water core, then the number of AOT molecules N_s, will increase proportionally with r_w^2, which is the radius of the water core. In order to account for this, the relative amplitude ($G(D)$) is divided by N_s. This must be carried out for each droplet size within the droplet distribution to produce the number distribution. This scaling method, however, needs *a priori* knowledge. In order to determine N_s for the AOT/*n*-octane/water microemulsions, the size of the droplet core, r_w, was calculated[11] for each value of R_h, using eq 3.2.

$$R_h = \left(r_w^3 + 3\delta r_w^2\right)^{\frac{1}{3}} \qquad \text{eq 3.2}$$

and the size parameters which had been previously determined for the AOT/iso-octane/water microemulsions by Maitra (Table 3.5).[43,57] The value of 1.5 nm was used for the thickness of the surfactant layer[11] in equation 3.2.

ω	N_s	R_h / nm	r_w / nm
4	35	2.5	1.0
6	50	2.8	1.4
8	72	3.2	1.6
10	98	3.4	1.9
12	129	3.7	2.2
14	176	4.0	2.6
16	215	4.2	2.9
18	257	4.3	3.2
20	302	4.4	3.5
25	447	5.2	4.3
30	613	6.2	5.1
35	778	7.6	5.8

Table 3.5: *Size parameters for the AOT/iso-octane/water system.*[43,56]

There are limitations when scaling by the factor N_s as this needs a priori information. The number of surfactant molecules expected in the interface at each R_h is required as a function of r_w.[43,57] This information is available for well-characterised systems such as AOT/water/iso-octane but for systems involving CTAB, this information is unavailable. An alternative technique to scale the distributions would be to use r_w^2 as a scaling factor, with an offset value to account for the AOT surfactant aggregation number in the absence of water (N_{agg}). Previous studies have shown this aggregation number to be 22 for AOT in iso-octane.[58] Therefore the scaling factor will be (r_w^2+N_{agg}). However this does assume that the area occupied by the head of the surfactant (a_s) at the interface of the water core, remains the same for all droplet sizes. This assumption has also been made by other studies.[11,59] In order to obtain the numbers of RMs at particular sizes, this factor must be scaled. The limitations in the mechanisms for scaling size distributions for RMs means that these methods should be applied with caution, specifically in the second case, as (a_s) of the surfactant head does vary

as a function of the droplet size.[60] As the size of the RM changes, the radius of curvature changes, which affects the packing of the surfactant molecules and the interfacial tension of the RM.[61,62] As Ruckenstein *et al.*[63] previously discussed, the area of a molecule in the interface is dependent on the curvature of the RM. Another study,[64] showed that there was a rapid increase in the surface area of the RM up to a limiting value ω > 16.5, where the packing parameter became independent of the droplet size and the area of the surfactant headgroup remained similar.

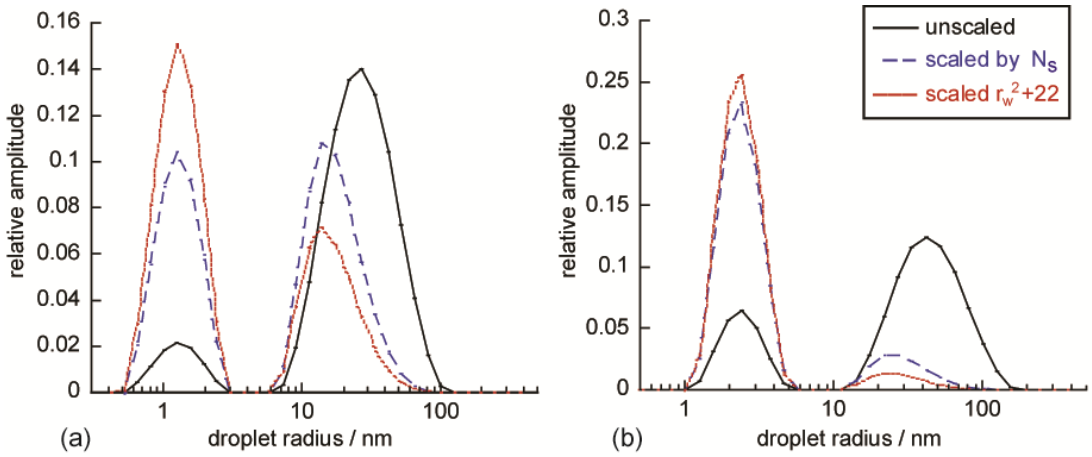

Figure 3.15: *Droplet size distributions for RM in AOT/n-octane/water microemulsions loaded with (a) [H_2SO_4] = 0.4 M, [malonic acid] = 0.6 M at ω =15,ϕ_d = 0.55 (unscaled data from Figure 3.12) and (b) [H_2SO_4] = 0.25 M and [malonic acid] = 0.25 M and [$NaBrO_3$] = 0.16 M at ω =12 and ϕ_d = 0.15 – 0.5 (unscaled data from Figure 3.14) R_h values are given for data that is unscaled (——), scaled by N_s (- - - -) and scaled by (r_w^2+22)(.....).*

Another consideration is that as the RM size decreases, particularly for ω < 10, studies have shown the shape of the RM becomes more elliptical, which affects the area the surfactant head occupies at the RM interface. The intermolecular forces between the dispersed and continuous phase also vary as the droplet size changes and this may also affect the area of the

surfactant head at the interface.[63] Using both scaling techniques, the number distributions were obtained for the AOT microemulsions with additives (Figure 3.15). The distributions now show a higher proportion of smaller droplets compared with the unscaled distributions. The average sizes, using the mode, are also slightly smaller. It must be noted though, that changes in droplet shapes as the droplet size increases are not considered in these scaling procedures and the RMs at each ω are assumed to be spherical. Hence these scaling procedures may not be applicable in these cases and alternative and more appropriate methods need to be investigated and developed. The need for a scaling factor has implications for the accuracy of the average diffusion coefficients determined from the ST equation and their application, when determining droplet sizes in multimodal systems, as the use of the average diffusion coefficient in determining the R_h for unimodal systems may be sufficient but this may not be the case for multimodal systems as the signal from the surfactant molecules in larger droplets will contribute more towards the diffusion data than molecules from smaller droplets. In the ST analysis the relative contributions are not given as a function of droplet size, hence there is no direct mechanism where the data can be directly scaled, without prior knowledge of the droplet size distribution. Therefore this shows that MR measurements of average diffusion coefficients should be treated with caution for multimodal systems.

3.3.7. Relaxation T_1 and T_2 for AOT/n-octane/water Microemulsions at varying ω with Acidic Additives

The T_2 and T_1 relaxation times of the H_3 AOT headgroup proton and the water molecules were measured (Section 3.2.7 and 3.2.8, respectively). There was no significant difference in the T_1 relaxation between the microemulsions with or without the acidic additives for the water or the AOT H_3 protons (Figure 3.16). The T_1 relaxation for the AOT H_3 proton

remained constant, as a function of ω, whereas the T_1 relaxation for the water protons increased in the microemulsions, with and without acidic additives, as a function of ω. The trend of increasing T_1 with ω with the micellar water has been reported previously.[42] The relaxation time T_1 increases as a function of ω due to the increase in free water within the droplet. As the droplet size increases, the water in the droplet behaves more as bulk water and the mobility of the water protons increases, hence the increase in T_1.[65,66]

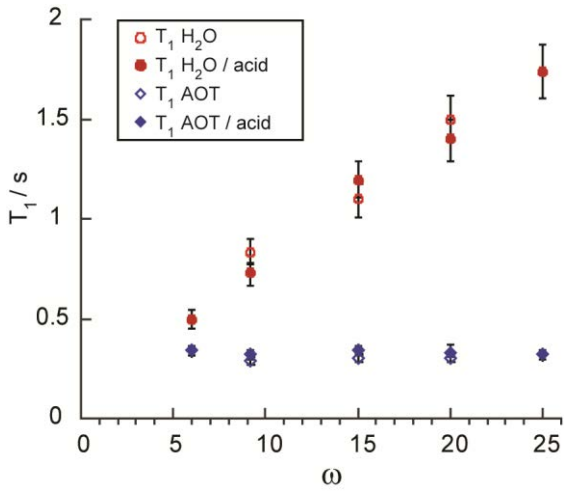

Figure 3.16: *Plot of T_1 relaxation times for the water and AOT protons in AOT /n-octane/water microemulsions with and without [H_2SO_4] = 0.12 M and [malonic acid] = 0.12 M.*

The T_2 relaxation time increased as a function of ω for the water protons in both the acidic and non-acidic microemulsions, (Figure 3.17 (a)) following the same trend as for the T_1 relaxation times with an increase in T_2, due to increased mobility of the water molecules, and a decrease in the dipolar coupling. There are two T_2 relaxation times for the AOT H_3 protons, with and without malonic and sulfuric acid (Figure 3.17 (b)), indicating there are two populations of AOT in the microemulsion. The T_2 relaxation contributions for the AOT

molecules at varying ω were between 8 and 10% for the longer T_2 relaxation time from the free AOT molecules in the continuous phase with 90% of the AOT with the shorter T_2 time from the AOT molecules in the RMs. There was little variation in the contributions from the interfacial and free AOT at varying ω or between the microemulsions with and without acid. To further investigate the exchange processes, experiments could be carried out at varying τ to analyse any changes in the contributions of free and interfacial AOT.

The higher value of T_2 may originate from the AOT monomers present in the continuous phase with the faster overall rotational motion, relaxing at a slower rate through decreased dipolar coupling. The lower value of T_2 may originate from slower tumbling AOT molecules residing in the micelle interface, which have restricted mobility, producing an increase in dipolar coupling and shorter relaxation time. In the RMs, the T_2 values with acid and without acid are the same at ω = 9.2, but at $\omega \geq 15$, the AOT protons in the RM with acid have increased T_2, suggesting that the acid additives cause more restriction on the motion of the RMs. The T_2 times for the AOT monomers are shorter with the acid additives, which would again indicate that the acid causes restriction on the motion of AOT molecules in the microemulsion. However at ω = 5.3, there is an increase in T_2 times for the AOT molecules in the RM and continuous phase compared to larger values of ω, with acid additives because of the increased motion and dynamics of the smaller droplets. The addition of malonic and sulfuric acid causes disruption to the motion of the RMs at $\omega \geq 15$, resulting in an increase in the dipolar coupling and hence the decrease in T_2 relaxation. More studies are required at varying acid concentrations and at more values of ω and ϕ_d.

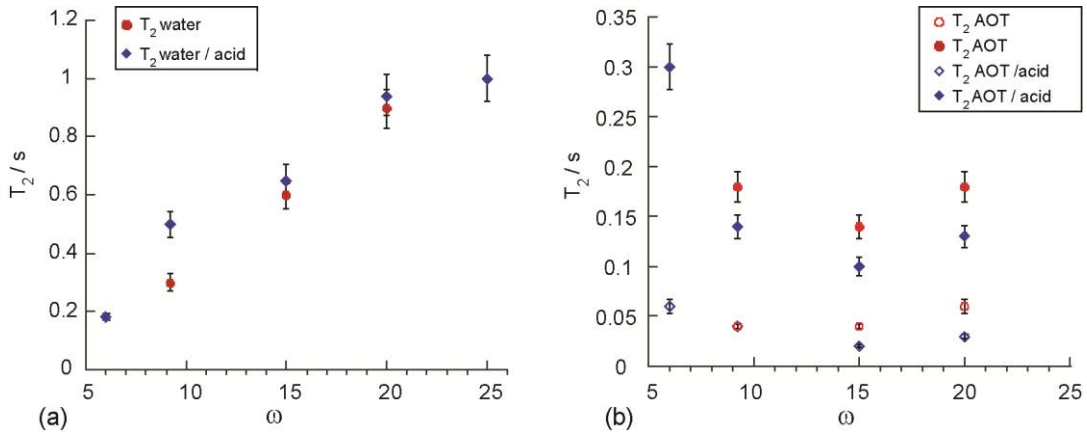

Figure 3.17: *Plots of T_2 relaxation times for the water (a) and AOT (b) protons in AOT/n-octane/water systems with and without $[H_2SO_4]$ = 0.12 M and [malonic acid] = 0.12 M.*

3.4. Conclusions

The droplet size distributions for RMs in AOT and CTAB microemulsions were determined by applying the inverse Laplace transform and using the Stokes-Einstein relation to NMR measurements of diffusion for the surfactant protons residing in the RM interface. These measurements are complementary to the methods previously used to size RMs. However, RM sizes in the AOT/*n*-octane/water microemulsion were found to be larger compared to those measured by optical methods, particularly at lower ω values. These differences were due to ϕ_d being too high, such that the increase in the concentration and collision rate of the droplets caused an obstruction to the diffusion of the RMs. Diffusion measurements are therefore required at lower ϕ_d in order to suppress the obstruction effects and measure D which are tending towards infinite dilution.

The polydispersity of the microemulsions cannot be obtained from the distribution widths, which are generated by the ILT; however, it is possible to use these methods to compare

changes in size distributions as a function of ω, ϕ_d and composition. In the bimodal systems, scaling factors were investigated which enabled number distributions to be generated and, when used, were shown to shift the distributions towards smaller droplet sizes, reducing the average droplet size. The appropriate use of scaling factors requires further investigation.

3.5. References

(1) Vanag, V. K. *Phys. Usp.* **2004**, *47*, 923.

(2) Vanag, V. K.; Epstein, I. R. *Phys. Rev. Lett.* **2003**, *90*, 098301.

(3) Capek, I. *Adv. Colloid Interface Sci.* **2004**, *110*, 49.

(4) Chen, M. J.; Yang, W. T.; Yin, M. Z. *Small* **2013**, *9*, 2715.

(5) Eastoe, J.; Hollamby, M. J.; Hudson, L. *Adv. Colloid Interface Sci.* **2006**, *128*, 5.

(6) Schatzel, K. *Adv. Colloid Interface Sci.* **1993**, *46*, 309.

(7) Filipe, V.; Hawe, A.; Jiskoot, W. *Pharm. Res.* **2010**, *27*, 796.

(8) *Particle size distribution: assessment and characterization*; Provder, T., Ed.; American Chemical Society: Washington, D.C., 1987.

(9) Ruf, H. *Langmuir* **2002**, *18*, 3804.

(10) Ruf, H.; Gould, B. J.; Haase, W. *Langmuir* **2000**, *16*, 471.

(11) Pal, N.; Verma, S. D.; Singh, M. K.; Sen, S. *Anal. Chem.* **2011**, *83*, 7736.

(12) Chen, S. H. *Annu. Rev. Phys. Chem.* **1986**, *37*, 351.

(13) Balakrishnan, S.; Javid, N.; Weingartner, H.; Winter, R. *Chemphyschem* **2008**, *9*, 2794.

(14) Caboi, F.; Capuzzi, G.; Baglioni, P.; Monduzzi, M. *J. Phys. Chem. B* **1997**, *101*, 10205.

(15) Dahirel, V.; Ancian, B.; Jardat, M.; Meriguet, G.; Turq, P.; Lequin, O. *Soft Matter* **2010**, *6*, 517.

(16) Fedotov, V. D.; Zuev, Y. F.; Archipov, V. P.; Idiyatullin, Z. S.; Garti, N. *Colloids Surf., A* **1997**, *128*, 39.

(17) Gradzielski, M. *Curr. Opin. Colloid Interface Sci.* **2008**, *13*, 263.

(18) Hedin, N.; Furo, I. *Langmuir* **2001**, *17*, 4746.

(19) Knackstedt, M. A.; Ninham, B. W.; Monduzzi, M. *Phys. Rev. Lett.* **1995**, *75*, 653.

(20) Lasic, S.; Aslund, I.; Oppel, C.; Topgaard, D.; Soderman, O.; Gradzielski, M. *Soft Matter* **2011**, *7*, 3947.

(21) Walderhaug, H.; Johannessen, E. *J. Sol. Chem.* **2006**, *35*, 979.

(22) Song, Y.-Q. *Con. Magn. Reson. A* **2003**, *18A*, 97.

(23) Chen, A.; Wu, D. H.; Johnson, C. S. *J. Am. Chem. Soc.* **1995**, *117*, 7965.

(24) Vieville, J.; Tanty, M.; Delsuc, M. A. *J. Magn. Reson.* **2011**, *212*, 169.

(25) Griffiths, P. C.; Cheung, A. Y. F.; Davies, J. A.; Paul, A.; Tipples, C. N.; Winnington, A. L. *Magn. Reson. Chem.* **2002**, *40*, S40.

(26) Valentini, M.; Vaccaro, A.; Rehor, A.; Napoli, A.; Hubbell, J. A.; Tirelli, N. *J. Am. Chem. Soc.* **2004**, *126*, 2142.

(27) Callaghan, P. T.; Godefroy, S.; Ryland, B. N. *Magn. Reson. Imag.* **2003**, *21*, 243.

(28) Callaghan, P. T. *Translational dynamics and magnetic resonance : principles of pulsed gradient spin echo NMR*; Oxford University Press: Oxford ; New York, 2011.

(29) Fang, X. L.; Yang, C. F. *J. Colloid Interface Sci.* **1999**, *212*, 242.

(30) Halliday, N. A.; Peet, A. C.; Britton, M. M. *J. Phys. Chem. B* **2010**, *114*, 13745.

(31) Sedgwick, M.; Cole, R. L.; Rithner, C. D.; Crans, D. C.; Levinger, N. E. *J. Am. Chem. Soc.* **2012**, *134*, 11904.

(32) Mills, A. J.; Wilkie, J.; Britton, M.M. *J. Phys. Chem. B* **2014**, *118,*10767.

(33) Alvarez, E. V.; Carballido-Landeira, J.; Guiu-Souto, J.; Taboada, P.; Munuzuri, A. P. *J. Chem. Phys.* **2011**, *134*, 094512.

(34) Tofts, P. S.; Lloyd, D.; Clark, C. A.; Barker, G. J.; Parker, G. J. M.; McConville, P.; Baldock, C.; Pope, J. M. *Magn. Reson. Med.* **2000**, *43*, 368.

(35) Provencher, S. W. *Comput. Phys. Commun.* **1982**, *27*, 213.

(36) Provencher, S. W. *Comput. Phys. Commun.* **1982**, *27*, 229.

(37) Borgia, G. C.; Brown, R. J. S.; Fantazzini, P. *J. Magn. Reson.* **1998**, *132*, 65.

(38) Fordham, E. J.; Sezginer, A.; Hall, L. D. *J. Magn. Reson., Ser. A* **1995**, *113*, 139.

(39) Song, Y. Q.; Venkataramanan, L.; Hurlimann, M. D.; Flaum, M.; Frulla, P.; Straley, C. *J. Magn. Reson.* **2002**, *154*, 261.

(40) Prospa version2.1 Magritek, **http://www.magritek.com/prospa.html.**

(41) Kaleidagraph 4.1; Software, Synergy, USA, 2011.

(42) Binks, D. A.; Spencer, N.; Wilkie, J.; Britton, M. M. *J. Phys. Chem. B* **2010**, *114*, 12558.

(43) Maitra, A. *J. Phys. Chem.* **1984**, *88*, 5122.

(44) American Society for Testing and Materials, In *ASTM Standard E2490*; ASTM International: West Conshohocken, PA, 2009.

(45) Baruah, B.; Roden, J. M.; Sedgwick, M.; Correa, N. M.; Crans, D. C.; Levinger, N. E. *J. Am. Chem. Soc.* **2006**, *128*, 12758.

(46) Nazario, L. M. M.; Hatton, T. A.; Crespo, J. P. S. G. *Langmuir* **1996**, *12*, 6326.

(47) Vasquez, V. R.; Williams, B. C.; Graeve, O. A. *J. Phys. Chem. B* **2011**, *115*, 2979.

(48) Zulauf, M.; Eicke, H. F. *J. Phys. Chem.* **1979**, *83*, 480.

(49) Hirai, M.; Hirai, R. K.; Iwase, H.; Arai, S.; Mitsuya, S.; Takeda, T.; Seto, H.; Nagao, M. *J. Phys. Chem. Solids* **1999**, *60*, 1359.

(50) Liu, J. C.; Li, G. Z.; Han, B. X. *Chin. Chem. Letts.* **2001**, *12*, 1023.

(51) Jonsson, B.; Wennerstrom, H.; Nilsson, P. G.; Linse, P. *Colloid Polym Sci* **1986**, *264*, 77.

(52) Jada, A.; Lang, J.; Zana, R. *J. Phys. Chem.* **1989**, *93*, 10.

(53) Ekwall, P.; Mandell, L.; Solyom, P. *J. Colloid Interface Sci.* **1971**, *35*, 266.

(54) Rodenas, E.; Valiente, M. *Colloids Surf.* **1992**, *62*, 289.

(55) Halliday, N. A., PhD Thesis School of Chemistry University of Birmingham, 2010.

(56) Jones, A. R. *Prog. Energy Combust. Sci.* **1999**, *25*, 1.

(57) Eicke, H. F.; Rehak, J. *Helv. Chim. Acta* **1976**, *59*, 2883.

(58) Tovstun, S. A.; Razumov, V. F. *J. Colloid Interface Sci.* **2010**, *351*, 485.

(59) Ricka, J.; Borkovec, M.; Hofmeier, U. *J. Chem. Phys.* **1991**, *94*, 8503.

(60) Zana, R.; Xia, J. *Gemini surfactants : synthesis, interfacial and solution-phase behavior, and applications*; Marcel Dekker: New York, 2004.

(61) Degennes, P. G.; Taupin, C. *J. Phys. Chem.* **1982**, *86*, 2294.

(62) Mitchell, D. J.; Ninham, B. W. *J. Chem. Soc., Faraday Trans.* **1981**, *77*, 601.

(63) Nagarajan, R.; Ruckenstein, E. *Langmuir* **2000**, *16*, 6400.

(64) Moilanen, D. E.; Fenn, E. E.; Wong, D.; Fayer, M. D. *J. Chem. Phys.* **2009**, *131*, 014704.

(65) Levinger, N. E. *Science* **2002**, *298*, 1722.

(66) Wong, M.; Thomas, J. K.; Nowak, T. *J. Am. Chem. Soc.* **1977**, *99*, 4730.

4. Using NMR Measurements of Diffusion to Investigate the Dynamics of Microemulsions

4.1. Introduction

In the previous chapter, the hydrodynamic radii of water-in-oil reverse micelles (RMs) in the AOT/*n*-octane/water microemulsion were determined at varying water to surfactant ratio ω values at $\phi_d = 0.15$. R_h increased as a function of ω, as expected, but the R_h values were higher than those obtained from scattering methods, particularly at lower ω values.[1,2] The reasons for the differences between the R_h values obtained from scattering techniques and PFG methods are explored here. Scattering methods measure the mutual diffusion coefficient (D_m), which describes the collective diffusion of particles in a system and the overall net movement of molecules is governed by the flux which is proportional to the concentration gradient. PFG techniques, however, measure the self-diffusion coefficients (D_s) of the separate molecular species present within a system.[3-5] The various scattering techniques used to measure the sizes of RMs[1,2,5,6] include, dynamic light scattering, (DLS), fluorescence correlation spectroscopy, (FCS), small angle neutron scattering (SANS) and small angle x-ray scattering (SAXS). The literature values for R_h of RMs from these techniques were reported at lower droplet volume fractions (ϕ_d). However, ϕ_d is not always stated in studies of sizing RMs. More often, the molarity of the AOT/octane is directly stated, resulting in a variation of the droplet volume fraction measured at different omega values[2,7] Zulauf *et al.*[2] in a DLS study of AOT/iso-octane/water used a range of $\phi_d = 0.02 - 0.08$, whereas others have used $\phi_d = 0.11 - 0.13$ in using a 0.02 M AOT/iso-octane stock solution.[7] Measuring the diffusion coefficient at $\phi_d < 0.15$ is necessary, as measurements of diffusion are sensitive to inter-

droplet interactions or collisions. This is known as the *obstruction effect*.[8-11] One explanation for the differences in the resulting R_h values between scattering techniques and our PFG experiments was that the obstruction effect had not been taken into account, therefore further measurements at $\phi_d \leq 0.15$, were made at various values of ω and at different temperatures. The self-diffusion coefficients of the RMs were calculated at infinite dilution,[3,12,13] implementing eq 4.1 to extrapolate D to D_0[9,10,14,15] (1.3.1), where D is the observed diffusion coefficient, D_0 is the diffusion coefficient at infinite dilution, ϕ_d is the droplet fraction and α is the *virial* coefficient.

$$D = D_0(1+\alpha\phi_d) \qquad \text{eq 4.1}$$

The virial coefficient originates from the friction and the osmotic pressure of the system which are determined from the hydrodynamic interactions and is therefore directly related to ϕ_d. The conversion of the diffusion coefficient to R_h, using the Stokes-Einstein equation, assumes that the RMs are spherical and the viscosity of the microemulsion is governed solely by the organic solvent in the continuous oil phase. These assumptions can lead to errors when evaluating R_h, depending on the microemulsion parameters, due to changes in the shape, viscosity and dynamics at varying ω and ϕ_d. The dynamics and behaviour of the AOT/*n*-octane/water microemulsions were probed by measuring the diffusion coefficient as a function of observation times (Δ) in the PFG experiments at varying ω, ϕ_d. and temperature.[11] The effect of changing the viscosity of the continuous phase on the resulting R_h of the RMs was also explored. Consideration was given to the type of PFG experiment used and the range of accessible experimental timescales available.[9,10]

4.2. Experimental

4.2.1. Preparation of Reverse Micelles

A stock solution of 1.5 M AOT (sodium bis(2-ethylhexyl) sulfosuccinate (Fluka 96%) in *n*-octane (Acros 97%) was prepared by dissolving 27.79 g AOT in 17.5 ml *n*-octane. The *n*-octane was purified by stirring octane with concentrated sulphuric acid in a ratio of 4:1 over a period of 4 days. Microemulsions were prepared at water-to-surfactant ratios of $\omega = 5.3 - 35$ by adding the correct volume of water (Nanopure filtered, 18 MΩ) to the 1.5 M AOT solution to produce the required ω and diluted initially with the appropriate volume of *n*-octane to give $\phi_d = 0.45$. The mixtures were shaken for at least 30 seconds until a transparent microemulsion formed and were used within a 24 hour period. Aliquots were taken from this solution and diluted further with *n*-octane, giving a range of volume droplet fractions $\phi_d = 0.05 - 0.2$. Diffusion measurements were taken 1 hr after the samples were prepared.

4.2.2. Pulsed Field Gradient (PFG) Experiments

All the Pulsed Field Gradient (PFG) experiments were performed at temperatures between 289 – 298 K on a Bruker DMX300 spectrometer equipped with a 7.0 T superconducting magnet, operating at a frequency of 300.13 MHz. Pulsed Field Gradient Stimulated Echo (PGSTE) experiments were carried out with a 25 mm radiofrequency coil, using a micro2.5 probe. PGSTE and Bipolar Pulsed Pair Stimulated Echo Experiments (BPSTE) experiments have been used with BPSTE for experiments with short Δ. In order to achieve shorter observation times, to observe if there was any variation in the diffusion coefficient as a function of Δ, higher gradient strengths were accessed up to 9 T m^{-1} (900 G cm^{-1}) on the

DIFF30 probe, compared to 0.9 T m^{-1} (90 G cm^{-1}), which was the maximum gradient accessible on the micro2.5 probe. When using the DIFF30 probe, PGSTE experiments produced artifacts, due to the production of eddy currents induced by the higher gradient strengths, therefore BPSTE experiments were used to suppress this effect.

The parameters used in the PGSTE experiments were typically, δ = 4 ms, Δ= 100 ms, with a maximum gradient, $\boldsymbol{G}_{max}$, 0.9 T m^{-1} with 32 or 256 gradient steps, ensuring the signal attenuated so that S(G)/S(0) at $\boldsymbol{G}_{max}$ was $\leq$ 0.01 and 128 signal averages were collected with a repetition time of 1s. The temperature of the sample was maintained using the Bruker Variable Temperature (BVT 1000_VT Unit) control. The samples were left to equilibrate at the required temperature for at least 20 minutes. Samples were measured at the higher temperature, 298 K, first and then the temperature was lowered.[2] To minimise convection effects during the PFG experiments at higher temperatures (298 K) and lower droplet volume fractions, ϕ_d = 0.05, 3 mm NMR tubes (Wilmad) were used. The diffusion data was collected for each system measuring the proton resonance, H_3, in the headgroup of the AOT surfactant.

BPSTE experiments were performed at 298 ± 0.2 K with a 5 mm radiofrequency coil using a DIFF30 probe. Typically 64 or 256 signal averages were collected, with 64 signal averages collected for microemulsions where $\phi_d > 0.15$. Parameters used in these experiments were δ = 1.5 ms, Δ = 10 – 100 ms, with a maximum gradient, $\boldsymbol{G}_{max}$, from 1.5 – 9 T m^{-1} and $\boldsymbol{G}_{min}$ = 0.02 T m^{-1} with 32 gradient steps at a repetition time of 1.5 s. The BPSTE experiments were run using TOPSPIN 1.3 software.[16] The temperature of the sample was maintained using the water bath which regulates the temperature of the probe.

4.2.3. Viscosity Measurements

The viscosities of mixtures of AOT/*n*-octane between 0 – 0.1 M were measured using a Cannon-Fenske routine viscometer (size 25), which measures kinematic viscosities over the range 0.5 – 2 cSt. The viscometer and solutions were immersed in a water-bath maintained at 298 K and were initially allowed to equilibrate for 40 minutes. The density of the solutions was measured, which allowed the conversion from kinematic to dynamic viscosity[17] (eq 4.2)

$$\nu = \frac{\mu}{\rho} \qquad \text{eq 4.2}$$

where ν is the kinematic viscosity, μ is the dynamic viscosity and ρ is the density. The viscosity and density measurements were repeated 3 times.

4.3. Results and Discussion

4.3.1. Variation of the Droplet Volume Fraction

The diffusion coefficient for the H_3 proton in the AOT/*n*-octane/water microemulsion at ω = 15 was measured at decreasing ϕ_d = 0.05 – 0.3 at 289 K at $\boldsymbol{G}$ = 0.9 T m^{-1}, δ = 4 ms and Δ = 100 ms (Figure 4.1 (a)) using PGSTE experiments. The self-diffusion coefficient (D_s) increased as ϕ_d decreased, which has been observed previously in microemulsion systems.[8,10]

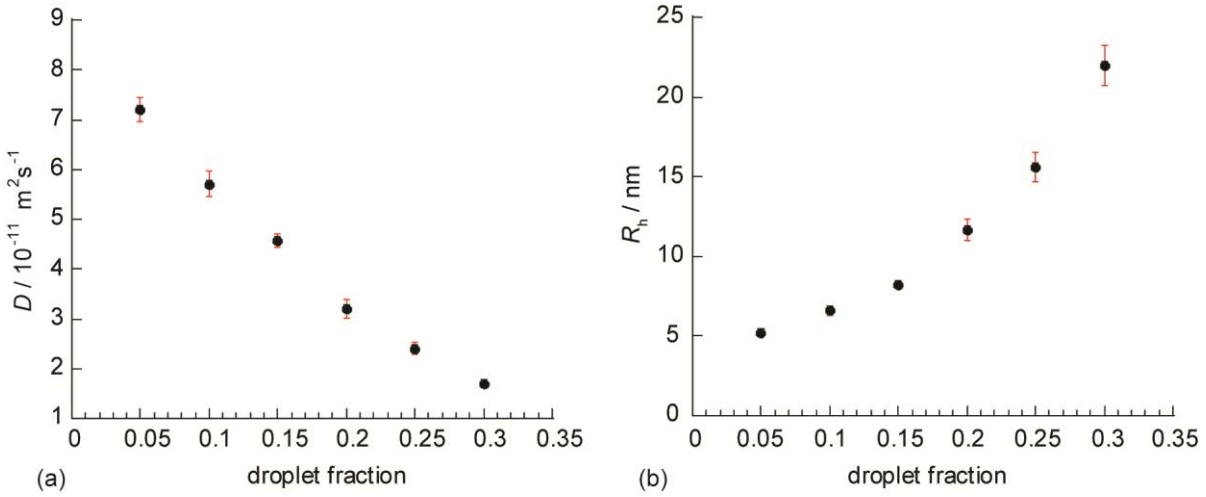

Figure 4.1: *A plot of the self-diffusion coefficient D_1 (a) and droplet sizes (R_h) (b) in AOT/n-octane/water microemulsions at ω = 15, at 289 K, with* $\boldsymbol{G}$ *= 0.9 T m $^{-1}$, δ = 4 ms and Δ = 100 ms, analysed fitting to the Stejskal-Tanner equation.*

Also, as expected, due to the inverse relationship between the diffusion coefficient and R_h using the Stokes-Einstein equation, the R_h decreased as ϕ_d decreased (Figure 4.1 (b)). However, at ϕ_d = 0.05, when fitting the diffusion data to the Stejskal-Tanner (ST) equation, the AOT molecules were observed diffusing at two different rates. This gave rise to a population that was bimodal, where $D_1 = 7.2 \times 10^{-11}$ m^{2}s^{-1} and $D_2 = 1.12 \times 10^{-9}$ m^{2}s^{-1} with relative contributions of 89% and 11% respectively (Table 4.1). The same values were obtained when applying the inverse Laplace transform (ILT).

ϕ_d	D_1/ 10^{-11} m^2s^{-1}	D_2 / 10^{-11} m^2s^{-1}	$R_h^{(1)}$/ nm	$R_h^{(2)}$/ nm
0.05	7.2 (89%)	112 (11%)	5.32	0.34
0.1	5.7	–	6.6	–
0.15	4.6	–	8.2	–
0.2	3.2	–	11.7	–
0.25	2.4	–	15.6	–
0.3	1.7	–	22	–

Table 4.1: *Summary of diffusion data and R_h values for the AOT/n-octane/water microemulsion at ω = 15; 289 K. The data was analysed by fitting to the Stejskal-Tanner relation.*

The slower diffusion coefficient (D_1) is expected from AOT situated in the RM interface. However, what is the origin of the faster diffusion coefficient, (D_2), which is up to twice the order of magnitude than D_1? One possible explanation is that the D_2 originates from AOT monomers, which are present in the continuous phase. The continuous phase, *n*-octane, has a self-diffusion coefficient of 1.988×10^{-9} m^2s^{-1} at 289 K and the diffusion coefficient for AOT H_3 proton, for a solution of 0.15 M AOT in *n*-octane = 2.32×10^{-10} m^2s^{-1}. The value for D_2 in the system ω = 15, ϕ_d = 0.05 lies at the same order of magnitude at 1.12×10^{-9} m^2s^{-1} (Table 4.1), between the values of the diffusion coefficient of pure *n*-octane and 0.15 M AOT in *n*-octane, showing that AOT monomers may be present at a concentration < 0.15 M in the *n*-octane continuous phase. There are two possible explanations for the presence of the AOT monomers at the higher dilution. There may be a change in the composition of the microemulsion[11,18] with the intermolecular forces between the droplets changing as the system becomes more dilute. Another possible explanation for the presence of AOT monomers is that as the concentration of the microemulsion changes, so do the dynamics of the system and the exchange processes between monomer and interfacial AOT are being observed.

Due to potential compositional changes, it has been suggested[11] that when extrapolating to D_0, it is not advisable to use low droplet volume fractions. However, when extrapolating the values for $\omega = 15$ (Table 4.1) and omitting the data point at $\phi_d = 0.05$, the resulting $D_0 = 7.6 \times 10^{-11}$ m^2s^{-1}, and the virial coefficient (α) = –2.68 resulting in $R_h = 4.9$ nm. The extrapolation, with the data point at $\phi_d = 0.05$, resulted in $D_0 = 8.01\times10^{-11}$ m^2s^{-1}, virial coefficient (α) = –2.76 with $R_h = 4.6$ nm, giving a 2% increase in the virial coefficient and 5.4% increase in D_0. The virial coefficient for an ionic surfactant such as AOT, which has attractive inter-particle interactions, is –2. This is taken from a model system where the D_s and the hydrodynamic interactions are calculated based on the hard sphere model.[3] The experimental value obtained for the system, ω =15 was α = –2.68, which is in good agreement with the theoretical model value. Zulauf *et al.*[2] obtained $R_h = 3.6$ nm at $\omega = 11$ and $R_h = 5$ nm at $\omega = 22$, at a range of $\phi_d = 0.02 – 0.08$, with another study obtaining $R_h = 4.5$ nm at ω =15 from dynamic light scattering measurements.[19] The DLS measurements from the literature were made at the higher temperature of 298 K, so the experimental measurements from this study cannot be directly compared with the diffusion coefficient values from the literature, as they were measured at the lower temperature of 289 K. The comparison illustrates, however, that R_h values become more comparable between scattering and NMR methods at similar ϕ_d, as the obstruction effect is minimised.

Further PGSTE experiments were carried out at $\omega = 5.3 – 35$, with the same experimental parameters and conditions that were used to investigate the AOT/water/*n*-octane microemulsion at $\omega = 15$ (Table 4.2), (Figure 4.2). This was to observe how the diffusion coefficient of AOT H_3 changed at varying ω at lower ϕ_d, with the possibility of extrapolating to D_0 (eq 4.1). This would enable the determination of R_h without obstruction effects and

further comparison with the values from scattering methods. However, at ω = 25 and 35, two diffusion coefficients were obtained at ϕ_d = 0.05 from fitting to the Stejskal-Tanner equation and applying the ILT (Figure 4.2).

ω	ϕ_d	AOT	AOT	R_h / nm	water
		D_1 / 10^{-11} m^2s^{-1}	D_2 / 10^{-11} m^2s^{-1}		D / 10^{-11} m^2s^{-1}
5.3	0.05	11.5	–	3.27	18.5
	0.1	7.4	–	5.08	11.1
	0.15	5.5	–	7.5	6.52
15	0.05	7.2 (89%)	112 (11%)	5.32	9
	0.1	5.7	–	6.6	7.78
	0.15	4.6	–	8.2	5.4
25	0.05	5.34 (79%)	103 (21%)	7.04	7.54
	0.1	4.51 (88%)	37 (12%)	8.34	6.15
	0.15	3.84	–	9.8	5.3
35	0.05	4.97 (84%)	87 (16%)	7.56	5.89
	0.1	3.92	–	9.6	4.95
	0.15	3.11	–	12	4.1

Table 4.2: *Summary of AOT H_3 and water diffusion data, analysed fitting to the Stejskal-Tanner relation with the resulting R_h values for the AOT/n-octane/water microemulsion at 289 K.*

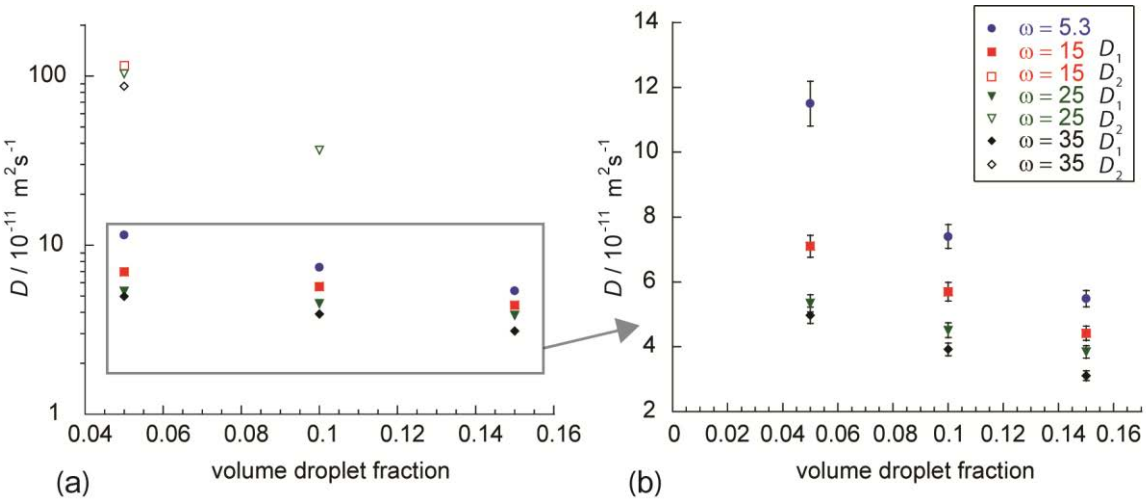

Figure 4.2: *Plots of the diffusion coefficients for AOT H_3, with D_1 associated with the RM and D_2 (a) and D_1 (b) for AOT/n-octane/water at ω=5.3 – 35 at 289 K.* $\boldsymbol{G}$ *= 0.9 T m* $^{-1}$*, δ = 4 ms and Δ = 100 ms.*

ω	α	D_0 / 10^{-11} m^2s^{-1}	R_0
5.3	–4.2	14.1	2.7
15	–2.8	8.01	4.6
25	–2.5	6.06	6.2
35	–2.8	5.68	6.6

Table 4.3: *A table showing the calculated virial coefficients from the plot shown in Figure 4.2(b), with the estimated values of D_0 and corresponding R_0.*

The expected trend of a decreasing self-diffusion coefficient (D_s) as a function of ϕ_d was observed. For ω = 15 – 35, D_2, the faster diffusion component ranged from 3.7×10^{-10} m^2s^{-1} to 1.12×10^{-9} m^2s^{-1}. However, the system remained monomodal at ω = 5.3. Extrapolating to infinite dilution (eq 4.1) for the system ω = 5.3, resulted in $D_0 = 14.1 \times 10^{-11}$ m^2s^{-1} with a virial coefficient, α = –4.2 resulting in R_h = 2.7 nm. Light scattering measurements have reported ω = 5; R_h = 2.9 nm.[19] However there is a difference between the experimental and

literature values for the virial coefficient (α) (Table 4.3). This may be due to a proportion of AOT monomer at $\phi_d = 0.05$, causing changes to the viscosity of the system, with an increase in frictional forces, or a decrease in the osmotic pressure between the RMs and the continuous phase, leading to a decreasing rate of change of the diffusion coefficient. The decrease in α at ω = 5.3 may also be due to a change in the attractive potential interactions between the surfactant molecule tails.[20,21] As ϕ_d decreases, there is a decrease in attractive interactions, as there is less micellar overlap and less interpenetration of surfactant tails. The attractive interactions between RMs are short-range and result from London dispersion, van der Waal inter-atomic forces.[22] As RMs overlap there is a favourable decrease in the concentration of oil molecules in the overlapping region. However, as RMs fuse together, a repulsive interaction starts to dominate due to the increase in surfactant molecules and restricted volume.[22,23] There is a linear increase of attractive interactions with the size of RMs, as there is an increase in the overlap between RMs.[22-24] The rate at which the attractive interactions decrease, as ϕ_d decreases, is greater for the RMs at ω = 5.3 leading to a greater rate of decrease in the frictional coefficient of the smaller RMs, hence α becomes more negative than for RMs at ω > 10. The AOT monomer may not be observed at ω = 5.3 because at ω < 10, as the RMs diffuse at a faster rate[20] the inter-droplet and molecular exchange may occur at an increased rate than systems at ω >10.

At all ω and ϕ_d values, the water molecules were observed diffusing at one rate, including the systems where two diffusion coefficients were obtained for the AOT molecules at $\phi_d = 0.05$. The water diffusion coefficient increased as ω increased and the values were consistently higher than the corresponding AOT values. The diffusion coefficient values of water (Table 4.2) are averages of the water molecules which are in fast exchange between the free and the

bound water within the droplet and droplet interface.[25] The free water behaves increasingly like bulk water as the RM size and ω increases.[25] It has been previously suggested that the reason for water diffusion coefficients being consistently higher than the surfactant is that there is "non-negligible" water between the droplets[7,26] which leads to the possibility of free water being present in the continuous phase.

It is known that the diffusion coefficient values obtained from scattering and NMR methods are different,[10] as are the values in virial coefficients at varying ω.[27] It is often discussed in the literature that RMs at $\omega < 10$ have different characteristics than those at $\omega > 10$, with more rigid, less flexible interfaces and closer to being spherical than those at $\omega > 10$.[9,18,28] At higher values of ω, the surfactant interface is more flexible[9,18,20] and undergoes more shape fluctuations with increasing size.[29] The inter-relating factors of size, interfacial tension and intermolecular forces, effect the behaviour and dynamics of RMs and may explain the differences in the rate of change of the diffusion coefficient observed in RMs above and below ω = 10. When extrapolating to D_0, using D_1 at varying ω= 15 – 35, α were more comparable with the literature value, which is interesting, as these systems have a second diffusion coefficient D_2 for the AOT H_3 protons.

The variation of the diffusion coefficient as a function of ϕ_d was also investigated at a shorter observation time of 10 ms, using a BPSTE experiment at δ = 1.5 ms (Figure 4.3). The systems at ω= 15 and 25 were investigated. At the higher temperature of 298 K, the H_3 AOT proton for ω = 5.3 at varying ϕ_d could not be analysed, as a shift in the water peak masked the H_3

AOT peak of interest. The data was noisier than the measurements at Δ = 100 ms, observed in (Figure 4.2).

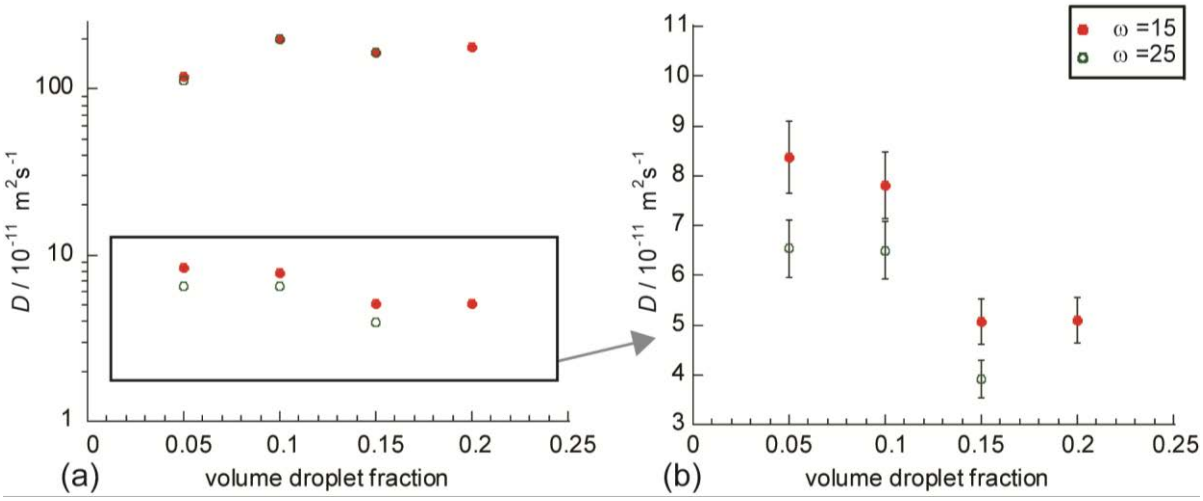

Figure 4.3: *Plots of the diffusion coefficients of AOT H_3, D_1 (RM) and D_2 (monomer)(a) and D_1 (b) for AOT/n-octane/water system at ω=15 and 25 with δ =1.5 ms, Δ = 10 ms at 298 K.*

Two diffusion coefficients were observed at both ω = 15 and 25 at ϕ_d = 0.05 – 0.2, which means that at the shorter observation time, Δ = 10 ms, the AOT monomer is observed at higher ϕ_d and not just at ϕ_d = 0.05, as observed in the experiments performed at Δ = 100 ms. Therefore there was the possibility that molecular exchange processes were observed between the AOT in the continuous phase and the RMs at lower Δ. The PFG parameters used in the experiments have a significant effect on the experimental outcomes. The diffusion coefficients at all values of ω and ϕ_d are slightly higher than obtained at Δ = 100 ms at T = 289 K (Figure 4.2) due to an increase in the temperature. The values are however in line with those obtained from scattering methods.

As AOT monomers are present in the continuous phase, the viscosity of the continuous phase may change from that of pure *n*-octane, which would affect the resulting values of R_h using the Stokes-Einstein equation. The effect of the presence of AOT monomers in the continuous phase was calculated for the AOT/water/*n*-octane microemulsion at ω = 15 and 25 for volume fractions 0.05 and 0.15. The viscosities of AOT in octane mixtures were measured at 298 K in the range of [AOT] = 0 – 0.1 M and a significant variation was observed in the viscosity from 0.51 – 0.58 cP (Figure 4.4).

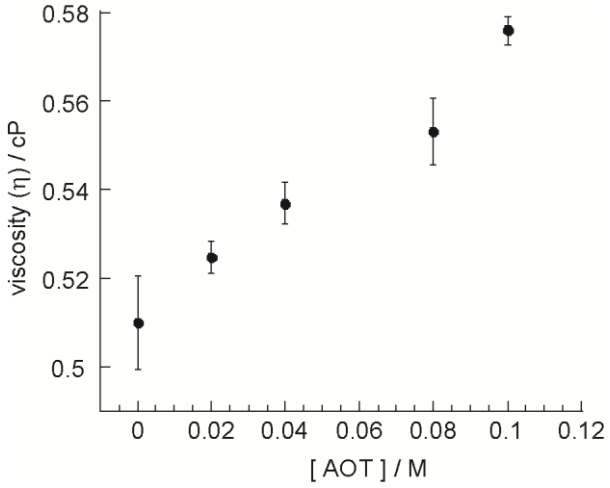

Figure 4.4: *A plot of the viscosity versus concentration for AOT in n-octane at 298 K.*

The dynamic viscosities of the continuous phase were calculated, accounting for the percentage of AOT monomer present and the values of R_h were calculated using the BPSTE experiments at Δ = 10 ms (Table 4.4). It was found that the change in R_h was not significant but there was a slight decrease in all systems. The decrease in R_h was greater at higher droplet fractions, decreasing by 11.5% and 7.3% for ω = 15 and 25 at ϕ_d = 0.15 and 4.3% and 3% for ω = 15 and 25 at ϕ_d = 0.05, respectively.

ω	ϕ_d	D /10^{-11} m^2s^{-1}	$R_h^{(a)}$/ nm	*%[AOT] CP	[AOT] / M	η /cP	$R_h^{(b)}$/nm
15	0.15	5.1	8.42	40	0.104	0.574	7.45
15	0.05	8.4	5.11	40	0.031	0.530	4.89
25	0.15	3.9	11.0	30	0.057	0.546	10.2
25	0.05	6.5	6.61	40	0.023	0.523	6.41

Table 4.4 : *Values of the R_h for AOT/n-octane/water microemulsions, R_h (a) with 100% n-octane and R_h (b) with the viscosity calculated from the free AOT monomer present in the continuous phase. *The proportion of AOT present in the continuous phase (CP).*

The intrinsic viscosity of microemulsions has been previously explored at varying ω, ϕ_d and temperatures.[14,30] Fletcher reported that changes in viscosity do not have a significant effect on the inter-droplet dynamics of the AOT system, and this is reflected in this study.[31]

The values of R_h for RMs in the AOT/*n*-octane/water become more comparable with the literature values from scattering experiments, as ϕ_d is decreased. However, decreasing ϕ_d and diluting the microemulsion in order to extrapolate to infinite dilution, D_0 has previously been thought not just to lead to a decrease in the obstruction effect, but to changes in the composition of the microemulsion.[11,18] Therefore with two diffusion coefficients for AOT molecules evident at $\omega > 5.3$ at lower droplet fractions, this produced issues when extrapolating to D_0. It is evident, however, that comparing the results obtained from the PGSTE with the BPSTE experiments, where δ and Δ were decreased, there were changes in the resulting diffusion data and therefore what was actually being measured. Two diffusion coefficients were obtained at all ϕ_d, from the AOT molecules in the RMs and the AOT monomer present in the continuous phase. There is the possibility that exchange processes

were being observed between the AOT in the RMs and continuous phase. The experimental parameters, δ and Δ, as well as the choice of PFG experiment, have a more significant bearing on what may be probed in microemulsions.[32-34] There was no significant change in R_h when accounting for the free AOT monomer present in the continuous phase and changes in the viscosity of the systems.

4.3.2. *Variation of the Gradient Pulse Length δ*

In order to minimise the effect of potential molecular exchange processes between the AOT in the RMs and the AOT in the continuous phase, which were observed when lowering Δ, the value of δ was varied from δ = 4 ms ($\boldsymbol{G}$ = 0.9 T m^{-1}) to δ = 1.5 ms ($\boldsymbol{G}$ =2.61 T m^{-1}) in PGSTE experiments keeping Δ constant at 100 ms.

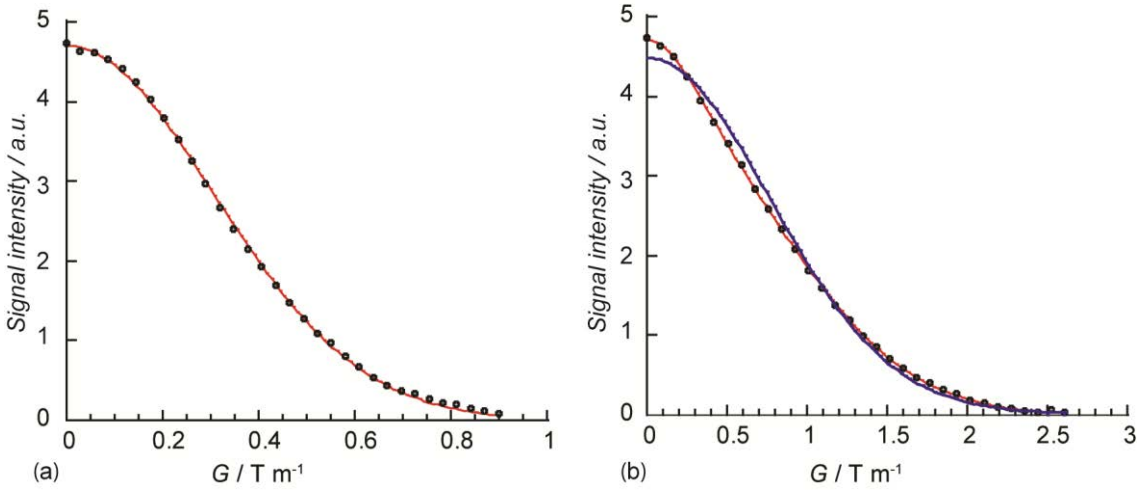

Figure 4.5: *Plots of the signal attenuation for the H_3 proton in the AOT molecule for an AOT/water/n-octane microemulsion at ω = 25; ϕ_d =0.15 and Δ = 100 ms at δ = 4 ms showing a mono-exponential (a) and δ = 1.5 ms showing a mono-exponential (—) and bi-exponential fit (—) (b).*

A change was observed in the signal attenuation for the H_3 proton in the AOT molecule (Figure 4.5) with a mono-exponential decay obtained from the experiment at δ = 4 ms and a bi-exponential decay obtained from the experiment at δ = 1.5 ms. It is important to note these experiments were run in succession with the same sample and the only changes in the experimental parameters were δ and $\boldsymbol{G}$. In these experiments where ϕ_d = 0.15, obstruction effects as well as exchange processes are taking place, the shorter gradient pulses and increasing $\boldsymbol{G}$ encodes the positions of the molecules with increased sensitivity. Although both experiments were at the same Δ of 100 ms, the shorter gradient pulse of 1.5 ms encodes the positions of the ensemble of spins moving at shorter displacements. The longer gradient pulse of 4 ms encodes the spins over longer displacements and may be more sensitive to the obstruction effects and exchange processes taking place within this time span. Price[35] commented that the obstruction effect can be viewed as a type of restricted diffusion. Malmborg *et al.*[36] conducted investigations on restricted diffusion with emulsions and found that the diffusion coefficient of molecules moving through the porous system varied as a function of the gradient pulse length. The change from mono-exponential to a bi-exponential decay for AOT is minimal but as Figure 4.5 (b) shows, the mono-exponential fit for the experiment at δ = 1.5 ms was poor. The diffusion coefficient value at δ = 4 ms was 4.72 × 10^{-11} m^2s^{-1} and at δ = 1.5 ms there were two values at $D_1 = 4.66 \times 10^{-11}$ m^2s^{-1} (83%) and D_2 = 4.21×10^{-10} m^2s^{-1} (17%). The decrease in δ therefore affects the signal attenuation.

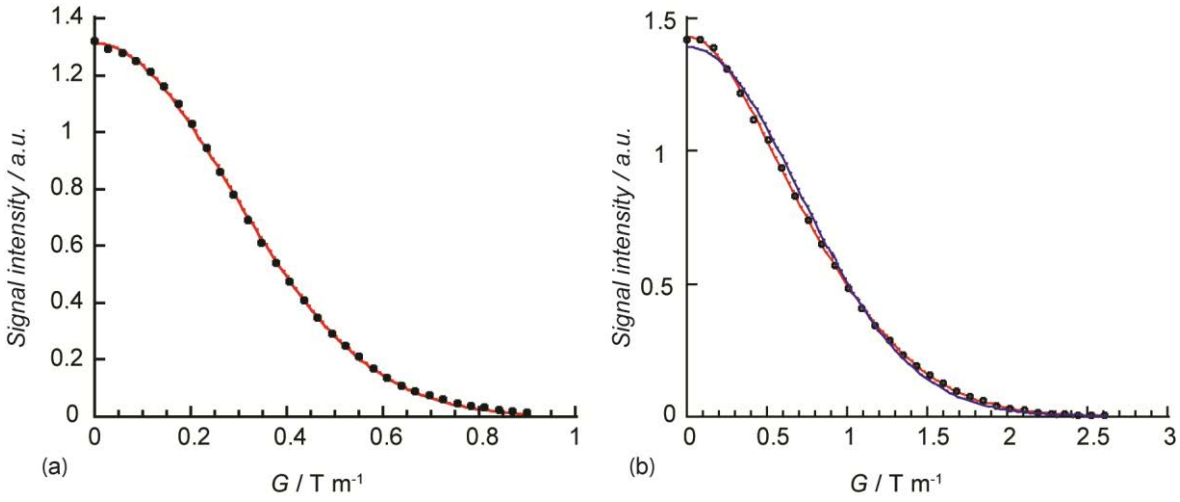

Figure 4.6: *Plots of the signal attenuation for the water molecules in an AOT/water/n-octane microemulsion at ω = 25; ϕ_d =0.15 at δ = 4 ms, with a mono-exponential fit (a) and δ = 1.5 ms (b) showing a mono-exponential (—) and bi-exponential fit (—).*

The diffusion coefficients for the water protons at $\delta = 4$ ms were 5.43×10^{-11} m^2s^{-1} and at $\delta =$ 1.5 ms, again two diffusion coefficients were observed at $D_1 = 5.56 \times 10^{-11}$ m^2s^{-1} (84%) and $D_2 = 2.65 \times 10^{-10}$ m^2s^{-1} (16%) (Figure 4.6).

4.3.3. Variation of Diffusion Coefficients as a Function of Observation Time

In order to further explore exchange processes occurring between the AOT molecules between the RMs and continuous phase, shorter observation times were implemented, using higher gradient strengths. Most of the literature values for the diffusion coefficients for AOT/water/*n*-octane microemulsions were made prior to the development of diffusion probes.[37,38] These probes have since given the capability of accessing higher gradient strengths on spectrometers (up to 9 T m^{-1} (900 G cm^{-1}). The PGSTE experiments produced

artifacts at $\Delta < 20$ ms, with the diffusion coefficient increasing rapidly with the data from the experiments at 10 ms unable to be analysed. This was due to the effect of eddy currents induced by the higher gradient strengths,[39,40] therefore BPSTE experiments were used. Shorter δ were also applied with $\delta = 1.5$ ms compared to $\delta = 4$ ms from previous experiments. At the higher temperature of 298 K, the H_3 AOT peak of interest for $\omega = 5.3$ at varying ϕ_d could not be measured (4.3.1) so the systems at ω =15 and 25 at $\phi_d = 0.05$ and 0.15 were analysed. For all ω values at all ϕ_d, two diffusion coefficients were obtained and consistently observed for the H_3 AOT proton, with D_2 consistently greater than D_1 by 1.5 orders of magnitude. The literature value for the diffusion[41] of the *n*-octane, which constitutes the continuous phase, at 298 K is 2.356×10^{-9} m^2s^{-1}. As the observation time decreased, the diffusion coefficient and (Figure 4.7(a)) the percentage contribution from the AOT monomers increased.

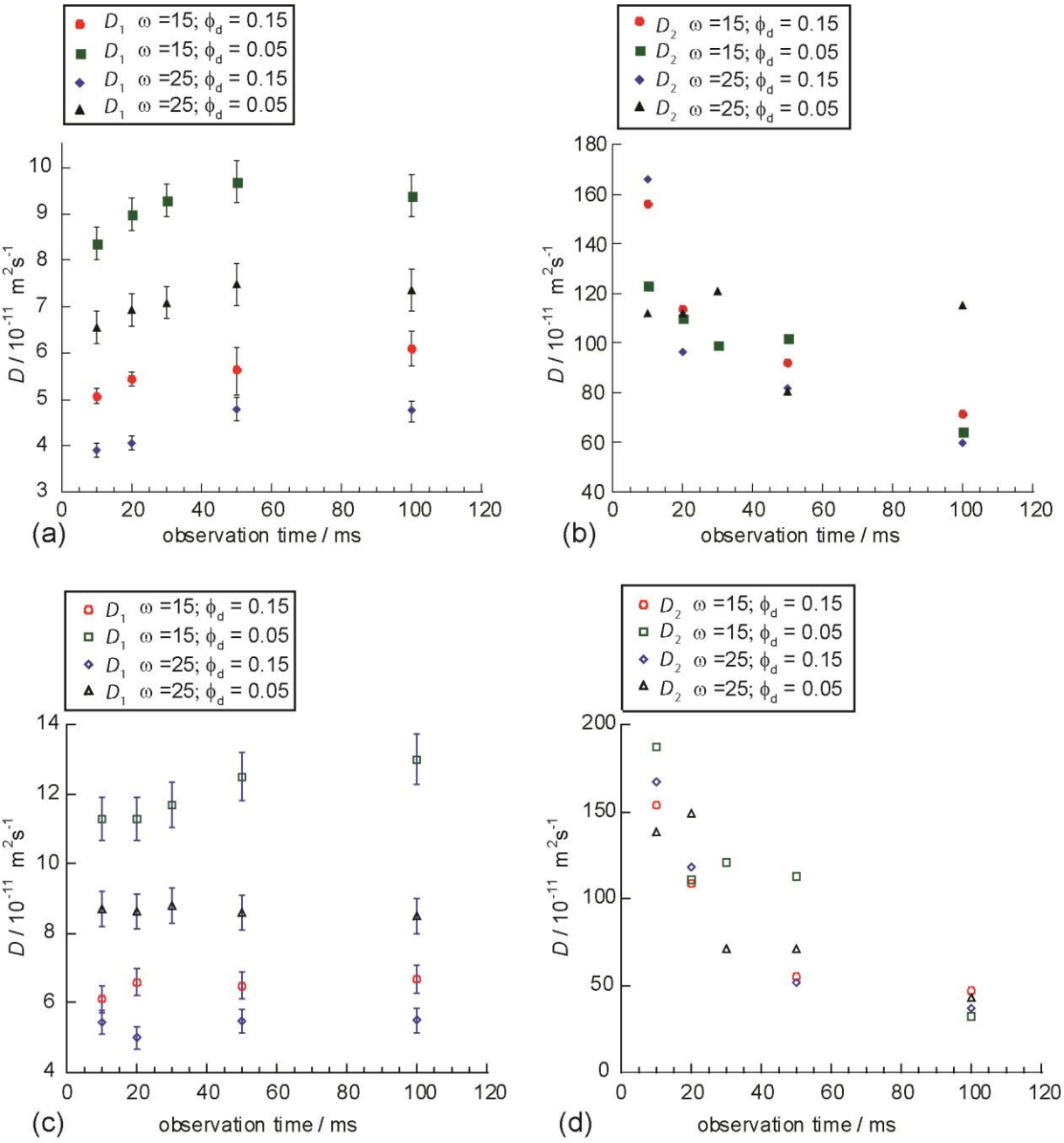

Figure 4.7: *Plots of the diffusion coefficients for the AOT molecule D_1 (a) and D_2 (b) and water D_1 (c) and D_2 (d) for AOT/n-octane/water at varying ϕ_d at ω=15 and 25 at 298 K.*

The D_1 for the AOT molecules in the microemulsion at ω = 15 and 25 at ϕ_d = 0.05 – 0.15 (Figure 4.7 (a)) decreased as the observation time (Δ) decreased with a corresponding increase in D_2. As previously suggested,[37] if the diffusion in microemulsions is unrestricted then the

diffusion coefficient should remain constant with decreasing Δ. Also if the obstruction effect was minimised at shorter observation times for ϕ_d = 0.05 and 0.15, an *increase* and not a decrease in the diffusion coefficient of the RMs was expected. However as the faster diffusion coefficient D_2 is changing with observation time, this is further evidence that the exchange processes between the AOT molecules are being observed. Two T_2 relaxation times have been observed in AOT/*n*-octane/water microemulsions with the AOT monomer T_2 = 0.2 s and AOT in the RM interface being approximately 0.06 s (ω = 20), then also with shorter observation times, an increasing proportion of the faster D_2 for AOT is observed (Table 4.5).

	ω =15; ϕ_d = 0.15		ω =15; ϕ_d = 0.05		ω =25; ϕ_d = 0.15		ω =25; ϕ_d = 0.05	
Δ / *ms*	% D_1	% D_2	% D_1	% D_2	% D_1	% D_2	% D_1	% D_2
100	76	24	64.6	35.4	76	24	65	35
50	70	30	65.7	34.3	73	27	68.3	31.7
20	68	32	59.4	40.6	69.8	30.2	65.8	34.2
10	62	38	60.2	39.8	68.1	31.9	62	38

Table 4.5: *A table showing the % contribution of AOT from the RM and monomer for ω = 15 (a) and ω = 25 (b) at varying Δ and ϕ_d = 0.05 and 0.15.*

Similar trends were observed with the water diffusion coefficients with two values at ω = 15 and 25; ϕ_d = 0.05 – 0.15, with D_1 for the water molecules, as expected being consistently higher than the D_1 for the AOT molecules. As water exchanges on a fast timescale, two diffusion coefficients were unexpected. However, these results show that AOT and water molecules may not just be present in the RMs. The presence and nature of free AOT monomers within the microemulsion has been previously discussed.[42] Exchange processes in microemulsions are reported and described using different models with molecular exchange between surfactant monomers and RMs occurring on a microsecond timescale.[31] However a

recent report has observed molecular exchange occurring on a millisecond timescale in a CTAB quarternary microemulsion.[43] There is the possibility, therefore, that molecular exchange processes are also being observed here on a millisecond timescale. The inter-droplet exchange (solubilisate exchange) occurs on a millisecond timescale, depending on the size and concentration of the droplets.[31] Based on the models of Zana, [9,44] dimers are temporarily formed when droplets collide, increasing in size before splitting into RMs again. As this occurs, free AOT monomers may be released.[9] Therefore an alternative consideration is that as the observation time is decreased, the equilibrium between the formation of RMs and dimers and the release of the AOT monomer through collisions is being observed. At shorter observation times, D_2 is observed in all the systems because the time for the inter-droplet and molecular exchange is further reduced and the obstruction effect is further minimised.[9,20,45]

At a longer observation time, Δ = 400 ms, a mono-exponential fit to the ST relation, was obtained, resulting in an average of the AOT diffusion coefficients for the RMs and the monomer (Table 4.6).

ω	ϕ_d	D / 10^{-11} m^2s^{-1}	R_h / nm
15	0.05	12.00	3.57
15	0.15	7.42	5.80
25	0.15	6.16	6.97

Table 4.6: *Values of diffusion coefficients and R_h for AOT/n-octane/water microemulsion at ω = 15 and 25 at varying ϕ_d at 298 K and Δ = 400 ms.*

The diffusion coefficient values at Δ = 400 ms, (Table 4.6) where mono-exponential fittings to the Stejskal-Tanner equation were observed, should be a weighted average of the AOT D_2

in the RM and D_1 in the continuous phase, as stated by Lindman's Law. When the values and proportions for the system at $\omega = 15$ $\phi_d = 0.15$, were applied to Lindman's Law, the calculated D_{obs} at varying observation times differed and were not comparable to the experimental value at $\Delta = 400$ ms.

Alternative explanations for the bi-exponential behaviour were explored with respect to the type of PFG experiments used, with the possibility of the results being the product of cross relaxation processes, also known as the nuclear Overhauser effect.[32,33,46] The presence of cross-relaxation processes[32] was considered as a potential cause of artificially creating the bi-exponential trends in the AOT and water diffusion data. The nuclear Overhauser effect may arise from through-space interactions[32] between adjacent water and surfactant molecules within the RM interface[32] and has been observed in macromolecular systems when $\Delta > 20$ ms.[46] In the case of these experiments, however, the non-exponential behaviour in the signal decays became more prominent with decreasing Δ, contrary to what is found in the literature.

4.3.4. Variation in temperature in AOT/n-octane/water System

The variation of temperature has an interesting influence on the dynamics of the AOT/water/*n*-octane microemulsions. The diffusion coefficients were therefore obtained and the resulting R_h values were determined at $\omega = 15$ and varying ϕ_d, at the small range of temperatures T = 289 – 298 K. The viscosity of *n*-octane at varying temperatures was determined from plotting $\ln(\eta)$ against $1/T$ (K^{-1}) data obtained from literature sources (Figure 4.8).[47]

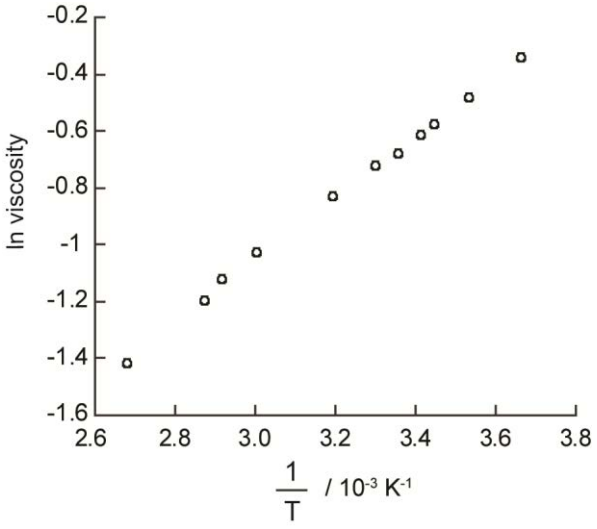

Figure 4.8: *A plot of ln viscosity (η) against the reciprocal of the temperature for n-octane.*

A linear plot was produced, from which the viscosity at a specific temperature could be obtained. In section (4.3.1) bi-exponential decays and bimodal distributions were observed for $\omega = 15$ at the lower droplet fraction, $\phi_d = 0.05$ at 289 K. When increasing the temperature for this system to 298 K, the system transformed to a mono-modal system with an increase in the diffusion coefficient and corresponding decrease in R_h (Table 4.7 and Figure 4.9).

ϕ_d	D / 10^{-11} m^2s^{-1}	R_h / nm
0.15	5.51 ± 0.4	7.79
0.1	7.61 ± 0.6	5.64
0.05	12.4 ± 1.1	3.46

Table 4.7 : *Calculated R_h values for $\omega = 15$ at varying droplet volume fractions at 298 K at* ***G*** *$= 0.9$ T m^{-1}, $\delta = 4$ ms and $\Delta = 100$ ms.*

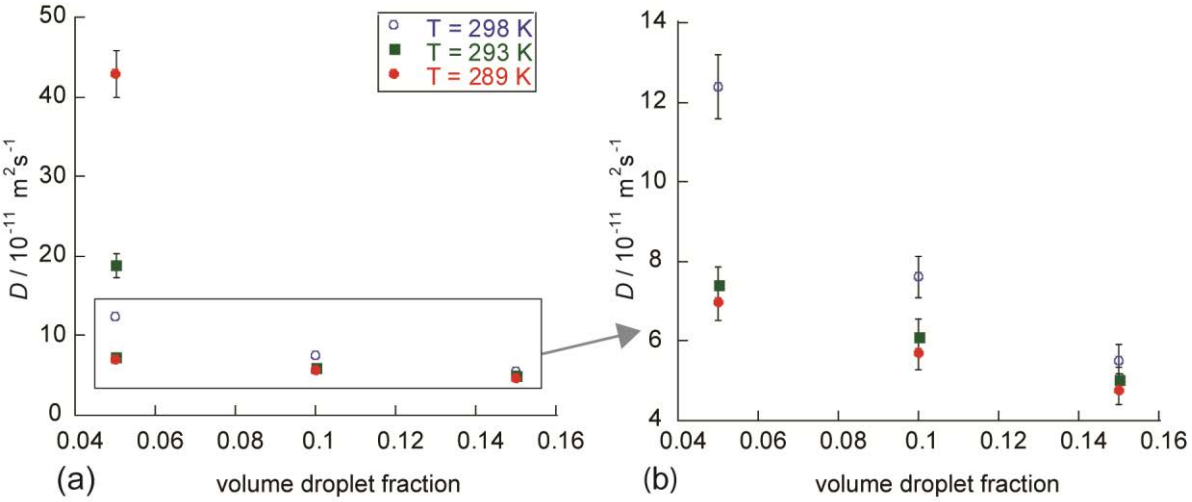

Figure 4.9: *Plots of the diffusion coefficients D_1 and D_2 (a) and D_1 (b) for AOT/n-octane/ water microemulsions at ω = 15 and ϕ_d = 0.05 at varying temperatures.* ***G*** *= 0.9 T m^{-1}, δ = 4 ms, and Δ = 100 ms.*

When extrapolating to infinite dilution at ω = 15 and 298 K, $D_0 = 15 \times 10^{-11}$ m^{2}s^{-1}, the virial coefficient, α = – 4.47 and R_h = 3 nm, compared to α = –2.26 and R_h = 4.6 nm at 289 K (4.3.1).[19] Light scattering measurements (DLS) report ω = 15; R_h = 4.5 nm (Refer to 4.3.1). The value of α is not in agreement with the model literature value of –2, as observed with ω = 5.3 at 289 K (4.3.1). As ϕ_d decreases, the diffusion of the RMs and AOT molecules increases at a greater rate at 298 K than at 289 K. This may be due to there being less surfactant-surfactant interactions,[24] as there is less overlap between the RMs, as previously discussed in section 4.3.1 (pg 128). As ϕ_d decreases, there is a decrease in the attractive interactions between the RMs, with a greater rate of decrease in the frictional coefficient with increasing temperature, hence α becomes increasingly negative.

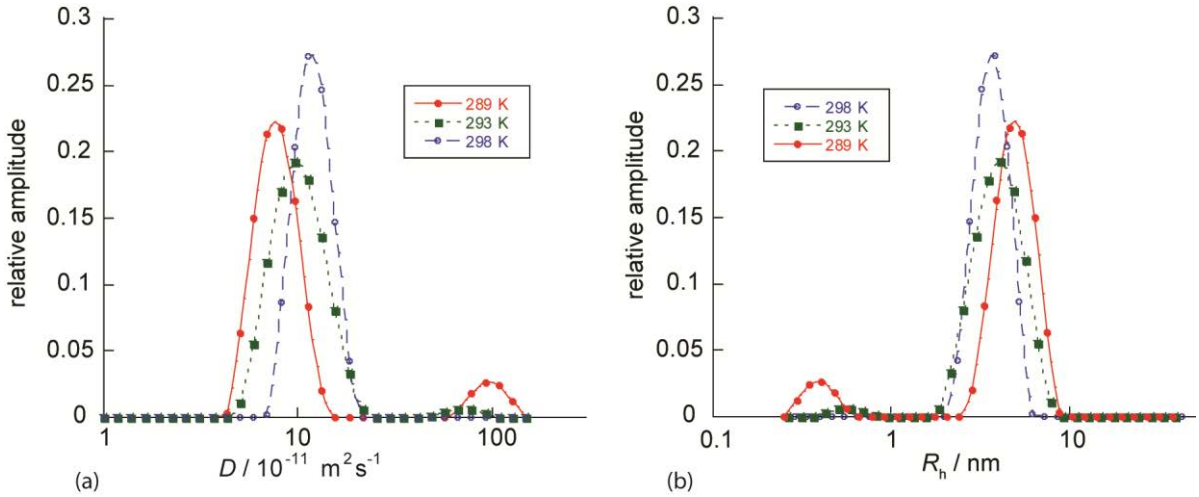

Figure 4.10: *Plots showing the diffusion coefficient distributions (a) and R_h distributions (b) for AOT/n-octane/water microemulsions at ω=15 ϕ_d = 0.05 at different temperatures using the ILT.*

The application of the ILT mirrors what is observed when fitting the diffusion data to the Stejskal-Tanner relation. The plot of diffusion coefficient distributions shows the transition to a single distribution at 298 K (Figure 4.10 (a)). Rather than changes in the structure or composition of the microemulsion as discussed in (4.3.1), these results further support the explanation that the dynamics of the system is changing as the temperature is increased, resulting in an increase in molecular and inter-droplet exchange. The viscosity of the microemulsions changes with temperature and interestingly when measuring R_h and the diffusion coefficient distributions for the ω = 15, ϕ_d = 0.15 AOT/water/*n*-octane microemulsion at T = 289 – 298 K, the R_h values obtained were the same. This is due to the rate of increase in the diffusion coefficient for the microemulsion specifically at the droplet volume fraction, 0.15 is the same as the apparent rate of decrease in the viscosity in the continuous phase at 289 – 298 K (Table 4.8 and Figure 4.11).

ϕ_d	298 K		293 K		289 K	
	$D/10^{-11}$ m^2s^{-1}	R_h / nm	$D/10^{-11}$ m^2s^{-1}	R_h / nm	$D/10^{-11}$ m^2s^{-1}	R_h / nm
0.05	12.4	3.46	7.43	–	7.00	–
0.10	7.71	5.64	6.13	6.45	5.70	7.25
0.15	5.51	7.79	5.03	7.86	4.76	7.89

Table 4.8: *The diffusion coefficients and R_h values for ω = 15 at varying ϕ_d and temperature.*

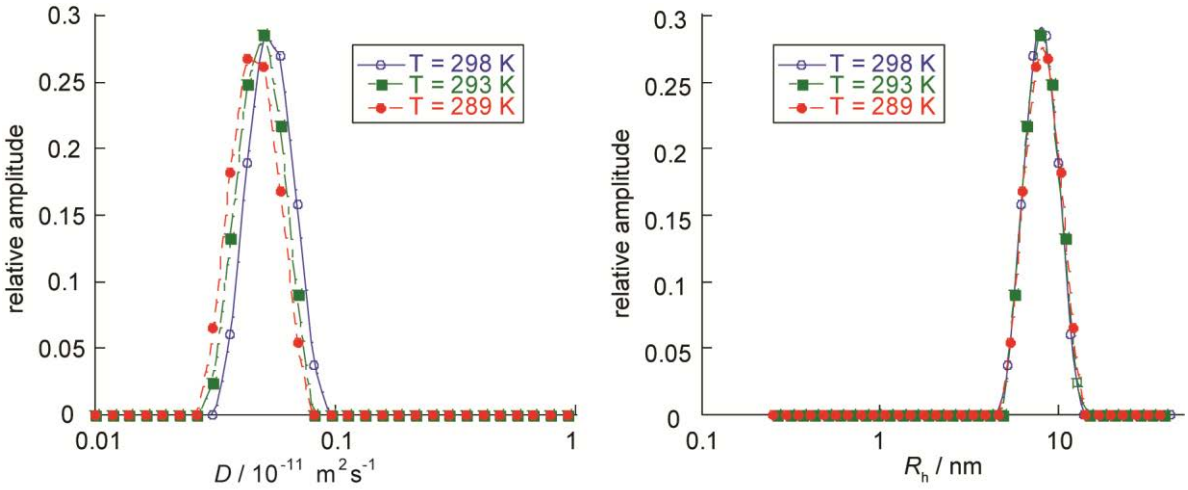

Figure 4.11: *Plots showing the diffusion coefficient distributions (a) and R_h distributions (b) for the system ω = 15; ϕ_d =0.15 at varying temperatures.*

Therefore as the droplet fraction increases to ϕ_d = 0.15, in the system ω = 15, the change in temperature, although the range is limited here, has less impact on the resulting R_h for the RMs than at ϕ_d = 0.05.

For the system at ω = 35 at ϕ_d = 0.05, with larger RMs, the faster diffusion coefficient, D_2 was observed throughout the range of temperatures. The system did not become monomodal at 298 K, which was observed in the system ω = 15; ϕ_d = 0.05. Indeed no significant change

was observed in D_1 and resulting values of R_h from 289 – 298 K (Table 4.9) but there was a significant increase in D_2 with increasing T.

T/ K	D_1 /10^{-11} m^2s^{-1} (ST)	D_2 /10^{-11} m^2s^{-1} (ST)	R_h / nm (ST)
289	4.9	87	7.7
298	5.12	190	8.4

(a)

T/ K	D_1 /10^{-11} m^2s^{-1} (ILT)	D_2 /10^{-11} m^2s^{-1}(ILT)	R_h / nm (ILT)
289	4.83	76	7.8
298	5.23	140	8.2

(b)

Table 4.9: *Tables of diffusion coefficients and R_h values for the AOT H_3 in the AOT/n-octane /water at ω = 35; ϕ_d =0.05 at 289 –298 K. The data was analysed by fitting to the ST relation (a) and applying the ILT (b).*

The proportions of D_2 and D_1 (Table 4.9) suggest that there is an increase in free AOT at the lower temperature of 289 K. However, further experiments are needed to explore variations in temperature at wider ranges of ω and ϕ_d.

From the data presented, it is clear that microemulsions are sensitive to changes in temperature depending on the size and ϕ_d of the microemulsion. As the droplet size increased from ω = 15 to 35, the effects of increasing temperature decreased as two diffusion coefficients were observed at all temperatures at ϕ_d = 0.05, with no significant change in D_1 and resulting R_h at ω = 35. Also the variation in the droplet size decreased as a function of the droplet volume fraction with increasing temperature. Many studies have shown that microemulsions are affected by changes in temperature. Zulauf *et al.*[2] commented that

reversible phase changes in the AOT/water/*n*-octane system were previously observed at T < 293 K in microemulsions where $\omega > 10$.

4.4. Conclusions

This work has shown that molecular exchange in AOT/*n*-octane/water microemulsion is slower than previously believed and has been observed in this work on a millisecond rather than a microsecond timescale. At certain ω, ϕ_d and Δ it is possible to observe two diffusion coefficients for the AOT and water molecules. This indicates therefore that AOT and water may not be present only within the RM, but may be released in the continuous phase through molecular and inter-droplet exchange. The parameters used in PFG experiments are important to consider, as they are sensitive to exchange processes, as observed when decreasing the value of δ. The variation in the droplet volume fraction was observed to have less effect as the droplet size increased. Potential changes in the viscosity of the continuous phase have been found not have a significant effect on the resulting R_h in the AOT/*n*-octane/water system, whereas changes in temperature of the microemulsions, particularly at decreasing values of ω and ϕ_d , affected the dynamics and exchange processes of the systems.

4.5. References

(1) Law, S. J.; Britton, M. M. *Langmuir* **2012**, *28*, 11699.

(2) Zulauf, M.; Eicke, H. F. *J. Phys. Chem.* **1979**, *83*, 480.

(3) Ohtsuki, T.; Okano, K. *J. Chem. Phys.* **1982**, *77*, 1443.

(4) Finsy, R. *Part. Part. Syst. Char.* **1990**, *7*, 74.

(5) Chen, S. H. *Annu. Rev. Phys. Chem.* **1986**, *37*, 351.

(6) Pal, N.; Verma, S. D.; Singh, M. K.; Sen, S. *Anal. Chem.* **2011**, *83*, 7736.

(7) Baruah, B.; Roden, J. M.; Sedgwick, M.; Correa, N. M.; Crans, D. C.; Levinger, N. E. *J. Am. Chem. Soc.* **2006**, *128*, 12758.

(8) Fedotov, V. D.; Zuev, Y. F.; Archipov, V. P.; Idiyatullin, Z. S.; Garti, N. *Colloids Surf., A* **1997**, *128*, 39.

(9) Fletcher, P. D. I., Howe, A.M. Perrin N.M. Robinson B.H. Toprakcioglu C. Dore J.C In *Surfactants in Solution.* Edited by Mittal and Lindman; Plenum Press: 1984; Vol. 3, p 1745.

(10) Caboi, F.; Capuzzi, G.; Baglioni, P.; Monduzzi, M. *J. Phys. Chem. B* **1997**, *101*, 10205.

(11) Soderman, O. Olsson, U. *Encyclopedia Magn. Reson.* **2007**.

(12) Lekkerkerker, H. N. W.; Coulon, P.; Vanderhaegen, R.; Deblieck, R. *J. Chem. Phys.* **1984**, *80*, 3427.

(13) Monduzzi, M.; Olsson, U.; Soderman, O. *Langmuir* **1993**, *9*, 2914.

(14) Bohidar, H. B.; Behboudnia, M. *Colloids Surf., A* **2001**, *178*, 313.

(15) Nazario, L. M. M.; Hatton, T. A.; Crespo, J. P. S. G. *Langmuir* **1996**, *12*, 6326.

(16) TOPSPIN1.3, Bruker.

(17) Weast, R. C.; Astle, M. J.; Beyer, W. H.; Chemical Rubber, C. *CRC handbook of chemistry and physics*; 69th / editor-in-chief Robert C. Weast; associate editors Melvin J. Astle, William H. Beyer. ed.; CRC Press: Boca Raton, Fla., 1988.

(18) Charlton, I. D.; Doherty, A. P. *J. Phys. Chem. B* **2000**, *104*, 8061.

(19) Vasquez, V. R.; Williams, B. C.; Graeve, O. A. *J. Phys. Chem. B* **2011**, *115*, 2979.

(20) Jain, T. K.; Cassin, G.; Badiali, J. P.; Pileni, M. P. *Langmuir* **1996**, *12*, 2408.

(21) Ruckenstein, E. In *Surfactants in Solution.* Edited by Mittal and Lindman; Plenum Press: 1984, p 1551.

(22) Lemaire, B.; Bothorel, P.; Roux, D. *J. Phys. Chem.* **1983**, *87*, 1023.

(23) Brunetti, S.; Roux, D.; Bellocq, A. M.; Fourche, G.; Bothorel, P. *J. Phys. Chem.* **1983**, *87*, 1028.

(24) Huang, J. S.; Safran, S. A.; Kim, M. W.; Grest, G. S.; Kotlarchyk, M.; Quirke, N. *Phys. Rev. Lett.* **1984**, *53*, 592.

(25) Levinger, N. E. *Science* **2002**, *298*, 1722.

(26) Lindman, B.; Stilbs, P.; Moseley, M. E. *J. Colloid Interface Sci.* **1981**, *83*, 569.

(27) Hou, M. J.; Shah, D. O. *Langmuir* **1987**, *3*, 1086.

(28) Mudzhikova, G. V.; Brodskaya, E. N. *Colloid J.* **2006**, *68*, 729.

(29) Safran, S. A. *J. Chem. Phys.* **1983**, *78*, 2073.

(30) Guettari, M.; Ben Naceur, I.; Kassab, G.; Ponton, A.; Tajouri, T. *Appl. Rheol.* **2013**, *23*, 228.

(31) Fletcher, P. D. I.; Howe, A. M.; Robinson, B. H. *J. Chem. Soc., Faraday Trans.* **1987**, *83*, 985.

(32) Price, W. S. *NMR studies of translational motion*; Cambridge University Press: Cambridge, 2009.

(33) Dvinskikh, S. V.; Furo, I. *J. Magn. Reson.* **2000**, *146*, 283.

(34) Avram, L.; Cohen, Y. *J. Am. Chem. Soc.* **2005**, *127*, 5714.

(35) Price, W. S. *Concept Magnetic Res* **1997**, *9*, 299.

(36) Malmborg, C.; Topgaard, D.; Soderman, O. *J. Magn. Reson.* **2004**, *169*, 85.

(37) Clarkson, M. T.; Beaglehole, D.; Callaghan, P. T. *Phys. Rev. Lett.* **1985**, *54*, 1722.

(38) Callaghan, P. T.; Soderman, O. *J. Phys. Chem.* **1983**, *87*, 1737.

(39) Johnson, C. S. *Prog. Nucl. Magn. Reson. Spectrosc.* **1999**, *34*, 203.

(40) Claridge, T. D. W. *High-resolution NMR techniques in organic chemistry*; 1st ed.; Pergamon: Amsterdam ; New York, 1999.

(41) Tofts, P. S.; Lloyd, D.; Clark, C. A.; Barker, G. J.; Parker, G. J. M.; McConville, P.; Baldock, C.; Pope, J. M. *Magn. Reson. Med.* **2000**, *43*, 368.

(42) Nicholson, J. D.; Clarke. J. H. R. In *Surfactants in Solution.* Edited by Mittal and Lindman; Plenum: 1984; Vol. 3, p 1663.

(43) Mills, A. J.; Wilkie, J.; Britton, M.M. *J. Phys. Chem. B* **2014**, *118*, 10767.

(44) McPhee, J. T.; Scott, E.; Levinger, N. E.; Van Orden, A. *J. Phys. Chem. B* **2011**, *115*, 9585.

(45) Phillies, G. D. J. *J. Colloid Interface Sci.* **1982**, *86*, 226.

(46) Chen, A.; Shapiro, M. *J. Am. Chem. Soc.* **1999**, *121*, 5338.

(47) Haynes, W. M.; Lide, D. R. *Handbook of chemistry and physics [electronic resource] : editor-in-chief W. M. Haynes*; 92nd ed.; CRC Press: Cleveland, Ohio, 2011.

5. The Characterisation of a Quarternary Microemulsion Using NMR Measurements of Diffusion

5.1. Introduction

Previous chapters have mainly explored how PFG experiments are used to probe the characteristics of the ternary microemulsion AOT/water/*n*-octane. The focus here is the investigation of the quarternary microemulsion, AOT/water/iso-octane/pentanol. In various applications of microemulsions, including nanoparticle synthesis,[1-3] reactants and different chemical species are added to the systems, which can alter the characteristics, sizes and the pH of RMs. The quarternary AOT microemulsions, which include alcohols are of specific interest in drug targeting and delivery[4] because the variation in the type and concentration of the alcohol gives a varying degree of control on the solubility and hence the appropriate routes for drug administration.[5] Conductivity measurements[6,7] have been previously used to characterise quarternary microemulsions, by observing the changes in percolation with varying alcohols at different concentrations. Zhang *et al*.[7] reported changes in droplet sizes with the addition of alcohols, using small angle x-ray scattering and rationalised this variation by considering the changes in packing parameters, interfacial flexibility and attractive interactions. However, contrary to this, DLS measurements have previously shown that there are no significant changes to the sizes of RMs with the addition of alcohols as co-surfactant.[8] Therefore, it was important to initially characterise the AOT/water/iso-octane/pentanol system, using PFG experiments and methods which have been previously developed.[9] This was to understand the location and the relative proportions of the pentanol within the system, as alcohol molecules may be located in the micelle interface as a co-surfactant or in the organic continuous phase. Studies have shown that the position of molecules in the RMs

depends on not only the size and shape of a molecule, but also on the size of the RM.[10] Recent studies of a CTAB quarternary microemulsion have shown that different exchange processes of the alcohol co-surfactant exist within the RM interphase.[9] The exchange processes determine the proportions of co-surfactant in the interphase, which affects the viscosity of the continuous phase.[9] If the changes in the viscosity are not accounted for this can lead to an underestimation of R_h. The correct proportions of the alcohol present in the interphase are calculated from using Lindmans Law[9,11] (eq 5.1)

$$D_{obs} = PD_{mic} + (1-P)D_{free} \qquad \text{eq 5.1}$$

where, D_{obs} is the average diffusion coefficient which is observed, D_{mic} is the diffusion coefficient of the molecules in the RM and D_{bulk} is the diffusion coefficient of the molecules in the continuous phase. The initial characterisation of the AOT/water/pentanol/iso-octane microemulsion, using PFG experiments, gave an understanding of how the alcohol molecules changed the size, behaviour and dynamics of the RMs.

As well as characterising the AOT/water/iso-octane/pentanol system, the capability of the pentanol molecules as reporter molecules to monitor the pH and chemistry within the micellar water core was explored. This was achieved by observing NMR spectra at varying pH and ϕ_d to monitor the coalescence of the water and pentanol hydroxyl peaks and analysing the diffusion coefficients as a function of pH to observe any variation in the behaviour of system. Investigating the effect of varying the pH in the aqueous phase of the microemulsion has proved challenging,[12] as the water droplet environment does not follow the familiar pH conventions.[13] This is due to the RMs having nano-scale dimensions and the water pool not behaving as bulk water. Traditional methods of measuring pH using a pH meter are therefore

not appropriate. Variations in the pH within RM, particularly when exploring enzymatic reactions, can lead to the misinterpretation of results,[14] hence more understanding is needed of how changes in pH affect RMs.[13] Previously, NMR techniques have measured the variation in the RM proton relaxation times to successfully monitor chemical exchange in the CTAB/hexanol/water microemulsion at varying pH values, using hexanol, which resides in the RM interface as the co-surfactant, as well as acting as the continuous phase.[15] At microemulsion parameters of $\omega < 10$, $\phi_d = 0.45$, as the pH decreases, there is an increase in the number of fast exchanging protons with the alcohol molecules. The increase in fast exchanging protons produces changes in the position of peaks in the NMR spectrum of the microemulsion, as the alcohol hydroxyl proton and water peaks coalesce, giving the potential to monitor changes in pH. More recently, the changes in 2D HSQC spectra of the ^{1}H and ^{15}N resonances from proteins encapsulated within the micellar pool have been observed and used to monitor changes in pH of RMs.[16] The location of molecules in microemulsions depends on a number of factors, including the molecular size, shape and solubility of the surfactant and co-surfactant, as well as the microemulsion parameters, ω and ϕ_d. Pulsed field gradient (PFG) experiments were used to measure the diffusion coefficients of the molecules to understand the behaviour of the pentanol and the effect on the AOT/water/iso-octane microemulsion at varying ω and ϕ_d.

5.2. Experimental

5.2.1. Preparation of AOT/water/iso-octane/pentanol Microemulsions at varying pH

A 1 M stock solution of AOT (sodium bis(2-ethylhexyl) sulfosuccinate; Fluka ≥ 96%) in iso-octane was prepared by adding 11.12 g of AOT to 15.5 ml of iso-octane (2,2,4-trimethylpentane (Sigma Aldrich ≥ 99%). The microemulsions were made by adding the appropriate amounts of water (Nanopure filtered, 18 MΩ) to 1 ml of stock solution to obtain ω values of 5.3 – 25. The appropriate amounts of pentanol (Sigma Aldrich ≥ 99%) were added to obtain $\chi = 0.75$, where χ = [AOT] / [pentanol]. These solutions were diluted to ϕ_d = 0.45, 0.25 and 0.15 by adding the correct amounts of iso-octane. For a microemulsion of ω = 5.3, $\chi = 0.75$ and $\phi_d = 0.45$, 0.145 ml pentanol, 0.0954 ml water and 0.138 ml iso-octane were added to 1 ml of stock 1 M AOT in iso-octane. To obtain a solution at $\phi_d = 0.25$, 1.24 ml extra iso-octane was added. See APPENDIX II for details of microemulsions at other ω values. The solution was mixed for at least 30 seconds until it became transparent, indicating the formation of the microemulsion. The pH of the water was adjusted by adding 0.1 M NaOH (Fluka ≥ 97%) and 0.05 M H_2SO_4 (Fischer ≥ 98%). The pH was measured with a combination glass electrode (Radleys) connected to a digital pH-meter (Orion 720A). The system was calibrated, using buffer solutions at pH 4 and 7 (Sigma Aldrich).

5.2.2. Pulsed Field Gradient Stimulated Echo (PGSTE) Experiments

PGSTE experiments were performed as described in 3.2.5. Parameter ranges used in these experiments were typically: δ = 3 – 4 ms, Δ = 80 - 100 ms, with a maximum gradient, $\boldsymbol{G}_{max}$, 0.9 T m^{-1} with 32 gradient steps, ensuring the signal attenuated so that S($\boldsymbol{G}$)/S(0) at $\boldsymbol{G}_{max}$ was

≤ 0.01. The samples were left to equilibrate at the required temperature for a minimum of 20 minutes. The diffusion data was collected for the proton resonances, including the headgroup H_3 proton of the surfactant and the pentanol α proton, H_e next to the hydroxy group. These protons were expected to reside near or in the interface of the RM, being close to hydrophilic moieties. The numbering scheme for the proton signals in the NMR spectra for the AOT/iso-octane/water/pentanol microemulsion is shown in Figure 5.1.

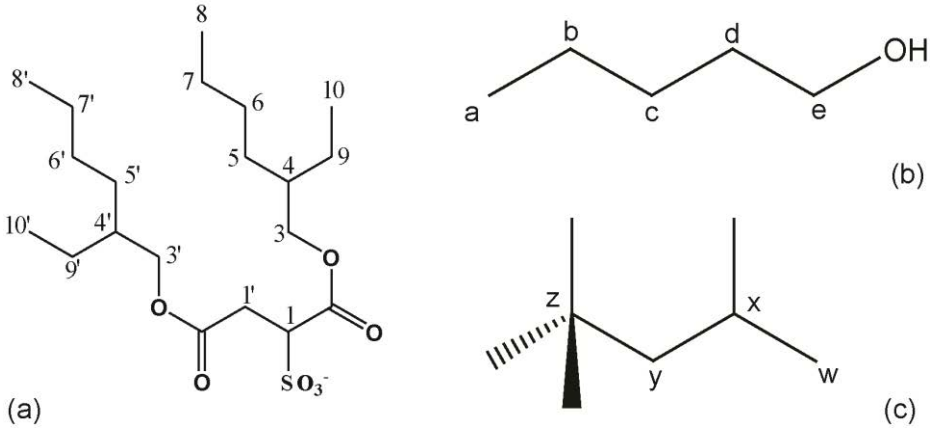

Figure 5.1: *The numbering scheme for the protons in AOT (a), pentanol (b) and iso-octane (c).*

5.2.3. Viscosity

The viscosity of pentanol/iso-octane mixtures at varying molarities (0 – 1.8 M) was measured using a Cannon-Fenske routine viscometer (size 25), which measures kinematic viscosities over the range 0.5 – 2 cSt. The viscometer and solutions were immersed in a water-bath maintained at 293 ± 0.5 K and were initially allowed to equilibrate for at least 40 minutes. The density of the solutions was measured, which allowed the conversion from kinematic to dynamic viscosity (4.2.3 eq 4.2). Measurements were repeated five times and averaged.

5.3. Results and Discussion

5.3.1. NMR Spectra for the AOT/iso-octane/water/pentanol Microemulsions

The ^{1}H NMR spectrum for the AOT/iso-octane/water/pentanol microemulsion is shown in Figure 5.2 with the corresponding peak assignments shown in Table 5.1. The AOT/iso-octane/water/pentanol microemulsion has been characterised using values previously obtained from NMR spectroscopy.[10,17] The water peak (δ = 4.4 ppm) shifts as a function of ω as explained in (3.3.1) but the spectrum also changes as a function of pH, and is dependent on the microemulsion parameters ω and ϕ_d. The changes in ^{1}H NMR spectra due to changing pH have been reported previously in CTAB ternary and quarternary microemulsions.[15] At lower pH values with increasing acidity within the system, coalescence of the pentanol hydroxyl (4.50 ppm) and water peaks (4.37 ppm) occurs, resulting in a coalesced single peak.

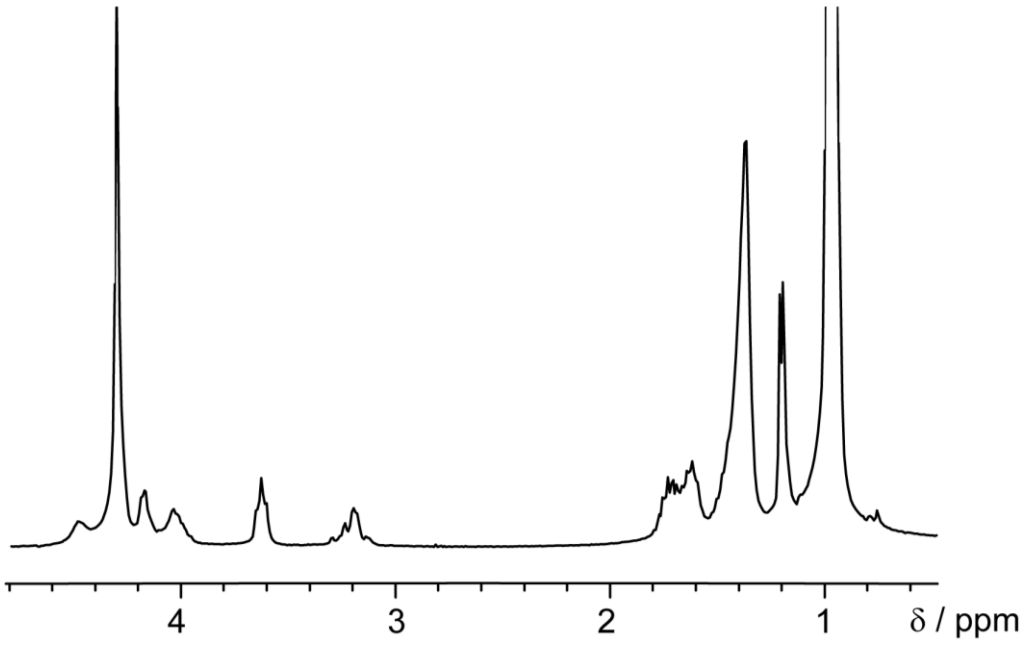

Figure 5.2: *^{1}H NMR spectrum for AOT/iso-octane/water/pentanol at ω = 5.3, ϕ_d = 0.45, χ = 0.75.*

peak assignments	δ / ppm
H_8, H_8', H_{10}, H_{10}', H_a, H_w,H_z	1.00
H_y	1.21
H_5, H_5', H_6, H_6', H_7, H_7', H_9, H_9',	1.34
H_b, H_c	1.44
H_d	1.62
H_4 H_4'	1.66
H_x	1.74
H_1'	3.20
H_e	3.63
H_3'	4.05
H_3	4.20
H_1	4.37
H_2O	4.37
$OH_{(pentanol)}$	4.50

Table 5.1: *^{1}H NMR peak assignments for the ^{1}H NMR spectrum for the AOT/iso-octane/water /pentanol microemulsion shown in Figure 5.2.*

5.3.2. Diffusion Measurements of AOT/iso-octane/water With and Without Pentanol

The values for D_{AOT} in the AOT/iso-octane/water microemulsion were comparable with those in the AOT/*n*-octane/water microemulsion at ϕ_d = 0.15 (Table 5.2 and reported in (3.3.3)). These measurements were taken to clarify there were no significant differences in D_{AOT} and hence the calculated sizes of the RMs in using branched or straight chained forms of octane as the oil. Comparisons of results between the systems with the two forms of octane could then be made.

ω	$D_{AOT}/10^{-11}$ m^2s^{-1} (iso-octane)	$D_{AOT}/10^{-11}$ m^2s^{-1} (*n*-octane)
5.3	6.1	5.9
15	5.2	5.0

Table 5.2: *A table showing the diffusion coefficients for AOT H_3 protons in AOT/water/iso-octane and AOT/water/n-octane systems.*

The diffusion coefficients of D_{AOT} and D_{water} (Table 5.3) in the AOT/iso-octane/water/ pentanol microemulsion decreased as a function of ω, at $\phi_d = 0.15$, which was also observed in the AOT/iso-octane/water system. At $\omega > 25$, AOT/iso-octane/water/pentanol microemulsions remained opaque, indicating that the solutions had not formed a water-in-oil microemulsion.

ω	$D_{AOT}/10^{-10}$ m^2s^{-1}	$D_{water}/10^{-10}$ m^2s^{-1}	$D_{1pent}/10^{-10}$ m^2s^{-1}	$D_{2\ pent}/10^{-10}$ m^2s^{-1}
5.3	1.2	1.7	1.1	5.6 (88%)
9.3	1.05	1.5	1.05	7.2 (81%)
15	0.80	1.1	0.7	6.6 (87%)
20	0.69	0.92	0.5	7.0 (81%)

Table 5.3: *A table showing the diffusion coefficients for AOT, water and pentanol in the AOT/water/pentanol/iso-octane microemulsion at varying ω at $\phi_d = 0.15$, T = 293 K at Δ = 80 ms and δ = 4 ms.*

The values for D_{AOT} in the system with pentanol were greater compared to those with the same ω in the AOT/iso-octane/water system without pentanol (Table 5.3). At $\omega = 5.3$, a 100% increase in the diffusion coefficient was observed from $D_{AOT} = 6 \times 10^{-11}$ m^2s^{-1} without pentanol to 1.2×10^{-10} m^2s^{-1} with pentanol. At $\omega = 15$, a 60% increase was observed from

$D_{AOT} = 5 \times 10^{-11}$ m^2 s^{-1} to 8×10^{-11} m^2 s^{-1} in microemulsions with pentanol. The D_{water} was consistently higher than D_{AOT}, which is a trend also observed in comparable systems without pentanol and as the ω increased, the difference between the D_{AOT} and D_{water} values decreased (Table 5.3). The RMs are diffusing at a faster rate due to the presence of the pentanol altering the dynamics of the system. One consideration is that the droplet volume fraction for this system is calculated by assuming all the pentanol is present in the RM interface. A proportion of the pentanol molecules in the continuous phase would have the effect of decreasing ϕ_d and increasing the diffusion coefficient D_{AOT}, with a relative decrease in the obstruction effect. On recalculating the droplet fraction accounting for the correct proportion of pentanol residing in the interface, the droplet volume fraction changed from 0.15 to approximately 0.12 (Table 5.4).

ω	*Adjusted* ϕ_d
5.3	0.11
9.3	0.125
15	0.126
20	0.130

Table 5.4*: A table showing the adjusted* ϕ_d *at varying* ω*, calculated from the proportion of pentanol present in the continuous phase.*

The changes in the droplet volume fractions are unlikely to account for the increase in the diffusion coefficient D_{AOT} in the systems with pentanol, which is up to 100% in ω = 5.3, as there is a 35% increase in D_{AOT} for in the systems without pentanol when diluting from ϕ_d = 0.15 to 0.1 for ω = 5.3 (See 4.3.1). It is important to consider the exchange processes,[9] which are occurring between the pentanol molecules located in the continuous and dispersed

phases to fully appreciate the proportion of pentanol which is in the continuous phase and therefore the changes in the viscosity of the system. This can be determined from the diffusion data of the pentanol molecules (Figure 5.3).

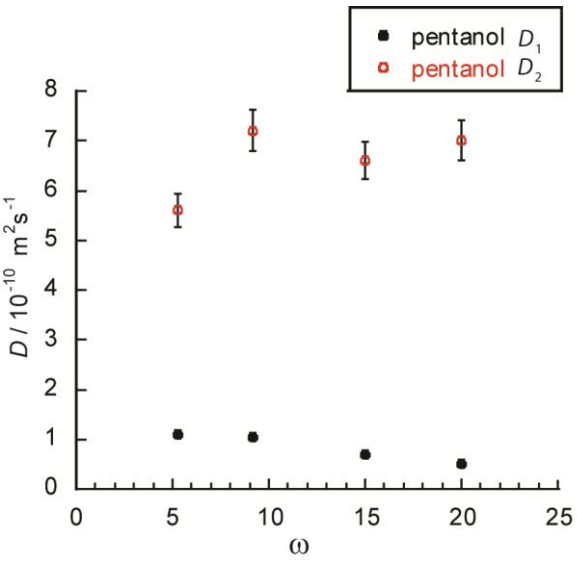

Figure 5.3: *Plot of the diffusion coefficients of the pentanol molecules in AOT/iso-octane/water/ pentanol systems as a function of ω at ϕ_d = 0.15, analysed fitting to the Stejskal-Tanner equation.*

In the AOT/iso-octane/water/pentanol microemulsion, two diffusion coefficients were consistently observed for the pentanol molecules with the faster diffusing pentanol (D_2), observed in greater proportions > 80%, than the slower diffusing pentanol molecules (D_1) at each ω value (Table 5.3). The slower diffusion coefficient D_1 of pentanol is compatible with the values of D_{AOT} and decreased as a function of ω, which also correlated with D_{AOT} (Table 5.3). This is regarded as the proportion of pentanol acting as a co-surfactant, which is situated in the RM interface. One study exploring the partition equilibria between RMs and alcohols at ω = 30 using PFG experiments observed one $D_{pentanol}$. However these PFG measurements were taken at longer observational times,[18] Δ = 140 ms than applied here at Δ = 80 ms.

When comparing the values of the fast pentanol diffusion coefficient D_2 with the diffusion coefficient measured for mixtures of pentanol/iso-octane at 0 - 1.1 M (Figure 5.4), which would be the diffusion coefficient of the continuous phase, the values differ significantly. The concentration of the pentanol in the continuous phase was 0.32 M in the system at ω = 5.3. The diffusion coefficient for the equivalent molarity of the pentanol/iso-octane mixture (Figure 5.4(a)) was determined as 12.5×10^{-10} m^2 s^{-1}. This value is significantly higher than experimental value obtained for the pentanol molecules in the continuous phase (D_2), which was 5.6×10^{-10} m^2 s^{-1}. The differences in the diffusion coefficients may be partly due to the obstruction effect, as discussed in (4.1), as the RMs occupy space within the system, causing the pentanol self-diffusion coefficient to decrease due to excluded volume.[18]

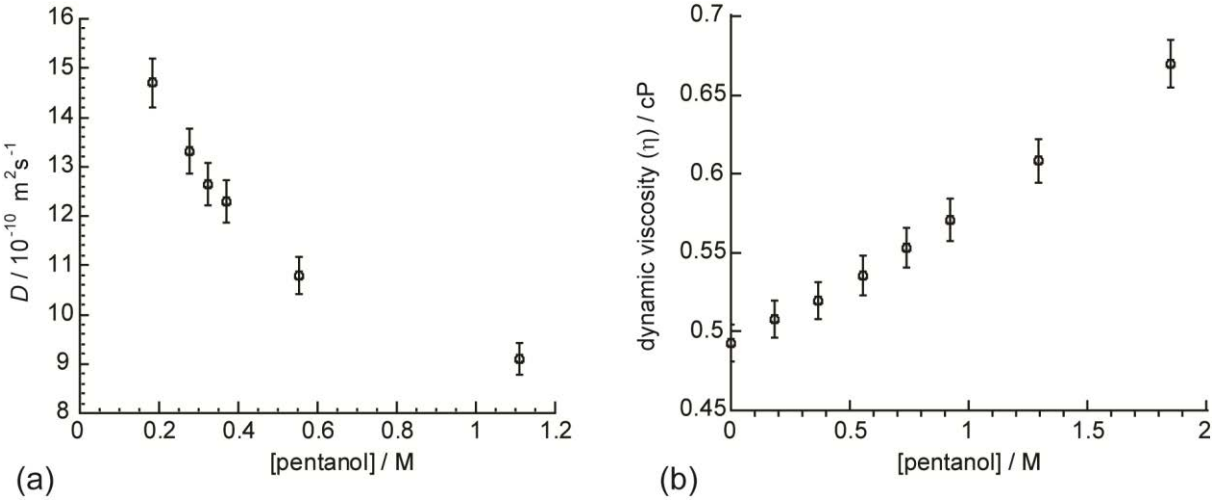

Figure 5.4: *A plot showing the self-diffusion coefficient of the pentanol molecules (a) and dynamic viscosity of pentanol/iso-octane mixtures (b) at varying molarities at 293 K.*

However, as reported recently,[9] the higher value, D_2, for the bulk pentanol present in the continuous phase is an average value of the pentanol molecules in fast exchange between the

interphase and the continuous phase. Lindman's relation (eq 5.1) can be used to calculate[9] the proportions of co-surfactant present in the interphase and continuous phase knowing the diffusion coefficients of the pentanol molecules, including D_{obs}, which is the average diffusion coefficient (D_2) and D_{mic} from the molecules in the RM and D_{bulk}, which is determined from (Figure 5.4(a)). The viscosity of the continuous phase was then obtained from the dynamic viscosity measurements of pentanol/iso-octane mixtures measured at 293 K (Figure 5.4(b)), resulting in a more accurate size determination for the RMs.

The proportions of pentanol in the continuous phase decreased after analysing the exchange of the pentanol molecules. This resulted in a decrease in the viscosities for each of the systems (Table 5.5).

ω	*% pentanol in CP*	*[pentanol]/M*	η /cP	R_h / nm
5.3	34.41	0.1303	0.499	3.58
9.3	40.34	0.1353	0.500	4.08
15	40.11	0.1175	0.497	5.59
20	37.91	0.1001	0.496	6.27

Table 5.5: *A table showing the R_h values for the RMs in the AOT/water/pentanol/iso-octane microemulsion at varying ω at ϕ_d = 0.15, determining the viscosity with consideration to the percentage of pentanol in the continuous phase.*

The R_h values of the RMs with pentanol were calculated and compared with the sizes of RM without pentanol (Figure 5.5).

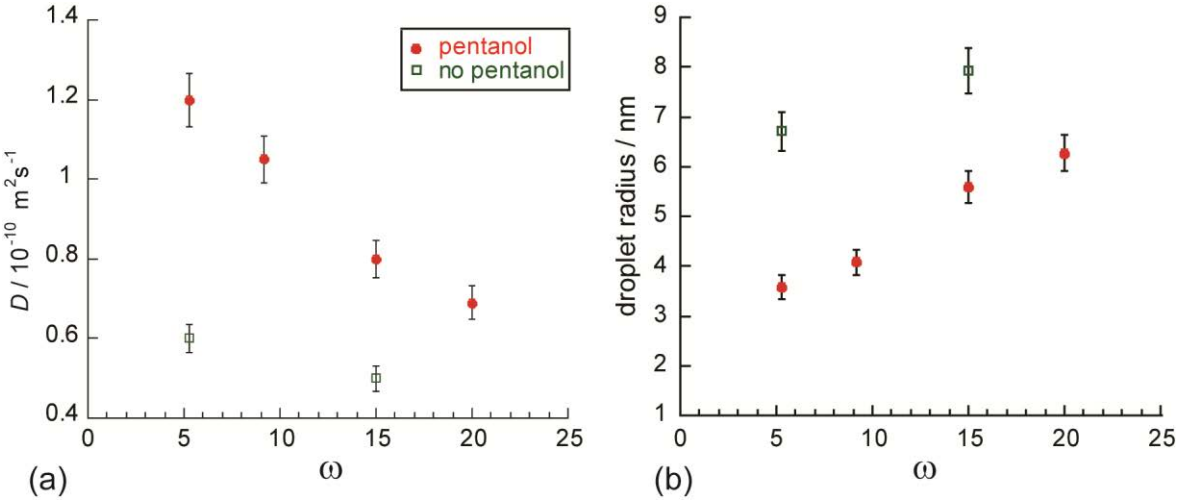

Figure 5.5: *Plots of the diffusion coefficients D_{AOT} (a) and R_h (b) of the RMs in AOT/iso-octane/water and AOT/iso-octane/water/pentanol microemulsions at varying ω at ϕ_d = 0.15.*

The resulting R_h values at varying ω at ϕ_d = 0.15 with pentanol were smaller than the RMs in microemulsions at varying ω and ϕ_d = 0.15 without pentanol (Table 5.5, Figure 5.5). At ω = 5.3, in the systems without pentanol R_h = 6.71 nm and 3.58 nm with pentanol, a 46.6% decrease, whereas at ω = 15, R_h = 7.93 nm and 5.59 nm, constituting a 29.5% decrease.

Alcohols are regularly used as a co-surfactant in microemulsion systems.[19,20] This is due to the hydroxyl group being attracted towards the micellar water droplet, as well as the potential to be soluble in the organic phase. The degree to which the alcohol penetrates the micellar interface is dependent on the alcohol chain length[18] and it has been found that where short chain alcohols, ethanol and methanol tend to reside within the micellar pool,[21] alcohols with longer chains are located in the interface and the continuous phase.[22] In the AOT/iso-octane/water microemulsion, the pentanol molecules have the potential to act as a co-surfactant and are partitioned between the RMs and the continuous phase,[18,23] as the small

molar volume of pentanol allows it to be part of the interface. This affects the curvature and hence the size of the RMs decreases.[7] The faster diffusion coefficients for AOT in the systems with pentanol compared those without (Figure 5.3(a)), giving evidence that the pentanol is causing the formation of smaller RMs. Previous studies, using small angle x-ray scattering and a DLS study to measure the sizes of RMs in the AOT/iso-octane/water/pentanol system, showed that the addition of alcohols caused changes in droplet sizes,[22] with a decrease in R_h reported with alcohols with chain lengths > butanol.[7,22] The decrease in R_h is due to an increase in the curvature and rigidity of the interface. Zhang *et al.*[7] explained that as the pentanol molecules can solubilize within the AOT surfactant tails, this will push the surfactant headgroups closer together, hence increasing the rigidity of the RMs.[7,24] The addition of co-surfactants changes the packing parameters (S_p) of RMs, which can change the curvature by having to accommodate the increased volume of surfactant headgroups.[25,26] (See 1.1.1) The inclusion of micellar pentanol will increase the total interfacial RM surface area, which causes a decrease in R_h with an increase in the number of droplets.[7]

The PFG diffusion measurements established that the majority of the pentanol resides in the interphase with a smaller proportion of pentanol in the continuous phase, which results in a decrease in the viscosity of the continuous phase. However after determining the change in viscosity due to the exchange processes of pentanol, smaller R_h were obtained in the AOT/pentanol/water/iso-octane RMs, than those without the alcohol at $\phi_d = 0.15$. There is a possibility that RMs develop into different shapes and do not exist as spheres. Zhang *et al.*[7] suggested there may be changes in shape to ellipsoidal RMs in AOT/alcohol /water/alkane systems using SAXS. Any changes in shape may be another factor in explaining why smaller R_h values are obtained with added pentanol. In order to investigate these ideas further and to

observe how the pentanol may affect the RM interface, molecular simulations were set up for single RMs at varying ω with and without pentanol in the continuous phase. The changes in size and shape were monitored and the findings are discussed in Chapter 6. As well as characterising the AOT/pentanol/water/iso-octane system, it was interesting to explore what other information could be obtained about the chemistry within the micellar water core at varying pH.

5.3.3. Investigating the pH of Microemulsions

One development from characterising the AOT/iso-octane/pentanol/water microemulsion was exploring if the pentanol could be used as reporter molecules to monitor the changes in the pH of the water core. The spectra of the AOT/iso-octane/pentanol/water microemulsion at ω = 5.3, ϕ_d = 0.45 were recorded between pH of 1.9 – 3.4. As the pH decreased, the hydroxyl proton and water peaks coalesce, producing a single peak at δ = 4.40 ppm (Figure 5.6). This has been previously observed in the CTAB/hexanol/water microemulsion.[15] It is important to note that the solutions required a longer time to become transparent and form the microemulsion as the acidity increased.

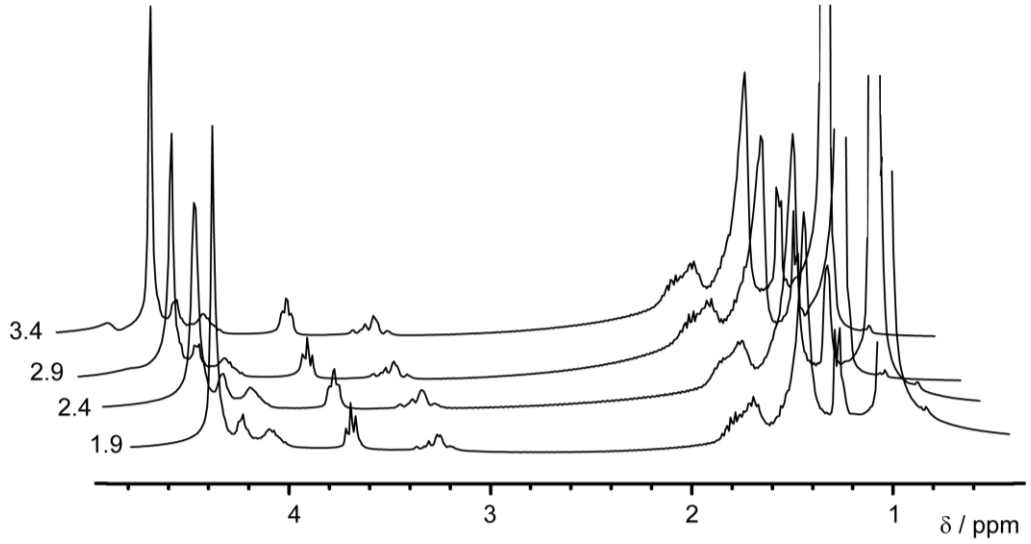

Figure 5.6: *NMR spectra of AOT/pentanol/water/iso-octane at $\omega = 5.3$ $\phi_d = 0.45$, $\chi = 0.75$ at pH 1.9 – 3.4.*

pH	D_{AOT} /10^{-10} m^2s^{-1}	D_{water} /10^{-10} m^2s^{-1}	$D_{1\ pent}$ /10^{-10} m^2s^{-1}	$D_{2\ pent}$ /10^{-10} m^2s^{-1}
1.9	0.37	0.8	0.36	2.4 (74%)
2.4	0.43	0.76	0.32	2.3 (85%)
2.9	0.5	0.75	0.31	2.0 (86%)
3.4	0.47	0.77	0.37	2.1 (81%)

Table 5.6: *A table showing the diffusion coefficients of AOT, water and pentanol in the AOT/water/pentanol/iso-octane microemulsion at varying pH at $\omega = 5.3$, $\phi_d = 0.45$ with the percentage of pentanol diffusing at the faster rate (D_2).*

However, as Table 5.6 shows, the diffusion coefficient for the water, AOT or the pentanol molecules remained the same, within error, as a function of increasing pH. The proportions of the pentanol also remained the same, which would suggest that the viscosity of the system

was also consistent as the pH decreased. Therefore there was no significant change in the size of the RMs as the pH changed. The investigation of a range of AOT/water /pentanol/iso-octane microemulsions at varying ϕ_d and ω at varying pH was carried out, to monitor any similar observations.

5.3.4. Measurements at varying ϕ_d and ω at varying pH

The coalescence of the hydroxyl proton and the water peaks was investigated at ω = 5.3 at a lower droplet fraction of ϕ_d = 0.25 in order to explore changes in the droplet size as a function of pH, with a decreasing obstruction effect. The coalescence point was observed at pH = 2.4, in the system at ϕ_d = 0.45, with the OH and water peaks resolving into 2 separate peaks at pH = 3.4. At ϕ_d = 0.45, the two separate water and hydroxyl peaks at δ = 4.37 ppm and 4.50 ppm were consistently observed as the pH was increased further up to pH = 9.4 (Figure 5.7(a)). This was not observed, however, at lower droplet volume fractions. At ϕ_d = 0.25, (Figure 5.7(b)), a single coalesced water and hydroxyl peak was observed at all pH values, up to pH = 9.4 and the resolution of two peaks from OH and water was not observed. This was also observed at ϕ_d = 0.15.

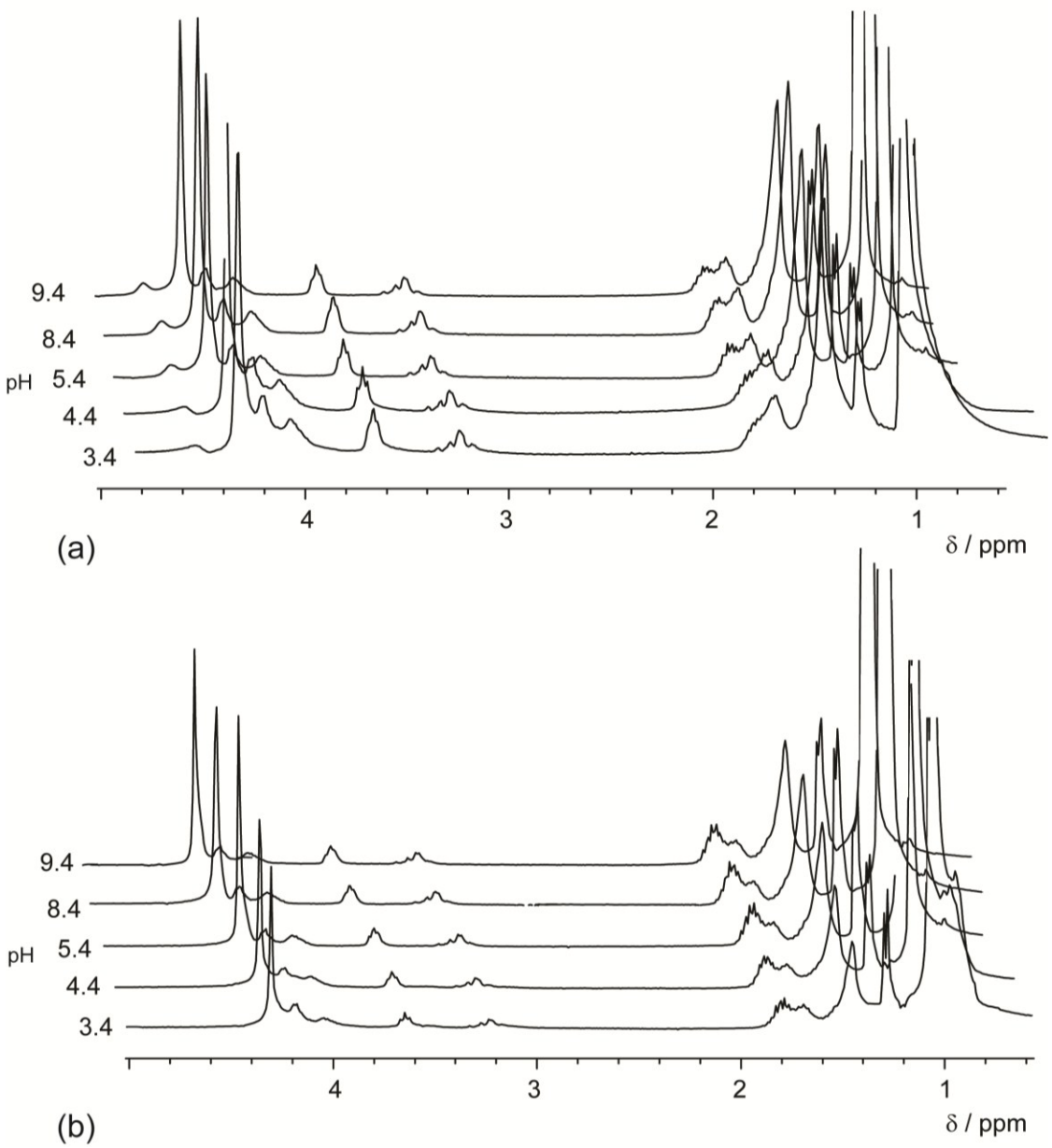

Figure 5.7: *^{1}H NMR spectra of AOT/pentanol/water/iso-octane at ω = 5.3 and χ = 0.75 at ϕ_d = 0.45 (a) and 0.25 (b).*

As there was more iso-octane in the system at ϕ_d = 0.25, there would be less inter-droplet and molecular exchange between the RMs in a more dilute system, with a relatively less number of droplets than at ϕ_d = 0.45. Hence, it was expected that with increasing pH, the two peaks of

the water and hydroxyl of the pentanol would be observed. However from the diffusion coefficient values in Table 5.7, at $\phi_d = 0.25$, the D_{AOT}, $D_{pentanol}$ and D_{water} are higher than at $\phi_d = 0.45$. There is no significant change of D_{AOT} as a function of increasing pH for both $\phi_d = 0.25$ and 0.45 (Table 5.7(a) and (b), respectively).

pH	$D_{AOT}/10^{-10}$ m^2s^{-1}	$D_{water}/10^{-10}$ m^2s^{-1}	$D_{1\ pent}/10^{-10}$ m^2s^{-1}	$D_{2\ pent}/10^{-10}$ m^2s^{-1}
3.4	0.41	0.79	0.37	2.1 (81%)
4.4	0.37	0.62	0.35	2.2 (87%)
5.4	0.31	0.51	0.32	2.0 (91%)
8.4	0.34	0.75	0.30	2.0 (90%)
9.4	0.35	0.60	0.27	1.9 (91%)

(a)

pH	$D_{AOT}/10^{-10}$ m^2s^{-1}	$D_{water}/10^{-10}$ m^2s^{-1}	$D_{1\ pent}/10^{-10}$ m^2s^{-1}	$D_{2\ pent}/10^{-10}$ m^2s^{-1}
3.4	0.93	1.33	0.89	3.9 (88%)
4.4	0.92	1.35	1.07	4.2 (86%)
5.4	0.85	1.38	0.99	3.9 (87%)
8.4	0.80	1.16	0.86	3.8 (89%)
9.4	0.85	1.44	1.13	4.0 (87%)

(b)

Table 5.7: *Tables showing the diffusion coefficients of AOT, water and pentanol in the AOT/water/pentanol/iso-octane microemulsions at $\omega = 5.3$ at $\phi_d = 0.45$ (a) and $\phi_d = 0.25$(b).*

The diffusion coefficient and proportions of pentanol in the continuous phase (D_2) at systems $\phi_d = 0.45$ were similar at all measured pH and this was also observed in the system at $\phi_d = 0.25$. However the faster diffusion coefficient, D_2 for the pentanol in the continuous phase increased in the system where $\phi_d = 0.25$, compared to $\phi_d = 0.45$. The D_1 of the pentanol and

the D_{AOT} were compatible, diffusing at similar rates at all pH values, indicating D_1 corresponded to the diffusion of the interfacial pentanol.

Measurements at ω = 15, ϕ_d = 0.15 were made at varying pH. The diffusion coefficients for AOT, pentanol and water show the expected trends, which were observed at ω = 5.3, with the D_{AOT} comparable with D_1 for the pentanol molecules.

pH	$D_{AOT}/10^{-10}$ m^2s^{-1}	$D_{water}/10^{-10}$ m^2s^{-1}	$D_{1\ pent}/10^{-10}$ m^2s^{-1}	$D_{2\ pent}/10^{-10}m^2s^{-1}$
1.5	0.78	1.08	0.81	6.4 (87%)
1.9	0.79	1.09	0.80	6.2 (88%)
2.4	0.83	1.17	0.77	6.7 (89%)
2.9	0.81	1.17	0.69	6.4 (89%)
3.4	0.78	1.03	0.67	6.3 (89%)
3.9	0.81	1.16	0.66	6.3 (89%)
4.6	0.80	0.97	0.77	6.6 (88%)

Table 5.8: *A table showing the diffusion coefficients of AOT, water and pentanol in the AOT/water/pentanol/iso–octane microemulsion at ω = 15, pH = 1.5 - 4.6 at ϕ_d = 0.15.*

The diffusion coefficients for the system at ω = 15, ϕ_d = 0.15 (Table 5.8) are of a similar magnitude to those at ω = 5.3, ϕ_d = 0.25, except the D_2 pentanol, which is higher than D_2 at ω = 5.3, ϕ_d = 0.25. Hence, with faster diffusion coefficients than those at ω = 5.3, ϕ_d = 0.45, the similar result of a single coalesced hydroxyl and water peaks was obtained. When the ^{1}H NMR spectrum was recorded for a neutral pH sample at ω = 15, ϕ_d = 0.45, the hydroxyl and water peaks were observed separately. It has been found previously that the exchange rate between RMs decreases as a function of ω,[27] therefore a range of higher droplet fractions at

ω = 15 should have been explored to determine at what ϕ_d the water and hydroxyl peaks are observed.

One important consideration why the average single coalesced peak is observed at ϕ_d = 0.25 at all pH values is that the relative proportions of the molecules in the continuous phase change as ϕ_d is varied. The ratio of AOT: pentanol in all systems at varying ϕ_d was kept constant, χ = 0.75, however as the ϕ_d decreased, the concentration of iso-octane increased in the system and the concentration of pentanol decreased. The pentanol is partitioned between the interface and the continuous phase, so as the pentanol concentration decreased in the continuous phase, there would also be a decrease in the quantity of hydrogen bonding taking place between the pentanol molecules. As the hydrogen bonding decreased, there would have been a change in the chemical shift[28] of the hydroxyl proton peak in the ^{1}H NMR spectrum. Oakes[29] previously explained how the hydroxyl proton chemical shift moves downfield with increasing alcohol concentration, due to the changes in hydrogen bonding, in a study of alcohol and water mixtures. The changes in chemical shift will also be relevant in the varying concentrations of water and alcohol within a microemulsion. Therefore the hydroxyl proton peak is not observed as the change in the chemical shift occurs with decreasing ϕ_d , the hydroxyl peak is masked by the water peak, which is further upfield.

Another consideration why the average single coalesced peak is observed at all pH at ϕ_d = 0.25, may be due to the RMs and the continuous phase diffusing at a faster rate compared to ϕ_d = 0.45 (Table 5.7). Therefore with increasing pH although there are decreasing numbers of protons, the exchange between the pentanol hydroxyl group and the water at ϕ_d = 0.25 is at

such an increased rate that the exchange rate overcomes the pH change within the RM. There are limiting values of diffusion coefficients, governed by specific droplet volume fractions and ω, where the exchange between water and pentanol is at a rate, which is sensitive to pH changes within the RMs. Pileni *et al*.[30] observed a decrease in the number of collisions and exchange processes between RMs, with an increase in the number of droplets, using small angle x-ray scattering. Although the RMs at the parameters ϕ_d = 0.45 have increased surface to volume ratio than at lower droplet fractions, the diffusion and exchange rate may decrease such that the pH can be probed using pentanol molecules. The decrease in droplet attractions with ϕ_d for larger RMs, which is known as the depletion model,[31] may also be applicable to the system at ω = 15. Diffusion measurements need to be made at ω = 15, ϕ_d = 0.45 and further investigations at droplet fractions between 0.25 and 0.45 to find the limiting values of ϕ_d , where the resolution of the hydroxyl and water peaks occurs.

5.4. Conclusions

In the microemulsion system AOT/water/iso-octane/pentanol, the diffusion coefficient of AOT RMs was greater than that of the AOT/water/iso-octane microemulsion, without pentanol. At all ω and ϕ_d values studied, the pentanol molecules were observed to be diffusing at two diffusion coefficients. The slower D_1 was from the interfacial pentanol, as the D_{AOT} values were comparable with the slow D_1 values of the pentanol. The faster D_2 was an average of the pentanol exchanging between the interphase and the pentanol located in the continuous phase. The viscosity of the continuous phase decreased when the proportion of pentanol in the continuous phase was accounted for, which resulted in an increase in the sizes

of the RMs. The resulting R_h values were, however, still smaller than the systems without pentanol.

The pH of the AOT/water/iso-octane/pentanol microemulsion may be measured using pentanol as a reporter molecule, but at higher droplet volume fractions. The coalescence of the hydroxyl and water peak was observed as a function of pH in the microemulsion at ω = 5.3 at ϕ_d = 0.45. However at lower droplet volume fractions, the coalesced hydroxyl/water peak was consistently observed with increasing pH. Further measurements are required for the system at ω = 5.3 between 0.45 > ϕ_d > 0.15 to discover the limiting values of ϕ_d and pH, to explore the correlations between the diffusion coefficients of the different molecules in the microemulsion, where the resolution of the water and the hydroxyl peaks occurs. Further diffusion measurements are also required, where the concentration of pentanol is consistent in the continuous phase at varying ϕ_d, to ensure that the chemical shift of the hydroxyl peak is minimal. The diffusion of the molecules within quarternary microemulsions needs to be explored with a variety of alcohols with varying chain lengths. The capabilities of alcohol molecules to monitor changes in pH within RMs will then be fully appreciated.

5.5. References

(1) Capek, I. *Adv. Colloid Interface Sci.* **2004**, *110*, 49.

(2) Chen, M. J.; Yang, W. T.; Yin, M. Z. *Small* **2013**, *9*, 2715.

(3) Eastoe, J.; Hollamby, M. J.; Hudson, L. *Adv. Colloid Interface Sci.* **2006**, *128*, 5.

(4) Nir, I.; Aserin, A.; Libster, D.; Garti, N. *J. Phys. Chem. B* **2010**, *114*, 16723.

(5) Gupta, S. *Curr. Sci. India* **2011**, *101*, 174.

(6) Bisal, S.; Bhattacharya, P. K.; Moulik, S. P. *J. Phys. Chem.* **1990**, *94*, 350.

(7) Zhang, X. G.; Chen, Y. J.; Liu, J. X.; Zhao, C. Z.; Zhang, H. J. *J. Phys. Chem. B* **2012**, *116*, 3723.

(8) Corbeil, E. M.; Riter, R. E.; Levinger, N. E. *J. Phys. Chem. B* **2004**, *108*, 10777.

(9) Mills, A. J.; Wilkie, J.; Britton, M.M. *J. Phys. Chem. B* **2014,** *118*, 10767.

(10) Binks, D. A.; Spencer, N.; Wilkie, J.; Britton, M. M. *J. Phys. Chem. B* **2010**, *114*, 12558.

(11) Nilsson, P. G.; Lindman, B. *J. Phys. Chem.* **1983**, *87*, 4756.

(12) Smith, R. E.; Luisi, P. L. *Helv. Chim. Acta* **1980**, *63*, 2302.

(13) Crans, D. C.; Levinger, N. E. *Acc. Chem. Res.* **2012**, *45*, 1637.

(14) Walde, P.; Mao, Q. C.; Bru, R.; Luisi, P. L.; Kuboi, R. *Pure Appl.Chem.* **1992**, *64*, 1771.

(15) Halliday, N. A.; Peet, A. C.; Britton, M. M. *J. Phys. Chem. B* **2010**, *114*, 13745.

(16) Marques, B. S.; Nucci, N. V.; Dodevski, I.; Wang, K. W. C.; Athanasoula, E. A.; Jorge, C.; Wand, A. J. *J. Phys. Chem. B* **2014**, *118*, 2020.

(17) Demarco, A.; Menegatti, E.; Luisi, P. L. *J Biochem. Bioph. Meth.* **1986**, *12*, 325.

(18) Walderhaug, H.; Johannessen, E. *J. Solution Chem.* **2006**, *35*, 979.

(19) Palazzo, G.; Carbone, L.; Colafemmina, G.; Angelico, R.; Ceglie, A.; Giustini, M. *Phys. Chem. Chem. Phys.* **2004**, *6*, 1423.

(20) Palazzo, G.; Lopez, F.; Giustini, M.; Colafemmina, G.; Ceglie, A. *J. Phys. Chem. B* **2003**, *107*, 1924.

(21) PerezCasas, S.; Castillo, R.; Costas, M. *J. Phys. Chem. B* **1997**, *101*, 7043.

(22) Lin, T. L.; Hu, Y.; Lee, T. T. *Prog. Colloid Polym. Sci.* **1997**, *105*, 268.

(23) Lissi, E. A.; Engel, D. *Langmuir* **1992**, *8*, 452.

(24) Nazario, L. M. M.; Hatton, T. A.; Crespo, J. P. S. G. *Langmuir* **1996**, *12*, 6326.

(25) Mitchell, D. J.; Ninham, B. W. *J. Chem. Soc. Faraday Trans. 2* **1981**, *77*, 601.

(26) Oldfield, C. In *Biotechnology and Genetic Engineering Review* 1994, p 255.

(27) Fletcher, P. D. I.; Howe, A. M.; Robinson, B. H. *J. Chem. Soc. Faraday Trans. 1* **1987**, *83*, 985.

(28) Hore, P. J. *Nuclear magnetic resonance*; Oxford University Press: Oxford, 1995.

(29) Oakes, J. *J. Chem. Soc. Faraday Trans. 2* **1973**, *69*, 1311.

(30) Jain, T. K.; Cassin, G.; Badiali, J. P.; Pileni, M. P. *Langmuir* **1996**, *12*, 2408.

(31) Cassin, G.; Badiali, J. P.; Pileni, M. P. *J. Phys. Chem.* **1995**, *99*, 12941.

6. Molecular Simulations of Reverse Micelles

6.1. Introduction

Molecular simulations have the capability of probing and visualising how molecules interact with each other in microemulsions. Therefore molecular simulations give the opportunity to observe fluctuations and changes in the shapes of reverse micelles (RMs) and analyse the dynamics and behaviour of the molecules within these self-assembling systems. This is particularly important with modelling RMs as it can determine any potential deviations from a spherical shape, which is the assumed shape when evaluating the sizes of RMs, using the Stokes-Einstein equation. If the shape is known, however, modified forms of the Stokes-Einstein relation can be used by incorporating shape factors to determine more accurately the dimensions of the macromolecular structures.[1] Molecular simulations were set up to study the motion, dynamics and behaviour of the molecules within AOT/iso-octane/water, AOT/iso-octane/water/pentanol and CTAB/hexanol/water single RMs. Models of AOT/iso-octane /water RMs have been investigated before,[2-5] however the effect of adding pentanol to this microemulsion system has, to the best of our knowledge, not been reported in the literature. The solvent boxes of iso-octane and hexanol used to solvate the RMs were set up using all-atom parameter forcefields. The use of organic all-atom solvent boxes has been previously used to construct AOT/water/iso-octane RMs[6] at $\omega < 7$ and recently in RM molecular simulations with the quarternary CTAB/water/pentanol/hexane system.[7] The united-atom solvent boxes have been used more frequently to minimise the computer time and resources.[8] However the all-atom solvent boxes provide more accurate molecular simulations. The molecular interactions between the continuous phase and the RMs can be observed, especially

in the CTAB/hexanol/water RM, where the hexanol has a dual role of co-surfactant and solvent.

In the AOT/iso-octane/water/pentanol system, a proportion of pentanol resides in the interface.[9-11] It has been reported that the pentanol affects the flexibility and rigidity of the interface causing a change in the packing parameter which results in a change of the shape and size of the RMs.[9,11] The PFG diffusion measurements of the AOT/iso-octane/water/ pentanol system (5.3.2) showed a significant increase in diffusion coefficients of the AOT molecules (D_{AOT}) compared to D_{AOT} in the system without pentanol. It was also observed that as ω increased the difference between D_{AOT} in the system with or without pentanol decreased. The proportions of pentanol in the interface and the resulting effect on the RM size and shape were explored through the molecular simulations.

NMR measurements of diffusion were also used to evaluate the size of CTAB/hexanol/water RMs. It has proven a challenge to probe the size of the RMs in this particular system, as unlike RMs formed from AOT, it has not been possible to characterise the CTAB/hexanol /water RMs using scattering methods.[12,13] The R_h was determined as 1 nm, (3.3.4) which was small compared to the extended length of the CTAB molecule of $\approx$ 2.8 nm.[14] In exploring the sizes of the CTAB/hexanol/water RMs using PFG experiments, it was not possible to know if the shape deviated from a spherical model, making it inappropriate to use the Stokes-Einstein equation to calculate R_h. A recent molecular simulation study of a CTAB/hexane/water /pentanol RM, illustrated that an oblate, rather than spherical RM was formed. These molecular simulations also gave the opportunity to quantify the aggregation number,

including the number of co-surfactant pentanol molecules.[7] Therefore in this study, the CTAB/hexanol /water droplet molecular simulation was set up, which has not been previously reported, to observe shape fluctuations and to estimate the proportions of hexanol, which are partitioned between the interface and the continuous phase.

In the molecular simulations, as single droplets are modelled, it is not possible to include inter-droplet interactions, therefore the effects of these encounters cannot be accounted for. The time and duration of the simulations can be challenging, as shorter simulations may not provide the full picture of the RM in equilibrium.[3,8] However, molecular simulations provide a valuable insight into the interactions between molecules within a reverse micellar environment and changes in the surfactant interface, the RM shapes and aggregation numbers at varying microemulsion parameters.

6.2. Experimental

6.2.1. Molecular Mechanics

Molecular simulations for the AOT/iso-octane/water, AOT/iso-octane/water/pentanol and CTAB/hexanol/water droplets were set up, with methods which have been used previously.[15] This involves the application of the combined ff03[16] and gaff[17] forcefields in AMBER (v12)[18] using a Silicon Graphics interface. The droplets were minimised for a varied number of cycles depending on the size of the droplet, until AMBER had reported the energy gradients had reached appropriate levels of RMS < 2 kcal mol^{-1} $Å^{-1}$ (8.36 kJ $mol^{-1}Å^{-1}$)and $\boldsymbol{G}_{max} < 1\times10^{2}$ kcal mol^{-1} $Å^{-1}$ (418 kJ $mol^{-1}Å^{-1}$). The energy gradient terms, G_{max}, and RMS (root mean

square of the first derivative of a potential energy term) are values of force that exist between the molecules in a simulation. During the minimisation process, as the molecules move into most favourable positions and orientations, the G_{max} and RMS values decrease and stabilise, signifying that the forces and therefore the interactions between the molecules have reached the most favourable and minimal energy possible. The droplets were minimised to the lowest optimized energies in preparation for equilibration dynamic runs of up to 30 ns. Periodic boundaries were applied with an EWALD cut-off at 12 Å, which is the distance where the interactions between the charges were no longer calculated. All the simulations were run at 300 K.

6.2.2. The Preparation of Solvent Boxes

Methods to make solvent boxes for organic solvents have been previously developed.[19] A hexanol solvent box was constructed by initially arranging an array of 4913 hexanol molecules in a cubic box of 100 Å, which resulted in a density of 0.8136 g cm^{-3}. The ordered hexanol box was initially minimised for 100000 cycles at constant volume. The minimized hexanol box was equilibrated for 1000 ps at constant volume, to ensure the positions of the molecules were randomised. The resulting box boundaries were set at 100 Å with the box being saved as an *off* file using the AMBER command *saveoff*. An iso-octane solvent box of 100 Å, containing 3648 molecules, was prepared by modifying the existing hexanol solvent box. The iso-octane box was minimised until the energy gradients were at the optimal values of RMS = 3.45×10^{-2} kcal mol^{-1} $Å^{-1}$ (0.14421 kJ $mol^{-1}Å^{-1}$) and G_{max} = 2.61 kcal mol^{-1} $Å^{-1}$ (10.91 kJ $mol^{-1}Å^{-1}$).

6.2.3. The Preparation of the Droplets

The AOT/iso-octane/water reverse micelle (RM) simulations were initially set up as a control to compare with RMs with added pentanol. The water droplet was formed by solvating a single water molecule using the AMBER LEAP program.[15] This was achieved from *solvateshell* command with the R_w of the droplets being 1.4 nm, 2 nm and 3 nm. The water droplet was surrounded with AOT surfactant molecules, which were distributed and orientated randomly using a purpose-built code, written by Dr. J. Wilkie,[20] which was built specifically for the formation of RMs so that the surfactant headgroups face towards the micellar water and the surfactant tails face away. An initial AOT molecule was placed at a distance, *r,* from the surface of the water droplet, with the other AOT molecules being placed at the same radial distance from the water droplet surface but at random spherical polar coordinates, at varying polar (θ) and azimuthal (φ) angles, thus creating a spherical shell of AOT molecules surrounding the water molecules.[15] New molecules are retained and added to the surfactant layer provided that the random positioning does not result in atoms falling within 1.5 Å of any other atom already added to the surfactant layer. Molecules with atoms within 1.5 Å of other atoms in the surfactant layer are discarded and another random position is chosen. The addition of molecules to the surfactant layer terminates when the number of consecutive fails is more than twice the number of molecules already added to the surfactant layer. The ω was calculated from the resulting numbers of surfactant and water molecules (Table 6.1) and were approximately the same as the range of values which were explored experimentally with the model values at ω = 7.1, 12.8, 23.6 and experimental ω values = 5.3, 15, 25. The precise reproduction of ω values proved challenging. The droplet was solvated with the iso-octane solvent box as prepared in (6.2.2), using the *loadoff* command. Sodium counter-ions were added to ensure the overall charge on the droplet was neutral. The

droplet was then minimised alleviating bad interactions between the molecules. This initial minimisation was continued at constant pressure until the density of the droplet stabilised (Table 6.2). This ensured that any gaps present between the layers of molecules on initial construction of the droplet would be eliminated and the minimisation at constant volume could proceed without voids appearing in the droplets. Three droplets were constructed at varying ω values and were repeated two times, using a random number generator to give different velocities to all of the atoms at the start of the simulations.

ω	7.1	12.8	23.6
H_2O	353	1060	3658
AOT	50	83	155
octane	1676	3458	5645
total	2079	4601	9458

Table 6.1: *A table of the number of molecules in the AOT/water/iso-octane RMs at varying ω*

ω	minimisation time / ps	no. of steps	density t_{start}	density t_{final}
7	500	250000	0.4743	0.7347
13	500	250000	0.5133	0.7193
24	945	242400	0.5389	0.7204

Table 6.2: *A table of minimisation times and resulting densities for AOT/iso-octane/water droplets at varying ω values*

AOT/iso-octane/water/pentanol RMs were prepared using the same methods and procedures as of the AOT/iso-octane/water RMs,[15,18] with the number of molecules in each RM shown in Table 6.3. After adding the surfactant layer, a layer of pentanol molecules was added, using the same procedure. The droplet was then solvated with the iso-octane solvent box (6.2.2).

The initial minimisations were at constant pressure until the density of the droplets stabilised (Table 6.3). A total of three droplets were constructed at varying ω values and repeated twice.

ω	7.4	11.8	23.3
H_2O	369	1086	3642
AOT	50	92	156
octane	2813	5348	8009
pentanol	480	670	1023
total	3712	7196	12830

Table 6.3: *A table showing the number of molecules in the AOT/pentanol/water/iso-octane RMs*

CTAB/hexanol/water RMs were constructed using the same method as the AOT/water/iso-octane RMs. However, after surrounding the water droplet with a layer of CTAB surfactant, a layer of hexanol was added prior to solvating with a hexanol solvent box (Table 6.4). After the minimisation at constant pressure the resulting droplet density stabilised at 0.8025 g cm^{-3}.

ω	7.2
H_2O	1980
CTAB	279
hexanol	4697
total	6956

Table 6.4: *A table showing the number of molecules in the CTAB/hexanol/water RM at ω = 7.2*

The time taken to carry out the simulations was dependent on the number of molecules and therefore the size of the droplet. Smaller droplets such as AOT/water/iso-octane at ω = 7, required 2 days to simulate 1ns, whereas 2 days were needed to simulate 0.5 ns for the larger

RMs, AOT/pentanol/water/iso-octane at ω = 24. The longest computational times were for ctab/hexanol/water droplets, where less than 0.5 ns of simulation time was obtained in 2 days.

6.2.4. Analysis

The program Visual Molecular Dynamics (VMD)[21] and InsightII[22] were used to visualise and to obtain the moments of inertia of the RMs. The values of the semi-axes, *a*,*b* and *c* could then be evaluated, using eq 6.1, where I_1, I_2 and I_3 are the moments of inertia and *M* is the mass of the RM.[5]

$$I_1 = \frac{1}{5}M\left(a^2 + b^2\right)$$

$$I_2 = \frac{1}{5}M\left(a^2 + c^2\right) \qquad \text{eq 6.1}$$

$$I_3 = \frac{1}{5}M\left(b^2 + c^2\right)$$

The eccentricity was then calculated using eq 6.2, to determine if the RMs were e = 0 for perfectly spherical RMs, or tending towards e = 1 for prolate or oblate ellipsoidal RMs or cylindrical RMs.[5]

$$e = \sqrt{1 - \frac{c^2}{a^2}} \qquad \text{eq 6.2}$$

The computer program InsightII[22] was used to determine the number and types of molecules present in the area around surfactant and the water molecules at distances of 3, 5 and 7 Å. This provided an estimation of the number of interfacial hexanol molecules of the CTAB/water/ hexanol RM. It also enabled the position and numbers of pentanol molecules to be determined in the micellar interface in the AOT/water/iso-octane/pentanol RMs.

6.3. Results and Discussion

6.3.1. AOT/iso-octane/water Droplets

The AOT/iso-octane/water RMs (Figure 6.1) shows AOT (yellow) as a space-filled CPK representation and water (blue) as a space-filled van der Waals representation. At t = 28 ns and ω = 7.1, 12.8 and 23.6, the semi-axes a = 26.1, 32.5 and 43.6 Å and the semi-axes c = 18.4, 25.9 and 39.2 Å with the eccentricities of e = 0.7, 0.6 and 0.4 respectively, indicating the RMs were ellipsoidal.

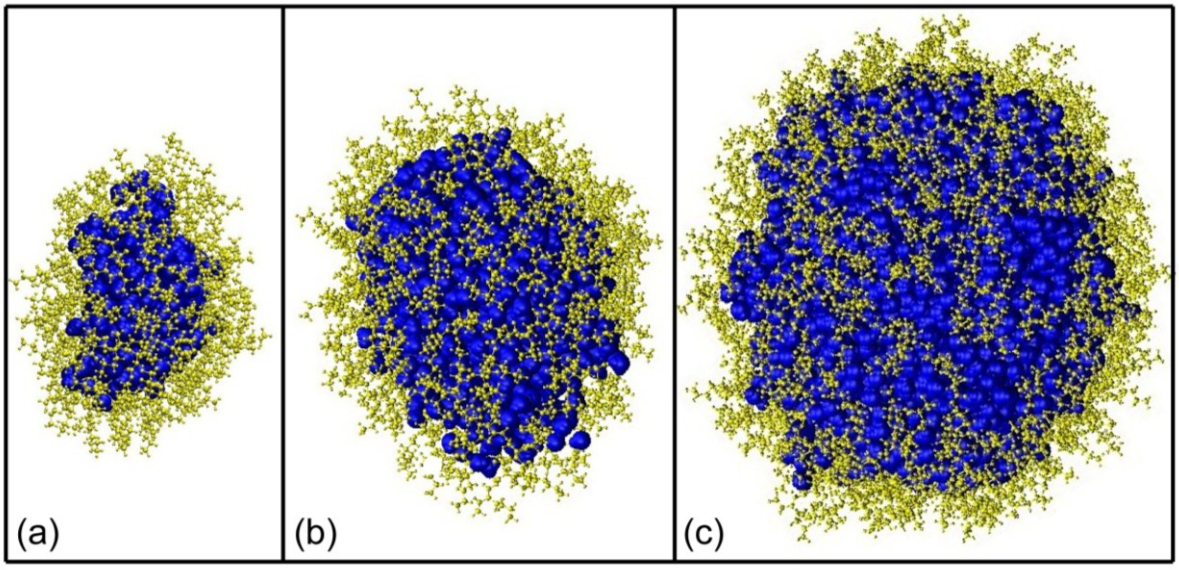

Figure 6.1: *Images of the AOT/iso-octane/water RMs at ω = 7.1 (a), 12.8 (b), and 23.6 (c) showing the AOT (yellow) and water (blue) molecules with at t = 28 ns.*

semi-axis / Å	$\omega = 7.1$	$\omega = 12.8$	$\omega = 23.6$
a	25.1 ± 1.2	32.2 ± 1.1	44.2 ± 1.0
b	22.2 ± 0.7	29.1 ± 0.8	41.6 ± 0.7
c	19.8 ± 0.9	26.8 ± 0.7	39.1 ± 0.9
eccentricity	0.6 ± 0.08	0.55 ± 0.07	0.46 ± 0.06

Table 6.5: *A table showing the mean average lengths of the semi-axes and the eccentricities for the AOT/iso-octane/water RM at varying ω.*

The average length of the semi-axes and the standard deviations for the RMs at ω = 7.1, 12.8 and 23.6 are shown in Table 6.5. The R_h of AOT/iso-octane/water RMs from PFG experiments at ω = 5.3 were 2.6 nm at infinite dilution (4.3.1), which is comparable with the values determined in the molecular simulations at ω = 7.1 (Table 6.5). The plots showing the variation in the lengths of the semi-axes and the eccentricities for ω = 7.1, 12.8 and = 23.6 are shown in Figure 6.2.

The plot of the length of the semi-axes as a function of time for the droplet at ω = 7.1 (Figure 6.2 (a)) showed larger fluctuations with semi-axes *a* and *c* than semi-axis *b*. The fluctuations also correlated with each other (Figure 6.2(a)) indicating that the RM is oscillating between an oblate and more spherical shape. This is reflected in the eccentricity (Figure 6.2(b)), reaching a maximum of 0.8 at t = 5.5 ns, forming an oblate shape and a minimum of 0.36 at t = 18 ns, tending towards a spherical shape. The molecular simulation, however, needs to be equilibrated for a significantly longer duration to determine if the fluctuations in the eccentricity are cyclic.

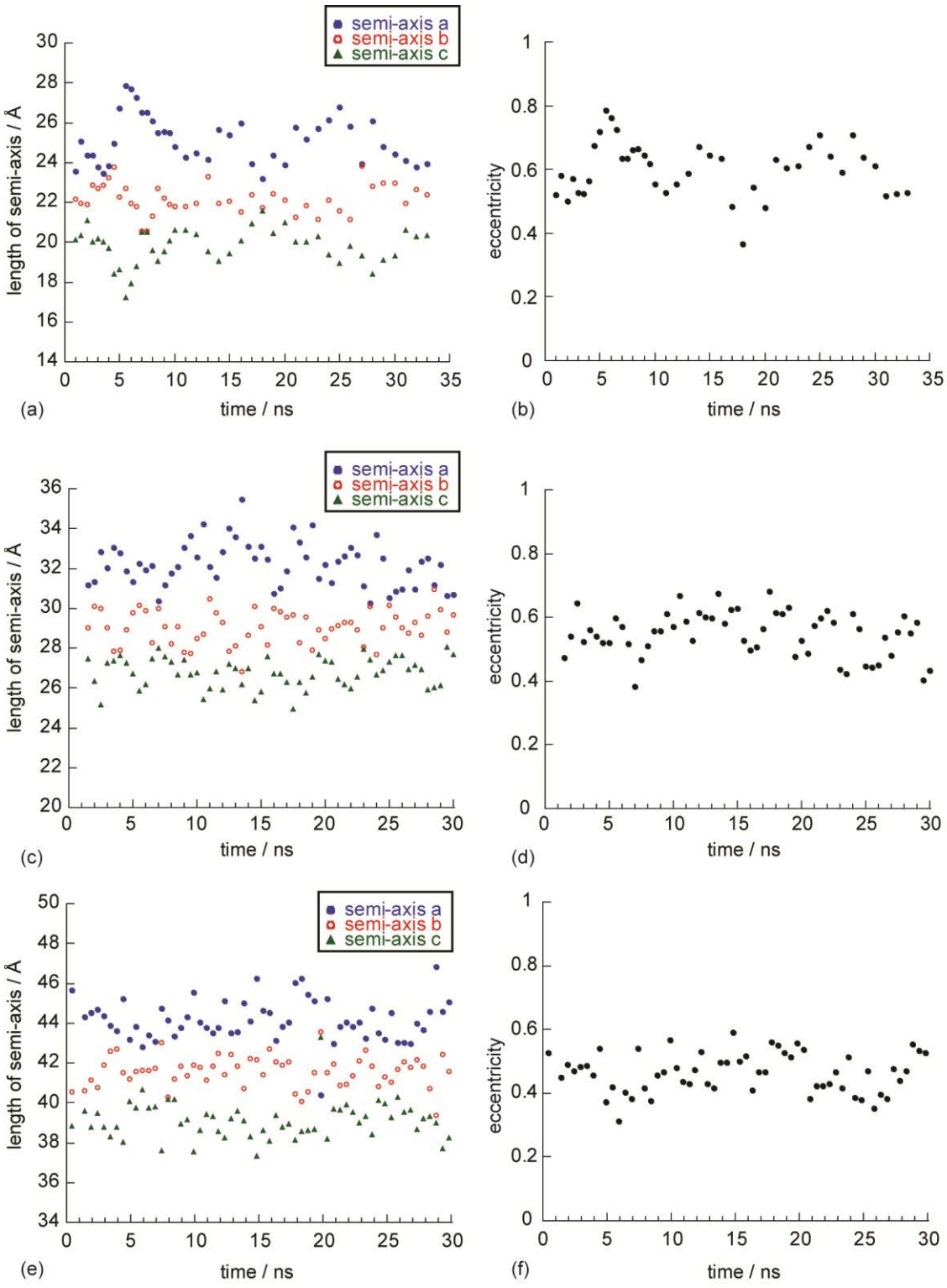

Figure 6.2: *Plots showing the lengths of the semi-axes and the eccentricities obtained from the molecular simulations of the AOT/iso-octane/water RM at ω =7.1 (a) and (b), ω = 12.8 (c) and (d) and ω = 23.6 (e) and (f).*

There were greater shape fluctuations observed at ω = 7.1 than at ω = 12.8 and 23.6 as observed from (Figure 6.2 (c – f)) with the eccentricity decreasing and becoming more spherical with as a function of ω (Figure 6.3).

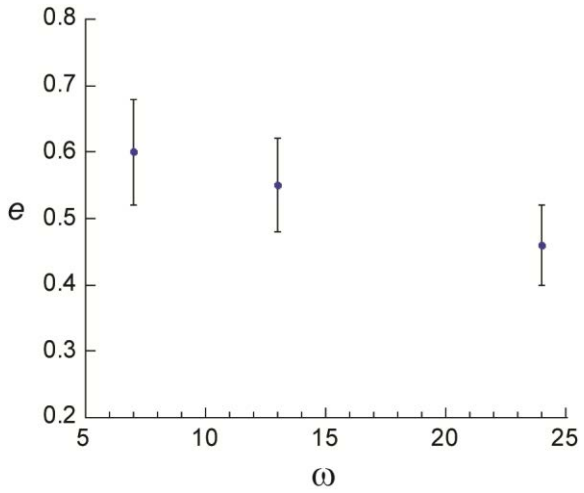

Figure 6.3: *A plot showing the eccentricity of RMs as a function of ω.*

Molecular simulations of the AOT/iso-octane/water RMs at ω < 5 have been previously reported as increasingly elliptical in shape.[8,23] Vasquez *et al.*[8] also observed greater fluctuations or oscillations in shape at values of ω < 5 in the AOT/iso-octane/water system and attributed this to the increasing dynamic behaviour of the RM with decreasing ω. These molecular simulations were different to those used here as the CHARMM27 forcefield[8] was used and a united atom approach was used to construct an 8-atom iso-octane solvent molecule, rather than using the whole solvent molecule of 26 atoms, as used to construct the solvent box in this study. In a previous molecular simulation study of AOT/water droplets at a comparable ω of 8.3, the RMs were observed to be perfectly spherical.[15] This was without the addition of a solvent. Therefore, it may be that the solvent also influences the curvature of the interface. As the RM decreases in size, the chains of the branched iso-octane may cause restriction to how the AOT surfactant headgroup embeds in the interface, hence influencing

the curvature. It would be interesting to observe how the solvent *n*-octane affects the shape of the RM in the AOT/water/*n*-octane system at $\omega < 10$, as this unbranched and more flexible solvent molecule may be more sterically favourable with the surfactant tails in the interface and have less influence on restricting the curvature of the RM. All the molecular simulations in the literature are based on using iso-octane or no solvent boxes.

There was no free AOT monomer observed throughout the molecular simulations of the AOT/water/iso-octane RMs, with the surfactant consistently remaining in the interface. This is contrary to what was observed in previous experiments (4.3.1) where at $\omega > 10$ and low droplet fractions of 0.05, two populations of AOT molecules were observed diffusing at two different rates (4.3.1). The two populations of AOT molecules were interpreted to be from the RM and from monomers, which were present in the continuous phase. One explanation why no AOT monomers were observed in the molecular simulations at $\omega = 12.8$ and 23.6, may be due to the simulation being a single RM and the free AOT observed in the previous experiments being the result of micellar collisions. Alternatively the molecular simulation may need longer equilibration times as the molecular exchange observed in (4.3.3) was observed on a millisecond timescale.

ω	No. of water molecules	%
7.1	3	0.9
12.8	8	0.8
23.6	13	0.3

Table 6.6: *A table of the number of water molecules in the continuous phase observed after 30 ns.*

There was a decrease in the percentage of free water molecules observed in the continuous phase with increasing ω (Table 6.6). The presence of water in the iso-octane continuous phase seems surprising, as it is contrary to what is expected. The polar water molecules would take a natural preference to reside in the RM core, rather than in the non-polar solvent. Therefore, the observation of free water molecules here may be the result of a limitation within the simulation.

6.3.2. AOT/ iso-octane/water/pentanol Droplets

The AOT/water/iso-octane and AOT/water/iso-octane/pentanol RMs were intended to be constructed at the same ω, so that the systems could be compared. The number of water molecules in the AOT/water/iso-octane/pentanol RMs differed slightly from the AOT/water /iso-octane RMs, due to the nature of the *solvateshell* command. There was, therefore, a slight variation in the ω values. There was also limited control on the number of pentanols added. The AOT/water/iso-octane/pentanol RMs formed different shapes and displayed different behaviour than the RMs in the AOT/water/iso-octane systems (6.3.1). The molecular simulations at ω = 7.4 illustrated the RM initially developing from an oblate ellipsoid to a prolate ellipsoid RM (Figure 6.4), with a proportion of pentanol molecules affecting the packing at the interface. Oblate ellipsoids have 2 longer and 1 shorter semi-axes (a=b>c), whereas prolate ellipsoids have one longer and 2 shorter semi-axes (a>b=c).

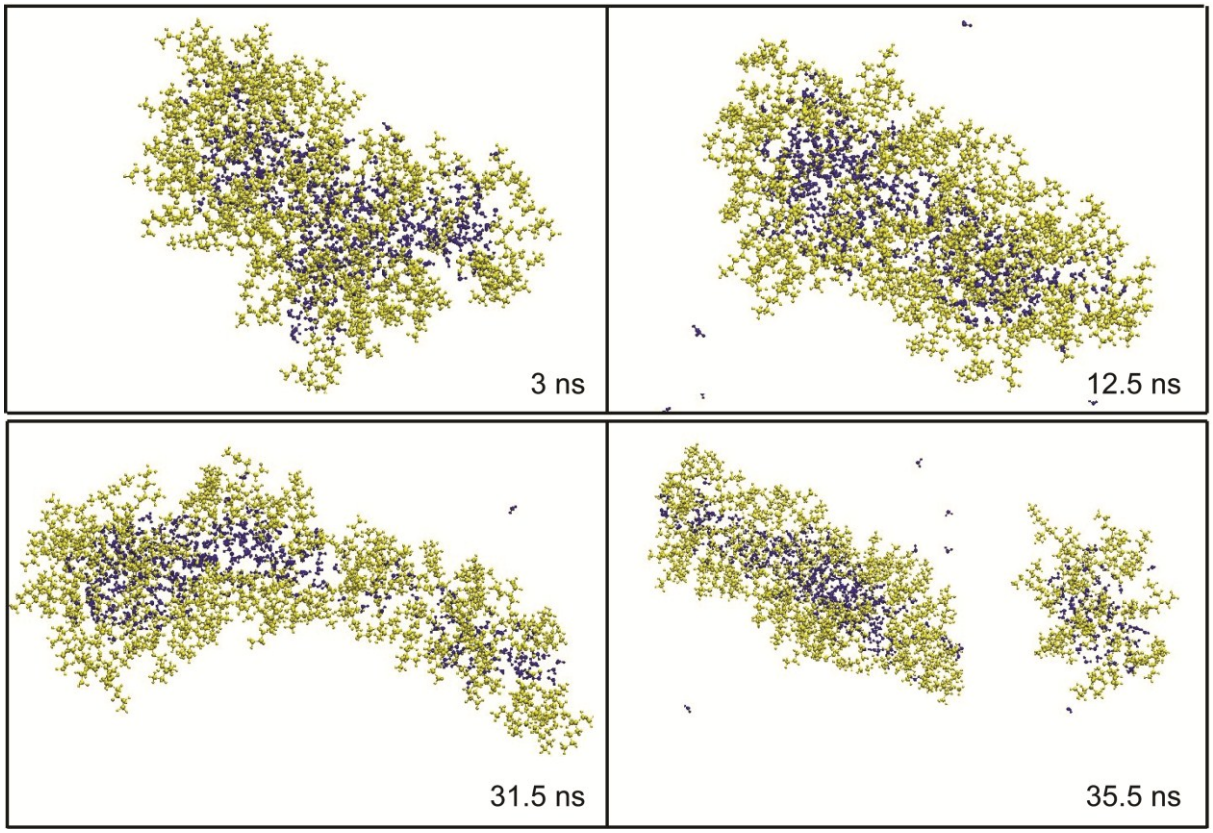

Figure 6.4: *An AOT/iso-octane/water/pentanol RM at ω = 7.4. The AOT molecules (yellow) and water (blue) molecules are shown in a CPK space-filling representation. Free water molecules are shown in the continuous phase.*

semi-axis	Mean average / Å	Standard deviation / Å
a	43.27	9.9
b	19.97	1.9
c	16.99	1.34
eccentricity	0.89	0.08

Table 6.7: *A table showing the mean average lengths for the semi-axes in the AOT/iso-octane/water/pentanol RM at ω = 7.4 up to 28 ns.*

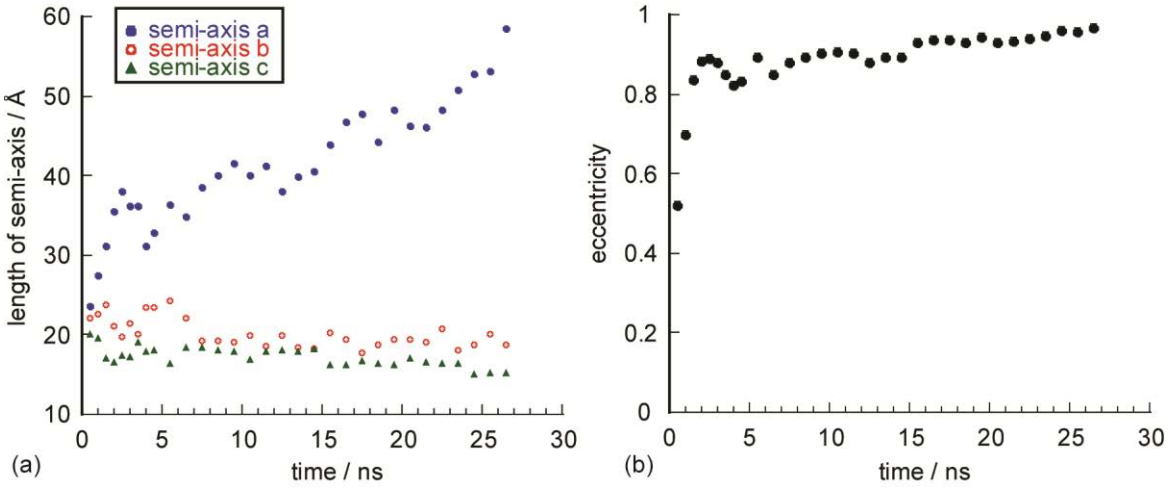

Figure 6.5: *Plots showing the lengths of the semi-axes (a) and the eccentricity (b) obtained for the AOT/iso-octane/water/pentanol RM at ω = 7.4.*

There was a slight decrease in semi-axes *b* and *c* and a sharp increase being observed in semi-axis *a* from 23.5 to 60 Å, which is also indicated by an increase in the standard deviation and a sharp increase in the eccentricity to 0.9 (Table 6.7 and Figure 6.5(a)). At t = 32 ns, the droplet split into two smaller droplets. As smaller droplets were formed from the splitting of the original RM, the ω value of 7.4 changed to 8.5 and 4 for the smaller droplets due to the variation in the ratio of surfactant to water molecules. The lengths of the droplets semi-axes changed to 3.5 nm and 1.5 nm respectively with the semi-axes *b* and *c* remaining constant at 1.8 and 1.5 nm, indicating that the larger droplet remained prolate, whereas the smaller droplet was more spherical in shape.

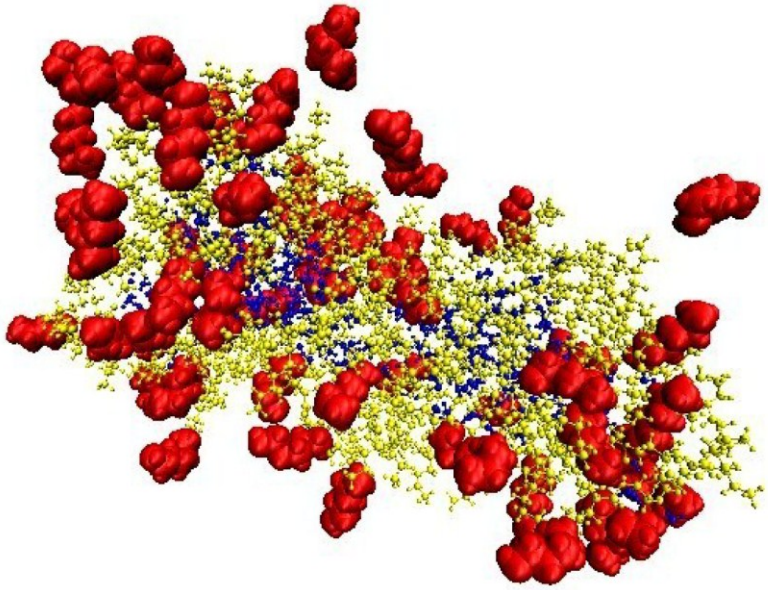

Figure 6.6: *An AOT/iso-octane/water/pentanol RM at ω = 7.4 at t = 13.5 ns. The AOT molecules (yellow) and water (blue) molecules are shown in a CPK space-filling representation. The pentanol molecules (red) are shown as a van der Waals representation.*

Chen *et al*.[24] discussed how when the packing parameter, $S_p > 1$, then RMs are formed with a *negative curvature* (See 1.1.1). Alcohols can cause an increase in negative curvature, depending on the chain length.[11] In the case of pentanol, the headgroup surface area (a_0) will have less effect than the volume of the tail group (υ) on the packing factor relationship, (S_p) = $\upsilon / (a_0 l)$.[11,24-26] Therefore as there is an increase in S_p and the negative curvature, there is the formation of smaller droplets.[24] The pentanol molecules are more densely populated at the ends of the RM, where there is a higher curvature (Figure 6.6). The molecular simulation needs more time to observe if the oblate droplet at ω = 8.5 splits further to make two droplets similar to the spherical droplet of ω = 4, tending towards a monodisperse rather than polydisperse microemulsion.

Over the simulation period, the number of pentanol molecules in the interface varied as shown in Figure 6.7, resulting in a pentanol : AOT ratios stabilising at 1 : 1.2 before the droplet split occurred.

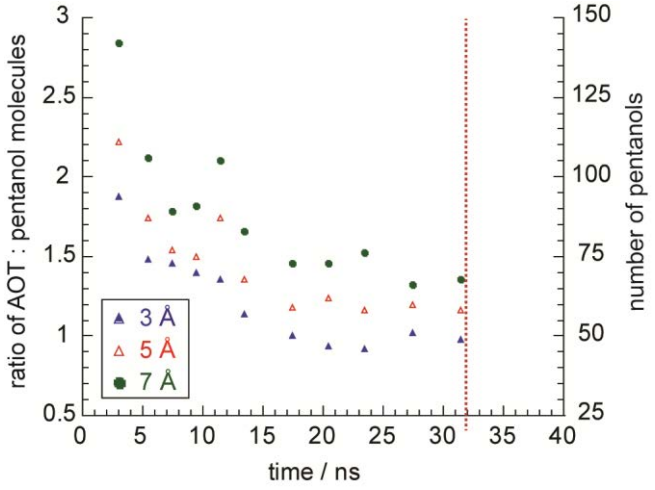

Figure 6.7: *A plot showing the ratios of AOT: pentanol and the number of pentanol molecules within the given distance of the AOT molecules at ω = 7.4. The red line indicates where the droplet split.*

At ω = 11.8, similar behaviour was observed as with the droplet at ω = 7.4. At t = 16 ns, the RM split into 2 smaller droplets as shown in Figure 6.8 and Figure 6.9. There was an increase in semi-axis a from 32 to 59 Å, with the RM changing from an ellipsoidal to a transitional rod-like RM, over a shorter period of 15 ns, with the eccentricity tending towards 1 (Figure 6.10). The increase in semi-axis a, shown in Figure 6.10 from t = 16 ns, therefore includes the distance between the two droplets.

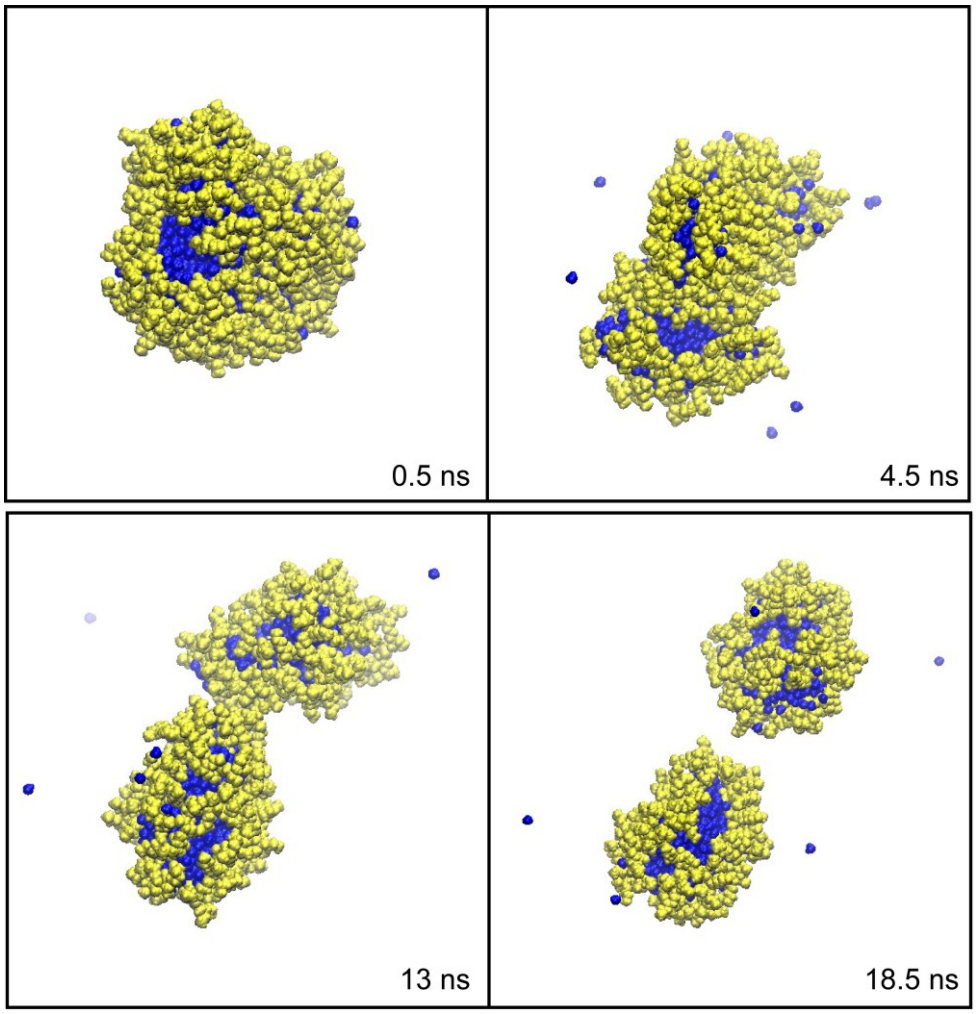

Figure 6.8: *Images of the AOT/iso-octane/water/pentanol RM at* ω = 11.8*, showing the AOT (yellow) and water (blue) molecules, shown in van der Waals representations.*

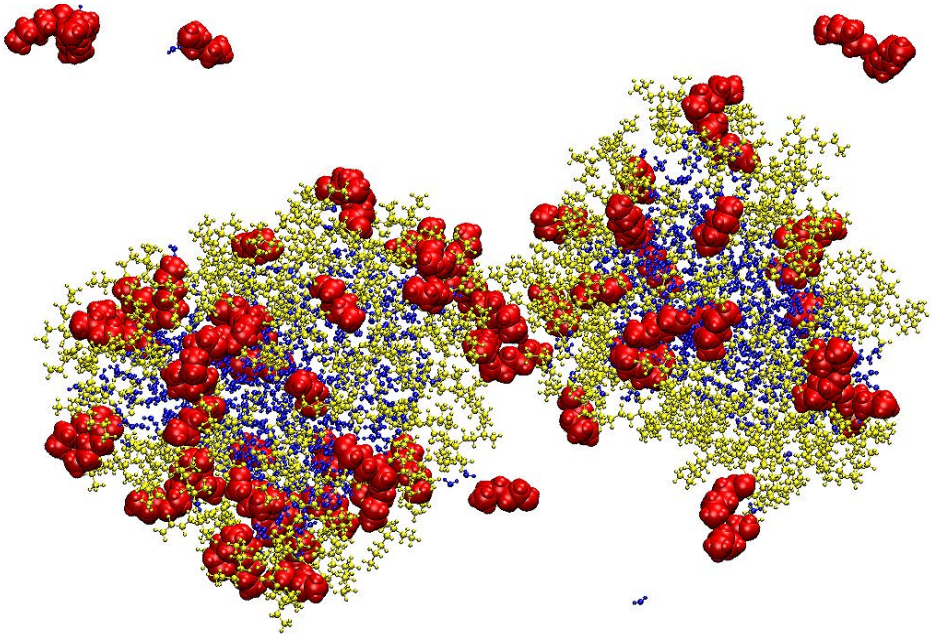

Figure 6.9: *An image showing the AOT (yellow - CPK) and pentanol molecules (red-van der Waals representations) within a 5 Å distance of the water molecules (blue-CPK) in the splitting AOT/iso-octane/water/pentanol RM, at ω = 11.8 and t = 15.5 ns. Pentanol and water molecules are shown present in the continuous phase.*

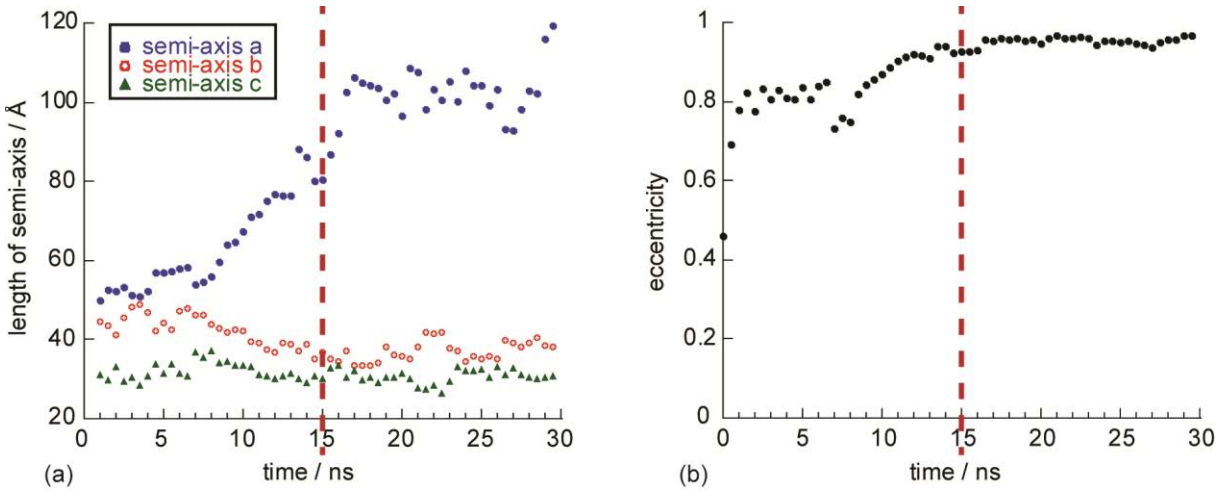

Figure 6.10: *Plots showing the lengths of the semi-axes (a) and eccentricity (b) for the AOT/ iso-octane/water/pentanol RM at ω = 11.8 up to 15 ns. The dotted line indicates the time at which the droplet split.*

The ω values of the smaller droplets were determined as 10.2 and 12.5 with semi-axis a = 2 nm and 2.5 nm respectively. The values for semi-axes b and c were 2.82 nm and 2.27 nm respectively, which were similar to semi-axis a, indicating that the smaller droplets formed a spherical shape after splitting. It has been previously reported that smaller RMs are formed in AOT/water/alkane microemulsions with pentanol as a co-surfactant, than those without pentanol.[9,11] The AOT/water /pentanol/iso-octane systems were investigated and characterised in chapter 5 and it was found that the RMs diffused at a faster rate than the systems without pentanol. The changes in viscosity were determined after considering the molecular exchange taking place between the pentanol molecules in the RM interface and continuous phase using methods previously developed. However, the R_h values were still smaller for RMs with pentanol compared to those in the AOT/water iso-octane systems. The formation of smaller droplets in the AOT/pentanol/water/iso-octane systems at ω = 7.4 and 11.8 may be an explanation for observing faster diffusion coefficients for the interfacial AOT molecules from the NMR experiments in (5.3.1). The changes in the diffusion coefficients may also be due to a variation in the viscosity of the continuous phase due to the presence of pentanol.

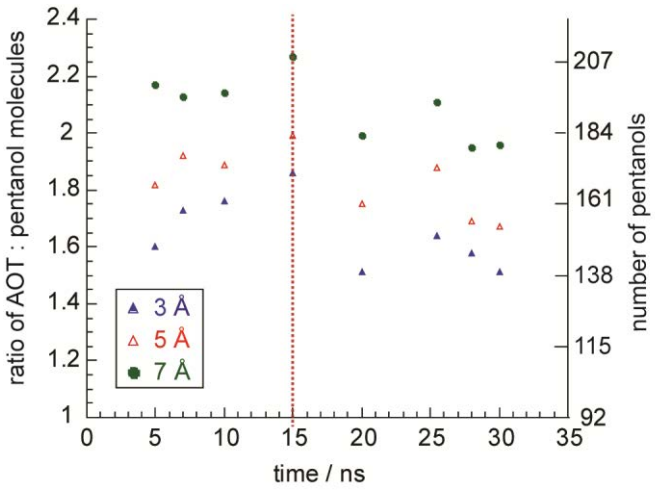

Figure 6.11: *A plot showing the AOT: pentanol ratios and the number of pentanol molecules within the given distance of the AOT molecules at ω = 11.8 with the red line indicating when the droplet split.*

The ratios of AOT: pentanol molecules at distances of 3, 5 and 7 Å from the AOT molecules are shown in Figure 6.11. Before the droplet split, there was a slight increase in the number of pentanols in the interface at 15 ns. As the two droplets formed, there was an initial decrease in the number of interfacial pentanol molecules. The two droplets are comparable in size with droplet 1 and 2 formed from 44 and 48 AOT molecules, respectively, with a ratio of AOT: pentanol molecules of approximately 1 : 2 (Table 6.8).

Time /ns	No. of interfacial pentanol molecules droplet 1	No. of interfacial pentanol molecules droplet 2	Ratio AOT: pentanol droplet 1	Ratio AOT: pentanol droplet 2
15.5	89	94	1 : 2.02	1 : 1.95
20	73	88	1 : 1.66	1 : 1.83
25	86	87	1 : 1.95	1 : 1.81
28	71	85	1 : 1.61	1 : 1.77
30	76	78	1 : 1.72	1 : 1.62

Table 6.8: *A table showing the number of pentanol molecules within 5Å of the AOT molecules.*

The ratio of AOT: pentanol in droplet 1 fluctuates over time but there is a decrease in the ratio in both droplets (Table 6.8). The simulations needed more time to reach a steady state, to establish the final numbers of interfacial AOT and pentanol.

At $\omega = 23.3$, there was less fluctuation in the overall RM shape, than with the RMs at $\omega < 12$ over the simulation period of 30 ns (Table 6.9, Figure 6.12 and Figure 6.13).

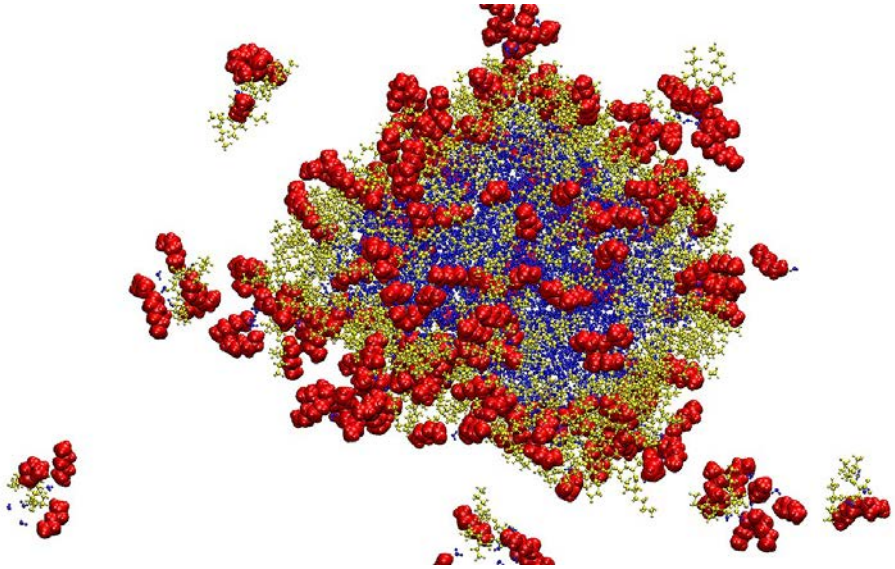

Figure 6.12: *An AOT/iso-octane/water/pentanol RM at ω = 23.3. The AOT (yellow) and pentanol molecules (red) are within 5 Å of water molecules (blue).*

semi-axis	mean average / Å	standard deviation / Å
a	58.3	4.7
b	50.9	2.3
c	42.9	2.4
eccentricity	0.66	0.08

Table 6.9: *A table showing the mean average lengths for the semi-axes in the AOT/iso-octane/water/pentanol RM at ω = 23.3.*

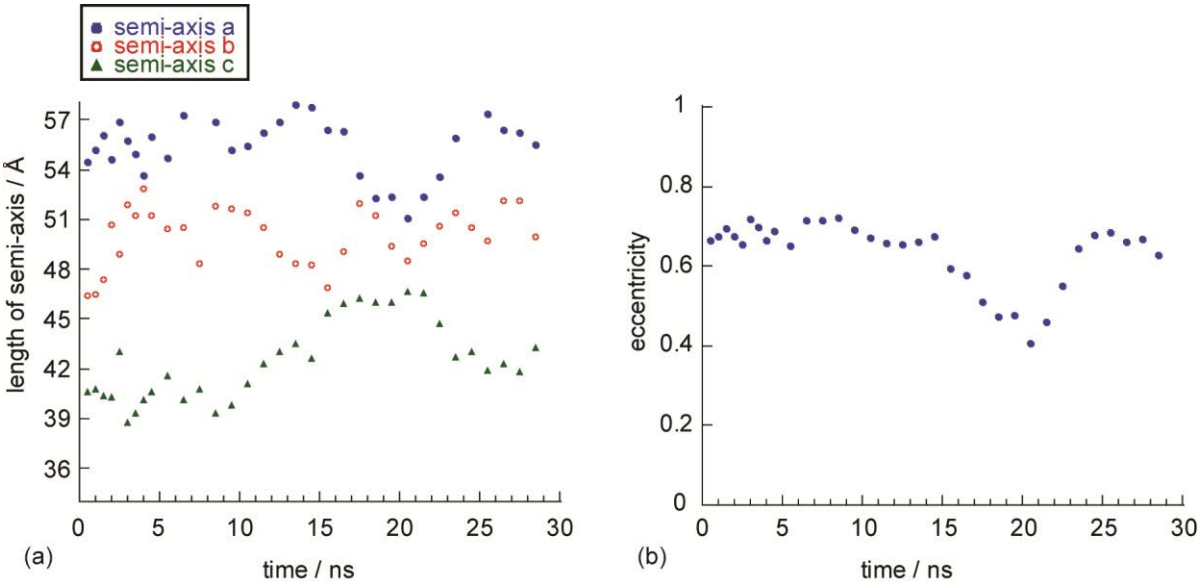

Figure 6.13: *Plots showing the lengths of the semi-axes (a) and eccentricity (b) for the AOT/iso-octane/water/pentanol RM at ω = 23.3.*

The formation of smaller droplets was observed breaking away from the original RM (Figure 6.12). Therefore as ω increased, the RM retained more of its original form. This may be one explanation why the difference between diffusion coefficients in systems with and without pentanol decreases at higher ω values, which was observed in the PFG experiments in 5.3.1.

More water molecules were observed in the continuous phase (Table 6.10) compared to the RM without pentanol (Table 6.6) in the system for all the droplets, with a decrease of 84, 81 and 89% of water molecules in the AOT/water/iso-octane RMs compared to AOT/water/iso-octane /pentanol RMs at the same ω values. There may be two reasons for there being more water in the continuous phase, one being that as the pentanol makes the interface more flexible and the increase in the negative, inward curvature may have the effect of forcing water molecules out of the core of the droplet. The water will also move into the continuous

phase more favourably, than in the system without pentanol, as hydrogen bonds are formed between the water and pentanol molecules. Clusters of pentanol and water molecules can be observed in the continuous phase in Figure 6.9.

ω	No. of water molecules	%
7.4	21	5.7
11.8	45	4.1
23.3	97	2.7

Table 6.10: *A table of the number of water molecules in the continuous phase observed after 30 ns.*

6.3.3. CTAB/hexanol/water Droplets

The CTAB/hexanol/water droplet changed from a spherical to an oblate shape after 27.5 ns, as observed from the images showing the RM with CTAB and water molecules only (Figure 6.14). A significant proportion of water molecules moved into the continuous phase of hexanol molecules over the simulation period.

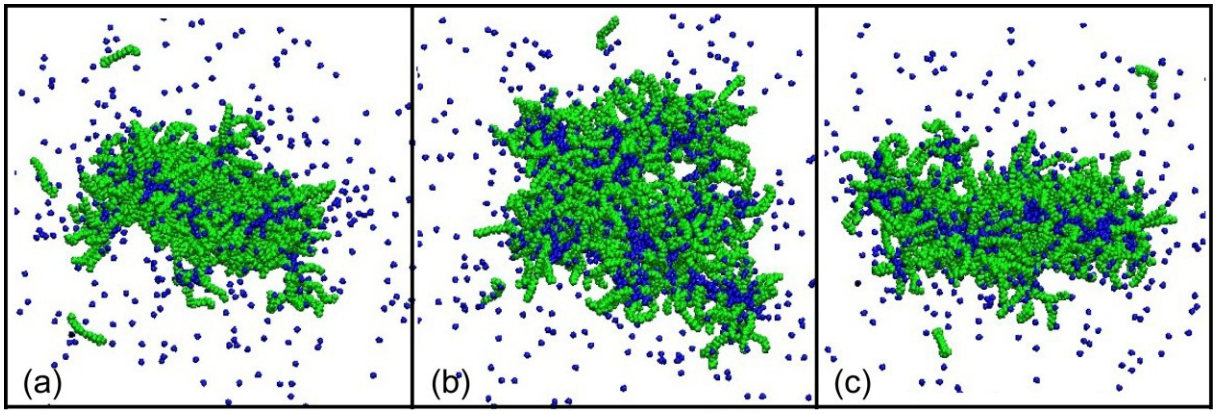

Figure 6.14: *Images of the CTAB/hexanol/water RM at ω = 7.2, showing the CTAB (green) and water (blue) molecules viewing along the x (a), z (b) and y (c) axes at t = 27.5 ns.*

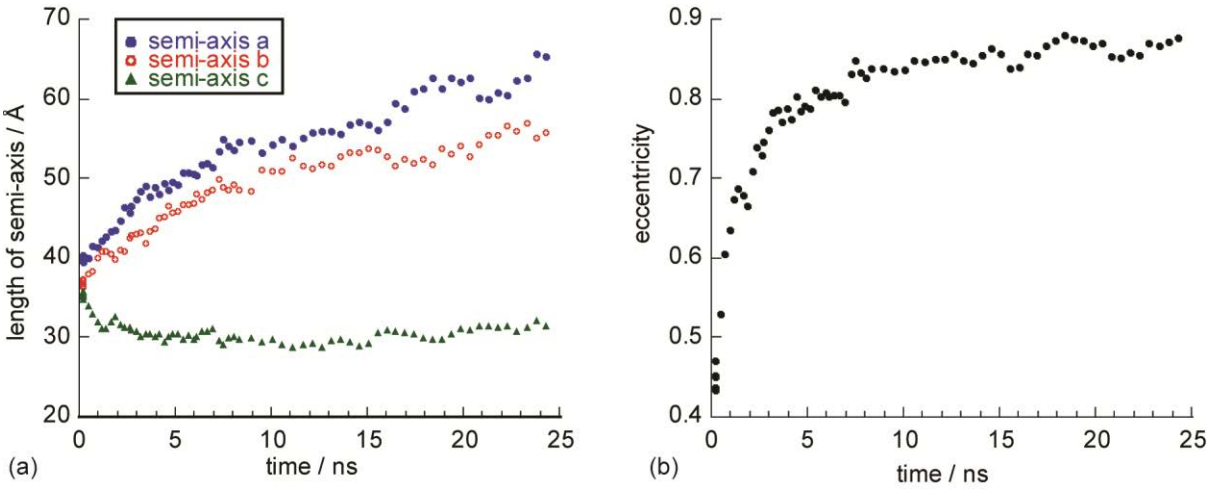

Figure 6.15: *Plots showing the lengths of the semi-axes (a) and eccentricity (b) for the CTAB/water/hexanol RM at ω = 7.2*

The eccentricity of the droplet increased from 0.4 to 0.88 over the simulation time (Figure 6.15(b)) with the semi-axes *a* and *b* increasing to 65 and 56 Å, respectively, with semi-axis *c* remaining stable at 31 Å (Figure 6.15(a)). The splitting of the droplet into smaller droplets is reflected by the continuing steady increase in the length of the semi-axes *a* and *b*. The molecular simulations need to be continued for longer periods to reach a steady state. The hydrodynamic radius of the CTAB/hexanol/water RMs obtained from NMR diffusion measurements was 1 nm, which is smaller than the semi-axes observed here. However one explanation for this may be that the development of smaller RMs continues from the original droplet over longer simulation times. A smaller droplet shown in Figure 6.16, shows the CTAB (green) and hexanol (purple) molecules forming the interface of the droplet around the water molecules (red and white).

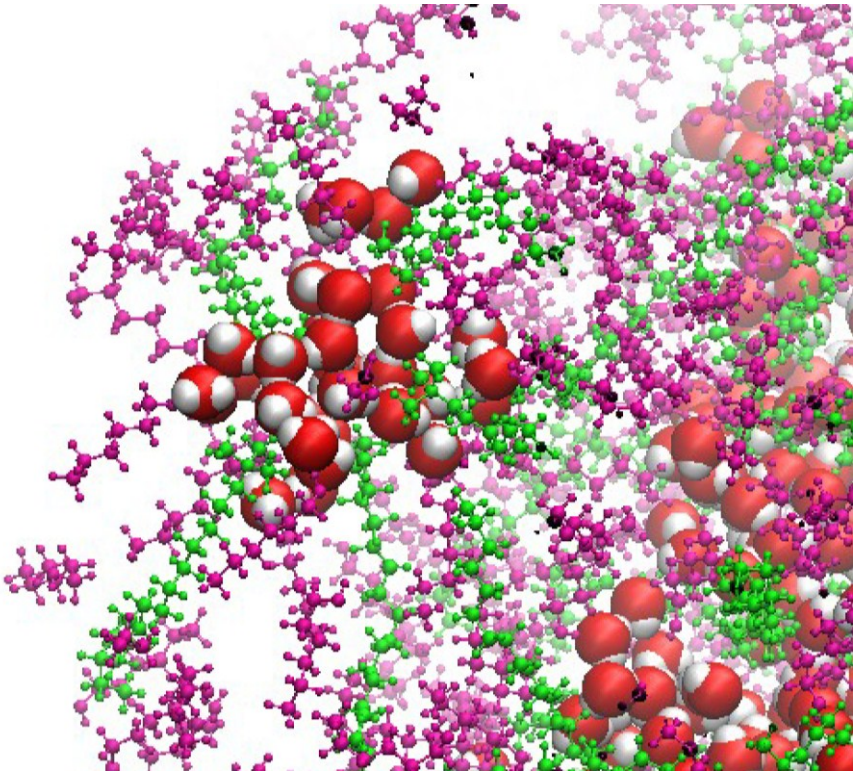

Figure 6.16: *An image of a smaller droplet formed from a CTAB /hexanol/water RM. (CTAB = green; hexanol = purple in CPK representation;water = red / white molecules as a van der Waals representation.*

This droplet has a radius of approximately 1.8 nm, which is more comparable with the R_h determined from the NMR diffusion measurements. It has a ω value of 4, being formed of 8 CTAB molecules and 32 water molecules with 18 hexanol molecules forming the co-surfactant, with a CTAB : hexanol ratio of 1: 2.25.

A second droplet constructed at the same value of ω also illustrates how the RM changed from an oblate shape into forming smaller droplets (Figure 6.17). The new ω values for the smaller droplets, 1 to 4, (Figure 6.17) were 4, 4.2, 4.2 and 2.7, respectively.

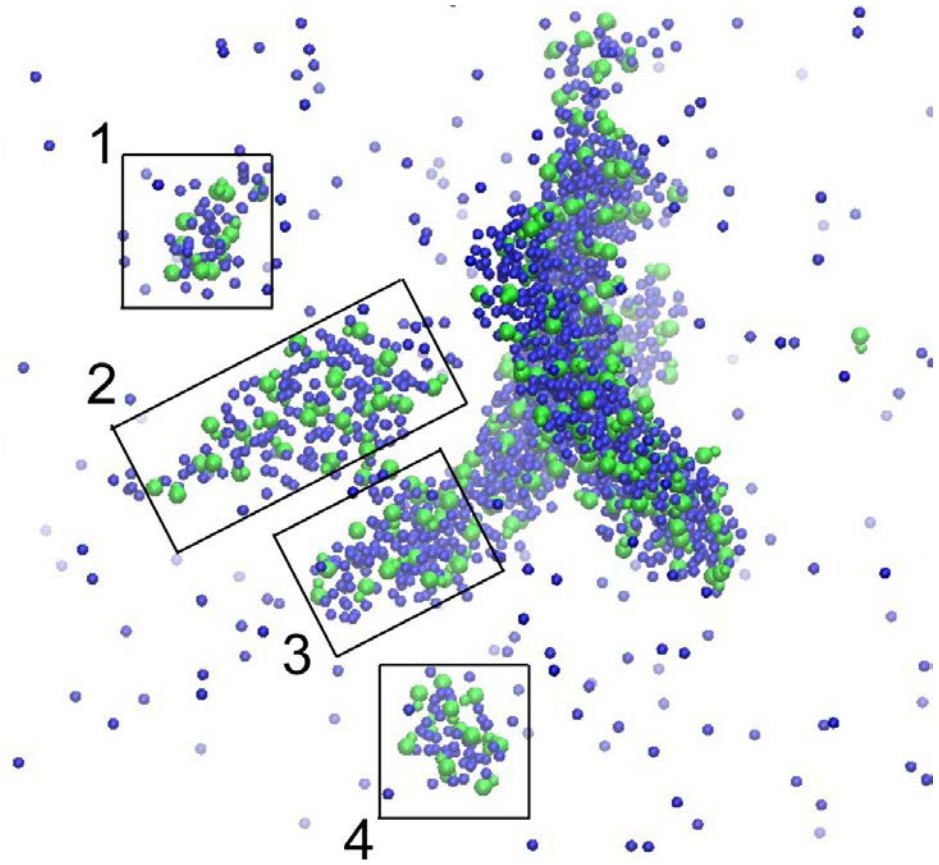

Figure 6.17: *A repeated CTAB/water/hexanol simulation, showing the formation of smaller droplets 1- 4; green = nitrogen atoms from CTAB molecules; blue = hydrogen atoms from water molecules.*

As well as exploring the shape and behaviour of the RM the molecular simulation was also used to observe the number of hexanol molecules which were present in the interface as the co-surfactant (Table 6.11).

radius / Å	CTAB	hexanol	ratio of CTAB:hexanol	interfacial water
3	279	1133	4.1	1473
5	279	1402	5.0	1688
7	279	1865	6.7	1713

Table 6.11: *A table showing the number of hexanol and water molecules within a given radius of the CTAB molecules at t = 20 ns.*

This was achieved by isolating and counting the number of hexanol molecules within a distance of 3, 5 and 7 Å of the CTAB nitrogen atom, encompassing the molecules at varying thickness of the interface (Figure 6.18). These methods have been used previously in CTAB quarternary systems to determine the number of interfacial co-surfactant molecules.[7]

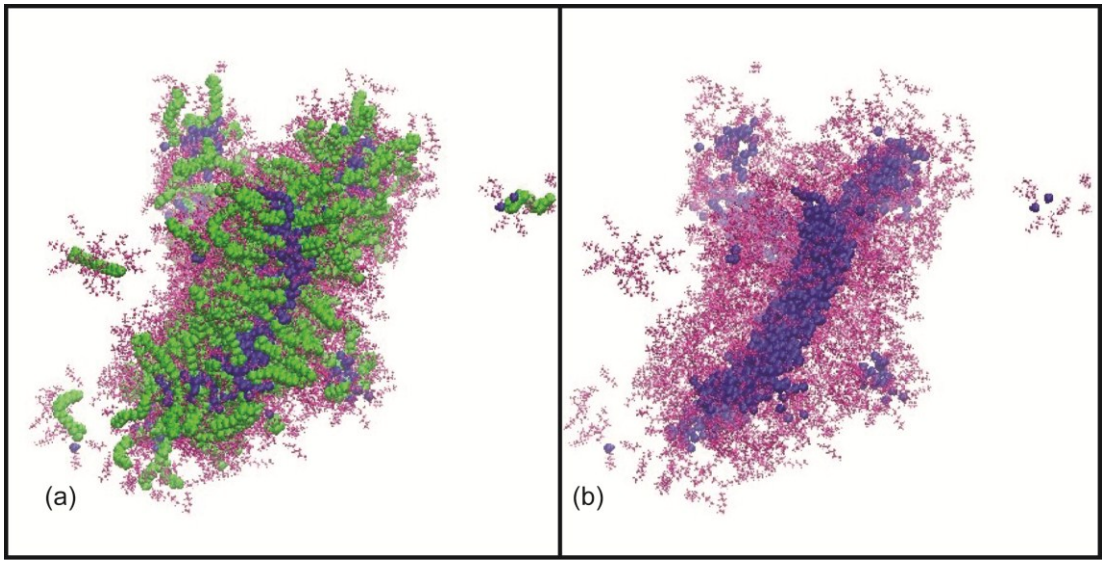

Figure 6.18: *Images of the CTAB/hexanol/water droplet, with hexanol molecules (purple) at a radius within 5 Å of CTAB nitrogen atoms. CTAB shown (green) (a) and CTAB hidden (b)*

The ratio of CTAB : hexanol in the interface was determined as 1 : 6 and 1 : 6.7, from analysing the number of pentanol molecules at distances of 5 Å and 7 Å from the CTAB nitrogen atoms. The formation of smaller droplets from splitting of the original RM is due to hexanol molecules moving into the micellar water, as observed at a 1 nm slice shown at 5 nm through the *yz* plane (Figure 6.19). Further analysis on molecular simulations at longer times is required to determine the number of interfacial hexanol molecules.

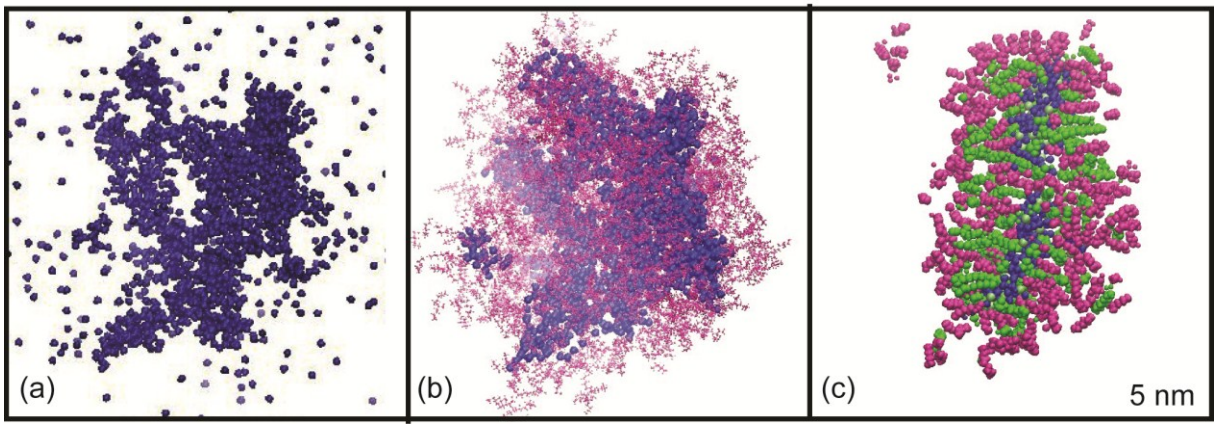

Figure 6.19: *Images of the the CTAB/hexanol/water droplet at 25 ns showing the water molecules forming fragmenting droplets(a), and the hexanol and water molecules (b) through the zy plane and a slice through the centre of the droplet at 5 nm in the xy plane (c). The slice at 5 nm shows the hexanol molecules (purple) residing centrally through the RM. CTAB;green, water;blue*

6.4. Conclusions

The molecular simulations demonstrated the molecular interactions between the RM, solvent and co-surfactant molecules in the continuous phase and the effects on the resulting RM shape fluctuations. The molecular simulations of the AOT/iso-octane/water showed that the RMs

were ellipsoidal in shape with the eccentricity decreasing as a function of ω. When pentanol was added to the system to form the AOT/iso-octane/water/pentanol RMs, a proportion of pentanol was observed present in the interface and initially at $\omega < 12$, rod-like RMs were formed, before splitting into two smaller droplets. The formation of smaller droplets, as well as changes in the viscosity of the continuous phase, may be one explanation why faster diffusion coefficients were observed for AOT molecules in AOT/water/pentanol/iso-octane RMs in (5.3.2) compared to RMs without pentanol. At higher ω, the AOT/water/pentanol /iso-octane RM was ellipsoidal and over the simulation period of 30 ns, smaller clusters of AOT/water/pentanol were observed breaking away into the continuous phase.

The CTAB/hexanol/water droplets initially formed an oblate shape. Smaller droplets were then observed forming and breaking away from the original RM, with R_h values more comparable with the values determined from the PFG experiments in (3.3.4). The ratio of CTAB : hexanol in the interface was determined at 1: 6. Due to using an all-atom solvent box, which was necessary as the hexanol is the co-surfactant as well as the continuous phase in the system, the molecular simulations required significant computer time and resources. Therefore CTAB/hexanol/water droplets need longer simulation times to reach the equilibration point and to observe whether more small droplets are formed from the original droplet. A more complete analysis of the aggregation numbers and sizing of the CTAB/hexanol/water droplets can then take place.

6.5. References

(1) Macchioni, A.; Ciancaleoni, G.; Zuccaccia, C.; Zuccaccia, D. *Chem. Soc. Rev.* **2008**, *37*, 479.

(2) Chen, Y. J.; Xu, G. Y.; Yuan, S. L.; Sun, H. Y. *Colloids Surf., A* **2006**, *273*, 174.

(3) Martinez, A. V.; Dominguez, L.; Malolepsza, E.; Moser, A.; Ziegler, Z.; Straub, J. E. *J. Phys. Chem. B* **2013**, *117*, 7345.

(4) Mudzhikova, G. V.; Brodskaya, E. N. *Colloid J.* **2006**, *68*, 738.

(5) Mudzhikova, G. V.; Brodskaya, E. N. *Colloid J.* **2006**, *68*, 729.

(6) Abel, S.; Sterpone, F.; Bandyopadhyay, S.; Marchi, M. *J. Phys. Chem. B* **2004**, *108*, 19458.

(7) Mills, A. J. Wilkie, J.; Britton, M.M. *J. Phys. Chem. B* **2014**. *118*, 10767.

(8) Gardner, A.; Vasquez, V. R.; Clifton, A.; Graeve, O. A. *Fluid Phase Equilib.* **2007**, *262*, 264.

(9) Lin, T. L.; Hu, Y.; Lee, T. T. *Prog. Colloid Polym. Sci.* **1997**, *105*, 268.

(10) PerezCasas, S.; Castillo, R.; Costas, M. *J. Phys. Chem. B* **1997**, *101*, 7043.

(11) Zhang, X. G.; Chen, Y. J.; Liu, J. X.; Zhao, C. Z.; Zhang, H. J. *J. Phys. Chem. B* **2012**, *116*, 3723.

(12) Halliday, N. A., PhD Thesis, School of Chemistry, University of Birmingham, 2010.

(13) Halliday, N. A.; Peet, A. C.; Britton, M. M. *J. Phys. Chem. B* **2010**, *114*, 13745.

(14) Anachkov, S. E.; Danov, K. D.; Basheva, E. S.; Kralchevsky, P. A.; Ananthapadmanabhan, K. P. *Adv. Colloid Interface Sci.* **2012**, *183*, 55.

(15) Binks, D. A.; Spencer, N.; Wilkie, J.; Britton, M. M. *J. Phys. Chem. B* **2010**, *114*, 12558.

(16) Duan, Y.; Wu, C.; Chowdhury, S.; Lee, M. C.; Xiong, G. M.; Zhang, W.; Yang, R.; Cieplak, P.; Luo, R.; Lee, T.; Caldwell, J.; Wang, J. M.; Kollman, P. *J. Comput. Chem.* **2003**, *24*, 1999.

(17) Wang, J. M.; Wolf, R. M.; Caldwell, J. W.; Kollman, P. A.; Case, D. A. *J. Comput. Chem.* **2004**, *25*, 1157.

(18) Case, D. A.; Cheatham, T. E.; Darden, T.; Gohlke, H.; Luo, R.; Merz, K. M.; Onufriev, A.; Simmerling, C.; Wang, B.; Woods, R. J. *J. Comput. Chem.* **2005**, *26*, 1668.

(19) Fox, T.; Kollman, P. A. *J. Phys. Chem. B* **1998**, *102*, 8070.

(20) Wilkie, J., The program is available from the author (J.W.) on request.

(21) Humphrey, W.; Dalke, A.; Schulten, K. *J. Mol. Graphics Modell.* **1996**, *14*, 33.

(22) Biosym/MSI;InsightII San Diego, CA.

(23) Vasquez, V. R.; Williams, B. C.; Graeve, O. A. *J. Phys. Chem. B* **2011**, *115*, 2979.

(24) Chen, S. J.; Evans, D. F.; Ninham, B. W.; Mitchell, D. J.; Blum, F. D.; Pickup, S. *J. Phys. Chem.* **1986**, *90*, 842.

(25) Evans, D. F.; Mitchell, D. J.; Ninham, B. W. *J. Phys. Chem.* **1986**, *90*, 2817.

(26) Oldfield, C. In *Biotechnology and Genetic Engineering Review* : 1994, p 255.

7. Concluding Remarks and Further Work

The sizes and dynamics of AOT/*n*-octane/water, CTAB/hexanol/water and AOT/iso-octane/water/pentanol reverse micelles (RMs) were probed using PFG measurements of diffusion. Where many studies have explored the diffusion behaviour of the water molecules in RMs, the work in this thesis has analysed the diffusion of the surfactant molecules. The molecular exchange of surfactant and co-surfactant molecules has also been observed, when changing the PFG experimental parameters. As well as determining the average sizes of RMs, the inverse Laplace transform (ILT) has also been implemented to obtain size distributions in 1D diffusion experiments. Therefore diffusion, relaxation and exchange processes can now be further explored using 2D diffusion exchange spectroscopy (DEXSY)[1-3] and relaxation exchange spectroscopy (REXSY)[1] experiments, which also implement the ILT.

DEXSY experiments[1-3] are useful when there are two populations of a molecule diffusing at two different rates, which are partitioned and exchanging between different phases, such as the co-surfactant and surfactant molecules in microemulsions. A DEXSY experiment comprises of two PGSE pulse sequences separated by a mixing time, τ, whereby two diffusion coefficients are obtained and are compared.[1] The mixing times can be varied and the diffusion behaviour monitored. If there is one population of molecules diffusing at a single rate then cross-diagonals will be observed on a (D_1, D_2) map, formed from applying the ILT, to give 2D distributions of diffusion coefficients.[2,3] However if there are two populations of molecules diffusing at two different rates, then after specific mixing times,

off-peak diagonals would be observed.[2,3] If the experiments are repeated at different mixing times then exchange rates between the molecules can be determined. REXSY experiments[1] have the same format and analysis as DEXSY experiments, however two CPMG pulse sequences measure two relaxation times, which separated by a mixing time (τ). If a molecular species has two populations which have two T_2 relaxation times, due to existing in different phases of a system, then like the DEXSY experiments, off-diagonal peaks would be observed on a (T_2,T_2) map[1,4] and the exchange rates between the phases could be determined. The molecular exchange processes of the surfactant molecules, AOT and CTAB between the dispersed and continuous phases need further investigation. The diffusion behaviour of the co-surfactant pentanol in the AOT/iso-octane/water has been explored in this thesis. However as the attractive interactions increase as a function of alcohol chain length,[5] the variation and trends in diffusion and exchange of the molecules in AOT systems with varying alcohols could be probed and further rationalised.

NMR techniques were used to explore the acid-catalysed chemical exchange in the AOT/iso-octane/water/pentanol microemulsion, where the coalescence of the water and the pentanol hydroxyl peaks were observed with decreasing pH at specific ϕ_d. However as the system was diluted, the composition of the continuous phase changed and further work is now required to keep the composition of the continuous phase constant in the systems at varying ϕ_d, which could include using titrations to ensure that the ratios of alcohol co-surfactant to alkane solvent is consistent in microemulsions at varying ω. Further investigations can then take place to observe the capability of pentanol molecules to monitor the changes of the pH in RMs at $\omega \geq 10$.

The molecular interactions between the dispersed and continuous phases have been observed in molecular simulations of the RMs from the systems, which were explored in the PFG experiments. It was important to use all-atom forcefields to construct the solvent boxes in molecular simulations of RMs, particularly when the solvent acts as the co-surfactant, as in the CTAB/hexanol/water system. The effects of the solvent and co-surfactant molecules on the fluctuations of shapes could be fully observed. The molecular simulations of the RMs in the AOT/iso-octane/water system showed that the RMs became more spherical as a function of ω and the RMs at comparable ω with added pentanol developed into cylindrical shapes, before splitting into smaller RMs. The results from the PFG experiments were in agreement with the molecular simulations. The CTAB/hexanol/water RMs were initially oblate, but smaller droplets were observed forming, as the hexanol co-surfactant penetrated the micelle interface. The molecular simulations need to be continued for longer times, so the system reaches equilibrium and the final number and sizes of smaller droplets can be determined. The CTAB/hexanol/water RMs could be constructed at varying ω, to compare the droplet sizes and shapes. Molecular simulations could also be run with AOT/*n*-octane/water/pentanol to compare the resulting shapes of the droplets with the AOT/iso-octane/water/pentanol system. The effects of different shaped solvent molecules penetrating the RM interface and any resulting changes in shape or size could be rationalised. Molecular simulations with different alcohols could be carried out to compare the changes in shapes or droplet sizes resulting from alcohols with different chain lengths. As there are more computer resources available, fully solvated RMs using organic solvent boxes constructed from all-atom forcefields can be simulated to probe systems at varying compositions, with different additives and at varying pH values. Hence, the shapes, sizes, aggregation numbers and molecular exchange processes can be probed in a wider range of microemulsions.

7.1. References

(1) Callaghan, P. T. *Translational dynamics and magnetic resonance : principles of pulsed gradient spin echo NMR*; Oxford University Press: Oxford ; New York, 2011.

(2) Callaghan, P. T.; Godefroy, S.; Ryland, B. N. *Magn. Reson. Imaging* **2003**, *21*, 243.

(3) Galvosas, P.; Qiao, Y.; Schonhoff, M.; Callaghan, P. T. *Magn. Reson. Imaging* **2007**, *25*, 497.

(4) Callaghan, P. T. Arns., C.H.; Galvosas, P.; Hunter, M.W.; Qiao,Y.; Washburn, K.E. *Magn. Reson. Imaging* **2007**, *25*, 441.

(5) Zhang, X. G.; Chen, Y. J.; Liu, J. X.; Zhao, C. Z.; Zhang, H. J. *J. Phys. Chem. B* **2012**, *116*, 3723.

APPENDIX I

The preparation of AOT/n-octane/water microemulsions

To make a 1.5 M stock solution of AOT/*n*-octane, dissolve 111.14 g into 70 ml of *n*-octane. Scale amounts as appropriate. Note that the solution above needs to be left overnight to dissolve.

The solutions for all values of ω are made at $\phi_d = 0.45$, based on a stock solution of 1.5 M. The solutions are then diluted to the appropriate ϕ_d by adding extra octane. The origins of this method come from work with BZ-AOT reactions where reactants had to be initially partitioned and then diluted to the appropriate ϕ_d .

Table of concentrations for the AOT/water/*n*-octane microemulsions

To add to 6 ml of 1.5 M AOT/*n*-octane stock solution. Scale as appropriate.

ω	Volume of water/ ml	Volume of octane / ml to make $\phi_d = 0.45$
5.3	0.8673	2.913
15	2.454	4.852
25	4.091	6.855
35	5.727	8.853

To dilute 1 ml of the solutions made at $\phi_d = 0.45$, the following ratios were calculated,

ϕ_d	Volume *n*-octane/ ml
0.25	0.8
0.2	1.25
0.15	2
0.1	3.5
0.05	8

APPENDIX II

The preparation of AOT/iso-octane/water/pentanol microemulsions

To make a 1 M stock solution of AOT/iso-octane, dissolve 11.12 g of AOT into 15.5 ml of iso-octane.

Table of concentrations for the AOT/water/iso-octane/pentanol microemulsions

These concentrations are added to 1 ml of 1 M AOT/iso-octane stock solution.

ω	Vol. of 1 M AOT/iso-octane / ml	Vol. water/ml	octane / ml $\phi_d = 0.45$	octane / ml $\phi_d = 0.15$
5.3	1	0.0954	0.138	2.895
9.2	1	0.1674	0.249	3.303
15	1	0.2702	0.352	3.885
20	1	0.3604	0.462	4.396
25	1	0.4504	0.572	4.906

In 1 ml of 1 M AOT/iso-octane, there is 0.37988 ml AOT and 0.62012 ml of iso-octane

To make solutions where $\chi = 0.75$, 0.145 ml pentanol were added.

APPENDIX III

The findings that have been discussed in Chapter 3 and the conclusions that have been drawn have been presented in the Journal, Langmuir, in a paper entitled “Sizing of Reverse Micelles in Microemulsions using NMR Measurements of Diffusion”.

A copy of the paper can be found overleaf.

dx.doi.org/10.1021/la300796u

Langmuir

Article

pubs.acs.org/Langmuir

Sizing of Reverse Micelles in Microemulsions using NMR Measurements of Diffusion

Susan J. Law and Melanie M. Britton*

School of Chemistry, University of Birmingham, Edgbaston, Birmingham, B15 2TT, United Kingdom

ABSTRACT: This paper reports the size of reverse micelles (RMs) in AOT/octane/H_2O and CTAB/hexanol/H_2O microemulsions using magnetic resonance (MR) pulsed field gradient (PFG) measurements of diffusion. Diffusion data were measured using the pulsed gradient stimulated echo (PGSTE) experiment for surfactant molecules residing in the RM interface. Inverse Laplace transformation of these data generated diffusion coefficients for the RMs, which were converted into hydrodynamic radii using the Stokes−Einstein relation. This technique is complementary to those previously used to size RMs, such as dynamic light scattering (DLS) and small-angle X-ray scattering (SAXS), but also offers several advantages, which are discussed. RM sizes, determined using the PGSTE method, in the AOT (sodium bis(2-ethylhexyl) sulfosuccinate) and CTAB (cetyltrimethylammonium bromide) microemulsions were compared with previous DLS and SAXS data, showing good agreement. Methods for determining number distributions from the PGSTE data, through the use of scaling factors, were investigated.

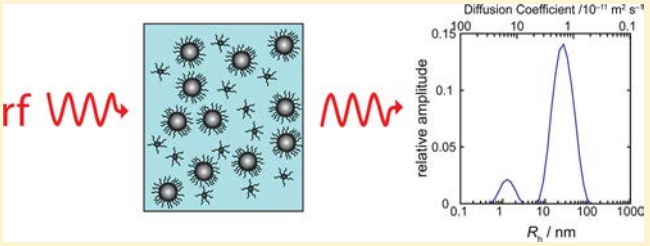

INTRODUCTION

Reverse micelles (RMs) are composed of nanosized water droplets sequestered by surfactants in a continuous organic phase. These self-assembled structures form thermodynamically stable droplets of water ranging in intramicellar diameter from approximately 1 to 20 nm, depending on the molar water-to-surfactant ratio (ω).[1] The aqueous core of RMs provides a highly adaptable environment for a variety of chemical and biochemical reactions,[2,3] protein extraction,[4] synthesis of nanoparticles,[5] as well as providing a model for biological systems.[6,7] For all of these applications, an understanding of the structure, size and polydispersity of the RMs is important, as well as an understanding of how these vary with ω and/or the presence of additional ions and molecules.

Dynamic light scattering (DLS), also known as photon correlation spectroscopy or quasi-elastic light scattering, is an extremely popular method[8] used for determining the size of RMs, as their hydrodynamic radii are typically in the submicrometer range. In DLS, the temporal fluctuations of light scattered by diffusing particles in liquid suspension are measured, which are sensitive to the diffusive motion of the particles. Analysis of the scattered light yields the diffusion coefficients (D) of the particles in suspension, which leads, where particles are spherical, to the hydrodynamic radii (R_h) using the Stokes−Einstein relation, eq 1:

$$D = k_B T/(6\pi\eta R_h) \quad (1)$$

where η is the viscosity of the pure solvent, T is the temperature, and k_B is the Boltzmann constant.

While DLS is widely used to probe the size and size distributions of submicrometer-sized particles, proteins, and RMs, it is known to have a few limitations and drawbacks.[9−12] It can struggle to find the correct particle size distributions in systems, which contain polydispersed particles or droplets, where their sizes range over several orders of magnitude. In these systems, the contribution of light scattered from smaller particles can be swamped by the light scattered by larger particles. The technique is also sensitive to the presence of dust particles, which produce bursts of high-intensity scattered light, as the larger, unwanted light-scatterers move through the illuminated sample.[10,11] Thus it becomes necessary to either completely remove all dust particles from the sample by filtration or perform additional analysis of the data.[11] However, this can sometimes require considerable effort and is sometimes not desirable or possible. Other problems arise when the dielectric constant for the droplet matches the continuous organic phase, a condition called the optical matching point, where the droplets become invisible in light scattering experiments.[13] Also, extreme caution is required in the transformation of the DLS data into number distributions, which are the distributions typically reported. DLS generates an intensity-weighted size distribution, which is converted in a volume distribution, using Mie theory[14] and then further transformed into a number distribution. Unfortunately, when using this method, small errors in data collection can lead to large errors in the number distribution[10,15] and is particularly a problem when the polydispersity of the sample is high.[16] Hence, conversion into number distributions is discouraged.[17]

An alternative method for measuring the diffusion coefficients of RMs is the magnetic resonance (MR) pulsed field gradient (PFG) experiment.[18,19] This method is known[20]

Received: February 24, 2012
Revised: July 13, 2012
Published: July 14, 2012

to provide accurate measurements of D and, while its analysis is analogous to the DLS method, requiring the inverse Laplace transform (ILT) and Stokes–Einstein relation to generate particle size distributions from diffusion measurements, it offers several advantages over DLS. First, MR methods are able to probe optically opaque or particularly turbid solutions. MR measurements are unaffected by the presence of dust particles or by the dielectric constant[13,21] of the constituents of the microemulsion. MR can also distinguish between different molecular species in a sample. A few studies have been reported in the literature[6,22−28] that measure the diffusion coefficients of RMs using PFG experiments, probing the restricted diffusion of molecules inside the emulsion droplet. These experiments have typically yielded single, averaged diffusion coefficients for the RMs by measuring the surfactant or cosurfactant signal and fitting the data to the Stejskal–Tanner relationship[29] (eq 2), which have then been converted into a single average value for the droplet size using the Stokes–Einstein relation. Droplet size distributions have been generated from PFG data for emulsions, by Ambrosone et al.[30] using a nonlinear least-squares fitting procedure and a "generating function" series. Other emulsion droplet sizing studies[31−33] use log-normal distribution fitting procedures or regularisation methods based on the distribution area or second derivative of the distribution.[34] However, to date, no studies have been reported where droplet size distributions have been determined using PFG methods for RMs in a microemulsion. Yet, PFG measurements have been successfully combined with the ILT to measure size distributions and polydispersity for polymers,[35,36] colloidal systems,[37,38] and porous media.[39]

In this paper, we demonstrate for the first time the application of PFG measurements with the ILT, to produce droplet size distributions of RMs in sodium bis(2-ethylhexyl) sulfosuccinate (AOT) and cetyltrimethylammonium bromide (CTAB) microemulsions. Using this method, we investigate the change in droplet size as a function of the water-to-surfactant ratio, ω, volume droplet fraction, ϕ_d, composition and solution age. While this paper has focused on the RMs formed using AOT or CTAB surfactants, the methods described in this paper can be readily adapted to investigate the size and distributions for a variety of micelle, RM, and microemulsion systems. These methods could also be developed into two-dimensional techniques,[40] providing insight into the dynamics of these systems, mixing of material between droplets, and the exchange of surfactant or water molecules between droplets.

EXPERIMENTAL SECTION

Reverse Micelle Preparation. A stock solution of 1.5 M AOT (Fluka, ≥96%) in *n*-octane (Acros, 97%) was prepared by dissolving 111.14 g of AOT in 70 mL of *n*-octane. Microemulsions were prepared at water-to-surfactant ratios of ω = 5.3−35 and at a droplet fraction of ϕ_d = 0.15, by adding the correct volume of water (Nanopure filtered, 18 MΩ) to the 1.5 M AOT solution to produce the required ω and diluting with *n*-octane to give ϕ_d = 0.15. By using a droplet fraction of 0.15, it is not necessary to make any correction for collisions, as would be the case in more concentrated solutions. Diffusion measurements were taken 2 h after the samples were prepared. Additional AOT microemulsions were also prepared, which included additives and were studied as a function of time and ϕ_d. The first[41,42] was prepared at ω = 15 and ϕ_d = 0.55, loaded with H_2SO_4 (Fisher >95%) = 0.4 M and malonic acid (Alfa Aesar 99%) = 0.6 M. Diffusion measurements were taken at t = 2 h and t = 24 h. The second[43] was prepared at ω = 12 and ϕ_d = 0.5, 0.4, 0.25, and 0.15, and was loaded with H_2SO_4 = 0.25 M, malonic acid = 0.25 M, and $NaBrO_3$(Alfa Aesar 99.5%) = 0.16 M. Lastly, a CTAB/hexanol/water microemulsion was prepared with CTAB (cetyltrimethylammonium bromide; Sigma ≥98%) and 1-hexanol (Acros 98%) at ω = 7.2, and ϕ_d = 0.4, giving a 3:1 w % ratio of CTAB/H_2O.[44]

Pulsed Gradient Stimulated Echo Experiments. ^{1}H NMR pulsed gradient stimulated echo (PGSTE) experiments[20] were used to measure the diffusion coefficients of the surfactant molecules in the RMs. This method applies two magnetic field gradient pulses of strength **G** and duration δ, which are separated by an observation time Δ.[45] In the case of diffusion, where molecular motion is incoherent, molecular displacements over the time scale Δ produce a distribution of phase shifts in the MR signal, resulting in an attenuation of the MR signal. The MR signal is acquired over a range of **G** values, and a diffusion coefficient can be calculated using the Stejskal–Tanner relationship:

$$\frac{S(\mathbf{G})}{S(0)} = \exp\left[-\gamma^2\delta^2\mathbf{G}^2D\left(\Delta - \frac{\delta}{3}\right)\right] \quad (2)$$

where $S(\mathbf{G})$ is the signal at gradient amplitude **G**, and $S(0)$ is the signal at zero gradient. In PGSTE experiments, a stimulated echo[20] is used, which stores the magnetization along the longitudinal axis during the relatively long observation time, making it less susceptible to T_2 relaxation. This is beneficial in samples where the T_2 is significantly shorter than T_1, which is frequently the case for protons in surfactant molecules in an RM. The stimulated echo experiment also has the advantage over the equivalent spin echo (PGSE) experiment, of not being so affected by peak distortions caused by J-coupling.[46]

PGSTE experiments were performed on a Bruker DMX300-spectrometer equipped with a 7.0 T superconducting magnet, operating at a frequency of 300.13 MHz. A 10 mm radiofrequency resonator was used, and measurements were performed at 289 ± 0.3 K. A total of 64 signal averages were collected with a repetition time of 1s. Typical parameters used in these experiments were δ = 4 ms, Δ = 100 ms, with a maximum gradient, $\mathbf{G}_{max}$, of 0.9 T m^{-1}, and 32 or 256 gradient steps, ensuring the signal attenuated so that $S(\mathbf{G})/S(0)$ at $\mathbf{G}_{max}$ was ≤0.01. The gradient system was calibrated by measuring the diffusion coefficient of *n*-octane. A value of 1.998 ± 0.01 × 10^{-9} m^2 s^{-1} was measured at 289 ± 0.3 K, which is the expected value compared to the previously reported temperature dependency of the diffusion coefficient for *n*-octane.[47] Diffusion data was collected for each system using a proton resonance that was in or near the headgroup of each surfactant. In the case of the AOT microemulsions, proton H_3 on the AOT molecule was used (Figure 1a), and, in the case of the CTAB

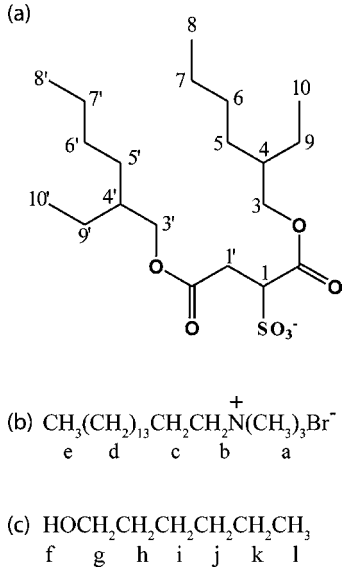

Figure 1. Molecular structure and numbering scheme for protons in the AOT (a), CTAB (b), and hexanol (c) molecules.

dx.doi.org/10.1021/la300796u | *Langmuir* 2012, 28, 11699−11706

microemulsion, proton H_a on the CTAB molecule was used (Figure 1b). Using these data, average diffusion coefficients were obtained using the Stejskal–Tanner relationship (eq 2), while diffusion coefficient distributions were determined using the ILT.[48,49] In the ILT analysis, plots of $\mathbf{G}(D)D$ vs $\log(D)$ are produced, where $\mathbf{G}(D)$ is the distribution function with respect to D. A constrained regularization ILT method[35,48−52] was used, which assumed $\mathbf{G}(D)$ was non-negative and smooth, and the noise was additive, Gaussian, and had a zero mean. The regularization parameter used was α, which measured the smoothness of $\mathbf{G}(D)$. The optimal value of α, was determined by repeating the ILT and measuring χ^2, where χ is the fit error, as a function of α.[51,52] The lowest value of α was then chosen, before χ^2 rapidly increased, corresponding to the point where the narrowest distribution was possible, without introducing spurious peaks generated by fitting the noise.[51] Typical signal-to-noise ratios, calculated as the maximum signal divided by the standard deviation of the noise, were around 65 for the H_3 peak in the AOT microemulsions and 1000 for the H_a peak in the CTAB microemulsions. Typical PGSTE diffusion data, for the H_3 peak in an AOT/octane/water microemulsion, are shown in Figure 2. Hydrodynamic radii, R_h, were

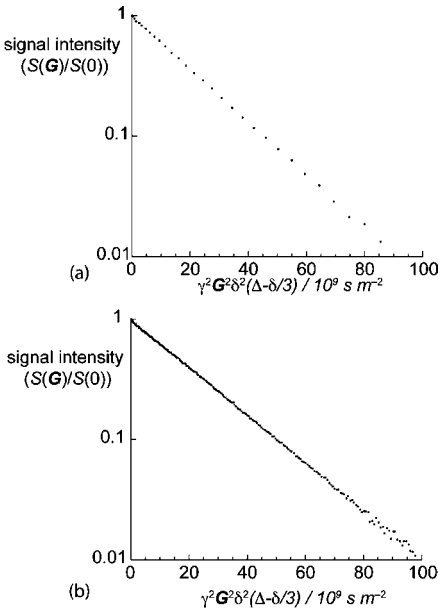

Figure 2. PGSTE diffusion data for the H_3 peak in an AOT/*n*-octane/H_2O microemulsion at $\omega = 15$ and $\phi = 0.15$, where $\Delta = 100$ ms, $\delta = 4$ ms, and $G_{max} = 0.9$ T m^{-1}. A total of 32 (a) or 256 (b) gradient steps were collected, with 64 signal averages.

determined from an average diffusion coefficient or diffusion coefficient distribution using the Stokes–Einstein relationship (eq 1). Viscosity values of 0.563 and 5.85 cP were used for *n*-octane and hexanol, respectively, at $T = 290$ K. Errors were determined from analysis of the variation between repeated experiments for a given system.

Dynamic Light Scattering. DLS measurements were performed on a Delsa-Nano Submicrometer (Class 1 Laser) Particle Size Analyzer. All solutions were filtered prior to measuring with a PTFE filter membrane (VWR). The microemulsions were allowed to equilibrate for 300 s at 290 K, and data was accumulated for 100 s with five repetitions. The time domain correlation method was used with CONTIN analysis.[48] A refractive index of 1.3975 was used for *n*-octane with a viscosity of 0.563 cP at 290 K. DLS measurements were made for the AOT/*n*-octane/H_2O samples at $\omega = 5.3 - 35$ with a droplet fraction of $\phi_d = 0.15$. The number distribution is reported.

RESULTS

^{1}H NMR spectra for the AOT/*n*-octane/water and CTAB/hexanol/water microemulsions are shown in Figure 3. These

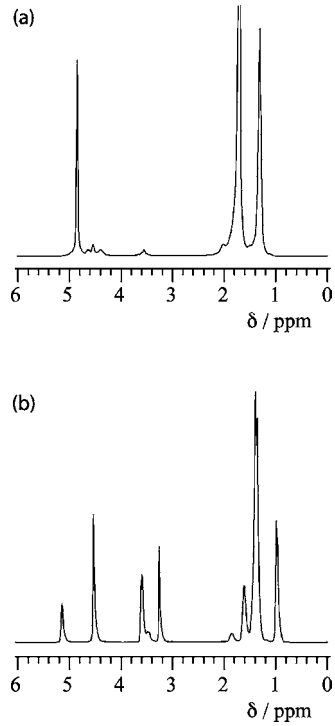

Figure 3. ^{1}H NMR spectra of AOT/*n*-octane/H_2O (a) and CTAB/hexanol/H_2O (b) microemulsions.

microemulsions have been previously characterized by NMR spectroscopy[44,53] and peak assignments for these spectra are given in Table 1 for the AOT microemulsion and Table 2 for

Table 1. ^{1}H NMR Peak Assignments for AOT/*n*-Octane/H_2O Microemulsion

peak assignments	δ/ppm
H_8, H_8', H_{10}, H_{10}', $H_{(octane)}$	1.29
H_5, H_5', H_6, H_6', H_7, H_7', H_9, H_9', $H_{(octane)}$	1.70
H_1	4.61
H_1'	3.54
H_3	4.52
H_3'	4.38
H_4, H_4'	1.99
H_2O	4.84

Table 2. ^{1}H NMR Peak Assignments for CTAB/Hexanol/H_2O Microemulsion

peak assignments	δ/ppm
H_f	5.09
H_2O	4.48
H_g	3.54
H_b	3.42
H_a	3.22
H_c	1.79
H_h	1.56
H_d, H_i, H_j, H_k,	1.34
H_e, H_l	0.94

dx.doi.org/10.1021/la300796u | *Langmuir* 2012, 28, 11699−11706

the CTAB microemulsion. Figure 4a gives the average diffusion coefficients for AOT surfactant molecules in the AOT/*n*-

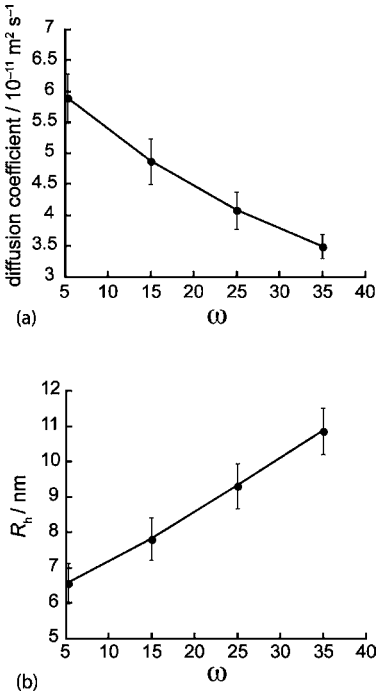

Figure 4. Plots of the average diffusion coefficient (a) and hydrodynamic radii (b) for RMs in AOT/*n*-octane/H_2O microemulsions, at varying ω and ϕ_d = 0.15. The diffusion coefficients were determined using the 32 gradient step PGSTE data from the H_3 proton on the AOT headgroup and fitted to the Stejskal–Tanner equation.

octane/water system, following fitting of the PGSTE data to the Stejskal–Tanner equation (eq 2). As the surfactant molecule resides in the interface of the RM, these diffusion coefficients provide a measure of the diffusion coefficient of the RM. By using the Stokes–Einstein relation (eq 1), droplet sizes for the RMs were calculated, as a function of ω, and are presented in Figure 4b. Analysis of the DLS data for the samples reported in Figure 4 gave average droplet sizes of 1.2 ± 0.3 nm at ω = 5.3; 1.65 ± 0.5 nm at ω = 15; 3.15 ± 0.8 nm at ω = 25 and 3.9 ± 1.1 nm at ω = 35.

ILT of PGSTE data produces a distribution of diffusion coefficients (Figure 5a), which have been converted into a distribution of molecular sizes (Figure 5b,c) using the Stokes–Einstein equation (eq 1). Analysis of the distribution maxima for the 32 gradient step (Figure 5b) PGSTE data produced R_h values of 6.5 ± 0.5 nm at ω = 5.3; 7.5 ± 0.7 nm at ω = 15; 9.1 ± 0.8 nm at ω = 25; and 11.8 ± 2 nm at ω = 35. R_h values for the 256 gradient step (Figure 5c) PGSTE experiments yielded values of 6.3 ± 0.5 nm at ω = 5.3; 7.8 ± 0.7 nm at ω = 15; 8.9 ± 0.8 nm at ω = 25; and 14.7 ± 2 nm at ω = 35.

The effect of additives on the size and stability of RMs was investigated by measuring diffusion coefficients and determining droplet size distributions for two AOT/*n*-octane/water microemulsions loaded with H_2SO_4 (0.4 M) and malonic acid (0.6 M)[42] or H_2SO_4 (0.25 M), malonic acid (0.25 M), and BrO_3^- (0.16 M)[43] as a function of time and droplet fraction, respectively. These systems are known[42,43] to produce bimodal droplet size distributions, which become unimodal after time[42] ($t \geq 24$ h) or lower droplet fraction[43] ($\phi_d < 0.5$). Droplet size

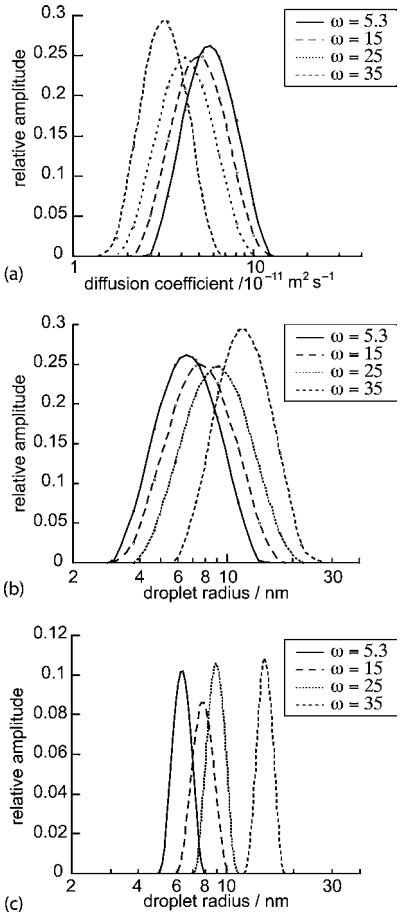

Figure 5. Plots of the diffusion coefficient distributions (a) and droplet size distributions using 32 gradient steps (b) and 256 gradient steps (c) for RMs at varying ω in AOT/*n*-octane/H_2O microemulsions at ϕ_d = 0.15. The diffusion coefficients were determined using the PGSTE data for the H_3 proton on the AOT headgroup, using the ILT. RM size distributions were generated from the diffusion coefficient distributions using the Stokes–Einstein relation.

distributions determined using PGSTE measurements are presented in Figure 6 for the system previously investigated by Vanag et al.[42] for fresh and 24 h old samples. Figure 7 shows the size distributions of RMs in the system previously investigated by Alvarez et al.,[43] at varying droplet fractions.

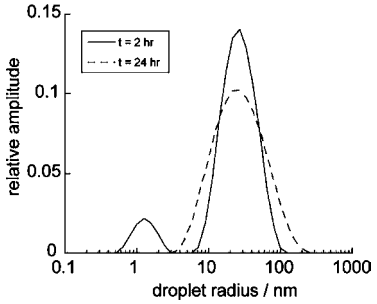

Figure 6. Droplet size distributions for RMs in the AOT/*n*-octane/H_2O microemulsion loaded with [H_2SO_4] = 0.4 M and [malonic acid] = 0.6 M at ω = 15 and ϕ_d = 0.55 at 2 and 24 h after preparation. Size distributions were produced by applying the Stokes–Einstein relation to diffusion coefficient distributions produced by ILT of the PGSTE data for AOT H_3 proton. 32 gradient steps were used.

dx.doi.org/10.1021/la300796u | *Langmuir* 2012, 28, 11699–11706

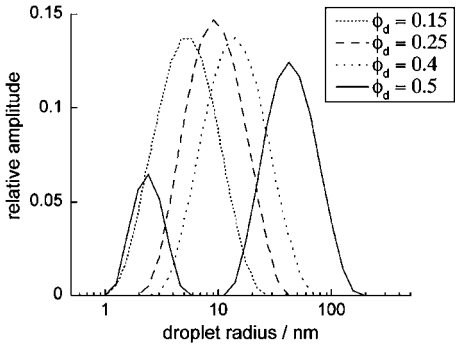

Figure 7. Droplet size distributions for RMs in the AOT/*n*-octane/H_2O microemulsion loaded with [H_2SO_4] = 0.25 M, [malonic acid] = 0.25, and 0.16 M [$NaBrO_3$] at ω = 12, at ϕ_d = 0.15−0.5. Size distributions were produced by applying the Stokes−Einstein relation to diffusion coefficient distributions produced by inverse Laplace transformation of the PGSTE data for AOT H_3 proton. 32 gradient steps were used.

Finally, the diffusion coefficients and droplet size distributions for the CTAB/hexanol/water microemulsion (ω = 7.2 and ϕ_d = 0.4) determined using PGSTE experiments, are presented in Figure 8. A droplet size of 0.9 nm was determined from the droplet size distribution.

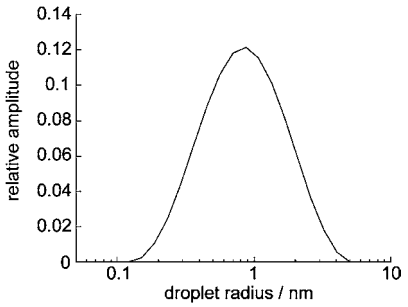

Figure 8. Droplet size distribution for RMs in a CTAB/hexanol/H_2O microemulsion at ω = 7.2 and ϕ_d = 0.4. Size distributions were produced by applying the Stokes−Einstein relation to diffusion coefficient distributions produced by inverse Laplace transformation of the PGSTE data for CTAB H_a proton. 32 gradient steps were used.

DISCUSSION

Comparison of the RM size distributions using 32 or 256 gradients steps shows good agreement between the R_h values produced. Yet, it can be seen, when comparing panels b and c of Figure 5, that the width of the distribution is dependent on the number of gradient steps acquired. As the width of the distributions are sensitive to the number of gradient steps collected, as well as the parameters used in the ILT, such as the α value, we do not suggest that these results can be used to determine the polydispersity of the RMs. However, even though the distribution widths are seen to change, the R_h values were not found to change significantly with these.

Comparisons between our R_h values were made with those previously reported. RMs in AOT/octane/water microemulsions are some of the most studied in the literature, with a number of papers reporting their size using DLS,[54−59] small-angle X-ray scattering (SAXS),[60−62] and fluorescence correlation spectroscopy (FCS),[13] as a function or ω and ϕ_d. The sizes typically reported using these methods are on the order of 2.5−9.5 nm for ω values of 5−35 (Figure 9). By comparing our PGSTE-determined droplet sizes with our DLS data and the

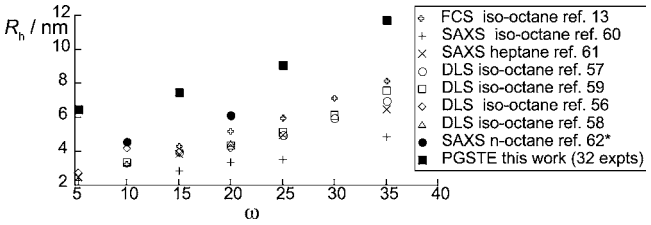

Figure 9. Plot of droplet size (R_h) dependence on ω for values reported in the literature using DLS,[56−59] FCS,[13] and SAXS[60−62] methods. *The values given for R_h were determined using the r_w value reported in ref 62 with 2 × 1.5 nm added to account for the width of the surfactant layer around the water core.

data previously reported, it is clear that our hydrodynamic radii are larger. The origins of these differences are, as yet, unclear. These discrepancies could lie in errors in the PGSTE data associated with exchange of surfactant molecules, during the observation time (Δ), between droplets of difference sizes. However, as previous investigations of AOT/octane/water microemulsions do not indicate the presence of larger RMs, it seems unlikely that the error can arise simply from exchange. It is possible that differences between PGSTE and DLS methods could lie in the errors introduced during the conversion of DLS data to number distributions. Indeed, the use of number distributions is discouraged,[17] although they are frequently reported in the literature. Yet, this does not explain why our values are larger than those determined by FCS and some SAXS studies. Further investigation is required.

While our droplet sizes for the AOT/octane/water microemulsions are larger than those previously reported, our values for the microemulsions containing additives actually compare well. In these systems, bimodal size distributions are produced, as have been previously observed[42,43] in DLS measurements. In the system studied by Vanag et al.,[42] the bimodal behavior was observed in fresh samples, which become unimodal with time. This behavior is also observed in the PGSTE data. In the fresh sample, there were peaks at 1.3 and 25.8 nm, which compares closely with the values observed by Vanag et al. of 2 and 20 nm. At 24 h after mixing, the sample was unimodal, with an average droplet size of 25.1 nm. This value is, however, significantly higher than that observed by DLS, which measured a size distribution centered at 3.6 nm. In the system previously studied by Alvarez et al., a transition from bimodal to unimodal size distributions was observed as a function of volume fraction, rather than time. Bimodal behavior was observed at a ϕ_d value of 0.5, with R_h values of 2.4 and 42.1 nm for the two peaks. This behavior was previously observed by DLS, with peaks centered at 2−3 nm and 20−30 nm.[43] As ϕ_d was reduced, the system became unimodal, and droplet sizes of 13.8 nm (ϕ_d = 0.40), 9.1 nm (ϕ_d = 0.25) and 5.2 nm (ϕ_d = 0.15) were observed. Unimodal distributions have also been observed by DLS; however, the peak for the distribution presented in ref 43 was lower at 2−3 nm, although the volume fraction for the data was not reported.

While the RM sizes show general agreement with previous DLS measurements, there are differences with the distribution of droplets. The origins of this lie in how the diffusion coefficients of the RMs are determined and what the PGSTE measures. Just as DLS measures intensity distributions, which

dx.doi.org/10.1021/la300796u | *Langmuir* 2012, 28, 11699−11706

are then converted into number distributions, so PGSTE data should also be scaled to produce a number distribution of droplet sizes. Such scaling is necessary where the droplet size ranges corresponded to a range of droplets containing different amounts of surfactant molecules. Thus, if larger droplets contain greater numbers of surfactant molecules, it is necessary to take this into account. Hence, the droplet size distributions need to be scaled in order to produce a number distribution.

In our experiments, droplet sizes are determined from diffusion coefficients calculated from the PGSTE data of the surfactant molecules, which are dominated by the diffusion rate of the RM (where all surfactant molecules are located in the RM). The surfactant molecules surround the water core of the RM, so their number, N_s, is expected to increase proportionally with r_w^2, where r_w is the radius of the water core. As the PGSTE signal is integrated over all surfactant molecules, it means that surfactant molecules in larger droplets will contribute more to the distribution of diffusion coefficients than smaller droplets. In order to correct the droplet size distributions for this, it is necessary to divide the relative amplitude by the number of surfactant molecules, N_s, contributing to the PGSTE decay for each droplet size (R_h). Calculation of N_s provides a method for scaling the PGSTE data, leading to a number distribution of RM droplet sizes. In order to determine N_s, the size of the droplet core, r_w, was first calculated for each value of R_h using eq 3 and a value of 1.5 nm for δ, the thickness of the surfactant layer.[13]

$$R_h = (r_w^3 + 3\delta r_w^2)^{1/3} \quad (3)$$

Using the size parameters determined previously[54,63] for the AOT/iso-octane/water system (Table 3), N_s was determined,

Table 3. Size Parameters for the AOT/Iso-octane/Water System Taken from Ref 54

ω	N_s	R_h/nm	r_w/nm
4	35	2.5	1.0
6	50	2.8	1.4
8	72	3.2	1.6
10	98	3.4	1.9
12	129	3.7	2.2
14	176	4.0	2.6
16	215	4.2	2.9
18	257	4.3	3.2
20	302	4.4	3.5
25	447	5.2	4.3
30	613	6.2	5.1
35	778	7.6	5.8

as a function of r_w, for each value of R_h in the droplet size distributions. Number distributions were then generated by dividing the relative amplitude by N_s at each value of R_h. A limitation with this method, however, is that it requires prior characterization of the system. An alternative method to scale the distributions would be to simply use r_w^2 as a scaling factor and include an offset to take into account the surfactant aggregation number in the absence of water. Previous studies have determined the aggregation number for AOT in iso-octane to be 22.[64] Using this, number distributions were produced by scaling the data by $(r_w^2 + 22)$. This scaling, however, assumes that the area (a_s) occupied by the surfactant headgroup at the water core interface remains constant over the range of droplet sizes observed, an assumption made by other studies.[13,21]

Using both N_s and $(r_w^2 + 22)$ scaling methods, number distributions were produced for the AOT microemulsions containing additives, which are presented in Figure 10. These

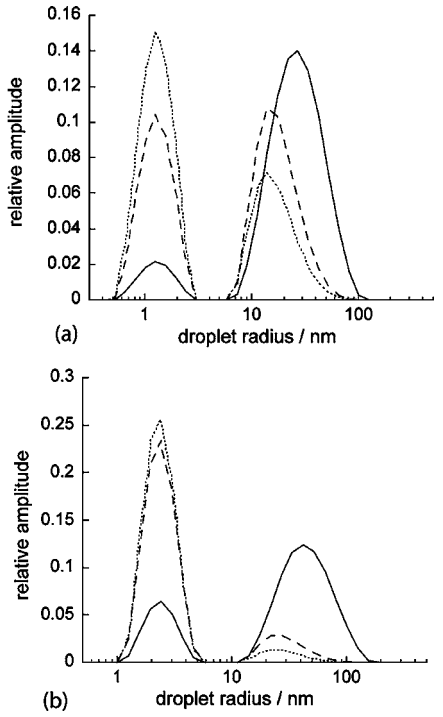

Figure 10. Droplet size distribution for RMs in an AOT/*n*-octane/H_2O microemulsion loaded with (a) $[H_2SO_4]$ = 0.4 M and [malonic acid] = 0.6 M at ω = 15 and ϕ_d = 0.55 (unscaled data from Figure 6) and (b) $[H_2SO_4]$ = 0.25 M, [malonic acid] = 0.25 and 0.16 M $[NaBrO_3]$ at ω = 12 and ϕ_d = 0.5 (unscaled data from Figure 7). R_h values are given for data that is unscaled (——), scaled by N_s (- - - -), and scaled by $(r_w^2 + 22)$ (·····).

distributions now show a higher proportion of smaller droplets, compared to the unscaled distributions. The average RM sizes for each mode are also slightly smaller. It should be noted that this method of scaling may not be applicable in these systems, as it assumes the larger droplets are also spherical, which may not be the case. Further work is required to determine which is the most appropriate scaling for these systems. However, regardless of the precise details of the scaling used, our method for determining number distributions of RMs in microemulsions has advantages over the methods used for determining size distributions in macroemulsions, which probe the restricted diffusion of molecules contained inside the droplets and hence require a scaling proportional to a^3, where a is the droplet radius.[34]

The need for a scaling factor also has further implications for the accuracy of average diffusion coefficients calculated using the Stejskal–Tanner equation, and their use in determining droplet sizes in multimodal systems. While the use of average diffusion coefficients may be sufficient to determine R_h for unimodal systems, they will struggle in multimodal systems. In multimodal systems, the signal from surfactant molecules in larger droplets will contribute more toward the diffusion data than molecules from smaller droplets. In the Stejskal-Tanner analysis, relative contributions are not produced as a function of

dx.doi.org/10.1021/la300796u | *Langmuir* 2012, 28, 11699–11706

droplet size, therefore, there is no mechanism by which the data can be directly scaled, particularly without prior knowledge of the droplet size distribution. Thus, this shows that MR measurements of average diffusion coefficients, should be treated with caution for multimodal systems.

The last system investigated using this method was the CTAB/hexanol/water microemulsion. While this microemulsion has been widely studied in the literature, droplet sizes of RMs in this system have been significantly less well characterized than AOT microemulsions. In this system, R_h was calculated to be 0.9 nm, which compares well with previous droplet size measurements,[65] where a droplet size of 1.1 nm was measured for a CTAB/hexanol/water microemulsion (2.6:1 ratio % wt of CTAB/H_2O)).

CONCLUSION

In this paper, we report the first application of MR measurements of diffusion to produce, using the ILT and Stokes−Einstein relation, droplet size distributions for RMs in AOT and CTAB microemulsions. Our measurements are complementary to the methods previously used to size RMs and yield values similar to those produced by DLS. However, RM sizes in the AOT/*n*-octane/water microemulsion were found to be larger compared to those measured by optical methods, particularly at lower ω values. While we do not suggest that our data should be used to determine the polydispersity of RM sizes, it may be possible to use these methods to compare changes in size distributions as a function of ω, ϕ_d, or composition. Scaling factors were investigated that enabled number distributions to be generated and, when used, were shown to shift the distributions toward smaller droplet sizes, reducing the average droplet size. The suitability and need for these scaling factors, however, needs further investigation.

Finally, while this paper has focused on MR methods to measure RM sizes, we would like to add that these experiments can easily be adapted into two-dimensional techniques, such as diffusion-relaxation correlation spectroscopy (DRCOSY)[66] and diffusion−diffusion exchange spectroscopy (DEXSY).[40] In these experiments, data is acquired in two-dimensions, followed by two-dimensional Laplace transformation,[52] enabling correlations between diffusion and relaxation behavior, for either surfactant or water molecules, which could lead to greater insight into the behavior of these dynamic structures.

AUTHOR INFORMATION

Corresponding Author

*E-mail address: m.m.britton@bham.ac.uk.

Notes

The authors declare no competing financial interest.

ACKNOWLEDGMENTS

The authors thank the reviewers for probing comments, which have been helpful in the development of this work, and EPSRC and the University of Birmingham for funding. The Delsa Nano Beckman-Coulter DLS instrument used in this research was obtained, through Birmingham Science City: Innovative Uses for Advanced Materials in the Modern World (West Midlands Centre for Advanced Materials Project 2), with support from Advantage West Midlands (AWM) and partly funded by the European Regional Development Fund (ERDF).

REFERENCES

(1) De, T. K.; Maitra, A. Solution behavior of Aerosol OT in nonpolar-solvents. *Adv. Colloid Interface Sci.* **1995**, *59*, 95−193.
(2) Fendler, J. H. Interactions and reactions in reversed micellar systems. *Acc. Chem. Res.* **1976**, *9*, 153−161.
(3) Pileni, M. P. Reverse micelles as microreactors. *J. Phys. Chem.* **1993**, *97*, 6961−6973.
(4) Cöklen, K. E.; Hatton, T. A. Protein extraction using reverse micelles. *Biotechnol. Prog.* **1985**, *1*, 69−74.
(5) Uskokovic, V.; Drofenik, M. Synthesis of materials within reverse micelles. *Surf. Rev. Lett.* **2005**, *12*, 239−277.
(6) Fedotov, V. D.; Zuev, Y. F.; Archipov, V. P.; Idiyatullin, Z. S.; Garti, N. A Fourier transform pulsed-gradient spin echo nuclear magnetic resonance self-diffusion study of microemulsions and the droplet size determination. *Colloids Surf., A* **1997**, *128*, 39−46.
(7) Levinger, N. E. Water in confinement. *Science* **2002**, *298*, 1722−1723.
(8) Schatzel, K. Light-scattering - Diagnostic methods for colloidal dispersions. *Adv. Colloid Interface Sci.* **1993**, *46*, 309−332.
(9) Filipe, V.; Hawe, A.; Jiskoot, W. Critical evaluation of nanoparticle tracking analysis (NTA) by NanoSight for the measurement of nanoparticles and protein aggregates. *Pharm. Res.* **2010**, *27*, 796−810.
(10) Provder, T. *Particle Size Distribution: Assessment and Characterization*; American Chemical Society: Washington, DC, 1987.
(11) Ruf, H. Treatment of contributions of dust to dynamic light scattering data. *Langmuir* **2002**, *18*, 3804−3814.
(12) Ruf, H.; Gould, B. J.; Haase, W. The effect of nonrandom errors on the results from regularized inversions of dynamic light scattering data. *Langmuir* **2000**, *16*, 471−480.
(13) Pal, N.; Verma, S. D.; Singh, M. K.; Sen, S. Fluorescence correlation spectroscopy: An efficient tool for measuring size, size-distribution and polydispersity of microemulsion droplets in solution. *Anal. Chem.* **2011**, *83*, 7736−7744.
(14) De Vos, C.; Deriemaeker, L.; Finsy, R. Quantitative assessment of the conditioning of the inversion of quasi-elastic and static light scattering data for particle size distributions. *Langmuir* **1996**, *12*, 2630−2636.
(15) Finsy, R. Particle sizing by quasi-elastic light-scattering. *Adv. Colloid Interface Sci.* **1994**, *52*, 79−143.
(16) Patty, P. J.; Frisken, B. J. Direct determination of the number-weighted mean radius and polydispersity from dynamic light-scattering data. *Appl. Opt.* **2006**, *45*, 2209−2216.
(17) ASTM Standard E2490, 2009. Standard Guide for Measurement of Particle Size Distribution of Nanomaterials in Suspension by Photon Correlation Spectroscopy (PCS). ASTM International: West Conshohocken, PA, 2009; DOI: 10.1520/E2490-09; www.astm.org.
(18) Lindman, B.; Stilbs, P.; Moseley, M. E. Fourier-transform NMR self-diffusion and microemulsion structure. *J. Colloid Interface Sci.* **1981**, *83*, 569−582.
(19) Stilbs, P.; Moseley, M. E. Multicomponent self-diffusion measurement by the pulsed-gradient spin-echo method on standard fourier-transform NMR spectrometers. *Chem. Scr.* **1980**, *15*, 176−179.
(20) Callaghan, P. T. *Principles of Nuclear Magnetic Resonance Microscopy*; Oxford University Press: Oxford, 1991.
(21) Ricka, J.; Borkovec, M.; Hofmeier, U. Coated droplet model of microemulsions - Optical matching and polydispersity. *J. Chem. Phys.* **1991**, *94*, 8503−8509.
(22) Caboi, F.; Capuzzi, G.; Baglioni, P.; Monduzzi, M. Microstructure of Ca-AOT/water/decane w/o microemulsions. *J. Phys. Chem. B* **1997**, *101*, 10205−10212.
(23) Dahirel, V.; Ancian, B.; Jardat, M.; Meriguet, G.; Turq, P.; Lequin, O. What can be learnt from the comparison of multiscale brownian dynamics simulations, nuclear magnetic resonance and light scattering experiments on charged micelles? *Soft Matter* **2010**, *6*, 517−525.
(24) Gradzielski, M. Recent developments in the characterisation of microemulsions. *Curr. Opin. Colloid Interface Sci.* **2008**, *13*, 263−269.

(25) Hedin, N.; Furo, I. Ostwald ripening of an emulsion monitored by PGSE NMR. *Langmuir* **2001**, *17*, 4746−4752.
(26) Knackstedt, M. A.; Ninham, B. W.; Monduzzi, M. Diffusion in model disordered media. *Phys. Rev. Lett.* **1995**, *75*, 653−656.
(27) Lasic, S.; Aslund, I.; Oppel, C.; Topgaard, D.; Soderman, O.; Gradzielski, M. Investigations of vesicle gels by pulsed and modulated gradient NMR diffusion techniques. *Soft Matter* **2011**, *7*, 3947−3955.
(28) Walderhaug, H.; Johannessen, E. Partition equilibria for alcohols in reverse micellar AOT-oil-water systems studied by PGSE-FT NMR. A comparison between AOT-containing and the corresponding AOT-free systems. *J. Sol. Chem.* **2006**, *35*, 979−989.
(29) Stejskal, E. O.; Tanner, J. E. Spin Diffusion Measurements: Spin Echoes in the Presence of a Time-Dependent Field Gradient. *J. Chem. Phys.* **1965**, *42*, 288−292.
(30) Ambrosone, L.; Ceglie, A.; Colafemmina, G.; Palazzo, G. A novel approach for determining the droplet size distribution in emulsion systems by generating function. *J. Chem. Phys.* **1997**, *107*, 10756−10763.
(31) Fourel, I.; Guillement, J. P.; Lebotlan, D. Determination of water droplet size distributions by low-resolution PFG-NMR. *J. Colloid Interface Sci.* **1994**, *164*, 48−53.
(32) Packer, K. J.; Rees, C. Pulsed NMR studies of restricted diffusion 1. Droplet size distributions in emulsions. *J. Colloid Interface Sci.* **1972**, *40*, 206.
(33) Johns, M. L.; Hollingsworth, K. G. Characterisation of emulsion systems using NMR and MRI. *Prog. Nucl. Magn. Reson. Spectrosc.* **2007**, *50*, 51−70.
(34) Hollingsworth, K. G.; Johns, M. L. Measurement of emulsion droplet sizes using PFG NMR and regularization methods. *J. Colloid Interface Sci.* **2003**, *258*, 383−389.
(35) Chen, A.; Wu, D. H.; Johnson, C. S. Determination of molecular weight distributions for polymers by diffusion-ordered NMR. *J. Am. Chem. Soc.* **1995**, *117*, 7965−7970.
(36) Vieville, J.; Tanty, M.; Delsuc, M. A. Polydispersity index of polymers revealed by DOSY NMR. *J. Magn. Reson.* **2011**, *212*, 169−173.
(37) Griffiths, P. C.; Cheung, A. Y. F.; Davies, J. A.; Paul, A.; Tipples, C. N.; Winnington, A. L. Probing interactions within complex colloidal systems using PGSE-NMR. *Magn. Reson. Chem.* **2002**, *40*, S40−S50.
(38) Valentini, M.; Vaccaro, A.; Rehor, A.; Napoli, A.; Hubbell, J. A.; Tirelli, N. Diffusion NMR spectroscopy for the characterization of the size and interactions of colloidal matter: The case of vesicles and nanoparticles. *J. Am. Chem. Soc.* **2004**, *126*, 2142−2147.
(39) Song, Y.-Q. Using Internal Magnetic Fields to Obtain Pore Size Distributions of Porous Media. *Con. Magn. Reson. A* **2003**, *18A*, 97−110.
(40) Callaghan, P. T.; Godefroy, S.; Ryland, B. N. Use of the second dimension in PGSE NMR studies of porous media. *Magn. Reson. Imag.* **2003**, *21*, 243−248.
(41) Vanag, V. K. Waves and patterns in reaction-diffusion systems. Belousov−Zhabotinsky reaction in water-in-oil microemulsions. *Phys. Usp.* **2004**, *47*, 923−941.
(42) Vanag, V. K.; Epstein, I. R. Dash waves in a reaction-diffusion system. *Phys. Rev. Lett.* **2003**, *90*, 098301.
(43) Alvarez, E. V.; Carballido-Landeira, J.; Guiu-Souto, J.; Taboada, P.; Munuzuri, A. P. Modulation of volume fraction results in different kinetic effects in Belousov−Zhabotinsky reaction confined in AOT-reverse microemulsion. *J. Chem. Phys.* **2011**, *134*, 094512.
(44) Halliday, N. A.; Peet, A. C.; Britton, M. M. Detection of pH in microemulsions, without a probe molecule, using magnetic resonance. *J. Phys. Chem. B* **2010**, *114*, 13745−13751.
(45) Britton, M. M. Magnetic resonance imaging of chemistry. *Chem. Soc. Rev.* **2010**, *39*, 4036−4043.
(46) Torres, A. M.; Dela Cruz, R.; Price, W. S. Removal of J-coupling peak distortion in PGSE experiments. *J. Magn. Reson.* **2008**, *193*, 311−316.
(47) Tofts, P. S.; Lloyd, D.; Clark, C. A.; Barker, G. J.; Parker, G. J. M.; McConville, P.; Baldock, C.; Pope, J. M. Test liquids for quantitative MRI measurements of self-diffusion coefficient in vivo. *Magn. Reson. Med.* **2000**, *43*, 368−374.
(48) Provencher, S. W. A Constrained Regularization Method for Inverting Data Represented by Linear Algebraic or Integral-Equations. *Comput. Phys. Commun.* **1982**, *27*, 213−227.
(49) Provencher, S. W. Contin - A general-purpose constrained regularization program for inverting noisy linear algebraic and integral-equations. *Comput. Phys. Commun.* **1982**, *27*, 229−242.
(50) Borgia, G. C.; Brown, R. J. S.; Fantazzini, P. Uniform-penalty inversion of multiexponential decay data. *J. Magn. Reson.* **1998**, *132*, 65−77.
(51) Fordham, E. J.; Sezginer, A.; Hall, L. D. Imaging multi-exponential relaxation in the (y, $\log_e T_1$) plane, with application to clay filtration in rock cores. *J. Magn. Reson., Ser. A* **1995**, *113*, 139−150.
(52) Song, Y. Q.; Venkataramanan, L.; Hurlimann, M. D.; Flaum, M.; Frulla, P.; Straley, C. T_1−T_2 correlation spectra obtained using a fast two-dimensional Laplace inversion. *J. Magn. Reson.* **2002**, *154*, 261−268.
(53) Binks, D. A.; Spencer, N.; Wilkie, J.; Britton, M. M. Magnetic resonance studies of a redox probe in a reverse sodium bis(2-ethylhexyl)sulfosuccinate/octane/water microemulsion. *J. Phys. Chem. B* **2010**, *114*, 12558−12564.
(54) Maitra, A. Determination of size parameters of water-aerosol OT-oil reverse micelles from their nuclear magnetic-resonance data. *J. Phys. Chem.* **1984**, *88*, 5122−5125.
(55) Zulauf, M.; Eicke, H. F. Inverted micelles and microemulsions in the ternary-system H_2O/aerosol-OT/isooctane as studied by photon correlation spectroscopy. *J. Phys. Chem.* **1979**, *83*, 480−486.
(56) Vasquez, V. R.; Williams, B. C.; Graeve, O. A. Stability and comparative analysis of AOT/water/isooctane reverse micelle system using dynamic light scattering and molecular dynamics. *J. Phys. Chem. B* **2011**, *115*, 2979−2987.
(57) Baruah, B.; Roden, J. M.; Sedgwick, M.; Correa, N. M.; Crans, D. C.; Levinger, N. E. When is water not water? Exploring water confined in large reverse micelles using a highly charged inorganic molecular probe. *J. Am. Chem. Soc.* **2006**, *128*, 12758−12765.
(58) Nazario, L. M. M.; Hatton, T. A.; Crespo, J. P. S. G. Nonionic cosurfactants in AOT reversed micelles: Effect on percolation, size, and solubilization site. *Langmuir* **1996**, *12*, 6326−6335.
(59) Wong, M.; Thomas, J. K.; Nowak, T. Structure and state of H_2O in reversed micelles. *J. Am. Chem. Soc.* **1977**, *99*, 4730−4736.
(60) Liu, J. C.; Li, G. Z.; Han, B. X. Characteristics of AOT microemulsion structure: A small angle X-ray scattering study. *Chin. Chem. Lett.* **2001**, *12*, 1023−1026.
(61) Hirai, M.; Hirai, R. K.; Iwase, H.; Arai, S.; Mitsuya, S.; Takeda, T.; Seto, H.; Nagao, M. Dynamics of w/o AOT microemulsions studied by neutron spin echo. *J. Phys. Chem. Solids* **1999**, *60*, 1359−1361.
(62) Balakrishnan, S.; Javid, N.; Weingartner, H.; Winter, R. Small-angle X-ray scattering and near-infrared vibrational spectroscopy of water confined in aerosol-OT reverse micelles. *ChemPhysChem* **2008**, *9*, 2794−2801.
(63) Eicke, H. F.; Rehak, J. Formation of Water/Oil-Microemulsions. *Helv. Chim. Acta* **1976**, *59*, 2883−2891.
(64) Tovstun, S. A.; Razumov, V. F. On the composition fluctuations of reverse micelles. *J. Colloid Interface Sci.* **2010**, *351*, 485−492.
(65) Rodenas, E.; Valiente, M. The determination of some physical-properties of reverse CTAB micelles in 1-hexanol. *Colloids Surf.* **1992**, *62*, 289−295.
(66) Graham, R. G.; Holmes, W. M.; De Panfilis, C.; Packer, K. J. Characterisation of locally anisotropic structures within isotropic porous solids using 2-D pulsed field gradient NMR. *Chem. Phys. Lett.* **2000**, *332*, 319−323.